Instituut voor Kern- en Stralingsfysica

Single-Particle and Collective Properties around Closed Shells probed by In-Source Laser Spectroscopy

Promotoren:

Prof. Dr. M. Huyse
Prof. Dr. P. Van Duppen

Proefschrift ingediend tot het behalen van de graad van Doctor in de Wetenschappen door

Thomas Elias COCOLIOS

Leuven 2010

ISBN number 978-90-8649-316-6
D/2010/10.705/9

à Mme. Gauthier, pour avoir cru en moi dès mon plus jeune âge.

Acknowledgments

> Who's to say when you get older
> You don't need a toy collection?
> Who's to say when you get older
> That you have to follow convention?
>
> *Katie Melua - Toy Collection.*

A thesis represents the achievement of 4 years of hard work towards a single goal. While the cover bears only my name, it is actually the result of a group effort at many levels and I would like to acknowledge here the many contributions that made it possible.

First of all, I would like to thank my promotors Mark Huyse and Piet Van Duppen who gave me the opportunity to perform this research in IKS. Their continued support, encouragement and guidance have made these last 4 years a trully enlightening experience on all the aspects of academia. Never would I have thought, when meeting Mark for the first time in Vancouver, that I would benefit from such a rich experience.

I would also like to thank the members of the doctoral examination committee, Prof. Dr. Hans-Jürgen Kluge, Prof. Dr. Paul-Henri Heenen, Prof. Dr. Pieter Lievens, Prof. Dr. Gerda Neyens, and Prof. Dr. Nathal Severijns, for their attentive review of the thesis manuscript and the exciting discussions during the first thesis defense.

As evidenced by the long author lists for the different articles that constitute this thesis, none of the experimental work was performed by a single person. I would like to acknowledge in particular the work of Dr. Yuri Kudryavtsev, Dr. Tetsu Sonoda, and Dr. Maxim D. Seliverstov, present or past colleagues from our group on Nuclear Spectroscopy, for their hard work at LISOL or ISOLDE. Their contribution on the gas cell work, the LIST, or the polonium isotopes, respectively, made this whole research possible.

I would like to also extend my thanks to the many people who contributed to the nice research atmosphere within our research group: Prof. Dr. ANA, Beyhan, Deyan, Dieter, Hilde, Iain, Jan, Jarno, Jeroen, Johnny, Marijke, Martin, Nele, Nick, Nikolas, Paul, Prof. Dr.R^2, Thomas R., and Wim. A special note goes to the craziest group members who contributed to my (un)sanity, Maria and Irina. May your laughter propagate for long.

The fun extended well beyond the group itself. I had much fun with many others in IKS. There are so many people who deserve mentioning, it would take another

thesis just to honour them! Nonetheless, I would like to give a particular word for Vâche-Koe who taught me the intricate twists of the Belgian culture, for Π and his unmatched business skills, Simon for not dying on me half-way to Louvain-La-Neuve, and Marieke who grew a few pieces of white hair reading my Dutch. Talking of white hair, a big thanks must go the administration team, past and present: Sally, Katia, Josée, Isabelle, Martine. After so many years with physicists, I understand why Sally's hair is all white! Actually, the whole supporting team from IKS, Nancy, Willy, Dries, Luc, Bert, Pascal, deserve a warm acknowledgement, for their work behind the scenes is essential to our survival.

De taalcursus Nederlands was ook een groot deel van mijn doctoraatsopleiding. Ik wil al de docenten bedanken voor de toffe tijden: Ines, Kitty, Mit, Els, Evelien, Helga, en Ellen. Ik wil ook de Franse Erasmus Candice en Audrey en de Amerikaanse Chelly en Jennifer bedanken. Zonder jullie zou ik vergeten dat er buiten fysica nog een wereld bestaat! Ik bedank ook Ellen en de mensen van de Japanse lessen voor de steun en de kans om mijn Nederlands verder bij te schaven.

Enfin, parce qu'il y a quand meme une vie en dehors de l'université, je voudrais rendre grâce à toutes celles et ceux qui ont toujours été là, Aurélien, depuis des temps immémoriaux, Bénédicte, par-delà les océans, et enfin Andrée, pour toutes ces années et parce que *J'Ai Encore Rêvé D'Elle*. Ma famille fut aussi toujours très importante pour moi. Malgré la distance, vous êtes tous toujours avec moi, mes deux supers sis' Marnia Kaenzig Balibrera Cocolios Avalon et Iphigénie Marie Cocolios, Pépère Maurice et Mémère Missette, Papa Panos et Monique, Maman Brigitte et Wizz et Charly, ... Votre soutient continu et inconditionnel m'a permis d'atteindre mes objectifs les plus fous. Je partage aujourd'hui avec vous tous mes succès.

Ten slotte, miaou miaou miaou, meeeeoooow miaou miaouw rrr Alice. PRrrrhhh.

et Arne.

TEC

Samenvatting

Resonante laserionisatie is een veel gebruikte techniek in de kernfysica om zuivere radioactieve ionenbundels te produceren en om de eigenschappen van grond- en isomere toestanden te bestuderen. In dit doctoraatswerk worden twee verschillende aspecten van resonante laserionisatie onderzocht: de toepassing van de methode bij het bepalen van magnetische dipoolmomenten en ladingsstralen, en de optimisatie van laser ionenbronnen aan ISOL faciliteiten. De experimenten werden uitgevoerd aan de LISOL opstelling, waar een nieuwe gascelconfiguratie ontwikkeld werd en waar magnetische momenten van neutronarme koperkernen onderzocht werden, en aan de ISOLDE opstelling waar de ladingsstraal van poloniumkernen opgemeten werden.

De LISOL gascel ionenbron gebruikt resonante laserionisatie om een grotere efficiëntie en selectiviteit te bereiken. Met behulp van een ^{252}Cf spontane fissiebron werd de efficiëntie zonder laserionisatie opgemeten wat resulteerde in een brede spreiding gaande van 0.03% voor krypton isotopen tot 74% voor cesium isotopen. Er werd een verband vastgesteld tussen de eerste ionisatiepotentiaal en de opgemeten efficiëntie. Tevens volgden de rubidium en cerium isotopen deze trend niet.

Om de selectiviteit van de gascel te verhogen werden twee onderzoeksstrategieën uitgewerkt: een eerste maakte gebruik van de scheiding van het volume waarin de reactieproducten gestopt worden van het volume waarin de reactieproducten geïoniseerd worden. Het eerste volume wordt gebruikt om de reactieproducten te stoppen en te neutraliseren en het tweede om de atomen met behulp van laserlicht resonant te ioniseren . De scheiding tussen de twee ruimtes werd zodanig opgebouwd dat de laatste afgeschermd is van de fotonen en elektronen die door de doorgang van de primaire bundel door de eerste kamer gecreëerd worden. Hierdoor wordt de ladingsdichtheid in de ionisatiekamer veel kleiner en kunnen de foto-ionen enerzijds langer overleven en kunnen anderzijds elektrische velden aangelegd worden om de ongewenste ionen, de resterende elektronen en foto-elektronen te collecteren. De gascel werd offline getest met isotopen van nikkel en online met rhodium. De collectie van ongewenste ionen en elektronen werkte zoals verwacht.

Voor het tweede ontwerp werd de laserionisatie uitgevoerd in de RF-structuur achter de gascel (SPIG). Ongewenste ionen, die uit de gascel komen, worden door een elektrische potentiaal tussen de gascel en de SPIG afgestoten. De atomen die samen met het draaggas uit de gascel stromen worden met behulp van het laserlicht geïoniseerd, vervolgens gevangen in de RF-structuur en getransporteerd naar het versnellersgedeelte van de massaseparator. Deze techniek werd zowel off-line als online met succes getest. Omwille van geometrische en technische beperkingen werd de

LIST mode niet gebruikt om nieuwe bundels van radioactieve kernen aan te maken. Het gebruik van de LIST mode bracht bovendien aan het licht dat een grote fractie van de radioactieve kernen, die op de SPIG zijn gevangen, na verval eveneens in de RF-structuur worden gevangen. Dit veroorzaakt een substantieel lagere selectiviteit.

Naast de efficiëntie en de selectiviteit werd de lijnbreedte van de atomaire overgangen in de gascel en in de supersonische jet onderzocht teneinde in-bron laserspectroscopische metingen te optimaliseren. Een vergelijkende studie van de eigenschappen van de in-bron laserspectroscopie techniek tussen de gascel, LIST mode en hoge temperatuur ionenbron toonde aan dat, in optimale omstandigheden, de LIST mode de beste resultaten oplevert. Met behulp van de nieuwe twee-kamer gascel werd een laserspectroscopische studie van neutronarme koperisotopen uitgevoerd. Een nieuwe waarde van $\mu = +2.582(7)\ \mu_N$ voor het magnetische dipoolmoment van ^{57}Cu werd bekomen. Deze verschilt sterk van de vroeger geraporteerde waarde. De meting werd 68 keer herhaald, telkens gevolgd door een meting op het stabiele isotoop ^{63}Cu om systematische effecten uit te sluiten. ^{57}Cu is één proton verwijderd van de dubbelmagische $N = Z = 28$ ^{56}Ni kern waardoor het magnetische moment een ideale test vormt voor schillenmodelberekeningen. Ons resultaat wordt goed gereproduceerd door theoretische en fenomenologische berekeningen. Het dipoolmoment van ^{58}Cu werd ook bepaald, $\mu = +0.479(13)\ \mu_N$, in overeenstemming met wat wordt verwacht voor een $\pi p_{3/2} \otimes \nu p_{3/2}$ configuratie. Als finale conclusie kunnen we stellen dat onze meting aantoont dat de huidige modellen een behoorlijke beschrijving geven van de kernstructuur in de buurt van de $N = Z = 28$ gesloten schillenconfiguratie.

Aan de ISOLDE opstelling werden drie laserionisatieschema's bestudeerd en werd de bundelintensiteit van $^{193-204}$Po opgemeten. Een totale efficiëntie van meer dan 0.4% werd opgemeten. Dit getal is gebaseerd op werkzame doorsnede berekeningen met behulp van de ABRABLA code. Deze ontwikkeling maakte in-bron laserspectroscopie mogelijk op de $^{193-204,206-211,216,218}$Po isotopen. In dit doctoraatswerk werden enkel de even-A isotopen bestudeerd. Atomaire berekeningen werden met een experimentele King plot vergeleken gebaseerd op de studie van twee verschillende overgangen in $^{200-210}$Po. Dit resulteerde in nauwkeurige waarden voor de elektronische F-factoren, hoewel de specifieke massaverschuivingsconstanten niet gereproduceerd werden door de theorie. Dit laatste leidde tot een grote systematische onzekerheid op $\delta\langle r^2\rangle$. Ondanks deze grote systematische fout, vertonen de afgeleide experimentele $\delta\langle r^2\rangle$ waarden een grote afwijking van het sferische vloeistofdruppelmodel voor $A < 200$. Deze afwijking werd toegeschreven aan de sterke opmenging van de vervormde indringtoestanden in de grondtoestand van de neutron arme polonium isotopen, maar konden, rekening houdend met de verwachte statische vervorming, niet gereproduceerd worden. Beyond Mean Field berekeningen konden het verloop van de gemiddelde ladingsstraal goed reproduceren, maar faalden voor het isotoop ^{192}Po. Tot slot worden de bekomen relatieve ladingsstralen vergeleken met die van de even-Z isotopen in de naburige kernen: ^{78}Pt, ^{80}Hg, ^{82}Pb en ^{86}Rn. Deze verglijking toonde aan dat de afwijking van het sferische vloeistofdruppelmodel veel groter is voor de polonium isotopen dan voor andere $Z < 82$ kernen wat wijst op essentiële verschillen tussen de structuur boven en onder de $Z = 82$ gesloten protonschil.

Abstract

Resonant laser ionisation is a very versatile tool in nuclear physics, used for the production of clean radioactive ion beams as well as for the study of ground-state and isomer properties. In this Ph.D. work, many aspects of resonant laser ionisation are investigated, from improving the performance of laser ion sources at ISOL facilities to the measurement of magnetic dipole moments and charge radii.

The LISOL gas catcher ion source relies on resonant laser ionisation for increased efficiency and selectivity. Using a ^{252}Cf fission source, the element dependence of the non-resonant contribution to the ion beam has been investigated. The efficiency of extraction for a non-laser-ionised element ranges from 0.03% for krypton to 74% for ceasium. A relationship with the ionisation potential is proposed, although a few elements like rubidium and cerium do not verify this relationship.

In order to suppress those non-resonantly-ionised elements, two new approaches are proposed. First, the dual-chamber gas catcher is investigated. This gas catcher is separated in two volumes, one for the stopping and neutralising of the nuclear recoils and one for the laser ionisation. Both volumes are joined by a channel but no direct line of sight is possibe from one to the other. The reduced density of charges in the second volume increases the chances of survival of laser ions and also permits the use of DC electical fields inside the gas catcher to collect ions surviving the neutralisation process. The gas catcher has been characterised in off-line conditions with nickel and on-line conditions with rhodium. The ion collector has been found to perform as expected. However, another source of non-resonant ionisation has been identified in the form of decay of implanted activity on the surface of the gas catcher and of the SPIG rods, producing singly- and doubly-charged ions.

A second approach that has been investigated is that of the Laser Ion Source Trap (LIST) coupled to a gas catcher. By applying an electrical potential between the SPIG and the gas catcher, it is possible to repel any ion coming from the gas cell and get a pure atom beam into the SPIG. The lasers are then overlapped with this beam in order to ionise the element of interest. The LIST mode has been achieved both off-line and on-line, although various restrictions in geometrical overlap and duty factor do not allow for the use of this technique for efficient radioactive ion beam production at the LISOL facility. The same effect of decay from the surface of the SPIG rods is responsible for non-resonant ion contaminants.

A thorough study of the atomic transition linewidth has been performed inside the gas cell and in the super sonic jet using the LIST approach in order to determine in which limits in-source laser spectroscopy in a gas catcher is possible. It concluded

that the conditions in a gas catcher, in spite of the pressure broadening, are more favorable than in a hot-cavity ISOL facility. The study of the isotope shift of the stable nickel isotopes showed however that no information on the changes in the mean-square charge radii can be extracted for the light and medium heavy nuclei.

The hyperfine structure of the copper isotopes, however, is very large and can be resolved with in-gas-cell laser spectroscopy. The magnetic dipole moment of the neutron-deficient copper isotope ^{57}Cu is a key parameter in challenging nuclear models as it should be determined by the outermost proton outside the $N = Z = 28$ closed core ^{56}Ni. This measurement could not be performed in a hot-cavity ISOL facility as this short-lived isotope ($T_{1/2} = 199$ ms) decays before it can diffuse out of the target matrix. A new value for the magnetic dipole moment of $\mu = +2.582(7)\mu_N$ is proposed, in disagreement with the previous β-NMR value but in good agreement with all presently available calculations. The measurement has been repeated 68 times to ensure its accuracy and systematic effects on the stable isotope ^{63}Cu are thoroughly discussed. A more precise value for the magnetic moment of ^{58}Cu is also proposed to be $\mu = +0.479(13)\mu_N$, consistent with a $\pi p_{3/2} \otimes \nu p_{3/2}$ configuration. Similarly as for the nickel isotopes, no information could be extracted from the isotope shifts.

At the ISOLDE facility, the polonium isotopes have been studied. Three laser ionisation schemes have been characterised and the yields for $^{193-204}$Po have been measured. Comparing the yields to the estimated production rates with the ABRABLA code concluded on an ionisation efficiency of at least 0.4%. The contaminants at mass $A = 200$ have been estimated to be less than 5%.

Using these new beams, in-source laser spectroscopy has been performed on the isotopes $^{191-204,206-211,216,218}$Po with counting rates ranging from 0.01 ion·s^{-1} in ^{191}Po to over 10^7 ions·s^{-1} in ^{208}Po, and with half lives ranging from 33 ms in ^{192}Po to 102 years in ^{209}Po. In this Ph.D. work, the analysis of the even-A isotopes is reported. Large-scale atomic calculations were compared to the King plot made from the two transitions studied for $^{200-210}$Po. While high confidence is found on the electronic F-factors, the specific mass shift constants M are in disagreement. This result in a large systematic uncertainty in the extraction of the $\delta\langle r^2\rangle$. Those show nonetheless a large departure from the spherical droplet model for $A < 200$. This departure is not reproduced by including predicted static deformation parameters and the Beyond Mean Field calculations also fail to reproduce the trend of the most neutron-deficient isotope ^{192}Po. Finally, relative charge radii are compared between the neighbouring even-Z elements $_{78}$Pt, $_{80}$Hg, $_{82}$Pb, $_{84}$Po and $_{86}$Rn. It shows that the magnitude of the departure from sphericity is much larger than for $Z < 82$ and highlights the importance that the specific proton shells are playing above $Z = 82$.

Résumé

L'ionisation résonante par radiation laser est un outil très polyvalent en physique nucléaire car il peut être utilisé aussi bien pour la production de faisceaux radioactifs que pour l'étude des propriétés fondamentales et isomériques du noyau. Cette thèse présente de nombreux aspects de l'ionisation résonante par radiation laser, de l'amélioration des performances des sources laser au sein des installations ISOL à l'étude de moments magnétiques dipolaires et de rayons de charge moyens.

La source d'ion de la cellule gazeuse de LISOL repose sur la ionisation résonante par laser pour améliorer son efficacité et sa sélectivité. A l'aide d'une source fissible de ^{252}Cf, la dépendence élémentaire de la partie non-résonante du faisceau d'ion a été étudiée. L'efficacité d'extraction varie de 0.03% pour le krypton à 74% pour le césium. Une relation entre cette efficacité et le potentiel d'ionisation est proposée, bien que certains éléments tels que le rubidium et le cérium ne la suivent pas.

Afin de réduire l'importance de la partie non-résonante du faisceau, deux approches ont été examinées. Tout d'abord, la cellule gazeuse à double chambre: il s'agit d'une cellule gazeuse avec deux volumes distincts, un pour stopper et neutraliser les produits de la réaction nucléaire et un autre pour la réionisation des atomes par les lasers. Les deux volumes sont raccordés l'un à l'autre par un coude, de sorte qu'ils soient optiquement disjoints. La densité de charges dans le deuxième vo-lume étant réduite, les ions qui y sont produits ont une plus grande probabilité de survie; en outre, cela rend possible l'utilisation de champs électriques continus pour la collecte des ions qui survivent au processus de neutralisation dans le premier vo-lume. La cellule gazeuse a été caractérisée hors ligne à l'aide des isotopes stables de nickel et en ligne avec des faisceaux de rhodium. Le collecteur d'ion opère de façon attendue. Cependant, de nombreux ions parviennent encore à rejoindre le faisceau: en effet, les atomes radioactifs implantés sur les parois de la cellule gazeuse ainsi que sur la surface du SPIG forment une source d'ions lorsqu'ils se désintègrent et que le noyau fils recule dans le faisceau sortant, produisant ainsi des ions 1+ et 2+.

Ensuite, la deuxième approche étudiée est celle du LIST couplée à une cellule gazeuse. En appliquant un potentiel entre la cellule gazeuse et le SPIG, il est possible de repousser tous les ions sortant de la cellule. Seul un faisceau atomique atteint le SPIG où les lasers sont utilisés pour ioniser un élément de façon résonante. La technique du LIST a été validée hors ligne ainsi qu'en ligne, bien que certaines restrictions sur la géométrie du système expérimental ne permettent pas d'utiliser cette technique pour la production efficace de faisceaux radioactifs à LISOL. Les contaminants issus de la désintégration de l'activité implantée sur la surface du SPIG restent présents.

Une étude détaillée de la largeur de la résonance atomique dans la cellule gazeuse et dans le jet super sonique a été réalisée afin de déterminer dans quelle mesure il est possible de faire de la spectroscopie en source dans une cellule gazeuse. Elle conclut que, malgré les effets dûs à la pression, les conditions sont généralement meilleures que dans une source chaude. L'étude des changements isotopiques des isotopes stables de nickel révèle cependant que les changements du rayon de charge moyen ne peuvent pas être déterminés pour les isotopes légers et moyennement lourds.

Avec seulement un proton de plus que le noyau doublement magique $N = Z = 28$ ^{56}Ni, l'isotope ^{57}Cu présente un intérêt particulier car son moment dipolaire devrait, normalement, être déterminé par une seule particule. La structure hyperfine des isotopes de cuivre est assez large pour être déterminée par spectroscopie laser en source. Cepedant, ce noyau ne peut pas être étudié dans une source chaude à cause de sa courte demi-vie ($T_{1/2} = 199$ ms) comparativement au temps de diffusion de l'élément dans la cible, et la cellule gazeuse s'impose comme choix de prédilection. Un moment magnétique dipolaire d'une valeur de $\mu = +2.582(7)\mu_N$ est proposé, en désaccord avec la valeur déterminée par β-NMR mais en bien meilleur accords avec les calculs théoriques et phénoménologiques. La mesure fut répétée 68 fois et les effets systématiques ont été analysés à l'aide de l'isotope stable ^{63}Cu afin de garantir l'exactitude de cette valeur. Une valeur plus précise du moment magnétique dipolaire du ^{58}Cu de $\mu = +0.479(13)\mu_N$ est également proposée, consistente avec une configuration du type $\pi p_{3/2} \otimes \nu p_{3/2}$. De même que pour les isotopes de nickel, aucune information sur les rayons de charge moyens ne peut être extraite.

A l'installation ISOLDE, les faisceaux de polonium ont été le sujet d'une investigation. Trois nouveaux schémas d'ionisation ont été découverts et caractérisés. L'intensité des faisceaux de $^{193-204}$Po a été déterminée et, en comparant ces intensités aux prédictions du code ABRABLA, une efficacité supérieure à 0.4% a été déterminée. Les contimants pour la masse $A = 200$ sont évalués à moins de 5% du faisceau.

Grâce à ces nouveaux faisceaux, la spectroscopie laser en source des isotopes $^{191-204,206-211,216,218}$Po a été réalisée avec des intensités allant de 0.01 ion·s^{-1} pour ^{191}Po à 10^7 ions·s^{-1} pour ^{208}Po, et couvrant des demi-vies allant de 33 ms pour le ^{192}Po à 102 années pour le ^{209}Po. Dans cette thèse, seule l'analyse des isotopes de masse paire est discutée. Le résultat des calculs atomiques à grande échelle est comparé aux données expérimentales par le tracé de King comparant les isotopes $^{200-210}$Po étudiés par deux transitions différentes. Cette comparaison montre que les facteurs F sont calculés avec justesse mais que les constantes de changement de masse spécifique M sont mal estimées. Il s'en suit une large erreur systématique pour l'extraction des $\delta\langle r^2\rangle$. Une divergence par rapport au modèle de la gouttelette sphérique est néanmoins évidente pour $A < 200$. Cette divergence n'est pas reproduite par l'introduction des paramètres de déformation statique ni par les calculs au-delà du champ moyen dont l'allure est brisée au ^{192}Po. Enfin, les rayons de charge moyens relatifs des elements avec un nombre pair de protons voisins, $_{78}$Pt, $_{80}$Hg, $_{82}$Pb, $_{84}$Po et $_{86}$Rn, sont comparés mutuellement. La magnitude de la divergence par rapport à la gouttelette sphérique n'est observée dans aucun des éléments avec $Z < 82$ et cela montre l'importance que les couches peuvent avoir au-delà de $Z = 82$.

Contents

List of Figures

List of Tables

List of Abbreviations

ANL	Argonne National Laboratory
BRIX	Belgian Research Initiative on eXotic nuclei
BW	Bohr-Weisskopf
CERN	Conseil Européen pour la Recherche Nucléaire
CPT	Canadian Penning Trap
CRC	Centre de Recherche du Cyclotron
CVL	Copper Vapour Laser
DC	Direct Current
FS	Field Shift
EC	Electron Capture
es	excited state
EURISOL	EURopean ISOL
EURONS	EUROpean Nuclear Structure
FC	Faraday Cup
FRDM	Finite Range Droplet Model
FRIB	Facility for RIB
FWHM	Full Width at Half Maximum
FWO	Funds Wetenschappelijk Onderzoek
GANIL	Grand Accélérateur National d'Ions Lourds
GLM	GPS Low Mass beam line
GPS	General Purpose Separator

gs	ground state
GSI	Gesellschaft für SchwerIonenforschung mbH
HF	Hindrance Factor
HIE-ISOLDE	High Intensity and Energy ISOLDE
HPGe	High-Purity Ge detector
HRS	High Resolution Separator
hs	high spin
IC	Ion Collector
IGISOL	Ion Guide ISOL
IT	Internal Transition
I(U)AP	InterUniversity Attraction Pole
ISAC	Isotope Separation and ACceleration
ISCOOL	ISOLDE COOLer
ISOL	Isotope Separator On-Line
ISOLDE	ISOL DEvice
ISOLDE-SC	ISOLDE at the Synchro-Cyclotron
JINR	Joint Institute of Nuclear Research
JYFL	Jyväskylän Yliopisto Fysiikan Laitos
LA1	beam line Left A1
LaSpec	Laser Spectroscopy
LISOL	Leuven ISOL
LIST	Laser Ion Source Trap
LLN	Louvain-La-Neuve
ls	low spin
MS	Mass Shift
MSU	Michigan State University
Nd:YAG	neodymium-doped Yttrium Aluminium Garnet

NMR	Nuclear Magnetic Resonance
NMR/ON	NMR on Oriented Nuclei
NMS	Normal Mass Shift
NSCL	National Superconducting Cyclotron Laboratory
PALIS	PArasitic Laser Ion Source
PIPS	Passivated Implanted Planar Silicon
PSB	Proton Synchrotron Booster
REX-ISOLDE	Radioactive beam EXperiment at ISOLDE
RF	RadioFrequency
RIB	Radioactive Ion Beam
RIKEN	RIkagaku KENkyusho
RILIS	Resonant Ionisation Laser Ion Source
RITU	Recoil Ion Transport Unit
se	SPIG-end
SEM	Secondary Electron Multiplier
SHIP	Separator for Heavy Ion reaction Products
SHIPTRAP	SHIP TRAP
SLOWRI	SLOW Radioactive Ion beam facility
SMS	Specific Mass Shift
SPIG	SextuPole Ion Guide
SRIM	Stopping and Range of Ions in Matter
S^3	Super Separator Spectrometer
TAMU	Texas A&M University
TOPLIS	TwO-Photon LIthium Spectroscopy
TRIUMF	TRI-University Meson Facility
UNISOR	UNiversity Isotope Separator at Oak Ridge
UV	Ultra Violet

Preface

Nuclear structure research is a quest to understand the constituents of matter as we know it. That quest is often linked with the development of new technologies and applications. In this work, the importance of the resonant laser ionisation technique to nuclear structure is illustrated in many ways.

First of all, this technique provides the means of selective production of radioactive ion beams. By enhancing only one element, or even one isomer, of interest over a broad range of contaminants, cleaner conditions are reached and more accurate studies can be performed. The developments of the resonant laser ionisation technique has two main axes: the enhancement of the element of interest and the suppression of the unwanted contaminants.

This technique may also be used as a sensitive measuring tool in the study of hyperfine spectra and isotope shifts. Indeed, the lasers can probe resonances in the atom and provide information on the electronic structure or, through the interaction between the electrons and the nucleons, on the nucleus itself. Accurate electromagnetic moments of the nucleus may be extracted from the hyperfine spectra and shape evolution may be deduced from the isotope shifts.

In this work, all those aspects are investigated. In a first chapter, basic nuclear-structure pieces of information are presented, leading to key questions on the persistence of magic shells and collective behaviour away from the valley of β stability. In the following chapter, the necessary tools from atomic physics, necessary to understand the studies presented, are briefly described.

The experimental facilities CERN ISOLDE and CRC LISOL, where this work has been performed, are presented in the third chapter. The radioactive isotopes of interest are produced in high-energy proton-induced spallation (ISOLDE) or low-energy light-ion-induced fusion-evaporation (LISOL) reactions on different targets. At ISOLDE, the necessary atom plume is produced in a hot cavity in vacuum while in LISOL, the atoms are kept neutral in a buffer gas at room temperature. The specific techniques and devices of interest to the present research are more thoroughly described.

The fourth chapter is dedicated to the developments that have been performed for the beam production aspects of the resonant laser ionisation technique. The new laser ionisation schemes for the polonium element are introduced and characterised. The possible contaminants are discussed and specific solutions are proposed to suppress their contribution to the radioactive ion beams. Processes at a gas catcher facility are however very different. A broad range of non-resonant beam contaminants in

a gas catcher are also investigated using a ^{252}Cf fission source. A new gas catcher, with two independant volumes for catching the radioactive recoiling ions and for re-ionising the atoms, has been tested and characterised. By geometrically decoupling the two zones, it becomes possible to use electrical fields inside the gas catcher in order to collect non-resonantly produced ions and thus suppress beam contaminants, as well as unwanted electrons. An alternative way for geometrical decoupling is also presented in the LIST coupled to a gas catcher. This technique is demonstrated for the first time for gas catchers and could provide cleaner conditions for radioactive ion beam production but also for the sensitive measurement of atomic resonances.

These technical developments have lead to new research possibilities. The magnetic dipole moments of the neutron-deficient copper isotopes have been measured and compared to theoretical and semi-empirical models in an attempt to determine the persistence of magicity at $N = Z = 28$. The full study, including the thorough investigation of systematic effects, is presented in chapter five.

The last chapter is dedicated to the shape-coexistence phenomenon in the neutron-deficient polonium isotopes. Based on the newly-developped ionisation schemes, in-source laser spectroscopy in a hot cavity has been performed on the polonium isotopes, from the neutron-deficient ^{191}Po to the neutron-rich ^{218}Po. Those isotopes have half-lives ranging from 33 ms in ^{192}Po to 102 years in ^{209}Po. Many challenges were met in this study as the polonium isotopes cannot be studied off-line, since there is no stable isotope of that element, and as many isobaric contaminants were overwhelming the beam at many masses. The results from the isotope shift measurements in the even-A isotopes and a discussion on their impact on the understanding of shape coexistence are presented in that chapter.

Finally, a conclusion on the whole of the work is presented, together with an outlook on possible paths to explore further developments and research interests.

This work has already been partially reviewed and published in various scientific journals. Those articles, published or in preparation, make the back bone of this manuscript. They are incorporated directly in the text where their content is the most relevant. Those articles can be found as follows:

Paper I Resonant laser ionization of polonium at RILIS-ISOLDE for the study of ground- and isomer-state properties.
T.E. Cocolios, B.A. Marsh, V.N. Fedosseev, S. Franchoo, G. Huber, M. Huyse, A.M. Ionan, K. Johnston, U. Köster, Yu. Kudryavtsev, M.D. Seliverstov, E. Noah, T. Stora, P. Van Duppen.
*Nuclear Instruments and Methods in Nuclear Physics Research B*266(2008)4403–4406

Paper II Characterization of the LISOL laser ion source using spontaneous fission of ^{252}Cf.
Yu. Kudryavtsev, **T.E. Cocolios**, J. Gentens, O. Ivanov, M. Huyse, D. Pauwels, M. Sawicka, T. Sonoda, P. Van den Bergh, P. Van Duppen.
*Nuclear Instruments and Methods in Nuclear Physics Research B*266(2008)4368–4372

Paper III Dual chamber laser ion source at LISOL.
Yu. Kudryavtsev, **T.E. Cocolios**, J. Gentens, M. Huyse, O. Ivanov, D. Pauwels, T. Sonoda, P. Van den Bergh, P. Van Duppen.
*Nuclear Instruments and Methods in Nuclear Physics Research B*267(2009)2908–2917

Paper IV The Laser Ion Source Trap (LIST) coupled to a gas cell catcher.
T. Sonoda, **T.E. Cocolios**, J. Gentens, M. Huyse, O. Ivanov, Yu. Kudryavtsev, D. Pauwels, P. Van den Bergh, P. Van Duppen.
*Nuclear Instruments and Methods in Nuclear Physics Research B*267(2009)2918–2926

Paper V Magnetic dipole moment of ^{57,59}Cu measured by in-gas-cell laser spectroscopy.
T.E. Cocolios, A.N. Andreyev, B. Bastin, N. Bree, J. Büscher, J. Elseviers, J. Gentens, M. Huyse, Yu. Kudryavtsev, D. Pauwels, T. Sonoda, P. Van den Bergh, P. Van Duppen.
Physical Review Letters 103(2009)102501

Paper VI The magnetic dipole moments of ^{57,58,59}Cu.
T.E. Cocolios, A.N. Andreyev, B. Bastin, N. Bree, J. Büscher, J. Elseviers, J. Gentens, M. Huyse, Yu. Kudryavtsev, D. Pauwels, T. Sonoda, P. Van den Bergh, P. Van Duppen.
*Physical Review C*83(2010)014314

Paper VII Shape evolution of the nuclear ground state of the even-even polonium isotopes.
T.E. Cocolios, W. Dexters, M.D. Seliverstov, A.N. Andreyev, S. Antalic, B. Bastin, A. Barzakh, M. Bender, J. Büscher, I.G. Darby, D. Fedorov, V.N. Fedosseev, K.T. Flanagan, S. Franchoo, P.-H. Heenen, K. Heyde, G. Huber, M. Huyse, M. Keupers, U. Köster, Yu. Kudryavtsev, E. Mané, B.A. Marsh, P. Molkanov, R.D. Page, A.M. Sjoedin, I. Stefan, J. Van de Walle, P. Van Duppen, M. Venhart, J.L. Wood, S. Zemlyanoy.
Letter - in preparation

Paper VIII Intruder configuration and single-particle levels in ^{191}Pb.
T.E. Cocolios, A.N. Andreyev, S. Antalic, B. Bastin, A. Barzakh, J. Büscher, I.G. Darby, W. Dexters, D. Fedorov, V.N. Fedosseev, K.T. Flanagan, S. Franchoo, G. Huber, M. Huyse, M. Keupers, U. Köster, Yu. Kudryavtsev, E. Mané, B.A. Marsh, P. Molkanov, R.D. Page, M.D. Seliverstov, A.M. Sjoedin, I. Stefan, J. Van de Walle, P. Van Duppen, M. Venhart, S. Zemlyanoy.
Physical Review C - in preparation

Chapter 1

The structure of the nucleus

1.1 From elements to isotopes, the great leap into nuclear physics

The constituents of matter responsible for the properties of our world are the different elements of the periodic table of Mendeleev [Men69], also called atoms. The typical size of an atom is of the order of a few Å, or 10^{-10} m. An atom is then to a human step, what a human step is to the distance to the sun.

The elements are characterised by the number of protons (Z) they possess, ranging from 1 in hydrogen to 118 for the heaviest element observed[1]. For each element, there can be different isotopes according to how many neutrons (N) complete the protons. The neutrons and protons are called the nucleons. Together, they form the nucleus of the atom. The description of the nuclei is therefore a two-dimensional array, best illustrated in the chart of the nuclides (Fig. 1.1).

The nucleus is a very compact object with dimensions of the order of a few fm, or 10^{-15} m. If compared again to the distance to the sun, this is equivalent to the thickness of a hair. This also means that the nucleus of an atom is but as big as a hair compared to a person's step.

1.2 Nuclear structure

The four forces of nature are the gravitational, the electromagnetic, the weak and the strong forces. The one holding the protons and neutrons together, in spite of the Coulomb repulsion of the protons, is the latter, the strong force. This short-range force has an extent of only a few fm with a sharp cut-off, unlike e.g. the electromagnetic force, which potential scales as r^{-1} (see eq. 2.1). The potential for the strong force was proposed by H. Yukawa [Yuk35] and has the form

$$V_{ij} \sim \frac{e^{-\lambda r}}{r}, \tag{1.1}$$

[1] although only elements up to $_{112}$Cp have been fully recognised by the IUPAC [iup].

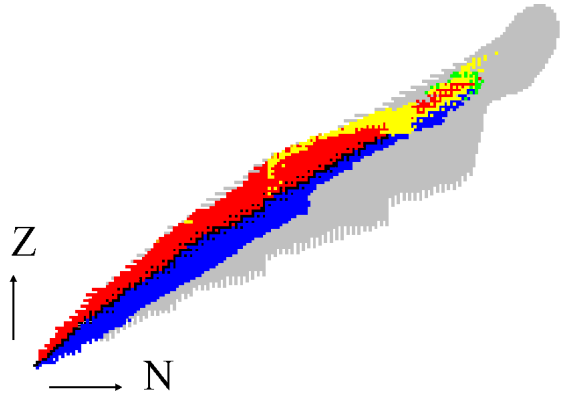

Figure 1.1: Chart of the nuclides. The x axis represents the number of neutrons N and the y axis represents the number of protons Z. Each square represents one isotope. The color code indicates the stability (black) or the decay mode (α in yellow, β^- in blue, β^+ and EC in red and fission in green).

where the subscripts i and j denote two nucleons and r is the distance between the two nucleons. This potential was explained by the fact that the force is mediated by massive bosons, called the pions. The Hamiltonian of this system is described as

$$H = \sum_{i=1}^{A} T_i + \sum_{i=1}^{A} \sum_{j>i}^{A} V_{ij}, \tag{1.2}$$

where T_i is the kinetic energy of the i^{th} nucleon and $A = N + Z$.

Through this short-range force, a nucleon can only interact with its closest neighbours. As such, the nuclear Hamiltonian can be reduced to include only 2-nucleon and 3-nucleon forces. Many efforts have been made to describe nuclei based on those fundamental interactions but those *ab initio* calculations are limited by the complexity of this many-body problem and require an exponentially growing computing power. As such, the current computations are limited to nuclei up to $^{12}_{6}$C [Nav00, Pie02]. For the description of heavier nuclei, one must rely on phenomenological models.

1.3 Nuclear models

In order to reduce the number of parameters involved in the description of the nuclear structure, different approaches can be taken. The nucleus can be seen as a whole, giving rise to macroscopic models, or as a combination of active and inert particles in microscopic models. Some models even use both concepts together, e.g. the cluster models, which describe the nucleus in terms of macroscopic clusters interacting like independent microscopic particles.

A complete review of those concepts can be found in many nuclear physics books. The ones that have been used in writing this chapter are *Introductory nuclear physics*

by K.S. Krane [Kra88], *Nuclear structure from a simple perspective* by R.F. Casten [Cas00], *The nuclear shell model* by K.L.G. Heyde [Hey90] and *The nuclear many-body problem* by P. Ring and P. Schuck [Rin80].

1.3.1 Macroscopic models

A macroscopic approach used to describe nuclear matter is that of an incompressible fluid, called the *liquid drop* model [vW35]. The nucleus is considered as a collection of nucleons, scattering on each other, giving rise to a collective behaviour. Depending on whether the nucleons are surrounded by others or located on the surface of the nucleus, they are subject to different forces; these effects are expressed by a volume term (from inside the nucleus) and a surface term. Finally, the charges involved in the nucleus have to be taken into account, involving a Coulomb term. This model very successfully described some collective properties of the nucleus, such as the binding energy.

It fails, however, to account for the finiteness of the nucleus. This effect was introduced in the *liquid droplet* model of the nucleus [Mye69, Mye74]. In this latter model, nonuniformities of the nucleon density are considered. Furthermore, this density is allowed to smoothly decrease to zero through a diffuse surface rather than with a sharp cutoff. This model was further completed by shell effects in order to predict the deformation of the ground state [Möl95].

Furthermore, the charge distribution of the nucleus can be estimated in the frame of this model [Mye83]. The mea square charge radius $\langle r^2 \rangle$ is then defined as

$$\langle r^2 \rangle = \langle r^2 \rangle_u + \langle r^2 \rangle_r + \langle r^2 \rangle_d, \tag{1.3}$$

where the subscripts u, r and d are the uniform distribution, redistribution and diffuseness terms, respectively. While the diffuseness term $\langle r^2 \rangle_d$ is independent of the shape of the nucleus and is considered a constant correction, the two other terms vary with the charge Z of the nucleus, the number A of nucleons and the shape of the nucleus. The deformation parameters calculated with the finite-range droplet model [Möl95] can then also be used in this description.

1.3.2 Shell model

Under a microscopic approach, a nucleus can also be described by its nucleons moving unperturbed in a spherically symmetric field U_i. The Hamiltonian from eq. 1.2 becomes

$$\begin{aligned} H &= \Big(\sum_{i=1}^{A} T_i + \sum_{i=1}^{A} U_i\Big) + \Big(\sum_{i=1}^{A}\sum_{j>i}^{A} V_{ij} - \sum_{i=1}^{A} U_i\Big) \\ H &= H_0 + H_{res}, \end{aligned} \tag{1.4}$$

where H_0 describes the independent motion of the nucleons and H_{res} is the residual part that accounts for the nuclear interactions; this second contribution is a perturbation of the main part.

For simplicity, the Hamiltonian is taken to be a harmonic oscillator. In order to make it more realisitic, an angular momentum term (l^2) is added to the harmonic oscillator potential. Calculations with such a potential fail, however, to reproduce the experimental magic numbers $N, Z = 2, 8, 20, 28, 50, 82, 126$ for which additional stability had been observed. The addition of a spin-orbit perturbation term ($l \cdot s$) is necessary to reproduce those magic numbers [GM50]. The successive shells are shown in Fig. 1.2. The magic numbers correspond then to the number of protons/neutrons that are necessary to fill a *shell* so that an additional proton/neutron requires a large amount of energy to reach the following. This amount of energy is called the energy gap.

In the shell model of the nucleus, the nucleons of a filled magic shell become inert to nuclear excitations and form a magic core. The properties of a nucleus can then be described by that of particles added outside this core. In this hard-core shell model, only nuclei in the direct vicinity of a closed core can be described. Nuclei with a single hole in a core can also be described in a similar way.

In modern nuclear physics, the shell-model calculations have been extended further away from the magic cores by considering the residual interactions H_{res}, either determined based on fondamental principles or fitted to a set of nuclei. Those calculations work only in a limited region of the nuclear chart where the interaction is at play. Moreover, it becomes hard to define a really inert core far from stability. The universality of the magic numbers is therefore questioned [Sor08]. Indeed, while some magic numbers seem to hold accross the nuclear charts, other disappear away from the valley of β stability and new local magic numbers are proposed [Oza00].

One of the evidences of the weakening of the magicity is the reduction of the energy gap between a magic shell and the following one. Particle-hole excitations accross that gap become possible, especially since the pairing of two identical particles in the excited level offers additional stability to the system [Woo92]. The closed-shell configuration usually gives rise to a spherical nucleus. The particle-hole excitations, however, are associated with deformed structures. In the case of $Z = 82$, the lead ground state is spherical while the suggested proton $2p-2h$ and $4p-4h$ excited states should be deformed. Beyond Mean Field calculations, as described in the following section, and experimental evidences concluded indeed that the excited states could be associated with deformed oblate and prolate shapes.

1.3.3 Mean Field and beyond

It is also possible to solve eq. 1.2 in a self-consistent way, using a given nucleon-nucleon interaction (e.g. the Skyrme or Gosny forces) and the Hartree-Fock variational method. Mean field calculations require however some correlations to be added, like the pairing of like particles in an orbital using the BCS formalism. Contrary to the shell model of the nucleus, only one configuration is considered but occupation in all the shells is made possible.

The Mean Field calculations produce a unique wavefunction, which symmetry is broken by the interaction. There exist now new methods to include additional corre-

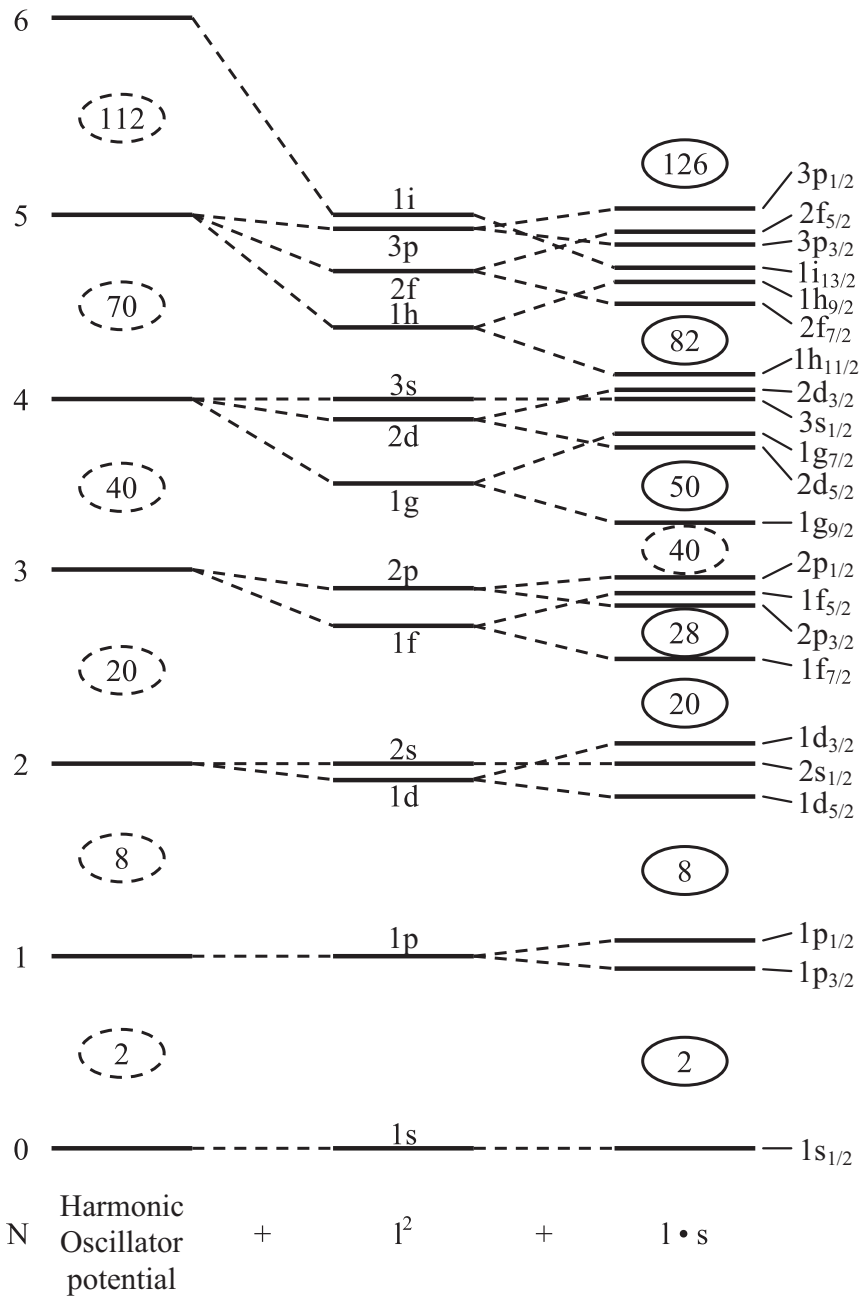

Figure 1.2: Shells of the shell model of the nucleus considering, from left to right, a harmonic oscillator potential, an added l^2 correction and the $l \cdot s$ spin-orbit correction. The magic numbers are circled with a full line while the gaps issued from the harmonic oscillator only are circled with a dotted line. [Cas00]

lations by symmetry restoration and configuration mixing [Dug03]. Those corrections allow to recover from artefacts due to the first mean-field correlations (e.g. from the BCS treatment of pairing) and the final wave functions have good quantum numbers (j). Finally, the projection along the axial quadrupole moment parameter allows for the identification of minima and the determination of the shape of the ground state and of excited states [Ben06], leading to the conclusions for the lead isotopes presented in the previous section.

1.4 Furthering our understanding of the nucleus

In the midst of all those models, conflictual pieces of information arise and experiments strive to challenge the models and to shed lights on new phenoma. Magic numbers have been introduced as being corner stones to the understanding of nuclear structure. As such, they are the subject of many investigations.

In this work, the persistence of the magic number 28 away from the valley of β stability is investigated. By studying the magnetic dipole moment of the isotope ^{57}Cu, with a proton outside the $N = Z = 28$ isotope ^{56}Ni, additional information can be brought on the magic number 28.

The effect of intruder configurations is also investigated beyond $Z = 82$ in the $Z = 84$ polonium isotopes. The study of the changes in the mean-square charge radii, an observable charasteristic of the shape of the nucleus, the interplay between collective and individual properties can be identified.

Chapter 2

Laser spectroscopy in the service of nuclear physics

2.1 Laser spectroscopy

2.1.1 Atomic excitation

Atomic spectroscopy has been developed in the beginning of the previous century after Pauli and Michelson discovered the existence of resonances in the atomic nucleus [Pau24]. One of the outmost electrons of an atom can be excited between two levels of its quantised structure and then spontaneously decays by the emission of a photon. The energy of this photon is simply given by the difference between the two energy levels. The study of such a transition (energy, width) provides information on the structure of the atom.

The atom is made of a positively-charged nucleus and a collection of negatively-charged electrons surrounding it. The Coulomb interaction exerts therefore its force over and between all the particles. The resulting energy levels are thus due to both the electronic cloud and the nucleus. It is therefore not surprising that information on the nucleus can be extracted from the knowledge of the atomic structure. The size of the nucleus compared to that of the cloud is however very limited, from a few fm (10^{-15} m) for the nucleus to several Å (10^{-10} m) for the atom. The energy levels are therefore evaluated assuming that the nucleus is a point-like charge using the Coulomb potential

$$V_{Coulomb} = \frac{Ze^2}{4\pi\epsilon_0 r}, \tag{2.1}$$

where Z is the element number, e is the charge of the electron, ϵ_0 is the permittivity of empty space and r is the distance between the electron and the nucleus.

In order to notice small variations in the atomic levels caused by the nucleus, high precision is required. The field of atomic spectroscopy was revolutionised in the 1960s with the discovery of the lasers [Mai60] and the ability to tune their frequency [Sch66]. Coherent light became the new tool to probe the atomic transitions. It remains today one of the most precise tool for atomic spectroscopy.

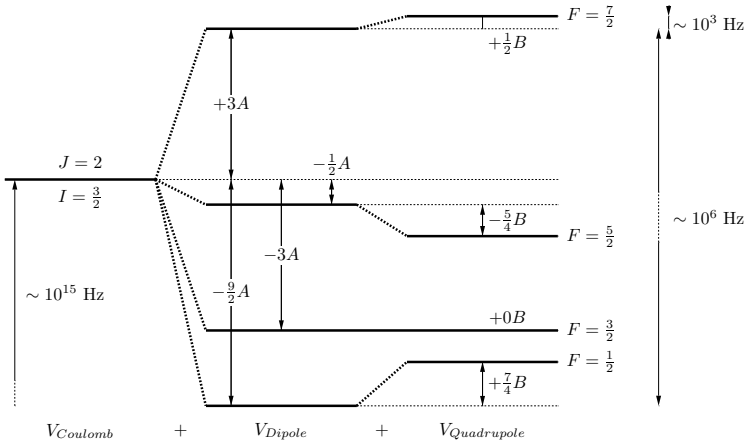

Figure 2.1: Hyperfine splitting of an $I = \frac{3}{2}$, $J = 2$ electronic level first from the magnetic dipole interaction (V_{Dipole}) and then from the electric quadrupole interaction ($V_{Quadrupole}$) as well.

2.1.2 Hyperfine structure

If one considers the higher order multipoles of the nucleus added to the Coulomb potential described in eq. 2.1, the potential becomes

$$V = V_{Coulomb}\Big(\mathcal{O}(R^{-1})\Big) + V_{Dipole}\Big(\mathcal{O}(R^{-3})\Big) + V_{Quadrupole}\Big(\mathcal{O}(R^{-5})\Big) + \dots \qquad (2.2)$$

where each part of the potential corresponds to a different effect from the nucleus on the electrons. In general, the higher the order of the term, the lesser the effect. The point-like potential $V_{Coulomb}$ will therefore determine the energy levels while the other components can be seen as perturbations on these energy levels. Two of those effects are of interest in this work; they are described in this section and illustrated in Fig. 2.1 .

Magnetic dipole moment

Both the nucleus and the electron carry angular momentum, in form of nuclear spin I and total electronic angular momentum J respectively. The motion of the charged particles within the nucleus, namely the protons, induces a magnetic field interacting with that created by the motion of the electrons. This process lifts the degeneracy of the electronic magnetic substates. J is not a good quantum number anymore and the new total angular momentum for each state is $\overrightarrow{F} = \overrightarrow{I} + \overrightarrow{J}$. The quantum number F verifies the triangle inequality

$$|I - J| \leq F \leq I + J. \qquad (2.3)$$

It follows that F is either an integer or a half integer going by increments of 1. Note that if $I = 0$ or $J = 0$, the degeneracy remains. Otherwise, the non-degenerate states

are shifted from their original energy by an amount

$$\Delta E_A = \frac{A}{2} \cdot \Big(F(F+1) - I(I+1) - J(J+1)\Big) \cdot h, \tag{2.4}$$

where h is Planck's constant and A is the hyperfine parameter related to the magnetic dipole moment by

$$A = \frac{\mu |H_0|}{IJ}, \tag{2.5}$$

where $|H_0|$ is the magnitude of the magnetic field made by the electron motion at the nucleus and μ is the magnetic dipole moment of the nucleus. The typical magnitude of this parameter ranges from 10^4 to 10^6 Hz.

$|H_0|$ cannot be easily nor accurately determined for a many-electron system. In a first approximation, its variations from one isotope to the next are however negligible. Laser spectroscopy provides therefore an accurate relative measurement of the magnetic dipole moment along an isotopic chain. A complementary measurement is required to determine the absolute magnetic dipole moment (e.g. β-Nuclear Magnetic Resonance) [Ney03].

Another feature of this approach is the sensitivity to the sign of the magnetic dipole moment. As all terms in the hyperfine parameter A are positive except for μ, the sign of A gives directly the sign of the magnetic dipole moment, even if the complementary measurement provided only its magnitude.

Electric quadrupole moment

If the nucleus is not spherically symmetric, the electrons will interact differently depending on the overlap of their angular momentum to the spin of the nucleus. If this deformation still holds some intrinsic symmetry, like an oblate shape (pancake-like) or a prolate shape (cigar-like), the resulting effect will be that of an electric quadrupole perturbation on the energy levels by an amount

$$\Delta E_B = \frac{B}{2} \cdot \frac{3K(K+1) - 2I(I+1)2J(J+1)}{2I(2I-1)2J(2J-1)} \cdot h, \tag{2.6}$$

where $K = F(F+1) - I(I+1) - J(J+1)$ and B is the hyperfine parameter related to the electric quadrupole moment by

$$B = \frac{eQ}{4} \cdot \frac{\partial^2 V}{\partial z^2}, \tag{2.7}$$

where $\frac{\partial^2 V}{\partial z^2}$ is the electric field gradient produced by the electrons at the center of the potential and Q is the spectroscopic quadrupole moment. Note that the effect of the electric quadrupole can only be observed if the magnetic dipole interaction has lifted the degeneracy on the levels ($I, J \neq 0$) and that no quadrupole moment exists in the case when $I = \frac{1}{2}$ or $J = \frac{1}{2}$. The typical magnitude of this parameter ranges from 10^2 to 10^6 Hz in the heaviest elements. Its value is usually smaller than that of the magnetic dipole moment.

Similarly as for $|H_0|$, $\frac{\partial^2 V}{\partial z^2}$ is assumed to be constant over the isotopic range and the hyperfine parameter only gives a relative measurement of the electric quadrupole moment. A complementary measurement is required to determine the absolute electric quadrupole moment (e.g. β-Nuclear Quadrupole Resonance) [Ney03].

It is interesting to note that, unlike the magnetic dipole effect which is symmetric around the original energy level, the electric quadrupole effect has an asymmetric action on the energy levels. The knowledge of the structure is required for the accurate determination of the energy level centroid which does no longer coincide with the center of gravity of the structure.

Hyperfine anomaly

In large nuclei, the electronic wave function of s- and $p_{1/2}$-electrons cannot be considered to remain constant within the nucleus as those have non-vanishing overlap with the nucleus. The effect on the hyperfine magnetic dipole was first observed by Bohr and Weisskopf who noticed a systematic discrepancy between their calculated hyperfine parameter A for s- and $p_{1/2}$-electrons to the experimental data [Boh50]. This effect is seen as a perturbation on the hyperfine parameter

$$A \rightarrow A(1 + \epsilon_{BW}), \tag{2.8}$$

where ϵ_{BW} is the correction due to the distribution of the nuclear magnetisation in the nucleus, also known as the Bohr-Weisskopf (BW) effect. It represents the fractional difference between the magnetic dipole for a point-like nucleus and that of a nucleus with extended nuclear magnetisation. The magnitude of that correction ranges from less than one part in 10^4 in the light nuclei to a few percent in heavier isotopes.

The radial electronic wave functions, involved in the calculation of the hyperfine constant A, are too complex to allow for the determination of the BW effect based on the measurement of the hyperfine structure. Instead, the hyperfine structure yields the hyperfine anomaly. Following the formalism of Büttgenbach [Büt84], the hyperfine anomaly ${}^1\Delta^2$ is defined from the comparison of the measured hyperfine energy shift in two different isotopes (isomers) to the independent measurement of their respective magnetic dipole moments as

$$\frac{\Delta E_A^{(1)}}{\Delta E_A^{(2)}} \frac{\mu^{(2)}}{\mu^{(1)}} = 1 + {}^1\Delta^2 = \frac{1 + \epsilon_{BW}^1}{1 + \epsilon_{BW}^2} \approx 1 + \epsilon_{BW}^{(1)} - \epsilon_{BW}^{(2)}. \tag{2.9}$$

The hyperfine anomaly can therefore simply be seen as the difference of the BW effect between those two isotopes (isomers):

$${}^1\Delta^2 = \epsilon_{BW}^{(1)} - \epsilon_{BW}^{(2)}. \tag{2.10}$$

This hyperfine anomaly is usually a small effect in atomic spectroscopy, of the order of 1%. High accuracy on both the hyperfine parameters and on the magnetic dipole moments is therefore required to observe this effect. This work, as discussed in all the coming chapters, does not provide sufficient accuracy for this effect to be studied with the applied method.

2.1.3 Isotope shift of an atomic transition

Between two isotopes or simply between two isomers, the ground- (isomer-)state properties of the nucleus, such as the mass or the size, are changing. When considering the interaction between the nucleus and the electrons, those parameters affect the energy levels directly and not only as described in the previous section on electromagnetic moments.

As all levels are shifting, so is the energy of the transition between any two levels. The difference in energy of a given atomic transition in two different isotopes, or isomers, is called the isotope shift, or isomer shift, respectively. This shift has two main contributions: the change in the mass of the nucleus-electrons system and the change in the size of the nucleus. Both are described in this section.

Mass effects

The changes in the reduced mass of the nucleus-electrons system has a direct influence on the forces acting on the electron cloud. The energy difference on an atomic level is then denoted

$$\Delta E_{MS}^{AA'} = \frac{1}{2} \cdot \frac{A' - A}{A \cdot A'} \cdot \Big(\Big\langle \sum_i \mathrm{p}_i^2 \Big\rangle + \Big\langle \sum_{i<j} \mathrm{p}_i \cdot \mathrm{p}_j \Big\rangle \Big), \tag{2.11}$$

where MS stands for Mass Shift, A and A' are now the masses of each isotope and p is the momentum of the electron. Applying this energy change on both levels of a transition gives a complicated expression for the isotope shift involving cross-terms between the electrons. Assuming however that the residual interaction between the electrons can be neglected, the mass contribution to the isotope shift can be written, in units of frequency, as

$$\delta\nu_{MS}^{AA'} = \delta\nu_{NMS}^{AA'} + \delta\nu_{SMS}^{AA'}, \tag{2.12}$$

where $\delta\nu_{NMS}^{AA'}$, the Normal Mass Shift, is related to the change in reduced mass of the atom-nucleus system and $\delta\nu_{SMS}^{AA'}$, the Specific Mass Shift, is related to the changes in the correlations between the electrons. Those contributions can be expressed as follows

$$\delta\nu_{NMS}^{AA'} = \frac{A' - A}{A \cdot A'} \cdot m_e \nu, \tag{2.13}$$

$$\delta\nu_{SMS}^{AA'} = \frac{A' - A}{A \cdot A'} \cdot K_{SMS}, \tag{2.14}$$

where m_e is the mass of the electron, ν is the transition frequency and K_{SMS} is a property of the electronic transition, independent of the isotope or isomer of interest.

While the normal mass shift can be calculated accurately, the specific mass shift becomes rapidly beyond computational power for exact calculations. Large scale computations [Fri02] or additional atomic studies are thus required to evaluate K_{SMS}.

Overall, it can be noted that $\delta\nu_{MS} \propto \frac{1}{A^2}$ and its contribution reduces quickly as the mass increases.

Table 2.1: C_i parameters for the polonium isotopes from Seltzer [Sel69] and ratio of the different orders $\delta\langle r^{2i}\rangle^{AA'}$ to the changes in the mean-square charge radius $\delta\langle r^2\rangle^{AA'}$ in the range $A = 191 - 218$ taking $A' = 208$ as a reference.

	$\delta\langle r^2\rangle^{AA'}$	$\delta\langle r^4\rangle^{AA'}$	$\delta\langle r^6\rangle^{AA'}$
$\frac{\delta\langle r^{2i}\rangle^{AA'}}{\delta\langle r^2\rangle^{AA'}}$	1	101	7667
C_i	2280	−2.66	0.0079

Volume effects

The changes in the shape of the nucleus are not directly felt by the electrons since those overlap with the nucleus without any preferred orientation. The electrons will probe the nucleus from all the possible directions and the effects will eventually average out to that of a sphere. However, the radius of this sphere, which is the average of the spread of the nucleus charge distribution, called the mean-square charge radius, increases as the nucleus goes from a spherical to an oblate distribution (pancake-like) and even further if the charges rearrange into a prolate distribution (cigar-like), giving rise to a size effect.

The contribution of this effect, called the Field Shift, to the isotope shift is

$$\begin{aligned} \delta\nu_{FS}^{AA'} &= -\frac{Ze^2}{6\epsilon_0 h}\cdot\Delta|\Psi(0)|^2\cdot\lambda^{AA'} \\ \delta\nu_{FS}^{AA'} &= F\cdot\lambda^{AA'}, \end{aligned} \tag{2.15}$$

where $\Delta|\Psi(0)|^2$ is the change in electron density at the nucleus between the upper and lower electronic states involved in the atomic transition and $\lambda^{AA'}$ is the nuclear parameter. $\lambda^{AA'}$ is a power series ($i = 1, 2, 3, \ldots$) of the changes in the mean charge radius $\delta\langle r^{2i}\rangle^{AA'}$:

$$\lambda^{AA'} = \delta\langle r^2\rangle^{AA'} + \frac{C_2}{C_1}\delta\langle r^4\rangle^{AA'} + \frac{C_3}{C_1}\delta\langle r^6\rangle^{AA'} + \ldots. \tag{2.16}$$

The parameters C_i are known for many isotopes [Sel69]. Moreover, one can relate the higher powers of the changes in the mean radii to the changes in the mean-square charge radius $\delta\langle r^2\rangle^{AA'}$ in the spherical constant nuclear density limit.

In the case of the polonium isotopic chain, of interest in chapter 6, we assume an approximated radius of the form

$$R_C = 1.2\cdot A^{1/3} \quad \text{fm}, \tag{2.17}$$

where A ranges from 191 to 218. Using equation 2.17, it is possible to estimate the ratio of any term to the changes in the mean-square charge radius. The first order terms, together with the C_i parameters, are shown in table 2.1.

The relation from equation 2.16 for polonium becomes

$$\begin{aligned} \lambda^{A\ 208} &= (1 - 0.116 + 0.027)\delta\langle r^2\rangle^{A\ 208} \\ \lambda^{A\ 208} &= 0.911(4)\cdot\delta\langle r^2\rangle^{A\ 208} \end{aligned} \tag{2.18}$$

The F-factor in eq. 2.15 is a property of the element which is independent of the isotope or isomer. Its accurate determination is of primary importance in the extraction of the changes in the mean-square charge radius. *Ab initio* calculations, relying solely on fundamental interactions between all the individual particles, can nowadays only be used for atomic systems with up to three electrons. Therefore, if no atomic studies have been performed on the used transition, the F-factor has to be determined by large-scale atomic computations [Fri02], using a limited valence space involving only the outmost electrons and selected energy levels, or by relating two data sets to one-another for a relative measurement of the F-factor, called the King plot method, detailed below.

It is important to note that, in an opposite way to the mass shift, $\delta\nu_{FS} \propto Z$. The contribution of the Field Shift to the isotope (isomer) shift becomes therefore larger the heavier the element of interest. The accurate measurement of the changes in the mean-square charge radius becomes therefore easier for heavier elements, like for polonium.

On the other hand, the volume shift is also proportional to the changes in electron density at the nucleus. Since only the s- and $p_{1/2}$-electrons overlap with the nucleus, only transitions involving such an electronic state can be used. The choice of transition is therefore crucial in tailoring the experiment.

King plot

The final expression for the isotope shift is

$$\delta\nu^{AA'} = \frac{A' - A}{A \cdot A'} \cdot (m_e\nu + K_{SMS}) + F \cdot \lambda^{AA'}, \tag{2.19}$$

where neither the specific mass shift constant K_{SMS} nor the field shift F-factor can be calculated exactly for large systems beyond ^{11}Li [Sán06]. Those have therefore to be evaluated experimentally by atomic techniques or estimated within large-scale calculations [Fri02], as discussed above.

The information on a transition of interest is not always available and a method exists to relate two data sets measured with different optical transitions or different techniques (e^- scattering, muonic decay, K x rays), provided they overlap over several nuclei [Kin84]. This method, called the King plot, removes the mass dependence from the isotope shift by normalising it to a reference isotope shift $\delta\nu^{A_{ref}A'_{ref}}$ using a mass factor

$$\mu^{AA'} = \frac{AA'}{A' - A} \cdot \frac{A'_{ref} - A_{ref}}{A_{ref}A'_{ref}}. \tag{2.20}$$

The modified isotope shifts $\mu\delta\nu_i^{AA'}$ obtained this way can be related to each other. The relation is then

$$\mu\delta\nu_2^{AA'} = \frac{F_2}{F_1} \cdot \mu\delta\nu_1^{AA'} + \frac{A'_{ref} - A_{ref}}{A_{ref}A'_{ref}} \cdot (K_{SMS2} - \frac{F_2}{F_1} \cdot K_{SMS1}). \tag{2.21}$$

The slope of the line formed by the graph of $\mu\delta\nu_2^{AA'}$ against $\mu\delta\nu_1^{AA'}$ gives the relative measurement of the two F-factors while the y intercept relates the SMS constants

K_{SMS}. This method requires that many nuclei be investigated with both possible transitions or techniques.

For a more detailed overview of the use of lasers in nuclear physics, I refer to the review by H.-J. Kluge and W. Nörterhäuser [Klu03, sur]; on hyperfine structure, I refer to the reviews by E.W. Otten [Ott76], S. Büttgenbach [Büt84] and G. Neyens [Ney03]; as for isotope shifts, I refer to the book *Isotope shift in atomic spectra* by W.H. King [Kin84].

2.2 Laser ionisation

In the last decade, the use of lasers in radioactive ion beam physics has broadened from a precision measurement tool to a versatile production device. Lasers are now commonly used to produce Radioactive Ion Beams (RIB) in many RIB facilities worldwide.

2.2.1 Brute force: ablation sources

This type of ion source uses the high power that can be delivered from a laser to a localised sample. The ions are produced by ablation of particles and clusters of particles. This source produces a wide range of clusters and charge states and can be used to study devices off-line as a stable ion source [Dav06].

It is, however, of low interest to the production of radioactive ion beams and is just mentioned here for completeness. Note that this system was also used in the COMPLIS [Le 93] experiment at CERN ISOLDE and in the TOPLIS experiment at TRIUMF ISAC [Sán06] to produce atomic samples in the vacuum from an on-line-accumulated radioactive sample.

2.2.2 Resonant ionisation laser ion sources

The Resonant Ionisation Laser Ion Source (RILIS) is of higher interest due to its additional element selectivity. By tuning several lasers on transitions in the atomic spectrum of a given element, it is possible to excite a valence electron from the ground or metastable state of an atom to beyond the continuum in an efficient way, thus ionising the atom without, in principle, affecting other elements, which could be potential contaminants.

By coupling this Z-selection of the ion source to the A/q-selectivity of an Isotope Separator On-Line (ISOL), it is in theory possible to produce isotopically pure beams and even, in some cases, isomerically pure beams [Van04, Ste07]. In practice, the production of the atom sample results in the ionisation of contaminants, limiting the purity of the RIB.

In a classical ISOL facility[1], such as ISOLDE, the ions are produced by the impact of a beam on a thick target, from which the radioactive nuclei diffuse and effuse until

[1] more details in section 3.1

they reach the ion source. In the case of ISOLDE RILIS, the atom source is a metal tube (atomiser) heated to a high temperature (≈ 2300 K) to produce an atom beam in its center. Although great care is taken in the choice of material, elements with low ionisation potential, such as the alkali elements, ionise when in contact with the hot surface and contribute directly to the contamination of the beam [Kös02]. At the ISOLDE RILIS, the beams of polonium are, e.g., contaminated with isobaric francium as discussed in section 4.1.1.

It is also possible to couple an ion catcher to the classical ISOL facility, as it is done at the Leuven Isotope Separator On-Line (LISOL[2]) in the Centre de Recherche du Cyclotron (CRC), Louvain-La-Neuve. The primary beam impinges on a thin target to allow the recoils to come out without losses due to diffusion. The target is placed in a noble buffer gas to catch and thermalise those recoils. The use of a noble gas minimises the possibility of chemical interaction between the recoils and the catching medium, hereby making the device less sensitive to the chemical nature of the element of interest. It also enhances the survival of the ions through the cell. The radioactive atoms are then kept in their atomic state to be laser ionised. Moreover, the temperature ($T \approx 350$ K) is not responsible for the non-resonant ionisation of isobaric contaminants. The reaction products, on the other hand, can survive as ions through the buffer gas and not all neutralise, as discussed in section 4.2.1, or some isotopes can even be reintroduced into the beam by the decay of implanted activity in the cell walls and electrodes, as developed in section 4.2.3.

The parameters that are of importance to a resonant laser ion source are the efficiency of the ionisation scheme and its selectivity. The laser ionisation efficiency ϵ_{ion} for a given ionisation scheme of an element is part of a much more complex expression for the total efficiency of the ion source [VD06]. First, ϵ_{delay} accounts for the survival probability against radioactive decay during the extraction of the ions; its importance varies greatly with the half-life, as shown later in Fig. 4.31. Then, ϵ_{trans} represents the transport efficiency through the mass analyser and up to the experimental setup; the transport through standard electrostatic lenses approaches 100% but other more specific devices, like the SPIG at the LISOL facility, can have a smaller efficiency ($\epsilon_{SPIG} = 75\%$). Additional factors, like ϵ_{cool}, the efficiency of the cooling and bunching of the beam, ϵ_{breed}, the charge-breeding efficiency, and ϵ_{acc}, the efficiency of the post-accelerator, do not have to be considered in this work as cooling, breeding and post-accerating are never used. The total efficiency is then given by

$$\begin{aligned} \epsilon &= \epsilon_{delay} \cdot \epsilon_{ion} \cdot \epsilon_{trans} \\ \epsilon &= \frac{\text{Number of ions at the experimental setup}}{\text{Number of atoms produced}}. \end{aligned} \tag{2.22}$$

The selectivity for a given element is defined as

$$s = \frac{\text{Number of ions extracted using the resonant laser ionisation}}{\text{Number of ions extracted without using the resonant laser ionisation}}. \tag{2.23}$$

[2]more details in section 3.2

The two parameters ϵ_{ion} and s illustrate the strength of a laser ionisation scheme. The efficiency gives an absolute strength while the selectivity also includes the idea of enhancement from non-resonant ionisation. Both concepts shall be developed while discussing new laser ionisation-related techniques at ISOLDE and LISOL in chapter 4.

Depending on the production mechanism and on the physico-chemical properties of the radioactive atoms, isobaric contamination from other elements can lead to intense non-resonant ion beams. Those concepts are also investigated in the development of new beams and will be discussed specifically in sections 4.1.2, 4.2.1 and 4.2.2.

2.2.3 Laser ion source traps

Laser ion source traps at classical ISOL facilities

The idea of the Laser Ion Source Trap (LIST) was first proposed by K. Blaum *et al.* to improve the quality of ISOL beams [Bla03]. By geometrically decoupling the regions where the laser ions and the unwanted ions are produced, it is possible to purify the beam and improve its overall quality (emittance, purity, time structure).

A positive potential is applied on an electrode at the exit of the classical ion source assembly to repel the ions produced on the hot surface of the atomiser. Only the atom beam can then exit this first region. The atom beam enters a segmented gas-filled radio-frequency ion guide where it overlaps with the laser beams. The ions produced are caught in the linear trap of the ion guide and are cooled by collisions with the buffer gas. They can then be extracted in cooled bunches.

In this ionisation technique, not only is the beam really pure, thanks to the suppression of the surface-ionised elements, but its emittance is also improved by the cooling process. The bunched release can be tuned to satisfy the timing requirements of the experimental setup.

LIST coupled to a gas catcher

Although the processes are different in a classical ISOL facility from a gas catcher facility like LISOL, the same limit is true in terms of unwanted ions and the same solution, i.e. geometrical decoupling, should provide a solution.

By applying a positive potential outside the gas catcher, e.g. on the SPIG rods, the ions in the jet are repelled and only the atoms remain. The gas pushes the atomic beam into a segmented radio-frequency ion guide where it overlaps with the laser beams as described above. A full study of such an ion source at LISOL is detailed in section 4.2.4.

Chapter 3

Experimental techniques and facilities

Nowadays, nuclear physics has left the counter top and the spoonful of polonium for the RIB facilities where beams of always more exotic species, i.e. with an usual ratio of neutrons to protons $\frac{N}{Z}$, can be created and where control of the radioactivity and safety are primary concerns.

RIB production is like shoe making: there is not a one-size-fits-all facility. Depending on the isotope of interest, its chemical and radioactive natures and the beam quality and intensity requirements, different facilities can be chosen. This chapter will focus on high-quality ion beam facilities where the emittance and selectivity are of primary interest. The tread-off is on the intensity and on how exotic the beam can be or how far from stability one can go.

Different elements, with different chemical natures, are the subject of this research. Due to those differences and to the various production means, they cannot all be investigated in a single facility. I shall therefore highlight in this chapter first the classical Isotope Separation On-Line (ISOL) facility taking the example of the ISOL DEvice (ISOLDE) at the Conseil Européen pour la Recherche Nucléaire (European Council for Nuclear Research - CERN), Geneva (Switzerland); I shall then describe a complementary facility designed for elements chemically trapped in the classical ISOL facility. The use of gas catchers at the Leuven ISOL facility (LISOL) installed at the Centre de Recherche du Cyclotron (Cyclotron Research Center - CRC), Louvain–La-Neuve (Belgium), will be given as an example; I shall finally describe the experimental facilities used in this work for the detection of stable and radioactive beams at those different facilities.

3.1 ISOL[DE]

3.1.1 Isotope Separation On-Line

The classical ISOL technique relies on a step-by-step production and on high control of each part of the production sequence. With high control comes also large delays and

slow processes, one major limit of the ISOL technique. A note of caution, however, needs to be stated as chemical effects can enhance or hinder those processes. The production of the radioactive isotopes comes first, followed by the ionisation of the elements of interest, their extraction, their selection and finally their transport. Each step will be shortly introduced in this section.

In this work, the study of the polonium isotopic chain at the ISOLDE facility at CERN, Geneva (Switzerland), is discussed. This particular case will be used to illustrate the technique while introducing the parameters of the experimental work, shown also in Fig. 3.1 and table 3.1.

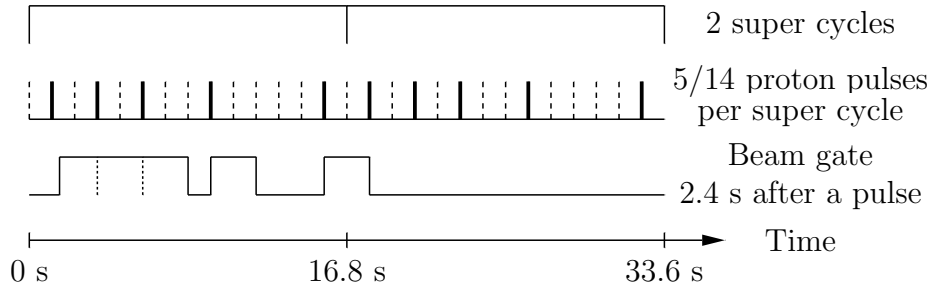

Figure 3.1: Supercycle sequence used for the in-source laser spectroscopy of ^{196}Po at ISOLDE. The bold lines show the proton pulses sent to ISOLDE.

The target

The radioactive nuclei used in RIB facilities can have several sources, from naturally occurring samples to intense-beam-induced reactions. In the case of ISOLDE, the radioactive isotopes are produced in proton- or neutron-induced reactions. The 1.4 GeV proton beam from the CERN Proton Synchrotron Booster (PSB), shown on Fig. 3.2, impinges on a target, which location is shown on Fig. 3.3, by 200-ns-long bunches of up to $3 \cdot 10^{13}$ protons per bunch spaced by 1.2 s in a repetitive sequence of 12 to 42 pulses per supercycle unit. The maximal average intensity on the target is limited to 2 μA for safety reasons and to ensure reasonable lifetime of the target material; not all proton bunches are used by ISOLDE in a given supercycle. A typical supercycle is shown in Fig. 3.1 for the study of ^{196}Po.

The target itself is chosen in order to produce the radioactive isotopes of interest. For the production of the polonium isotopes, the chosen reaction is the proton-induced spallation of ^{238}U from a UC_x target (density of 50 g·cm^{-2}). Note that the fragmentation and proton-induced fission channels are also present in the given energy range (1.4 GeV). A wide selection of radioactive nuclei is therefore produced in those reactions, as shown in Fig. 3.4. A drawing of the target-ion-source design for surface and laser ionisation is shown in Fig. 3.5.

The ABRABLA code [Luk06] predicts the production cross-sections of the different radioactive nuclei in this type of reactions. Although it is known to slightly overesti-

Table 3.1: Different parameters of the experiments at ISOLDE for the preparatory measurements on polonium and for the two experimental campains.

Run	Year	Separator	Isotope	Detection	Laser
0	2006	GPS	$^{193-198}$Po	α Windmill at GLM	CVL + dye
I	2007	GPS	$^{193-198}$Po	α Windmill at GLM	CVL + dye
			^{202}Po	β detector at the ISOLDE tape station	
			$^{199-200,204}$Po	γ detector at the ISOLDE tape station	
II	2009	GPS	$^{191-193,195-196,211,216,218}$Po	α Windmill at LA1	Nd:YAG + dye
			^{202}Po	β detector at the ISOLDE tape station	
			^{201,203}Po	γ detector at the ISOLDE tape station	
			$^{206-210}$Po	FC490 after GPS	

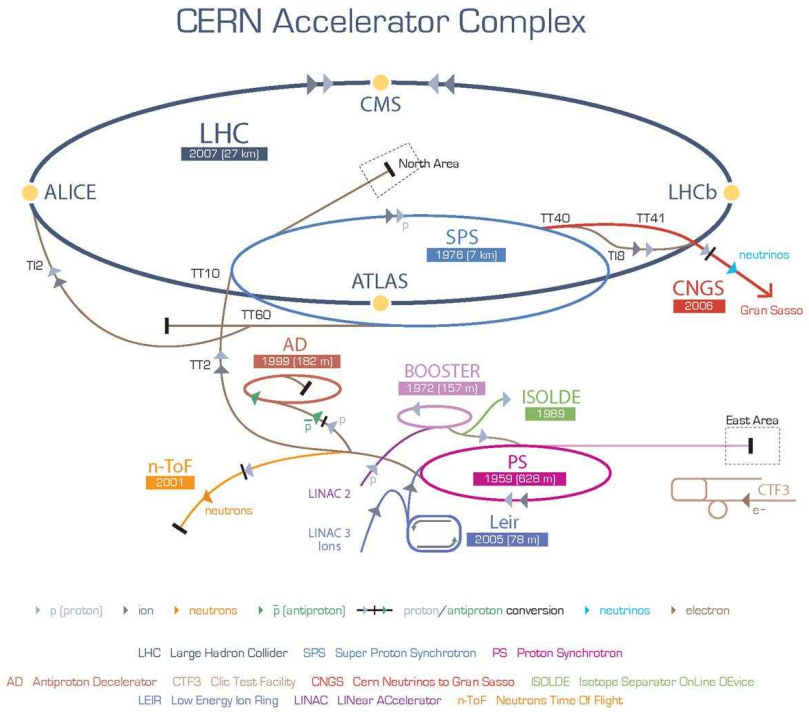

Figure 3.2: Layout of the CERN facilities [cer].

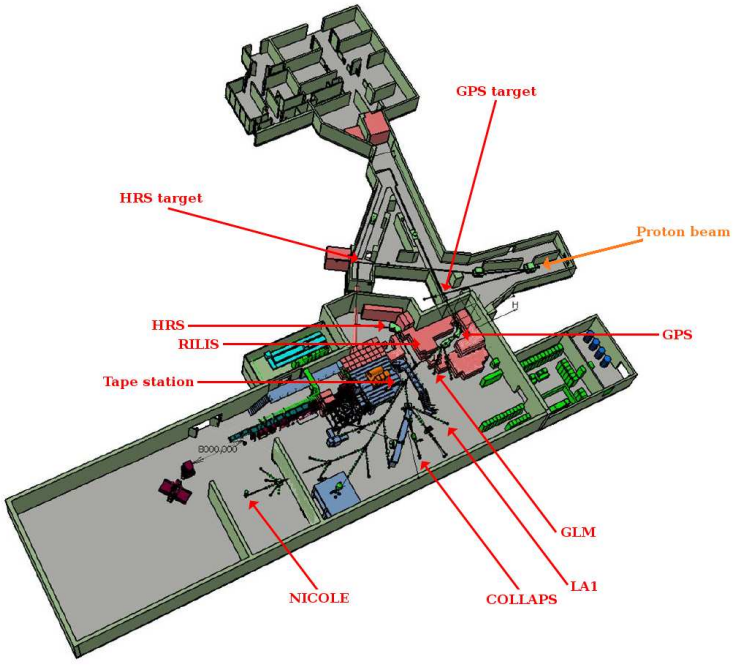

Figure 3.3: Layout of the CERN ISOLDE facility [iso].

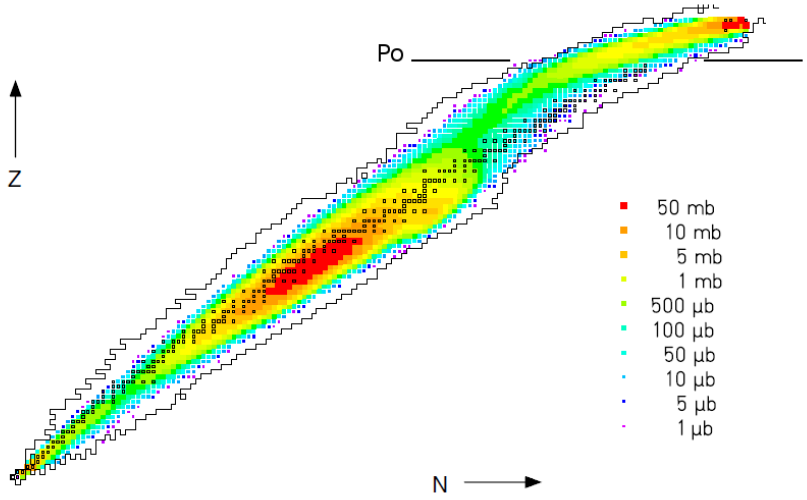

Figure 3.4: Cross-section for the production of nuclei from proton-induced reactions (1 GeV) on ^{238}U [Luk06].

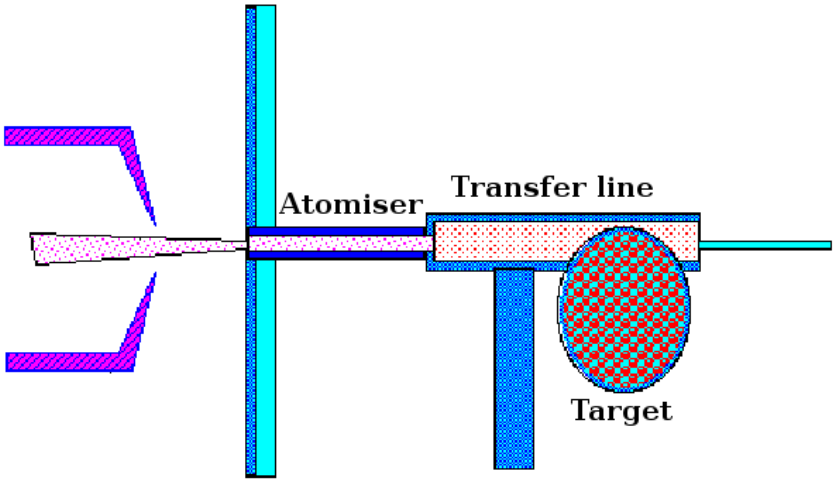

Figure 3.5: Design of the ISOLDE target-ion source assembly for surface and laser ionisation [iso].

mate the cross-section for the production of the polonium isotopes, it still provides a valuable input when preparing the experimental protocol for isotopes with unknown production rates. Comparison to the experimental production rates is discussed in section 4.1.1.

The ion source

The radioactive atoms produced in the target have to escape from the material (diffusion) and travel to the atomiser by collisions with the target material and the walls of the container and transfer line (effusion) before being manipulated on. Not all elements can easily diffuse out of the target matrix nor effuse to the atomiser [Kös02, Kös07]. The effusion through the transfer line can be also affected by the temperature of the line and by the material it is made of [Sun92, Bou07b]. The release of the atoms from the target-ion-source system as a function of time has been parametrised phenomenologically as [Let97]

$$P(t, \lambda_r, \lambda_f, \lambda_s, \alpha) \propto (1 - e^{-\lambda_r t})\Big[\alpha e^{-\lambda_f t} + (1 - \alpha)e^{-\lambda_s t}\Big], \tag{3.1}$$

where λ_r, λ_f and λ_s are time parameters defining the diffusion and effusion processes from the target material and α is a weight parameter between 0 and 1. The release of an element from the target can be measured experimentally by recording the flux of ions over time following the impact of a single proton bunch. This technique has been employed to study the release of the polonium isotopes from UC_x, as discussed in section 4.1.1, or the time dependence of the thallium and francium contaminants, described in section 4.1.3.

Radioactive elements irreversibly trapped inside the target material keep on decaying, hereby producing some isotopes from different elements that can be released even when the primary proton beam does not impinge on the target. This method has been employed to study the long-lived and neutron-rich polonium isotopes $^{204-211,216,218}$Po and is discussed in section 4.1.3.

The ionisation

Once released from the target, the elements of interest need to be ionised to be manipulated with electrostatic potentials and magnetic fields. The ionisation method depends on the chemical nature of the element. Those with a low ionisation potential, like the alkali elements (including francium) or thallium, can be ionised by simply entering in contact with a hot surface ($\approx$ 2300 K) which work function is higher than the ionisation potential of the element of interest. Typical materials favouring this surface ionisation process and at the same time operating at high temperatures are tungsten and tantalum.

At the other end of the table of Mendeleev, the noble gases are much harder to ionise and a plasma ion source is used to strip electrons from the atoms [Ber03]. This process is highly unselective and ionises all the elements that do not condensate prior to ionisation. This ion source is nonetheless very efficient ($\approx$ 30%).

The last type of ion source makes the bridge between the two extremes of the table of the elements. The laser ion source, as described in sections 2.2.2 and 3.1.2, is element selective and is not bound to the same chemical groups as the surface or plasma ion sources. This source requires an atom beam and laser beams to overlap. As shown in Fig. 3.5, this is achieved at ISOLDE by keeping the exit line of the target-ion source assembly hot ($\approx$ 2300 K). This design is however responsible for the surface ionisation of contaminants. This motivates the idea of the Laser Ion Source Trap (LIST) [Bla03], discussed in sections 2.2.3 and 4.2.4.

The extraction and separation of the beam

The target-ion source system is located on a high-voltage platform at 30 to 60 kV. When the ions leave this region and enter a section where the beam line is grounded, they convert this potential energy to kinetic energy. This mono-energetic beam is then analysed through a dipole magnet. The bending radius ρ of the ions through the magnetic field is proportional to the magnetic rigidity and yields eventually, for a mono-energetic beam, to the relation

$$\rho = \frac{1}{B} \cdot \sqrt{\frac{2m \cdot K_1}{q}}, \tag{3.2}$$

where B is the strength of the magnetic field, m the mass of the ion, q its charge and K_1 the energy of a singly-charged ion. Such a separator gives a mass-to-charge selection of the ion beam. As most of the ions arrive in a single charge state, those are commonly referred to as *mass separators*. The quality of a mass separator is defined by its resolving power

$$R = \frac{m}{\Delta m}. \tag{3.3}$$

The CERN ISOLDE facility has two different separators, as seen on Fig. 3.3. The General Purpose Separator (GPS) is a single analysing magnet with a resolving power of $R = 1200$. It is sufficient to separate two neighbouring isotopes from each other although the collisions with residual gas molecules in the vacuum chamber of the separator are responsible for contamination from one mass to the other. A particular feature of this separator is to have three outcoming beams at three different masses, provided those remain within 15% of each other. The second separator is the High-Resolution Separator (HRS) with two-stage separation through two dipole magnets (90° and 60°, respectively). This provides a greater resolving power of $R = 15000$. This second separator is also followed by a gas-filled radio-frequency quadrupole, ISCOOL, to offer the possibility of cooling and/or bunching of the beam [Man09a, Man09b]. In the study of the polonium isotopes presented in section 4.1.1, in chapter 6 and in appendix B, only the GPS separator was used (see Table 3.1).

The beam coming from either separator is then brought to the experimental area by means of electrostatic focusing lenses and benders. The typical transport efficiency ϵ_{trans} is high (around 90%) but to account for the fluctuations from one setup to the other, the beam intensities are always quoted in the focal plane of the mass separator.

Further reading on the ISOLDE facility and on the two separators can be found in Ref. [Kug92].

3.1.2 Laser ion source - RILIS

The Resonant Ionisation Laser Ion Source (RILIS [Mis93]) has already successfully ionised 27 different elements on-line, ranging from the beryllium to the polonium isotopes.

The laser setup, shown in Fig. 3.6, consists of several dye lasers pumped by two Copper Vapour amplifiers to a Copper Vapour Lasers (CVL, 510.6 and 578.2 nm). Using doubling and tripling of the fundamental frequency from the dye lasers, the system can provide laser light in a broad range of wavelengths, from 213 nm to 850 nm. For Run II, the CVL sequence has been replaced by a frequency-doubled Nd:YAG laser (532 nm).

The power available depends on the dye used as well as on the treatment of the frequency as doubling and tripling are very inefficient processes. The CVL amplifiers reach about 20 W in both green and yellow while the doubled Nd:YAG reaches 80 W in the green; a few W of infra-red light can be delivered and finally several mW can be achieved in the ultra-violet region.

For the production of RIB, the bandwidth of the laser is kept to a FWHM of 10 to 15 GHz. This allows, in most cases, to cover the possible hyperfine components and the isotope shifts accross the isotopic chain of interest. If one is interested in studying those structures, as is discussed in this work for the determination of moments and changes in the mean-square charge radii, it is possible to reduce the bandwidth of the laser to a much narrow line, down to a FWHM of $\approx$ 2 GHz, using an etalon in the resonance cavity.

In that mode, it is also possible to enhance the production of one isomer over the others through the differences in their hyperfine structures [Van04, Ste07]. This technique is also applied in appendix B to assign α-decay transitions in the decay of ^{195}Po or to discuss the β^+/EC decay of ^{199}Po.

3.1.3 Qualities and limits

ISOLDE provides pure beams up to the contaminations previously mentioned. Indeed, surface-ionised isobars can be mixed with the laser-ionised isotopes. Furthermore, noble gases can travel as neutral atoms in the beam line and, especially in the vicinity of the mass separator, like at GLM, α-emitting radon ($Z = 86$) isotopes can enter the detection chamber and provide additional background.

For example in the beams of polonium, one can find thallium and francium isotopes as well as neighbouring polonium isotopes. The decay of neutron-rich and neutron-deficient radon isotopes can also be found in the α spectra. A good example of contamination is that of the attempt at spectroscopy on ^{216}Po ($E_\alpha = 6.778$ MeV) during Run I; the α spectrum is shown in Fig. 3.7. The production of ^{213}Fr ($E_\alpha = 6.775$ MeV) is so high that in spite of the high reduction factor for three mass

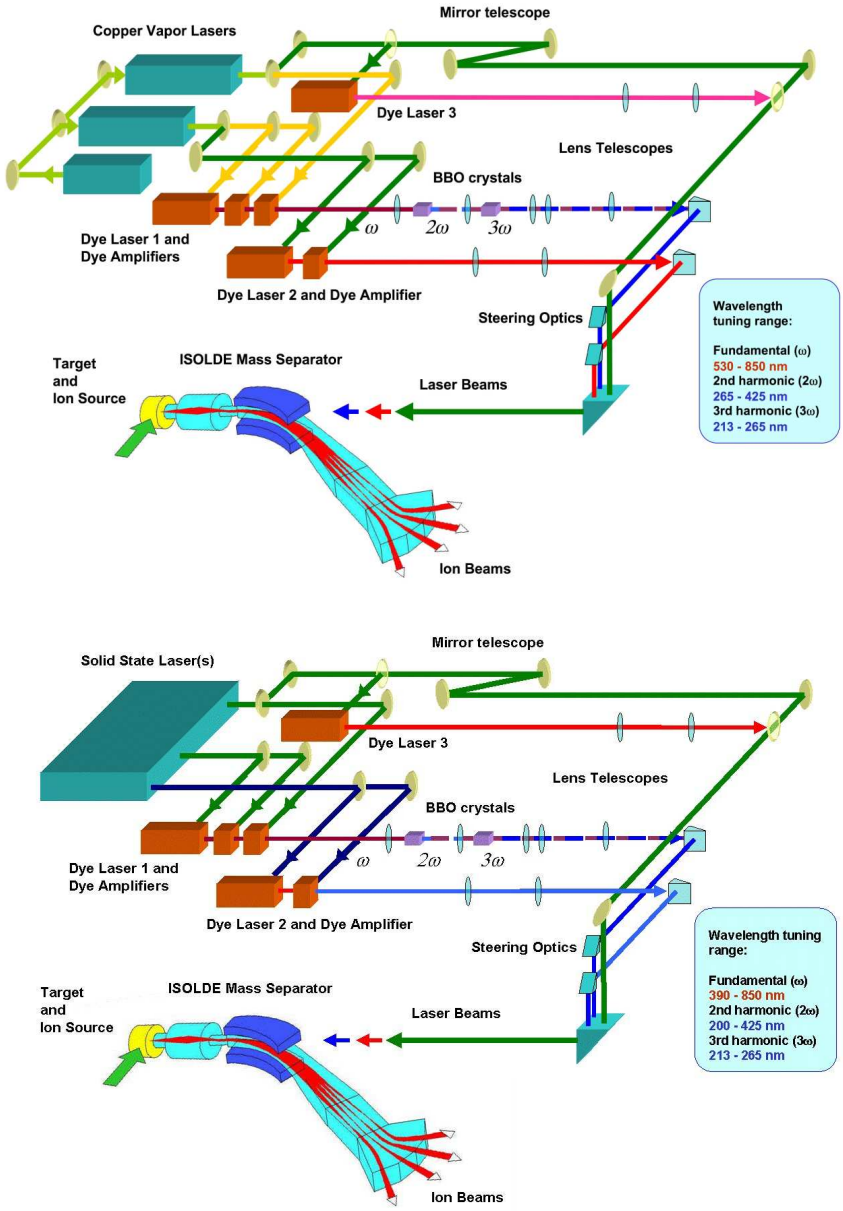

Figure 3.6: Layout of the RILIS lasers with the CVL pump lasers (top) or the Nd:YAG pump laser (bottom). The setups work with a repetition rate of 11 kHz and provide a pulse with a width of 15 ns [iso].

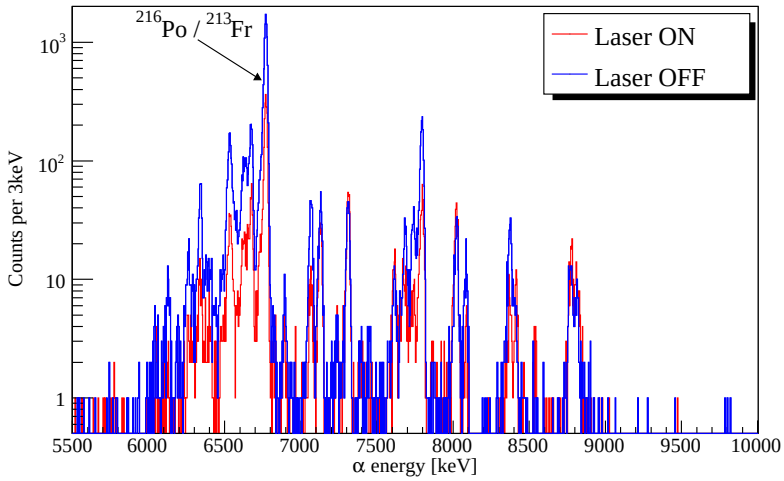

Figure 3.7: α spectrum at mass $A = 216$ with and without laser ionisation. The observed lines come either from the decay of ^{213}Fr and its daughter ^{209}At or from well identified Rn background lines.

units, it dominates the spectrum. An alternative for the study of that isotope during Run II, benefitting from in-target decay of a precursor, is discussed in section 4.1.3.

Another property of this system is the high temperature that is maintained at the atomiser ($\approx 2300K$). Beyond the surface ionisation process, this high temperature generates a broadening of the beam energy, called Doppler broadening, resulting in a Gaussian distribution of the velocity of the ions with FWHM of several GHz. This yields a similar broadening in the optical transitions of these atoms, well covered by the broad width of the lasers from the ion source; this is also a limit to the possibility of in-source spectroscopy; these effects are discussed in section 4.2.4. Only isotopes that display a large hyperfine structure (copper [Wei02, Sto08a, Coc09] and chapter 5) or a large field shift (heavy elements like lead [De 07, Sel09] or polonium, the subject of this work in chapter 6) can be studied.

Finally, it is worth mentioning an additional constraint coming from the RILIS. The first CVL, used to seed the two CVL amplifiers, is triggered by the discharge of a large capacitance. This discharge emits a large electromagnetic wave through the experimental hall. The intensity of this wave is such that it is picked up by the pre-amplifiers of the detectors and by the cables and gives additional noise in the detectors. It is then necessary to gate these events out of the acquisition window. A more detailed discussion on this issue can be found in appendix A. This effect disappears with the use of the Nd:YAG laser.

3.2 Gas catchers at LISOL, CRC (LLN)

Gas catchers come in a great variety of size and shape from rocket-like devices (as in the Canadian Penning Trap group at the Argonne National Laboratory, Argonne (Illinois, United States of America) [Tri04]) to pocket-cells. The larger devices, like those used at ANL and GSI (fusion reaction productions), or MSU and RIKEN (fragmentation reaction products), are used to catch very energetic beams. The ions are slowed down by the noble buffer gas and their charge state is reduced to mosty a 1^+ state. The ions are transported by a combination of forces from the gas flow, an electric DC field gradient and an electric RF field meant to keep the ions off the walls of the gas catcher. The electric fields ensure fast extraction of the ions before they can fully recombine or react with impurities in the gas. A full description of the ANL CPT gas catcher can be found in [Tri04]. At the Ion Guide ISOL (IGISOL) facility at the Physics Department of the University of Jyväskylä (JYFL, Finland), the gas catcher is based on the fast extraction of surviving ions. Since the reaction recoils in this gas catcher are not as energetic as in the other facilities, the required gas volume can be minimised and the extraction of the ions relies only on the use of the gas flow.

In this work, another approach is discussed. At the LISOL facility at the CRC, Louvain-La-Neuve (Belgium), the goal is to fully neutralise the recoils from the reaction. The atoms are then transported by the gas flow. Those are subsequently resonantly re-ionised by means of two-step two-colour resonant laser ionisation. In this approach, the aim is to achieve greater selectivity of the ion beam of interest over the isobaric contaminants and greater efficiency by accessing the large neutral fraction of the atoms. The gas catchers from the LISOL facility are described in this section.

The CRC facilities are shown in Fig. 3.8. The CYCLONE 110 cyclotron provides intense stable primary beams to the LISOL facility, shown in Fig. 3.9, from protons to heavy ions (^{36,40}Ar, ^{58}Ni). The beam from the cyclotron impinges on one or many thin targets to induce fission or fusion-evaporation reactions. The recoils are stopped and thermalised in the buffer noble gas (typically 500 mbar of He or Ar), transported along the gas flow towards the 0.5 mm exit hole, laser ionised inside the gas catcher just before the exit hole and extracted from the supersonic jet. The ions are captured by the pseudo-potential of a SextuPole Ion Guide (SPIG) while drifting with the push of the supersonic jet towards the extraction region. Once extracted to an energy of 40 keV, the beam is treated with the classical ISOL method, as described in section 3.1, with a separator similar in design to GPS.

The performance of the gas catchers in off-line and on-line conditions has been thoroughly studied in previous works [Kud01, Fac04a, Fac04b]. This section only aims at describing the tools necessary to the discussion in section 4.2, namely the gas cell itself, the SPIG and the laser ion source; the whole setup is shown in Fig. 3.10.

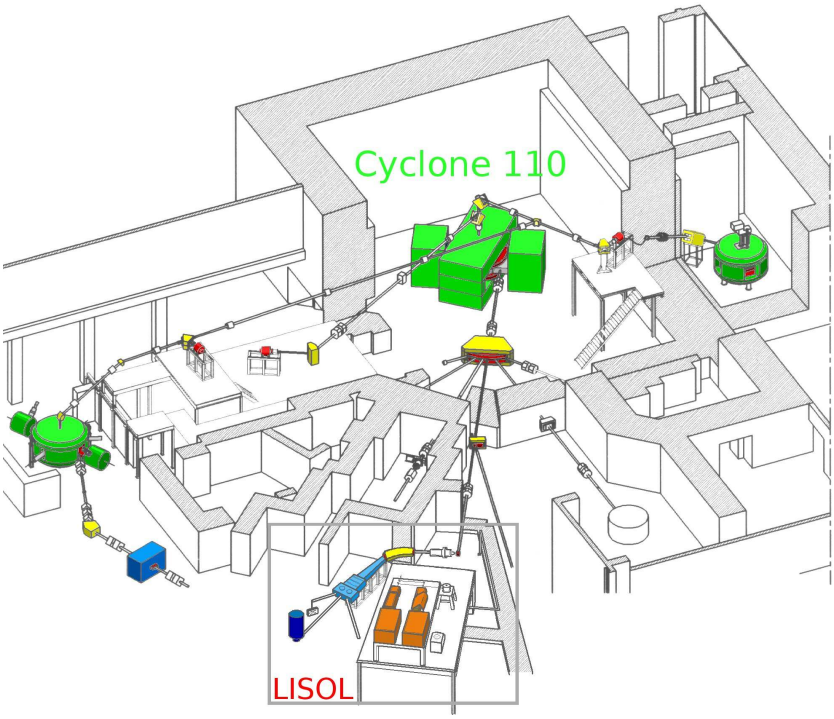

Figure 3.8: Layout of the CRC facilities [crc].

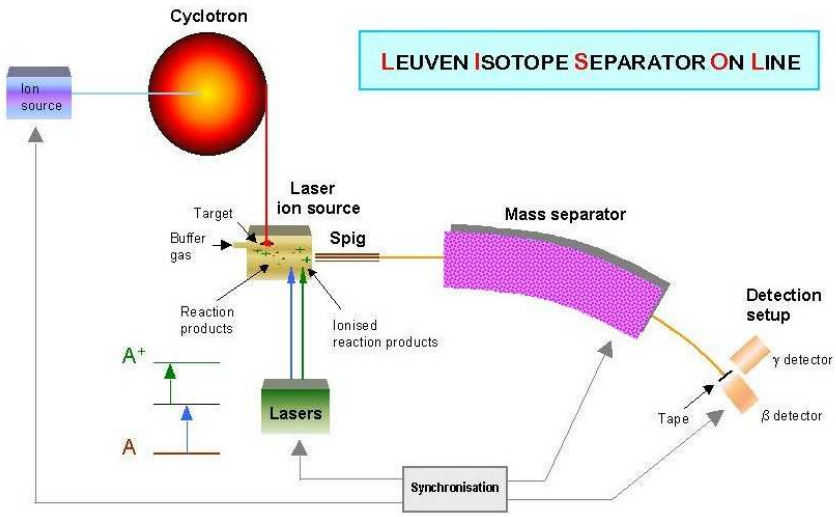

Figure 3.9: Layout of the LISOL facility.

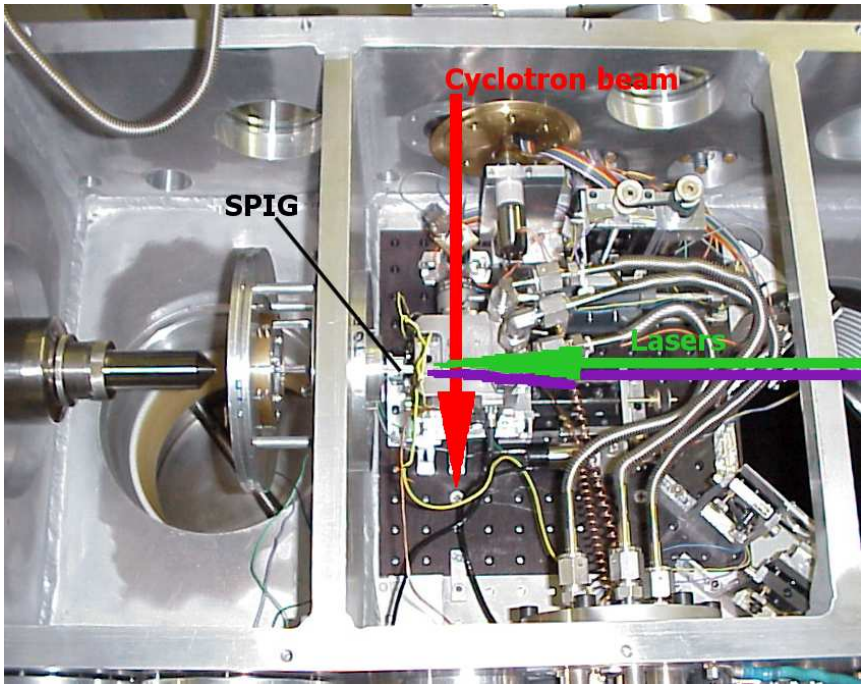

Figure 3.10: Gas cell-SPIG assembly at LISOL.

3.2.1 Gas catcher

The gas cell, as displayed in Fig. 3.10 is a large cylindrical volume filled with a noble gas (helium or argon). It is 50 mm long with a diameter of 50 mm, ended with a conical piece to guide the gas flow from a circular inlet (a ring of 0.3 mm in thickness at a radius of 35 mm) to an exit hole of typically 0.5 mm.

The pressure in the gas cell can be adjusted by changing the gas flow at the inlet and/or the size of the exit hole. Typical running conditions are a pressure of 500 mbar inside the gas catcher and 10^{-2} mbar outside the gas cell. In those conditions, the exiting gas forms a jet at supersonic velocities.

For off-line studies, the gas cell can be used in two configurations, shown in Fig. 3.11:

- stable ions can be created by resistive heating of a filament. Although the filament is off-center, the gas flow and the high amount of atoms produced from the resistive heating yield a sufficient population in the path of the lasers;
- radioactive ions can be created from the spontaneous fission of a ^{252}Cf sample mounted inside the gas cell. The ^{252}Cf source is mounted on the axis of the cell at a distance of 32 mm from the exit nozzle to optimise the survival of the fission fragments in ion form while ensuring high capture of the recoils by the buffer gas.

The mean evacuation time of the gas cell in both configurations is 500 ms.

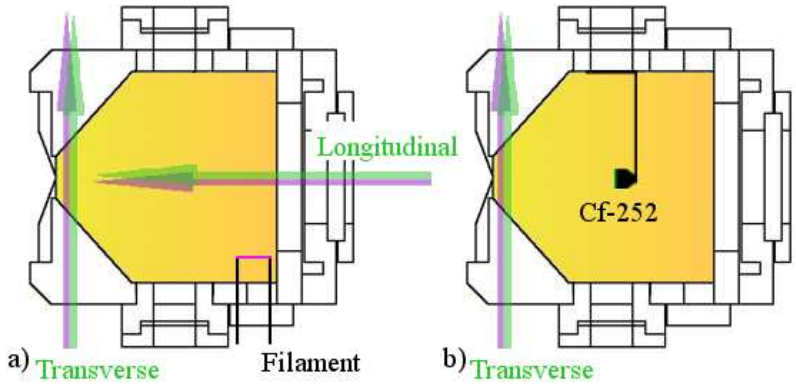

Figure 3.11: Gas cells used off-line at LISOL. The laser path, longitudinal or transverse, are indicated on each figure. a) Stable isotope filament; b) ^{252}Cf spontaneous fission source.

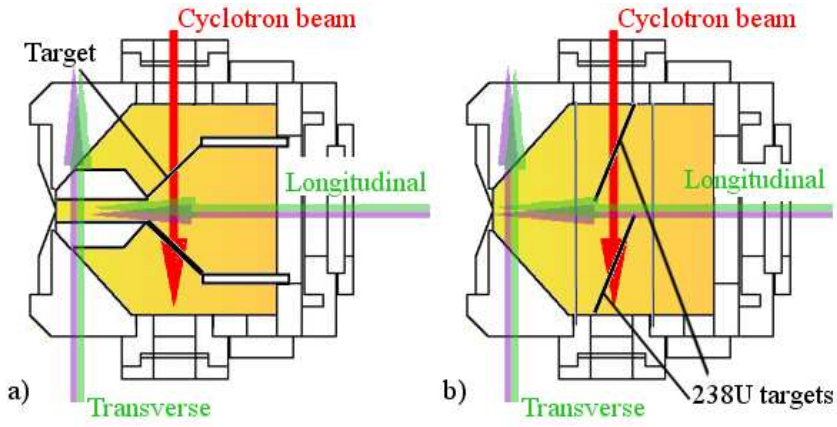

Figure 3.12: Gas cells used on-line at LISOL. The laser path, longitudinal or transverse, are indicated on each figure. a) Fusion-evaporation cell; b) fission cell.

For on-line studies, the cyclotron beam impinges on one or two thin targets tilted to some angle to maximise the beam-target overlap. Two configurations, shown in Fig. 3.12, are used on-line:

- fusion-evaporation reactions produce neutron-deficient isotopes. The target is tilted at 45°. The volume necessary to catch the recoil fragments can be small for light ions ($E \approx 2$ MeV) and a channel (length 22 mm and diameter 6 mm) is then introduced to reduce the gas volume and accelerate the evacuation of the cell. Mean evacuation times as low as 80 ms have been measured [Fac04a];

- proton-induced fission of ^{238}U produces neutron-rich isotopes (E up to 100 MeV). Two 10 mg·cm^{-2} targets are placed within the volume at an angle of 20°. Unlike for the fusion cell, the whole volume is kept as the emission of the fission fragments is energetic and isotropic. A large number of electron-ion pairs are also created by the proton beam, favoring the recombination of ions of interest. To overcome this issue, an aluminium cylinder with 16 mm diameter and 3 μm thickness is used to let the recoils through but not the electron-ion pairs created from the cyclotron beam interaction with the buffer gas.

3.2.2 SPIG

Once ejected from the gas cell, the atoms are pushed by the supersonic jet which diverges quite strongly. In order to increase the extraction efficiency of the ions over the divergence of the gas atoms, a radially confining pseudo-potential is created by a RF SextuPole Ion Guide (SPIG).

The 126-mm-long, 1.5-mm-diameter rods are placed to form a 3-mm-diameter cylinder. The typical transport efficiency of the SPIG is $\epsilon_{SPIG} = 75\%$ and its use has increased the extraction efficiency greatly while offering higher beam quality in comparison to the simple use of a skimmer [Ber97]. Its performance depends on the distance between the gas catcher and the SPIG; this distance is usually kept as low as possible while preventing discharge from the SPIG to the gas catcher, namely 0.5 mm. In some instances, the SPIG can be moved further, as discussed in section 4.2.4.

A DC potential can be added on top of the RF signal. Applying a negative potential (−210 V) with respect to the gas cell body breaks down weakly-bond molecules between impurities (H_2O, N_2) and the ions of interest [Fac04b]. Applying a positive potential ($\sim$ 40 V) can be used to repel positive ions; this is the essence of the LIST concept, discussed in section 4.2.4.

Alternative designs of the gas cell are currenty under investigation. The dual-chamber gas cell, separating the thermalising and ionising volumes, is one of the newest designs and is discussed in section 4.2.3.

3.2.3 Laser ion source

The LISOL laser ion source has successfully ionised 12 elements, focusing especially on those not available at thick-target facilities such as ISOLDE, like iron, cobalt,

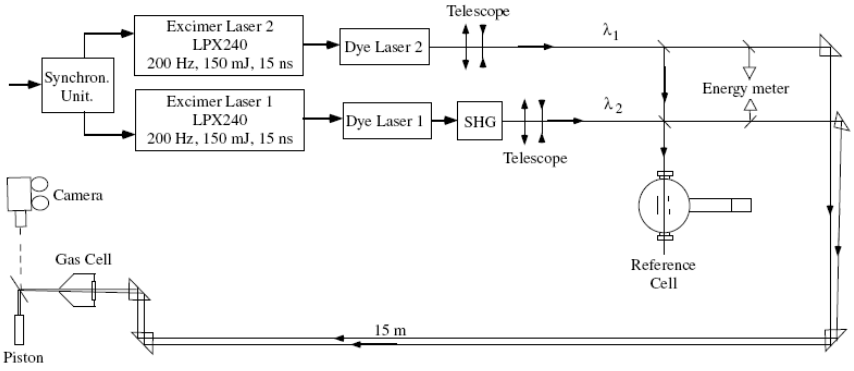

Figure 3.13: Layout of the LISOL lasers [Kud96]. The setup works with a repetition rate of 200 Hz and provides pulses with a width of 15 ns.

ruthenium or rhodium, or where the delay times of the thick-target ion sources prevent the study of the shortest-living isotopes, as for nickel or cupper.

The laser setup is shown in Fig. 3.13. Two excimer XeCl lasers are used to pump two dye lasers with a repetition rate up to 200 Hz. This lower repetition rate in comparison to RILIS is sufficient to irradiate all the atoms traveling through the gas catcher as the atoms travel with the gas flow, which is much slower to evacuate than atoms in the ISOLDE atomiser (100 ms vs. 100 μs). In order to reach the ultra-violet range, one of the dye lasers can be followed by a frequency-doubling cavity. Wavelengths from 225 nm up to 800 nm can be reached. Power up to 1 W in the fundamental and 0.1 W in the frequency-doubled transitions can be achieved [Kud96].

A fraction of the laser beam is diverted to a vacuum cell in close proximity to the laser setup. This reference cell is loaded with a natural sample of the element of interest in an atomiser and crossed-beam laser ionisation spectroscopy in vacuum is performed to tune the lasers and monitor the resonance specific to the element.

New features of the laser setup, installed recently to facilitate the development of new laser ionisation schemes and to allow the scanning of laser transitions, are the wavemeter and the scanning program. A reflection of the scanned laser beam from one of the optical elements is sent to a Lambdameter LM-007, with a precision of 1 part in 10^7. This device can present a drift of up to 1 GHz per day in absolute measurement, as shown in Fig. 3.14, but the relative measurements remain accurate. If studying a frequency-doubled laser beam, the fundamental frequency is measured by the wavemeter. The scanning program allows to change the position of the etalon and the grating of one of the dye lasers to tune the frequency accross a given range.

The laser beams are finally transported with prisms to the experimental setup. The beams are sent through the gas cell either longitudinally (along the gas flow towards the exit hole) or transversely (across the gas flow near the exit of the gas catcher) as shown in Fig. 3.10, 3.11 and 3.12.

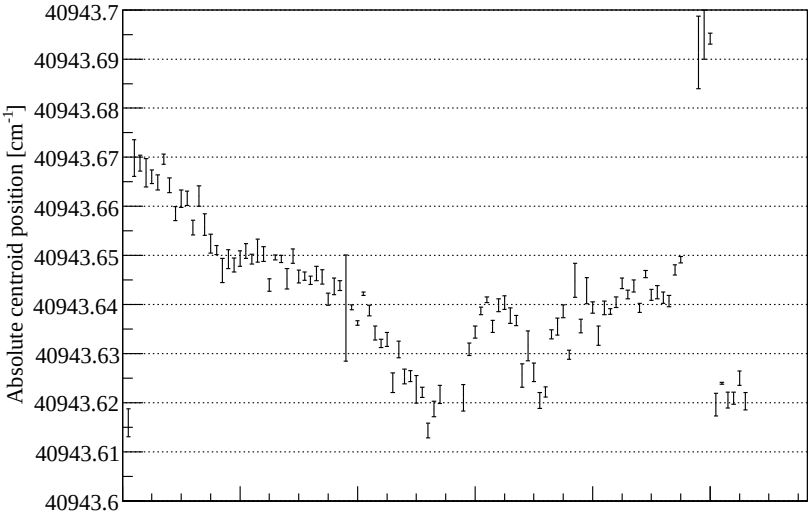

Figure 3.14: Sequential measurement of the transition center of gravity in the study of the hyperfine structure of ^{63}Cu (see Chapter 5). The x axis represents the sequential measurements in the course of seven days. The x axis is arbitrary and does not represent time.

3.2.4 Similarities, differences, benefits and draw-backs

Both ISOLDE and LISOL are ISOL facilities yet they are very complementary to each other. Where one leads the other one follows; where one stops the other one keeps on going.

The classical ISOL facility, like ISOLDE, provides intense beams of exotic nuclei far from stability. The thick targets employed yield large production rates and the high repetition rate of the laser system, though costly in power per pulse, allow for proper temporal overlap and thus efficient laser ionisation.

On the other hand, the release of the radioactive products from the target matrix is an important constraint and while alkali elements are both fastly released and surface ionised, some elements are irreversibly trapped, like iron or the refractory elements. This release property, described in section 3.1.1, can also limit the range of isotopes studied for a nucleus, as discussed in section 4.1 for the polonium isotopes or considering the case of ^{57}Cu discussed in chapter 5.

Coupling a gas catcher to an ISOL facility provides an alternative to that gap. By using thin targets in the gas, the radioactive isotopes recoil out of the target material and do not have to diffuse out of it. The limits are then not on the chemical nature of the element but rather on the half-life of the isotope as decay losses become more important in short-living isotopes. Gas catchers are therefore ideal to study iron, cobalt and nickel [Pau08a, Iva07, Pau09, Fra98, Fra99], ruthenium and rhodium

[Dea04b, Dea04a, Hag07] or the refractory elements [Kan05, Avg06, Hag06].

"For every action, there is an equal and opposite reaction." Indeed, for every gain, there must be a trade-off. In the case of the gas catcher, the production suffers greatly from the reduced effective thickness of the target. Moreover, the shorter-lived species, with half-lives of the order of a few ms, are still out of reach and can only be studied at fragmentation facilities (GANIL, GSI, RIKEN, ...). The fusion of the gas catcher technology with the fragmentation beam production technique is A New Hope for the next generation RIB facilities, combining the exotic products of a fragmentation facility to the high beam quality of a gas catcher coupled to an ISOL facility (S^3@GANIL, LaSpec@GSI, SLOWRI and PALIS@RIKEN, FRIB@MSU, Cyclotron Institute@TAMU).

3.3 Detection facilities

In the course of this work, several techniques are used to measure beam intensities, either as a mean of characterising a new laser scheme (section 4.1.1), as a means of characterising a new device (section 4.2.3), or as a mean of identification and counting (section 4.2.1 and chapters 5 and 6). The descriptions here are not comprehensive and only offer the information necessary to follow the discussion in the upcoming chapters.

3.3.1 Stable elements

Faraday cups

Faraday Cups (FC) are the most basic tools to monitor beam currents. By impinging on a metal surface, the ion beam current is absorbed and measured. If the emission of secondary electrons is suppressed, the measured current is exactly that of the ion beam. The sensitivity limit on this device comes from the construction of the Faraday cups and their matching to the ammeter, which usually results in a sensitivity down to 1 pA (ie. $\sim 10^7$ ions$\cdot$s^{-1}).

Secondary Electron Multiplier

The Secondary Electron Multiplier (SEM) is used at LISOL to measure ion currents below 1 pA and therefore out of reach of a Faraday cup with a current meter. The beam enters a cylinder at the end of which a plate is located. When the ions hit the plate, a shower of electrons is created with few electrons for the impact of a single ion. Those electrons are accelerated and the signal is amplified by electron multiplication. The output of the SEM is therefore a current signal proportional to the ion current.

This signal can be subsequently amplified, integrated and recorded. This device is used in the measurement of time profile of ions (section 4.2.2) or for the laser spectroscopy of stable nickel and copper isotopes (section 4.2.4 and chapter 5).

3.3.2 α decay

The study of the polonium isotopes, discussed in chapter 6, was partly performed by observing the characteristic α-decay lines for $^{191-198,211,216,218}$Po. In the case of ^{195}Po, new information on the decay is also obtained, as discussed in appendix B.1. The setup used is the Windmill [Den92]; for Runs 0 & I, the setup was as described in [DW04] while for Run II, the device has been upgraded, as required for experiment IS466 at ISOLDE on the EC-delayed fission of the neutron-deficient thallium isotopes [And, Els09].

Windmill - Runs 0 & I

The Windmill is a vacuum chamber with a rotating wheel that hosts 10 carbon foils (6 mm diameter, 20 μg·cm^{-2} thickness) mounted on copper rings. As shown in Fig. 3.15, the ion beam enters the Windmill through a double collimator that can also be set as an unsuppressed FC for ion beam transport tuning; the beam is then implanted in the carbon foil; the α particles emitted by the decay of the radioactive isotopes escape the foil and are collected by a PIPS silicon detector (300 μm thickness and 150 mm^2 active area). The solid angle covered by this setup is 20% of 4π. The energy resolution of the detector during the experiments was 30 keV FWHM. The setup was placed at the GLM beam line (see Fig. 3.3).

Once a measurement is complete, the wheel is rotated to bring away the activity and present a fresh foil in front of the ion beam. Another PIPS detector, similar to that in the implantation station, is located in front of another carbon foil. The wheel motion can be adjusted to bring the foil directly from the decay station to the implantation station or the other way around. In the study of the polonium isotopes, the measurement sequence (Fig. 3.1) is long with respect to the half-life of the isotopes. There is therefore little interest in observing the remaining activity at the decay station. The contamination of the foil can however be an issue as, in the normal running conditions, a foil comes back in front of the beam after 5 repetitions of the measurement sequence. It is therefore interesting to verify the contamination on the foil and the wheel was therefore turned from the decay station towards the implantation station. In the analysis of the data from these runs, only data collected at the implantation station are considered.

Windmill - Run II

Between Runs I and II, the detection setup of the Windmill has been upgraded to cover a larger solid angle, as shown in Fig. 3.16. Larger PIPS detectors (300 mm^2 active area) are installed in the previously described implantation and decay stations. Further increase of the solid angle is obtained by observing the decay on both sides of the wheel.

Although it is sufficient to add an extra detector at the decay station, it is more tricky at the implantation station as the ion beam has to pass through the detector to reach the carbon foil. A cylindrical surface barrier detector is used (350 mm^2 active

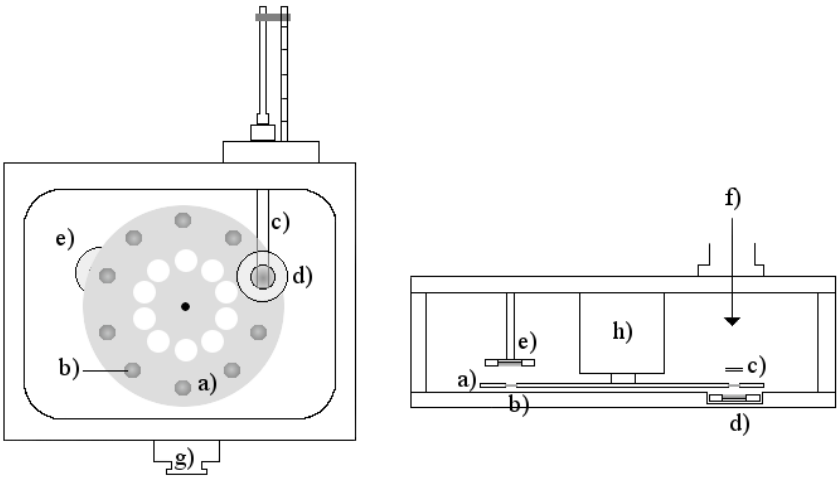

Figure 3.15: Windmill α setup for Runs 0 & I of experiment IS456. Left: back view of the chamber; right: top view of the chamber. a) Rotating wheel; b) carbon foil; c) collimator and Faraday cup; d) implantation station detector; e) decay station detector; f) incoming ion beam; g) vacuum exhaust; h) wheel motor.

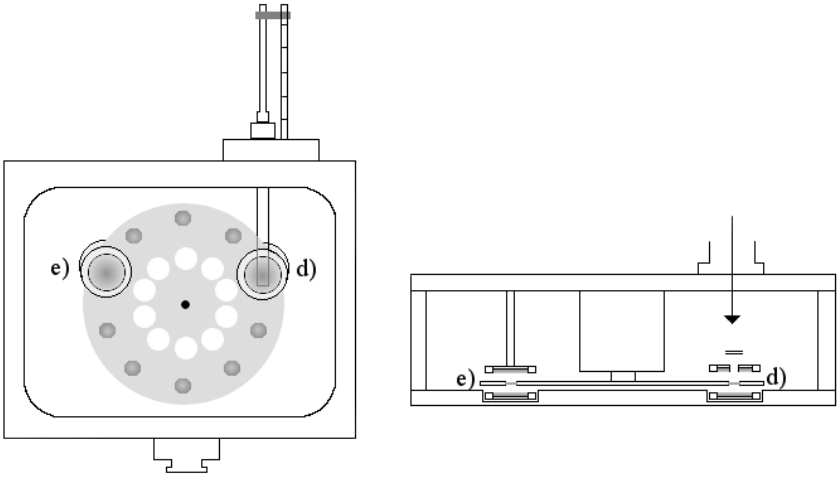

Figure 3.16: Windmill α setup for Run II of experiment IS456. Left: back view of the chamber; right: top view of the chamber. d) Implantation station detectors; e) decay station detectors.

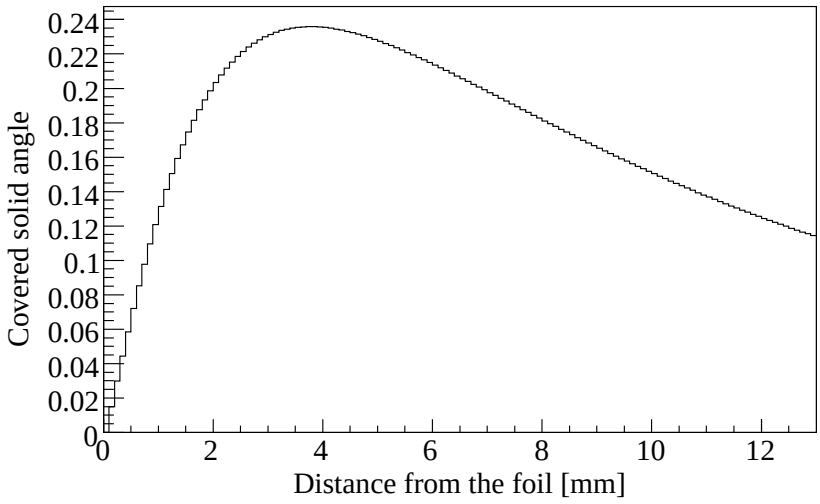

Figure 3.17: Solid angle covered by the annular detector as a function of the distance from the carbon foil. The solid angle peaks at a distance of 4 mm.

area, 6 mm aperture diameter). As this detector has no backing, an additional thick collimator (5 mm aperture diameter) is required to shield the detector from radioactive isotopes that could diverge from the collimators. With that particular shape, the distance from the detector has to be adjusted to maximise the solid angle; indeed, if the detector is too close, most of the α particles are sent through the aperture while if the detector is too far, too little solid angle is covered. The estimation of the solid angle coverage as a function of the distance from the foil is shown in Fig. 3.17; the position used is 4 mm.

The total solid angle covered at the implantation station is 66% of 4π, a large improvement factor with respect to Runs 0 & I. The spectra of the two detectors can however not be combined. Due to the depth of implantation of the ion beam in the foil, shown in Fig. 3.18, the α particles travel through much more material to reach the full detector than the annular one, yielding an energy shift and a low energy tail on the full detector. Meanwhile, nuclei recoiling out of the foil can be collected on the surface of the annular detector, hereby modifying the number of observed decays in the subsequent mother-daughter-grand daughter decay chain, of interest in appendix B.1. This recoiling effect is of great importance when studying branching ratios in daughter nuclei as 25% of the daughter nuclei may be affected [Wau91, DW04], of which about 50% are recaptured on the annular detector.

x and γ-ray detectors can be placed around the windmill to study $\alpha-$X and $\alpha-\gamma$ coincidences, as discussed for the specific case of ^{195}Po in appendix B.1.

Finally, the setup has also been moved to the LA1 beam line (see Fig. 3.3) to be placed further away from the separator and be less influenced by α-decaying noble gas contaminants, like radon, diffusing from the target area.

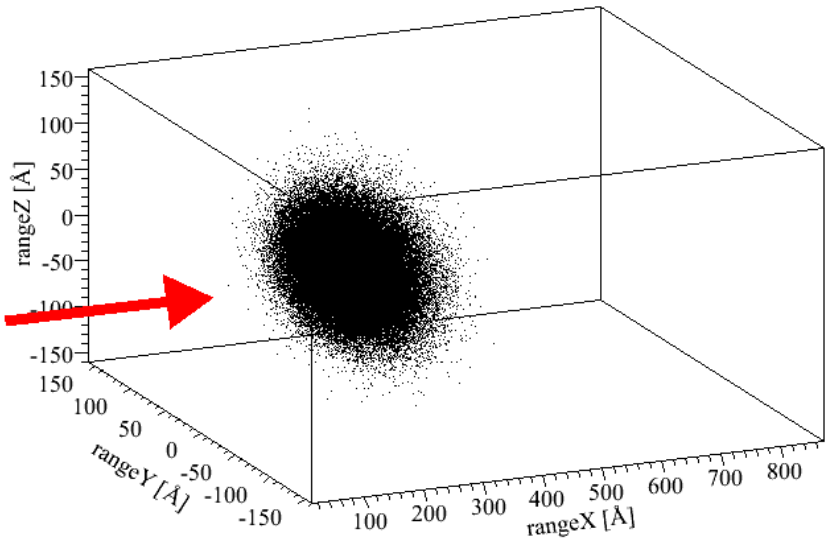

Figure 3.18: Depth of implantation of the ions in the C foil of the windmill. The arrow represents the incoming ion beam. The x axis represents the full depth of the foil (888 Å).

3.3.3 $\beta - \gamma$ decay

β-decaying isotopes can be found throughout this study, either as a probe for performance (radioactive rhodium at LISOL), or as a mean of counting (polonium isotopes at ISOLDE, radioactive copper isotopes at LISOL) or finally while studying their decay properties (^{199}Po).

ISOLDE tape station

During the laser spectroscopic study at ISOLDE, $^{199-204}$Po were studied with the ISOLDE tape station. The tape station is located in the experimental hall in proximity of the mergin vacuum chamber after GPS and HRS (see Fig. 3.3).

For Run I, the tape station was used simultaneously with the Windmill, accepting $^{199-200,202,204}$Po from the central mass of GPS while the low mass was sent to GLM. For Run II, it was used independently to study $^{201-203}$Po. The beam is implanted on a mylar tape that is transported in the middle of the measurement cycle towards the detection setup. The β^+ particles emitted by the decay of the radioactive isotopes are observed by a plastic scintillator and γ radiation subsequent to the decay is observed in a single HPGe crystal. All events from the scintillator detector are counted and all the γ events are recorded as well. α particles emitted by isobaric contamination of the beam (mostly francium) can also trigger the scintillators. $\beta - \gamma$ coincidences are possible but the statistics are too limited for this method to be of interest to this work.

For laser spectroscopic studies, the relative measurement of the intensity of a γ line is sufficient to yield the optical resonance. No absolute intensity is therefore

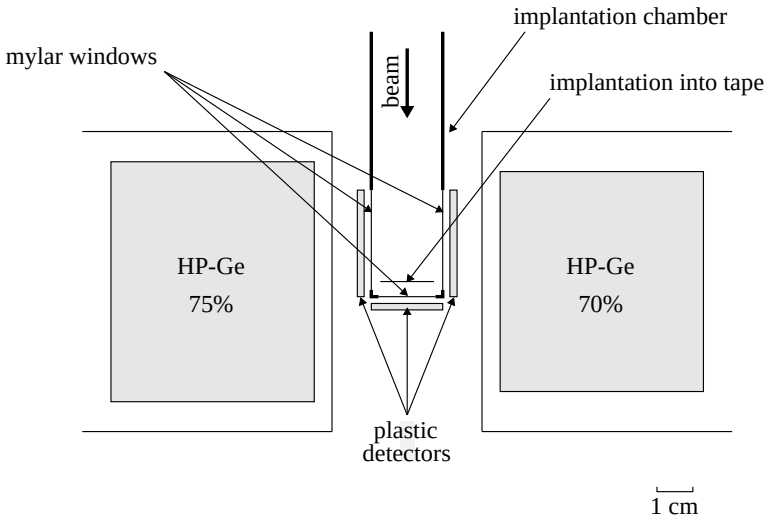

Figure 3.19: LISOL $\beta - \gamma$ decay setup.

required. It is however required for the study of the β decay of ^{199}Po, discussed in section B.2; a photopeak efficiency of 2% at 1.3 MeV was measured with the setup.

LISOL decay station

The LISOL $\beta - \gamma$ setup is used to measure, amongst many, the production of the neutron-deficient ^{94}Rh and neutron-rich ^{112}Rh isotopes to characterise the operation of the gas cell in on-line conditions (see section 4.2). It is also used to count the number of radioactive $^{57-59}$Cu ions for laser spectroscopy (see chapter 5).

The beam is implanted on a half-inch wide mylar tape from where it decays. The setup is shown in Fig. 3.19. The β particles are detected in one of the three ΔE plastic detectors that cover 68% of the solid angle and offer an efficiency of 50% [Pau08b]. Those are used as triggers for coincidence with the γ ray or to efficiently count pure beams of radioactive isotopes. The energy of the γ rays are measured with two coaxial HPGe crystals (70% and 75% respectively) for a total photopeak efficiency of 4% at 1.3 MeV. After a measurement, the activity is removed and a fresh portion of the tape is presented in front of the beam. For the study of the copper isotopes (chapter 5), the β counts are simply integrated by a scaler at each frequency step.

The signal processing associated with this setup is completely digital and the data is recorded in an event-by-event mode to allow for software reconstruction of the coincidences.

Chapter 4

Ion source developments

A nuclear physics experiment is like a soufflé recipe: a few key ingredients, the cook's know-how and a few hours (years) in the oven... A key ingredient nowadays is the Radioactive Ion Beam (RIB). Reaching for always more exotic regions of the nuclear chart and more intense and pure beams are the basic goals of beam development, yet it is always driven by the taste of physics motivation.

In this work, the main research focus is the polonium isotopic chain. The decay of the polonium isotopes has already been thoroughly studied [Wau93] at ISOLDE, using a hot plasma ion source. This source is, however, not element selective. The study of the mean-square charge radii of those nuclei by atomic spectroscopy required the development of a laser excitation scheme, both as a measurement tool and as a clean ion source.

At LISOL, the quest for magicity, or lack thereof, around $Z = 28$ has been driving the new gas cell developments for many years [Fra01, Fac04a, Fac04b, Iva07, Pau08a, Pau09]. In this work, the understanding of some contaminants in the beam as well as new purification techniques are discussed. The Laser Ion Source Trap (LIST) is the ultimate tool for selectivity and its first tests and developments are discussed. From the improved conditions emerges as well the possibility to perform in-source laser spectroscopy on isotopes unavailabe at other ISOL facilities.

4.1 New beams

4.1.1 Laser ionisation of the polonium atom with ISOLDE-RILIS at CERN

Paper I
T.E. Cocolios, B.A. Marsh *et al.*, *Nuclear Instruments and Methods in Nuclear Physics Research B*266(2008)4403 – 4406.

The interest in the laser ionisation of polonium is multifold: the production of pure beams for the Coulomb excitation of the neutron-deficient ^{196,198,200,202}Po isotopes with MiniBall at REX-ISOLDE [Basa]; and the study of the electromagnetic

moments and charge radii by laser spectroscopy of the whole isotopic chain (chapter 6).

The challenge in the determination of an efficient laser ionisation scheme comes from the radioactive nature of the polonium isotopes. As it is the first element beyond lead with no stable isotope, the study of its atomic structure is limited [Cha66]. Although few transitions from the atomic ground state have been clearly identified and even studied for nuclear physics purpose [Kow91], little is known on higher excitations and nothing on autoionising states.

The radioactive nature of polonium is also a problem for the off-line facilities where such properties could be studied. In order to preserve those facilities from radioactive contamination, it is not possible to study the polonium isotopes using large quantities of the long-lived isotopes $^{208-209}$Po. This is why the search for laser ionisation schemes for polonium had to be performed on-line at a RIB facility, namely CERN ISOLDE.

Three schemes, using two different possible transitions for the ground state, were successfully demonstrated; all schemes are made of three transitions with the last transition non-resonant. Once the sequence of transitions successfully identified, the properties of the different schemes are studied: saturation, yields, efficiency.

The saturation curves are mostly satisfying although some extra UV power could improve the production further. Additional power for the non-resonant ionisation step can also provide an increase in efficiency. This has been verified with the new solid state Nd:YAG pump laser after the publication of this article.

The yields were measured for $^{193-198,200,202,204}$Po with only one of the schemes and that of ^{196}Po was found to be similar using the other two schemes. Based on those yields, the in-source laser spectroscopy of the neutron-deficient polonium isotopes was shown to be possible down to ^{191}Po. The Coulomb excitation down to ^{196}Po is also within reach.

Based on the ABRABLA calculation [Luk06, Luk07] and the measured release of the polonium isotopes from the target, the efficiency of the laser ionisation of polonium was extracted. As the ABRABLA code is known to over-estimate the yields in this region of the nuclear chart, this efficiency is only a lower limit. The laser enhancement, not presented in the article, is discussed in section 4.1.2.

Finally, the α spectra from this test show very little contamination, unlike the previous studies using a plasma source. This proves the strong suppression in lead and bismuth that can be achieved with this type of ion source. Note however that no systematic study of the β^+/EC-decaying thallium isotopes has been performed. Moreover, the mass range studied was not favorable to study the possible francium contaminations. Those two elements,with low ionisation potential, can still be ionised on the surface of the hot atomiser for the laser ion source. A discussion on the contamination of the ^{200}Po beam by ^{200}Tl follows this article in section 4.1.2.

Resonant laser ionization of polonium at RILIS-ISOLDE for the study of ground- and isomer-state properties

T.E. Cocolios, M. Huyse, Yu. Kudryavtsev, P. Van Duppen
Instituut voor Kern- en Stralingsfysica, Katholieke Universiteit Leuven, B-3001 Leuven, Belgium

B.A. Marsh, V.N. Fedosseev, K. Johnston, E. Noah, T. Stora
ISOLDE, CERN, *CH-1211 Geneva 23, Switzerland*

S. Franchoo
Institut de Physique Nucléaire, F-91406 Orsay cedex, France

G.Huber
Institut für Physik, Johannes Gutenberg Universität, D-55099 Mainz, Germany

M.D. Seliverstov
Institut für Physik, Johannes Gutenberg Universität, D-55099 Mainz, Germany
and
Petersburg Nuclear Physics Institute, 188350 Gatchina, Russia

A.M. Ionan
Petersburg Nuclear Physics Institute, 188350 Gatchina, Russia

U. Köster
Institut Laue Langevin, F-38042 Grenoble cedex 9, France

Abstract

Three new ionization schemes for polonium have been tested with the Resonant Ionization Laser Ion Source (RILIS) during the on-line production of ^{196}Po in a UC_x target at ISOLDE. The saturation of the atomic transitions has been observed and the yields of the isotope chain $^{193-198,200,202,204}$Po have been measured. This development provides the necessary groundwork for performing in-source resonant ionization spectroscopy on the neutron-deficient polonium isotopes ($Z = 84$).

Laser ionization, polonium, production yield, optical transition, saturation
23.60.+e, 27.80.+w, 29.25.Ni, 32.80.Rm, 42.62.Fi

Introduction

Shape coexistence effects across the $Z = 82$ proton shell closure is an area of research of high interest to modern nuclear physics. The initial discovery of large isotope shifts and isomeric shifts in the neutron-deficient mercury isotopes ($Z = 80$) [1] from the measurement of the mean-square charge radii illustrated the complexity of the nuclear structure between the $N = 82$ and $N = 126$ neutron shell closures and the importance of excitations through the $Z = 82$ proton shell closure. The nuclear spectroscopic studies of the other elements in the same region of the nuclear chart, namely lead ($Z = 82$) [2] and polonium ($Z = 84$) [3], hinted at the importance of shape coexistence around the neutron mid-shell at $N = 104$.

In recent work at CERN ISOLDE, the shape of the neutron-deficient lead isotopes was directly observed from the changes in the mean-square charge radius, measured via in-source resonant ionization laser spectroscopy [4]. This study was made possible after the development of a laser excitation scheme for lead at the ISOLDE RILIS (Resonant Ionization Laser Ion Source).

In order to perform such a study on the polonium isotopes, an ionization scheme with an excitation step that can be used to determine the changes in the mean-square charge radii is needed. This excitation step will be obtained with a narrow bandwidth scanning laser to probe the resonance profile, yielding the hyperfine structure of the odd-A isotopes and the isotope shift between any two isotopes. As the element polonium does not have a stable isotope, a search for an efficient and effective ionization scheme, in terms of sensitivity to the changes in the mean-square charge radius, has been performed at the ISOLDE on-line separator using radioactive polonium isotopes. This paper reports on the observation of such ionization schemes and their properties.

Beam production

The isotopes are produced on-line with the 1.4 GeV CERN-PS Booster proton beam impinging on a UC_x target (50 g·cm^{-2} of depleted uranium with 99.6% of ^{238}U) at the ISOLDE facility. The produced isotopes diffuse from the high temperature (≈ 2000°C) target and enter the RILIS hot cavity where they are resonantly ionized with a three-step laser ionization scheme [5, 6]. After extraction and acceleration to 60 keV the ions are separated according to their mass-over-charge ratio with an analysing magnet. Details of the RILIS laser setup can be found in [7] and references therein.

Two different yield measurement setups were used. For measuring the α-emitting $^{193-198}$Po isotopes, the ion beam is implanted into thin carbon foils (30 μg·cm^{-2}) mounted on a rotating wheel with 10 foil holders (only 4 were used for this test). The α particles emitted by the decay of the isotopes are detected with a silicon detector (active area 150 mm^2, thickness 300 μm) placed behind the foil position. For the ^{200,202,204}Po isotopes, the ion beam is implanted into a mylar tape at the ISOLDE tape station. The tape is then moved and the β decay is observed along with its associated γ radiation. The yield, expressed in ions·μC^{-1}, extracted from each

α or γ spectrum, is used to determine the performance of the laser excitation and ionization schemes.

Study of the atomic transitions

This study was limited to the study of the three ionization schemes shown in Fig. 4.1. In the first scheme (shown on the left-hand side of Fig. 4.1) one valence electron is excited from its ground state with a UV transition at 255.8 nm[1] to a first excited state. The second excited state is reached with an infrared transition at 843.38 nm. An electron occupying this level is sufficiently energetic for subsequent excitation to the continuum by the non resonant absorption of a 510.6 nm photon, provided by the Cu vapour laser. The UV laser light is produced by tripling the frequency of a beam from a dye laser; its power reaches nearly 100 mW. The infrared laser light is produced with a dye laser and has up to 2 W of available power. The power from the Cu vapour laser used for the final step is 18 W.

The two remaining schemes (shown on the right-hand side of Fig. 4.1) also use a UV transition to reach the first excited state (245.011 nm). From this level both a 532.34 nm and a 538.89 nm transition were investigated and the 510.6 nm Cu vapour laser was used for the non-resonant final step. The laser powers available for each transition were similar to values quoted for the first scheme. All five resonant transitions involve one of the valence electrons in the $7s$ shell where the interaction with the nucleus is at its highest thus providing the information of interest to nuclear structure such as the change in the mean-square charge radius and the moments of the nucleus.

Ionization of ^{196}Po was achieved with each of the three schemes. Resonance laser ionzation was confirmed by the ability to completely suppress the ion production by blocking or de-tuning the UV laser beam. In the case of the UV+infrared ionization scheme, the resonance curve of the second step has been observed confirming the existence of the second excited state. This is the first confirmation of the existence of the excited states that were suggested in [9]. With the direct observation of the succession of the electron excitations, the position of the $6p^3 7p\ ^5P_2$ and the $6p^3 8p$ energy levels is now fixed.

Once each laser beam is optimised in frequency and position to maximise the production, the saturation of each resonant transition is studied. The power of the laser is controlled using an attenuator in the path of the laser beam of interest. Fig. 4.2 shows the saturation curves of the UV+infrared scheme while Fig. 4.3 shows the saturation curves of the UV+green schemes. All display the characteristic behaviour of saturated transitions except the UV transition at 255.8 nm; the latter is not saturated, meaning a higher power would further improve the ionization efficiency.

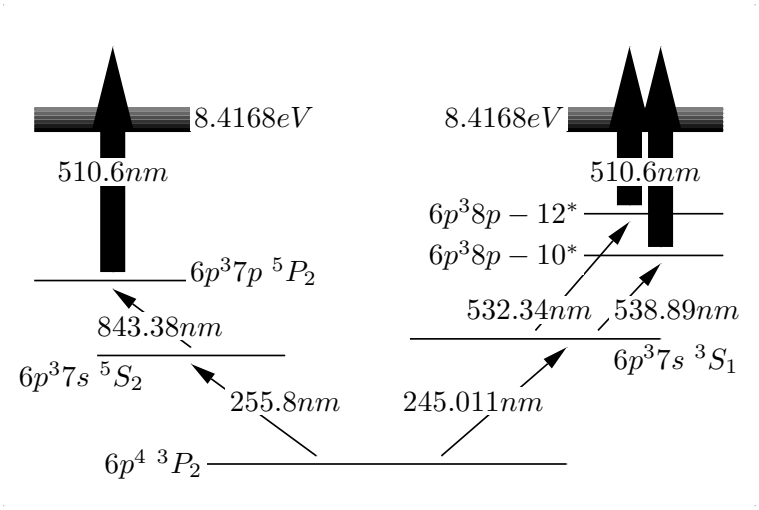

Figure 4.1: Laser ionization schemes, from the ground state to over the ionization potential. The last step (510.6nm) is non-resonant. The exact atomic configuration of the levels marked by a star (*) is undetermined.

Table 4.1: Polonium yields from the UV+infrared scheme. The yields for each mass are measured with different proton intensities and collection times but normalised to the same unit of ions·μC^{-1}. The top and bottom sections of the table correspond to two different targets.

Isotope	Half life [s]	Yield $\left[\frac{\text{ions}}{\mu\text{C}}\right]$	Isomer	Half life [s]	Yield $\left[\frac{\text{ions}}{\mu\text{C}}\right]$
^{193g}Po	0.45	$7 \cdot 10^1$	^{193m}Po	0.24	$1 \cdot 10^2$
^{194}Po	0.392	$2.7 \cdot 10^3$		.	·
^{195g}Po	4.64	$2.5 \cdot 10^4$	^{195m}Po	1.92	$5.5 \cdot 10^4$
^{196}Po	5.8	$4.8 \cdot 10^5$		.	·
^{197g}Po	53.	$5.8 \cdot 10^5$	^{197m}Po	25.8	$2 \cdot 10^6$
^{198}Po	105.	$1.2 \cdot 10^7$		.	·
^{200}Po	690.	$6.4 \cdot 10^6$		.	·
^{202}Po	2682.	$1.7 \cdot 10^7$		.	·
^{204}Po	12708.	$1.1 \cdot 10^7$		.	·

Yields of neutron-deficient polonium

The production yields of polonium for $A = 193 - 198$ and for $A = 200, 202, 204$ are measured from different targets, however in both cases the same target material and ionization scheme (UV+infrared) was used; the yields may therefore vary from one

[1]This transition was used by Kowlewska et al. to study the mean-square charge radii of $^{200,202,204-210}$Po and moments of ^{205,207,209}Po [8].

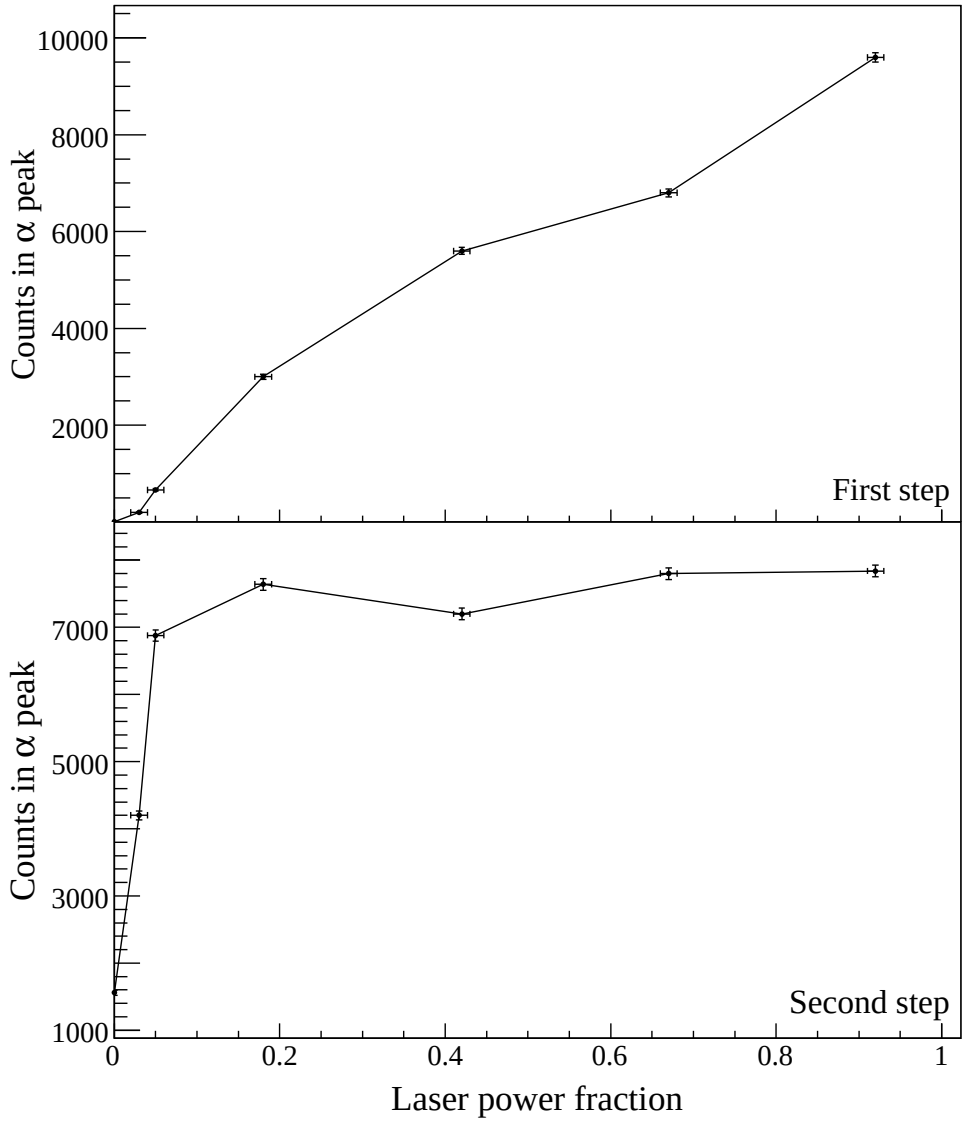

Figure 4.2: Saturation curves of the UV+infrared scheme using ^{196}Po. The top figure represents the curve of the first excitation step (255.8 nm) while the bottom figure, that of the second step (843.38 nm). While one transition is studied, the other transitions are kept at their maximal power. The lower figure shows over-saturation, meaning that more power than necessary is available.

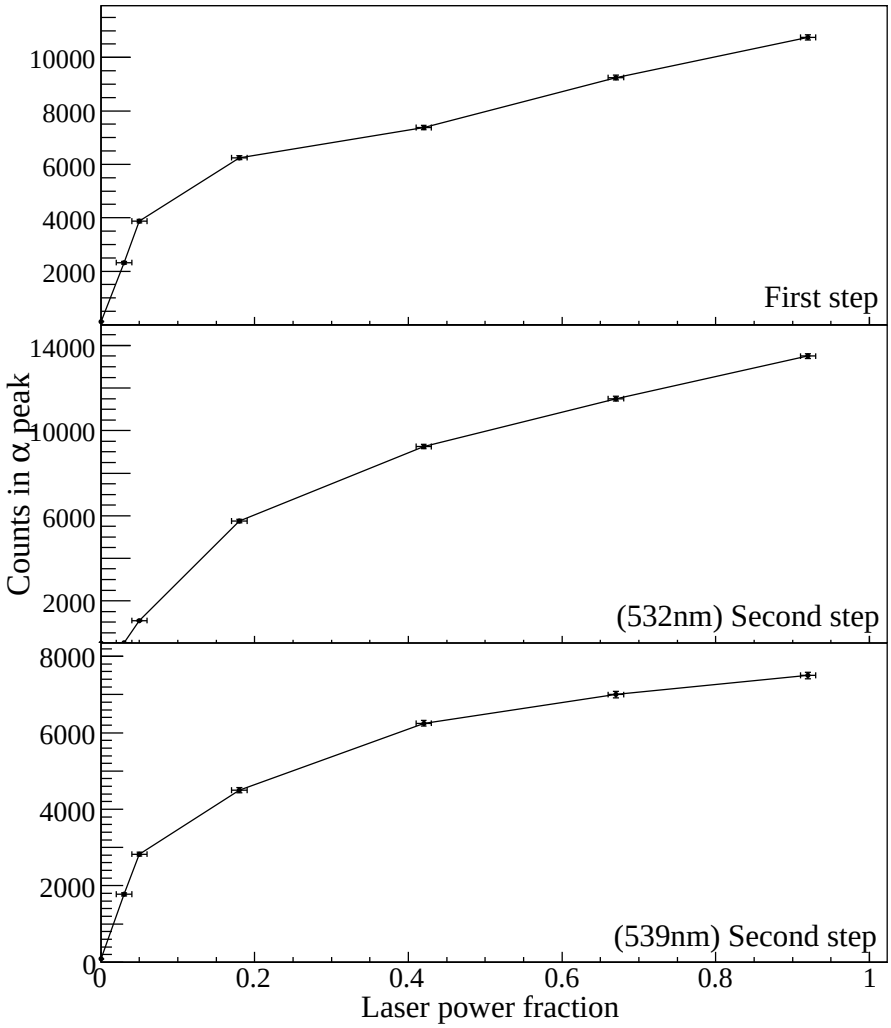

Figure 4.3: Saturation curves of the UV+green schemes using ^{196}Po. The top figure represents the curve of the first excitation step (245.011 nm), the middle figure, that of the first possible second step transition (532.34 nm) and the last figure, that of the other possible second step (538.89 nm). While one transition is studied, the other transitions are kept at their maximal power.

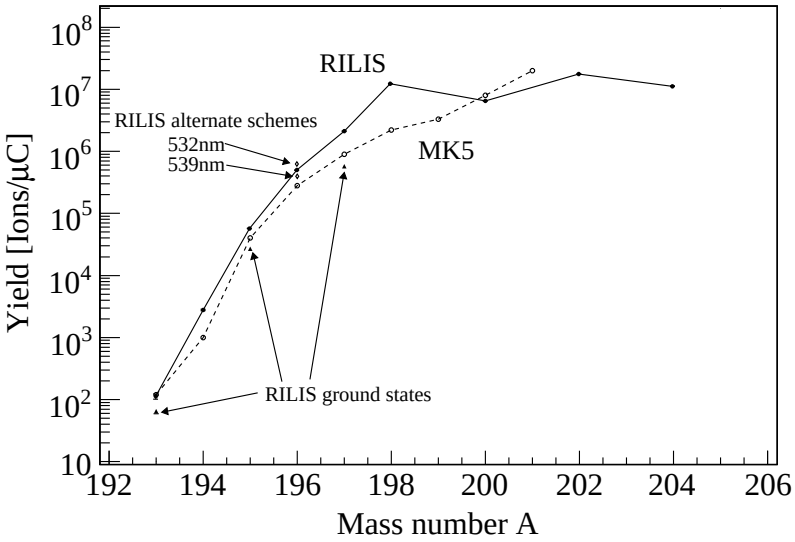

Figure 4.4: Yields of $^{193-198,200,202,204}$Po from laser ionization with the UV+infrared scheme (solid line) compared to those from the hot plasma source MK5 (dashed line). Note that the quantity of U in the target was a factor of 5 less in the study of the hot plasma source. The curve for the RILIS goes through the odd isomers while the odd ground states are displayed under the curve. The yields from the UV+green schemes are also measured for ^{196}Po and the two results are shown on the figure, labelled as wavelength of the second step.

set to the other. The resolution of the α detector is sufficiently high for resolving the ground state from the isomer decay in the case of the odd-A isotopes ^{193,195,197}Po. The acquisition times and the number of protons impinging the target were different for each isotope. The resulting yields, normalised to the proton current in ions$\cdot\mu$C^{-1}, are shown in Table 4.1 and displayed in Fig. 4.4.

The yield curve closely follows the yields obtained previously at the ISOLDE-SC (600 MeV protons) [10] with the unselective MK5 hot plasma ion source [11]. Note that the thickness of ^{238}U target for the latter was only 9.7 g$\cdot$cm^{-2} rather than 50 g$\cdot$cm^{-2} for this work. The advantage of the laser ionization source resides in its selectivity and although some ionization efficiency is lost, most of the contaminants are suppressed by this method. In the course of this work, only the decay of a few ^{193}Bi nuclei was observed as seen in Fig. 4.5. The contamination of the beam was not the subject of a thorough analysis during this study. A more complete assessment would require consideration of possible β-emitters which are not observed with the α-detection setup. The thallium isotopes, with a low ionization potential, are likely to be efficiently surface ionized. The yield of ^{196}Po has also been measured for the UV+green schemes and was found to be similar to that for the other scheme (Fig. 4.4).

For stable isotopes, the RILIS ionization efficiency is measured by complete evaporation of a sample with a known amount of atoms into the ion source and integrating

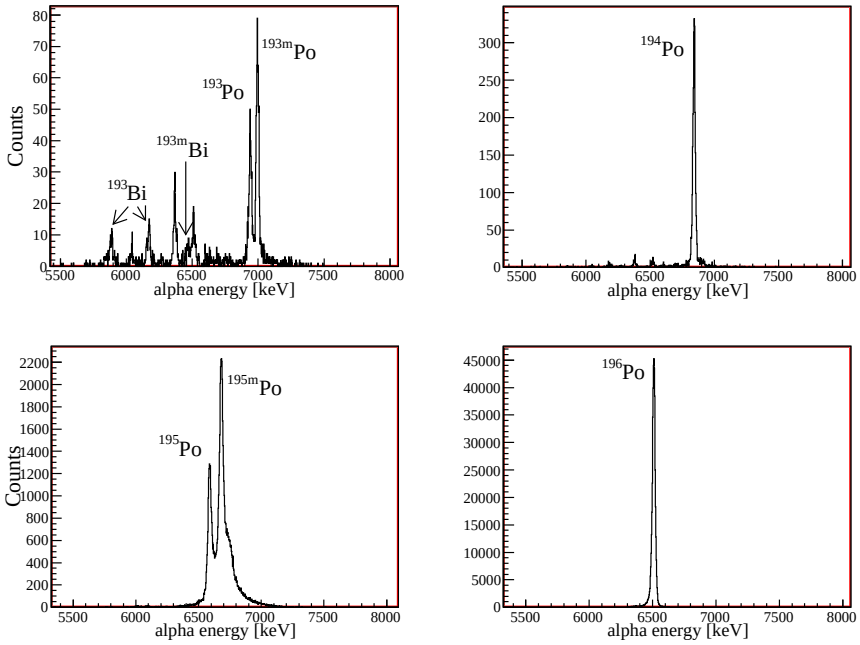

Figure 4.5: Alpha spectrum of ^{193,194,195,196}Po. All are acquired with the UV+infrared scheme over 120s.

the observed ion current after mass separation. Due to the absence of stable polonium isotopes, the overall release and ionization efficiency was instead estimated from a comparison of the measured radio-isotope yields to the in-target production rates based on ^{238}U spallation cross-sections calculated with the ABRABLA code for an incoming 1.4 GeV proton beam. Secondary reactions and feeding from α or EC/β decay precursors are then neglected [12, 13]. Fig 4.6 shows the trend of the overall efficiency as a function of the polonium isotope half-life. Using ^{202}Po, whose half-life is long enough to be completely released, one can determine a set of parameters to reproduce the release curve measured for ^{202}Po using a triple exponential approach. Integrating this release curve with the nuclear decay gives the released fraction of polonium for each isotope [14]. This function is then multiplied with the laser ionization efficiency which can now be fitted to the data, yielding a final result of 0.4%. This value is only a lower limit as the ABRABLA calculations in this region are known to over-estimate the production and a proportion of the polonium could be irreversibly trapped in the target.

Conclusion

Three different laser ionization schemes of polonium have been successfully tested online at the ISOLDE-RILIS. All schemes perform well and yields suitable for in-source laser spectroscopy measurements are achievable. The overall efficiency is limited by the very slow release of polonium. A lower limit for the laser ionization efficiency

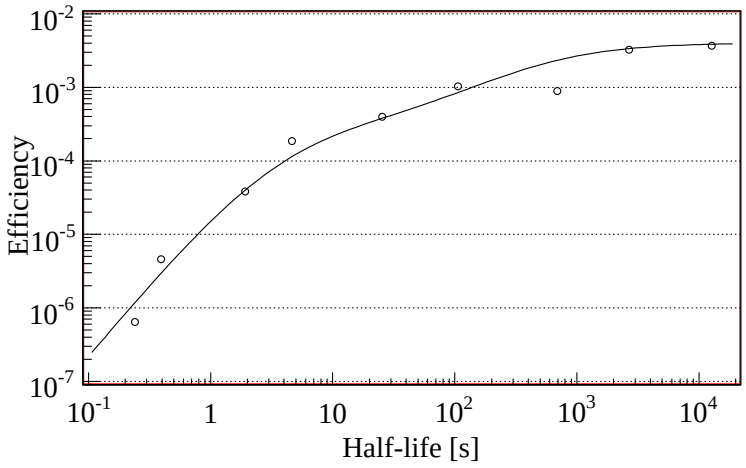

Figure 4.6: The circles represent the product of the release and the ionization efficiency of polonium isotopes, deduced from a comparison of the measured yields with calculations using the ABRABLA code for 1.4 GeV protons with no secondary reaction, while the solid line represents the fit to those values of a convolution of the release to the isotope half-life. The isotope and half-life ordering from ^{193}Po to ^{204}Po is similar. In the case of the odd isotopes, only the isomer is considered.

of 0.4% has been determined. This opens new possibilities for the study of neutron-deficient polonium isotopes where shape staggering effects are expected [3]. The first study will be on the change in mean-square charge radius of the neutron-deficient polonium isotopes by in-source laser spectroscopy as used for studying lead and bismuth isotopes [4].

The authors would like to acknowledge the contribution of Martin Eller. This work was performed thanks to the support of the European Union Sixth Framework through RII3-EURONS (contract no. 506065), the BRIX-IAP Research Program no. P06/23 and FWO Vlaanderen (Belgium).

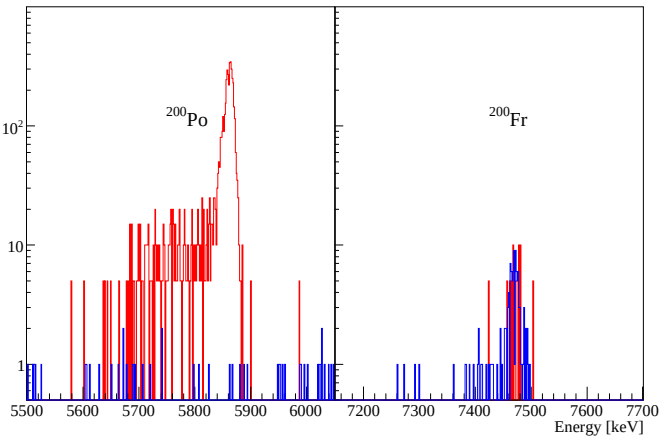

Figure 4.7: α spectra at mass $A = 200$ with the lasers ON (red) and OFF (blue). The right part of the spectrum shows ^{200}Po and the right part of the spectrum ^{200}Fr. The ON spectrum is rescaled for the ^{200}Fr peak to display an equivalent intensity in both ON and OFF cases.

4.1.2 Laser enhancement and beam contamination

During Run II, the beam at mass $A = 200$ was studied both with and without laser ionisation. The α spectrum for both cases is shown in Fig. 4.7. Normalising the content of the ^{200}Po peak to that of ^{200}Fr to account for any fluctuations in the experimental conditions, a selectivity of 1000 can be attributed to the lasers on the ionisation of polonium. Note however that ^{200}Tl does not emit any α particles in its decay and cannot be observed in the α-decay spectrum.

In the same study, with the lasers OFF only, the γ-ray energy spectrum of the decay of the beam components has been observed. The full spectrum is shown in Fig. 4.8. It is rather complicated as the foils had already accumulated much activity from different masses. The γ radiation associated with the β-decay of ^{200}Tl and ^{200}Po could however be clearly identified, as well as that of the internal decay of ^{200m}Tl. The properties of those transitions are given in Table 4.2.

The abundance ratio is given by comparing the different peak contents normalised to the lifetime correction η, accounting for those isotopes that did not decay directly, to the γ photopeak efficiency $\epsilon_\gamma \propto E_\gamma^{-0.62}$, to the branching ratios b_β and the absolute γ intensity in the β decay. The γ-ray spectra were acquired without the laser ionisation. In order to estimate what the beam composition would be with the lasers ON, the content of the polonium γ-ray transitions has to be rescaled by the laser selectivity extracted from the α spectra. Although the γ-ray transition for ^{200m}Tl is the most intense in the γ-ray energy spectrum of Fig. 4.8, the portion of ^{200m}Tl in the beam is found to be negligeable, because of the large difference in lifetime

[2] see appendix B for details.

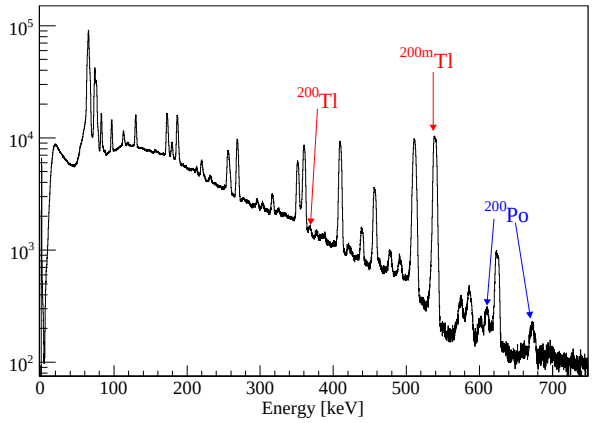

Figure 4.8: γ spectrum at mass $A = 200$ with the lasers OFF. The studied γ transitions in ^{200}Tl and ^{200}Po are indicated with an arrow.

Table 4.2: Properties of the γ transitions in ^{200}Tl, ^{200m}Tl and ^{200}Po: half-life $T_{1/2}$, lifetime correction factor η, β or IT branching ratio b_β, γ energy E_γ, γ absolute intensity I_γ and γ peak content A_γ. The estimated beam composition, if using laser ionisation (i.e. applying the laser selectivity enhancement factor on ^{200}Po), is then given.

	^{200}Tl	^{200m}Tl	^{200}Po
$T_{1/2}$	26.1 h	34.3 ms	11.5 min
η	0.0000708	1	0.00957
b_β	1	1	0.89
E_γ	368 keV	541 keV	617.7/671 keV
I_γ	87%	98%	20/34%
A_γ	8810(1111)	6113514(5805)	6929(351)/6326(221)
lasers ON	$\leq 5\%$	0.03(1)%	$\geq 95\%$

correction between the different isotopes/isomers. The portions of ^{200}Tl and ^{200}Po, of interest to the Coulomb excitation study at REX-ISOLDE, are $\leq 5\%$ and $\geq 95\%$, respectively. Experimentally, a contamination in the beam of 1% has been observed at MiniBall [Bas09].

4.1.3 Time dependence of the contamination

As discussed in section 4.1.1, the release of the polonium isotopes is slow. This effect limits the production of the most exotic species, which half-lives are so short that most of the radioactive products decay before they can reach the atomiser. On the other hand, it can be used as an advantage when studying longer-lived isotopes, otherwise overwhelmed by isobaric contaminants. The release parameters for polonium, as introduced in equation 3.1, are shown in Table 4.3; those for thallium [Basb] and francium [Bou07a] are shown as well.

Table 4.3: Release parameters for polonium, thallium and francium, as defined in equation 3.1.

	Polonium	Thallium	Francium
λ_r [s]	18.1	0	0.15
λ_f [s]	4.67	2.277	4.1
λ_s [s]	568	37.991	-
α	0.984	0.98	0

In practice, this means that the polonium isotopes are more likely to decay in the target matrix than the other two isotopes. For example, for a 100-ms-lived isotope of polonium, thallium or francium, the released fraction would be $5 \cdot 10^{-5}$, $2.2 \cdot 10^{-2}$, or $1.1 \cdot 10^{-2}$, respectively.

Pulsed-release of the neutron-rich polonium isotopes

In the study of the neutron-rich $^{211-218}$Po isotopes, the production of the isobaric francium contamination is at least comparable to the production of the isotopes of interest; in many cases, it is even overwhelming. The half-lives and production rates of those isotopes are shown in Table 4.4. Those isotopes with very short half-lives decay before they can successfully diffuse out of the target material; note however that the tails of the isotopes produced with very high intensity can reach neighbouring masses, as is discussed in section 3.1.3 for ^{213}Fr and ^{216}Po.

In order to suppress the francium contamination, the method of pulsed-release [Van98, De 04] can be used. It takes advantage of the pulsed structure of the proton beam from the PSB, shown in Fig. 3.1, by letting the beam through the separator only once the polonium concentration in the beam is higher than that of the francium.

The best example of this technique, in the polonium case, is that of ^{218}Po ($T_{1/2}$ = 183 s), shown in Fig. 4.9. The short half-life of ^{218}Fr ($T_{1/2}$ = 0.022 s) results in an

Table 4.4: Half-lives and yields (measured or calculated) of the neutron-rich polonium (ABRABLA calculations [Luk06, Luk07] and efficiency as presented in section 4.1.1) and francium isotopes at ISOLDE [iso]. The shorter-lived isotopes do not exit the target matrix and no yield are therefore available.

A	Polonium		Francium SC yields [iso]	
	Half-life [s]	Yield [μC^{-1}]	Half-life [s]	Yield [μC^{-1}]
211	$2.52{\cdot}10^{1}$	$5{\cdot}10^{5}$	$1.86{\cdot}10^{2}$	$1.5{\cdot}10^{8}$
212	$4.51{\cdot}10^{1}$	$4{\cdot}10^{5}$	$1.2{\cdot}10^{3}$	$1.6{\cdot}10^{8}$
213	$4.2{\cdot}10^{-6}$	–	$3.46{\cdot}10^{1}$	$3.4{\cdot}10^{7}$
214	$1.64{\cdot}10^{-4}$	–	$5{\cdot}10^{-3}$	$9.4{\cdot}10^{2}$
215	$1.78{\cdot}10^{-3}$	–	$9{\cdot}10^{-8}$	–
216	$1.5{\cdot}10^{-1}$	$1{\cdot}10^{0}$	$7{\cdot}10^{-7}$	–
217	$1.53{\cdot}10^{0}$	$2.2{\cdot}10^{1}$	$1.6{\cdot}10^{-5}$	–
218	$1.83{\cdot}10^{2}$	$1.83{\cdot}10^{2}$	$2.2{\cdot}10^{-2}$	$4.3{\cdot}10^{2}$

abrupt truncation of the francium release curve. If the beam is prevented from going to the experiment in the first second following the proton beam impact on the target, it becomes a pure beam of polonium.

In the case of ^{216}Po, the half-life of this isotope is the short one ($T_{1/2} = 0.15$ s) in comparison to that of ^{213}Fr ($T_{1/2} = 34.6$ s). As seen in section 3.1.3, the isotope ^{213}Fr overwhelmes the spectrum at mass 216, although it is three masses away, by about a factor 10. An alternative method is therefore needed to enhance the polonium production. If one applies a beam gate that only allows the beam to be extracted for the first 500 ms following the proton beam impact, the amount of extracted polonium and francium isotopes becomes similar, as shown in Fig. 4.10.

The other isotopes are less sensitive to the beam gate settings. Indeed ^{217}Po does not suffer from any contamination while $^{211-212}$Po cannot be cleaned sufficiently to overcome the very large francium contamination and the beam purity can be at most 10%. Finally, the shorter-lived isotopes $^{213-215}$Po are simply decaying in the target before they can diffuse out.

Pseudo off-line measurement

During Run II, yet a different approach was taken. By irradiating the target during the study of the neutron-deficient isotopes, high quantities of long-lived ($T_{1/2} \geq 30$ minutes) isotopes of astatine ($Z = 85$) are produced in the target matrix but not fully released. The isotopes $^{206-211}$At then β decay to the isobaric isotopes $^{206-211}$Po, hereby giving rise to the production of polonium isotopes even in the absence of the proton beam. This is illustrated in Fig. 4.11. The isobaric francium isotopes, however, do not have such precursors and their intensities are negligible when the proton beam is off. It then becomes possible to study the isotopes $^{206-210}$Po off-line using a FC to count the ions (see section 3.3.1).

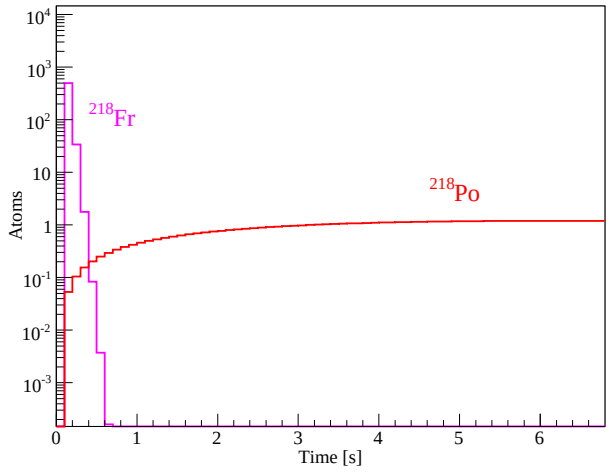

Figure 4.9: Calculated release curves for ^{218}Po and ^{218}Fr for a single proton impact on the target using the parameters from Table 4.3. If a beam gate is applied to suppress the beam for the first second, the beam is then purely made of polonium.

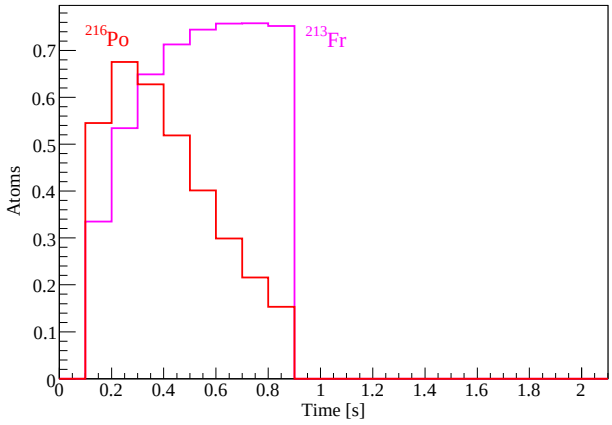

Figure 4.10: Calculated release curves for ^{216}Po and ^{213}Fr for a single proton impact on the target, assuming that the tail of ^{213}Fr is 10 times more intense than the production of ^{216}Po. If a beam gate is applied to allow the beam for only the first 500 ms, the beam is then evenly made of polonium and francium.

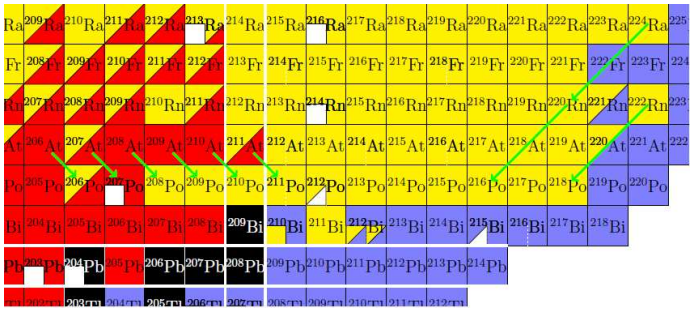

Figure 4.11: Part of the nuclear chart from Pb ($Z = 82$) to Ra ($Z = 88$) around $N = 126$. The decays of interest to populate the polonium isotopes off-line from long-lived trapped radioactive nuclei are shown in green.

Table 4.5: Isotopes of polonium measured in pseudo off-line conditions, their precursors and the half-lives of the precursors.

Polonium	Precursor	
^{206}Po	^{206}At	29.4 min
^{207}Po	^{207}At	1.8 h
^{208}Po	^{208}At	1.63 h
^{209}Po	^{209}At	5.4 h
^{210}Po	^{210}At	6.3 h
^{211}Po	^{211}At	7.22 h
^{216}Po	^{224}Ra	3.66 days
^{218}Po	^{222}Rn	3.825 days

In the same fashion, long-lived ^{224}Ra ($T_{1/2} = 3.66$ days) and ^{222}Rn ($T_{1/2} = 3.825$ days) are accumulated in the target and through their respective α-decay chains, highlighted in Fig. 4.11, produce the isotopes ^{216,218}Po in the absence of the proton beam irradiation. Although most of the radon has probably left the target matrix, there remains a sufficient amount trapped in the target to produce the polonium isotopes. The list of the studied isotopes in this pseudo off-line approach and their precursors is given in Table 4.5.

4.2 Gas catchers for tomorrow

In the quest for pure beams, two approaches have to complement each other: on one hand the contamination needs to be suppressed while on the other, the production of the element of interest should be enhanced. While extensive work has been done on the latter point with the development of many laser ionisation schemes [Kud03], relatively little is known about the contaminants. Much work has therefore been devoted to identifying the origins of the different contaminants and to suppressing

them efficiently.

The aim of the gas cell developments is ultimate purity, suppressing totally the contaminants while maximising the production of the exotic species of interest. This is of tremendous importance for the next generation facilities like S^3 [s3], SLOWRI [Wad09], PALIS [Son09], LaSpec [Nör06], FRIB [fri] or EURISOL [eur], where high intensities of contamination are foreseen and may overcome the very exotic beams of interest.

4.2.1 Survival of ions in a gas catcher

Paper II
Yu. Kudryavtsev, T.E. Cocolios *et al.*, *Nuclear Instruments and Methods in Nuclear Physics Research B*266(2008)4368 – 4372.

A first source of contamination comes from all the recoiling radioactive ions that do not recombine or ionise again to exiting the gas cell. The stopping process of the recoiling reaction products leave them in a high charge state but charge-exchange reactions with the noble gas atoms bring them quickly into a 1^+ charge state. The high energy deposited by the primary beam during its trajectory in the gas cell produces simultaneously a high density of ion/electron pairs. This plasma quickly recombines [Fac04a] leaving most of the isotopes in either a neutral state or ionised to a single charge. This effect should however be dependent on the element and little is known on the chemical dependence of this process.

Using a ^{252}Cf spontaneous fission source, many elements could be studied in conditions approaching the standard running conditions, with a high ion/electron density induced by the α decay of the ^{252}Cf isotopes and many radioactive recoils available.

The final result shows a clear chemical dependence on the survival of the ions although the reionisation processes could not be disentangled from the direct ion survival. In the comparison between the survival efficiency and the ionisation potential, a linear trend may also be outlined, as shown in Fig. 4.12.

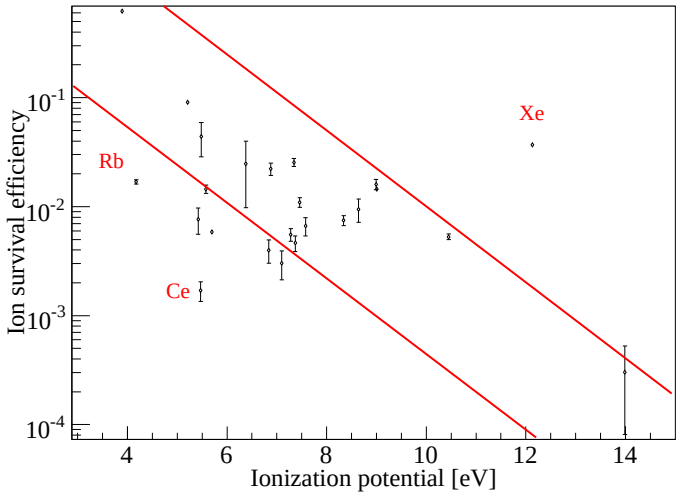

Figure 4.12: Efficiency for extraction of fission fragments as singly charged ions from ^{252}Cf in 500 mbar Ar as a function of the ionisation potential. The red lines show the possible trends followed by the survival efficiency. The special cases discussed further are highlighted.

Characterization of the LISOL laser ion source using spontaneous fission of ^{252}Cf

Yu. Kudryavtsev, T.E. Cocolios, J. Gentens, O. Ivanov, M. Huyse, D. Pauwels, M. Sawicka, T. Sonoda, P. Van den Bergh, P. Van Duppen.
Instituut voor Kern- en Stralingsfysica, Katholieke Universiteit Leuven, B-3001 Leuven, Belgium

Abstract

A spontaneous fission Californium-252 source was placed inside a gas cell in order to characterize the LISOL laser ion source. The fission products from ^{252}Cf are thermalized and neutralized in the plasma created by energetic particles. Two-step selective laser ionization is applied to produce purified beams of radioactive isotopes. The survival of fission products in a single charge state has been studied in argon as a buffer gas for different elements.

Laser resonance ionization, spontaneous fission, californium -252, ion catcher
25.85.Ca, 32.80.Fb, 41.85.Ar

Introduction

The LISOL laser ion source is used already for more than a decade for the on-line production of short-lived radioactive isotopes. The operational principle of the ion source is based on the element-selective multi-step laser resonance ionization of nuclear reaction products thermalized and neutralized in a high-pressure noble gas [15, 16, 17, 18]. The laser ion source made it possible to perform β and γ decay studies of nuclei that are produced in proton-induced fission of ^{238}U [19] and in light/heavy ion-induced fusion-evaporation reactions [20, 21]. Resonant laser ionization was also used to characterize the laser ion source whereby a highly energetic (185 MeV) ^{58}Ni beam was stopped in the gas cell and converted into a low energy mass-separated beam [22].

Recently, a ^{252}Cf fission source (0.78 mCi) was placed in a new gas cell in order to characterize the system and to study the survival of the fission products in atomic and ionic form in different experimental conditions. In this case, high energetic fission products are stopped in the argon buffer gas and are neutralized in the plasma created by ionizing particles. Purified beams of radioactive isotopes were produced using two-step laser resonant ionization via autoionizing states. The paper reports on the results obtained with this new set-up.

Experimental set-up

The spontaneous fission ^{252}Cf source allows to thermalize different fission products inside the gas cell. It has a half-life of 2.645 years and decays by alpha decay (96.9%) and spontaneous fission (3.1%). The source activity (on 21.04.2004) was 28.9 MBq. The yield of primary fission products is well determined [23]. Fig. 4.13 shows the independent yield of all fission isotopes in the mass range of $85 - 155$. In the low mass region, the maximum yield corresponds to technetium isotopes, while in the high mass region to ceasium and barium ones. The energy of the fission product lies around 105 MeV and 80 MeV for low- and high mass maximum, respectively.

The californium-252 source is located on a stainless steel substrate of 10 mm in diameter in the form of Cf-Pt alloy, Fig. 4.14. The active spot diameter is 4 mm. The source is placed on a moveable holder that allows changing the distance to the exit hole of the gas cell and its position relative to the cell axis. By measuring the energy of alpha particles emitted by ^{252}Cf it was concluded that the source is located at the distance of 0.1 μm from the surface and the emitted fission products are almost mono energetic. To reduce the energy of fission products, a 6 μm aluminum foil is placed above the source. Using the SRIM code [24], it was calculated that 34% of fission products are fed into the gas which corresponds to $5.3 \cdot 10^5$ atoms/s (November 2004).

The gas cell is made of aluminum and has an inner diameter of 7 cm and a length of 16 cm. It has a conical shape towards the exit hole, Fig. 4.14. The exit hole diameter is equal to 0.5 mm. The average evacuation time depends on the place where the fission products are stopped and equals to 2.7 s and 9.2 s at the distance of 52 mm and 100 mm to the exit hole respectively. High purity argon gas, purified

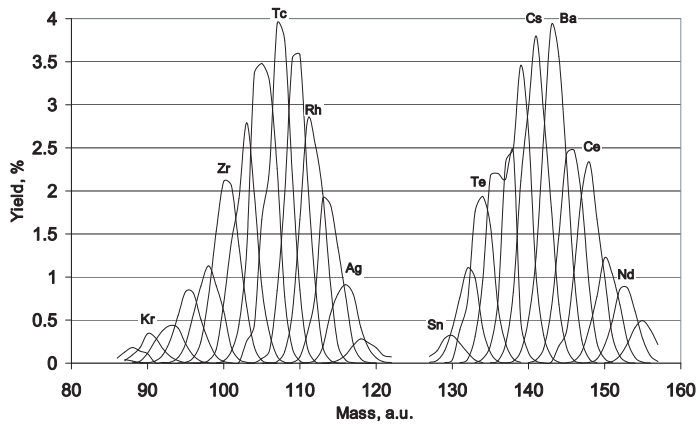

Figure 4.13: The independent yield of fission isotopes in the spontaneous fission of ^{252}Cf [23].

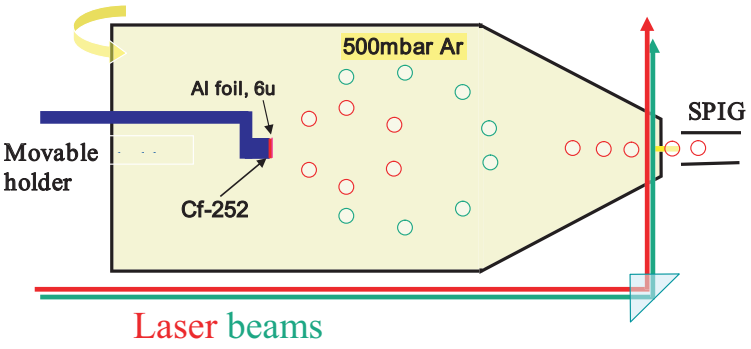

Figure 4.14: Layout the gas cell with the spontaneous fission source ^{252}Cf.

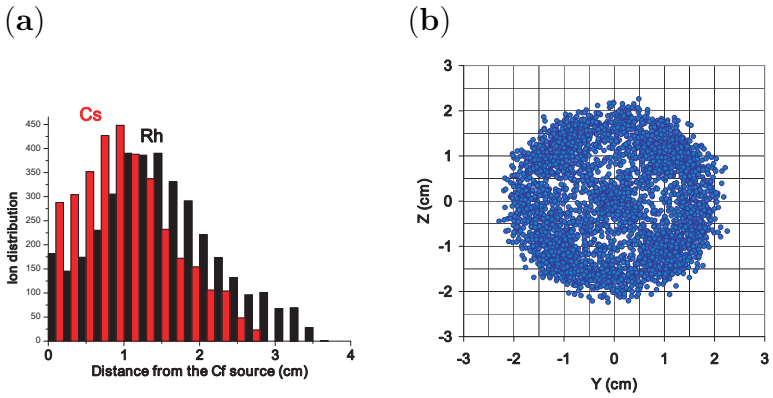

Figure 4.15: (a) Distribution of caesium (gray) and rhodium (black) ions along the cell axis at 500 mbar argon. (b) Rhodium ion distribution in the plane perpendicular to the cell axis at 500 mbar Ar.

down the ppb level in a getter-based purifier, was fed into the gas cell from the back site.

All fission products can be stopped inside the gas cell at argon pressure of 500 mbar. Fig. 4.15a shows the calculated distribution of rhodium and ceasium along the cell axis. Since ceasium ions have a smaller initial energy and a bigger stopping power they have a shorter range in argon. All rhodium ions (6800 ions calculated) are stopped within a distance of 3.5 cm and ceasium atoms within a distance of 2.7 cm. The rhodium ion distribution in a plane perpendicular to the cell axis is shown in Fig. 4.15b. The radial distribution (4 cm) is less than the inner diameter of the cell. The stopping range of alpha particles emitted by ^{252}Cf is more than a factor of 2.5 larger and part of them is implanted in the cell wall. The plasma density created by the fission products and the alpha particles is estimated to be around 10^8 ion-electron pairs/cm^3. The recombination time in argon at this density equals to 0.1 s [22]. This is much shorter than the evacuation time of the thermalized fission products. The neutral atoms are transported by the gas flow towards the exit hole region where they can be ionized by laser beams, Fig. 4.14. A two-step scheme is used for the selective laser ionization of the neutralized fission products. The diameter of the laser beams inside the ion source is between 4 and 6 mm. The laser optical system consists of two dye lasers pumped by two time-synchronized XeCl (308 nm) excimer lasers running with a maximum repetition rate of 200 Hz. The dye laser pulse length equals to 15 ns and the bandwidth equals to 0.15 cm^{-1}. To get UV light, the frequency of the first step laser radiation is doubled in the second harmonic generator. The dye laser beams are directed to the ion source located at a distance of 15 m where the two laser beams are overlapped at a small angle. Laser-produced ions are captured within the SextuPole Ion Guide (SPIG) [25] and are directed towards the mass separator. The mass separated beam is transported and deposited on a tape. The implantation point is surrounded by three plastic ΔE β detectors and two high purity Ge detectors for γ-detection.

Results and discussion

Different types of experiments can be performed using the ^{252}Cf source inside the laser ion source. First of all, the selective laser ionization provides yield enhancement of the desired isotopes. This gives the possibility to perform nuclear spectroscopy studies of exotic isotopes that are overwhelmed by more abundant isotopes. Also, the absolute laser ion source efficiency can be measured since the number of fission atoms fed into the gas is known. Without laser ionisation, the survival of ions of different elements that have different chemical properties can be studied and by comparing the survival efficiency of ions with different half-life of the same element the evacuation properties of the gas cell can be evaluated.

Selective laser enhancement

Fig. 4.16 shows the yield of ^{112m}Rh isotopes (November 2004) after mass separation as a function of the distance between the ^{252}Cf and the exit hole when lasers are tuned

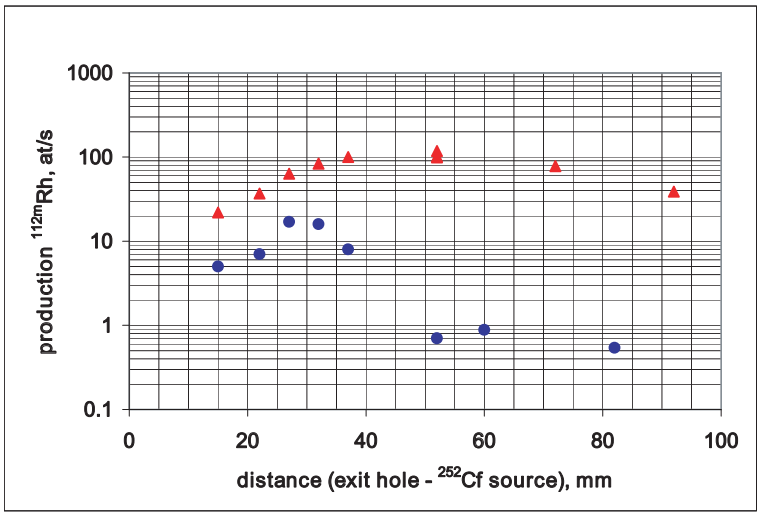

Figure 4.16: Production of ^{112m}Rh isotopes as function of the distance between the ^{252}Cf source and the exit hole of the gas cell when lasers are tuned on resonance with rhodium atoms (triangles) and when lasers are off (circles).

on resonance with rhodium atoms and when lasers are off. To extract the production rates, the intensity of the 560 keV γ line, that is characteristic for the decay of the high-spin isomeric state of ^{112}Rh [26, 27] was used. The points corresponding to the OFF case is a measure for the survival of rhodium ions in argon while the points corresponding to the ON case are dependent on the presence of neutral rhodium atoms, available for the laser ionization. For both cases the yield drops at small distance because part of the fission fragments are implanted in the wall. At a distance larger than 30 mm, the off-resonance production rate drops while the on-resonance production rate still increases even up to a distance of 50 mm. The former is mainly due to the recombination of the ions. At large distances the on-resonance production rate drops smoothly. This can be understood as due to the decay of ^{112m}Rh inside the gas cell ($T_{1/2} = 6.8$ s). The enhancement of the production rate due to resonant laser ionization at the distance of 52 mm equals to 160. The production rate of the ground state rhodium isotopes was measured using the 777 keV γ line. The total production of ^{112}Rh isotopes at a source to exit hole distance of 52 mm is 250 atoms/s, which corresponds to an overall efficiency of 3.75% defined as the number of ^{112}Rh atoms found after mass separation over the ones fed into a buffer gas. In the mass range $108-114$, the mass-separated ion current rate without lasers was less than 5 ions/s. This allowed us to measure the yield of the laser-ionised radioactive isotopes by direct counting the ions after mass separation. In this case the ground and metastable states of ^{112}Rh cannot be distinguished. The yield of rhodium isotopes in this mass range measured by this counting technique was in agreement with the one deduced by the radioactive decay studies and the distribution in mass corresponded to the theoretical one [23].

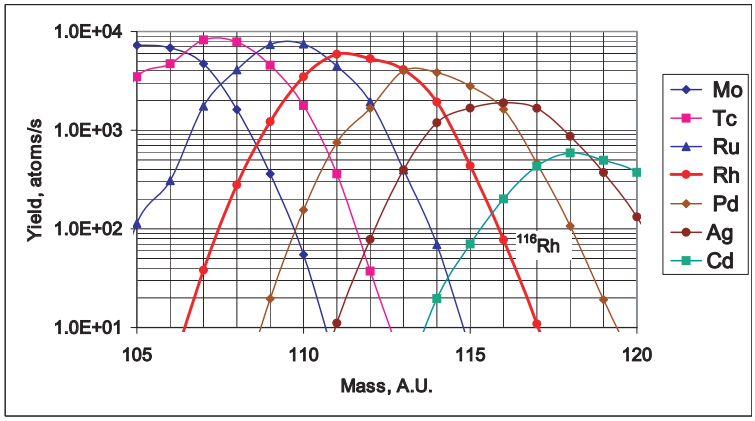

Figure 4.17: Calculated yield of fission isotopes (September 2005) in the mass range $105 - 120$ from ^{252}Cf [23].

Nuclear spectroscopy

If the isotope of interest is overwhelmed by more abundant isotopes, the laser enhancement can be very useful for its identification. As example, the $\beta - \gamma$ spectroscopy of ^{116}Rh has been performed using the ^{252}Cf source. As can be seen from Fig. 4.17, the ^{116}Rh is produced in much smaller quantities than the Pd, Ag and Cd isobars. Fig. 4.18 shows a β-gated γ spectrum obtained at mass 116. The line at 340 keV is present only when the lasers are on resonance with rhodium ($\lambda_1 = 232.258$ nm, $\lambda_2 = 572.55$ nm [15]). Since niobium, yttrium and zirconium ions form oxides very efficiently, γ rays of ^{100}Nb, ^{100}Y and ^{100}Zr are present in the spectrum of mass 116. The intensity of the ^{116}Rh line is comparable with that of the oxides; however, it has to be stressed that the calculated yield of ^{100}Y, ^{100}Nb and ^{100}Zr are respectively 16 times, 19 times and 57 times larger than the yield of ^{116}Rh. To get information on the time behavior of the gamma rays, the implantation is performed in a cycle 3s beam ON - 5s beam OFF. The inset on Fig. 4.18 shows a growing-decay curve of 340 keV γ line intensity. Based on this behavior, a half-life $T_{1/2} = 787(38)$ ms was obtained. This line is fed by the high spin and the low spin β decay of ^{116}Rh [28]. This value is larger compared to the previously reported half-lives for the high-spin isomer ($T_{1/2}$=0.57(5)s [28]) and low-spin isomer ($T_{1/2}$=0.68(6)s [29]). The available data do indicate a substantial feeding of the high-spin isomer in the present experiment but a precise ratio for the population of the high-spin versus low-spin isomer could not be determined.

Survival of ions in argon gas

Nowadays, gas cells are frequently used as gas catchers behind fragment separators [30, 31, 32]. Usually helium is used to stop recoils. Argon has a much higher stopping

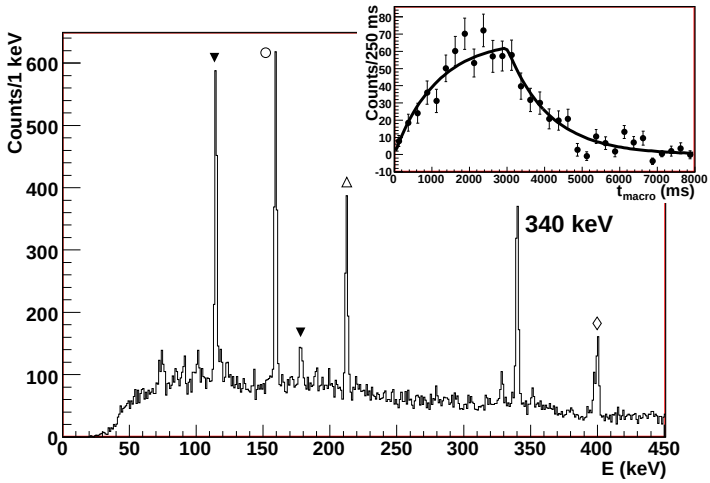

Figure 4.18: β-gated γ spectra at mass 116 with lasers tuned on resonance with rhodium atoms (full reversed triangle$-^{116}$Pd, open circle$-^{100}$Nb, open triangle$-^{100}$Y, diamond$-^{100}$Zr), the inset shows a growing-decay curve of 340 keV γ line.

power and can be used instead of helium. However, ions form molecular adducts with argon much faster leading to losses in sidebands [18]. Ion recombination in argon is also much faster than in helium. The spontaneous fission ^{252}Cf source gives us an opportunity to study the ion behavior of different atomic ions in noble gases. For this, the ^{252}Cf source is placed in the standard LISOL laser ion source gas cell and the surviving ions extracted from the gas cell and mass separated are measured by means of their respective β decay. Comparing this production rate to the yields of the californium source gives the efficiency of survival of ions in this particular buffer gas cell filled with 500 mbar argon.

This gas cell is much faster than the one shown on Fig. 4.14. The average evacuation time of the stopped fission products is about 200 ms. The gas cell is made of stainless steel and it is 5 cm in diameter. The ^{252}Cf source is placed on a mount attached to the side flange. Its position is chosen to be 32 mm, which corresponds to the maximum for the off-resonance production of rhodium, see Fig. 4.16. The argon gas is purified in a getter-based purifier to the sub-ppb level. The production of each isotope is determined from the intensity of γ emissions following its β decay and the mass-separated beam was periodically switched on and off to obtain growing-decay information. A correction is applied to deconvolute the production into direct feeding and feeding through parent decay; isotopes for which in-cell decay from a parent nuclide would have been a major contribution, have been discarded from this study in order to limit our study to fission-produced isotopes. Fig. 4.19 shows the efficiency of different elements extracted as singly charged ions from the cell. The efficiency is calculated for each measured isotope. The final element efficiency is the weighted average of the efficiency of its isotopes. The measured efficiencies range from 74% for ceasium down to 0.03% for krypton. The highest efficiency of ceasium can be

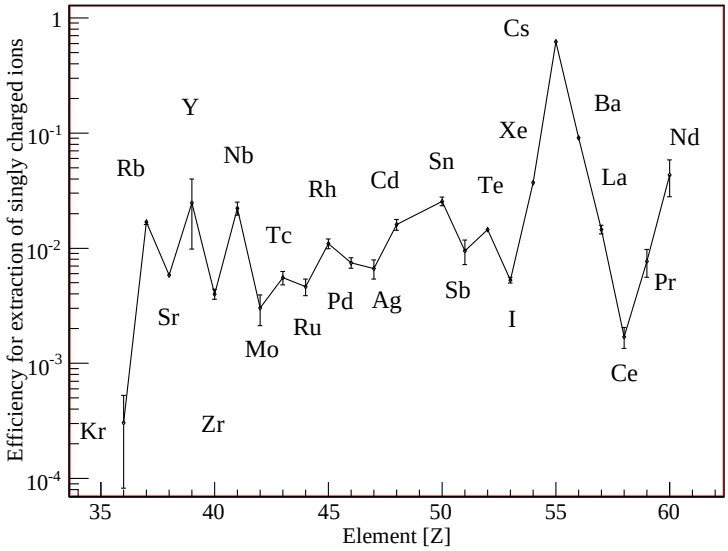

Figure 4.19: Efficiency for extraction of fission fragments as singly charged ions from ^{252}Cf in 500 mbar Ar as a function of the element.

related to the ionization potential, which is the lowest of all considered elements. Fig. 4.20 shows the yield and the efficiency of mass separated ceasium isotopes in the mass range $138 - 145$. The ratio of ions found on the tape after mass separation to the number of ions fed into the gas from the fission source is the same (40%) in the measured mass range. If we take into account the SPIG - (60%) and the mass separator - (90%) transport efficiencies, we obtain an efficiency of 74% for ceasium ions in a single charge state. Actually, most of the ions produced through fission of ^{252}Cf tend to recombine quickly with plasma electrons created by alphas and energetic fission products (note that there are no electrical fields in the gas cell, which could collect electrons). As a consequence it might be that what we observe as singly-charged ions is the result of survival of primary ions and reionization of the neutral atoms. It is difficult to explain the wide scattering of the efficiency values, but global as well as particular trends can be observed. Fig. 4.21 shows the efficiency of fission products extracted in a single charge state, as a function of the ionization potential. Apart from the results for Rb, Ce and Xe there is a general trend of smaller efficiencies for elements with a higher ionization potential, which might be explained if the re-ionization processes in the gas cell are important. However, other processes can also influence the efficiency. The high efficiency for xenon ions can be explained by Penning ionization; the ionization potential of xenon (12.13 eV) is close to the excitation energies of metastable argon atoms (11.55 eV and 11.75 eV). Also chemical reactions are not excluded.

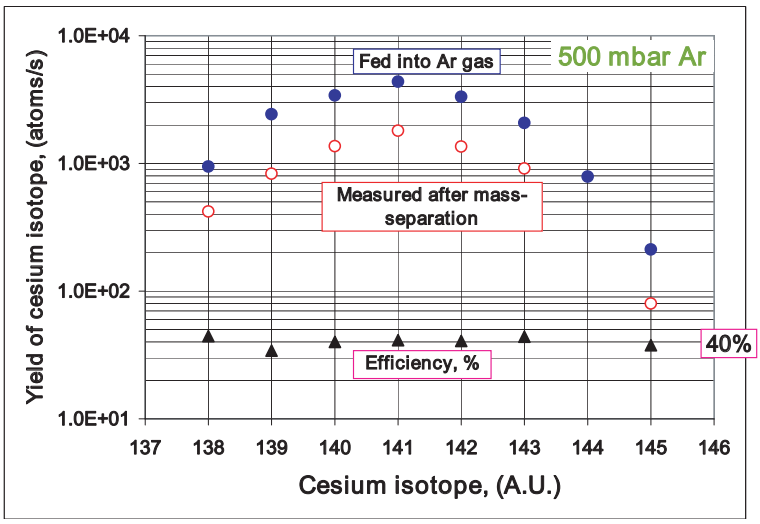

Figure 4.20: Yield of Cs isotopes from ^{252}Cf in the mass range $138 - 145$: open circles- measured after mass separation, filled circles- fed into argon gas (calculated [23]). The ratio gives the mass-separated extraction efficiency of Cs isotopes.

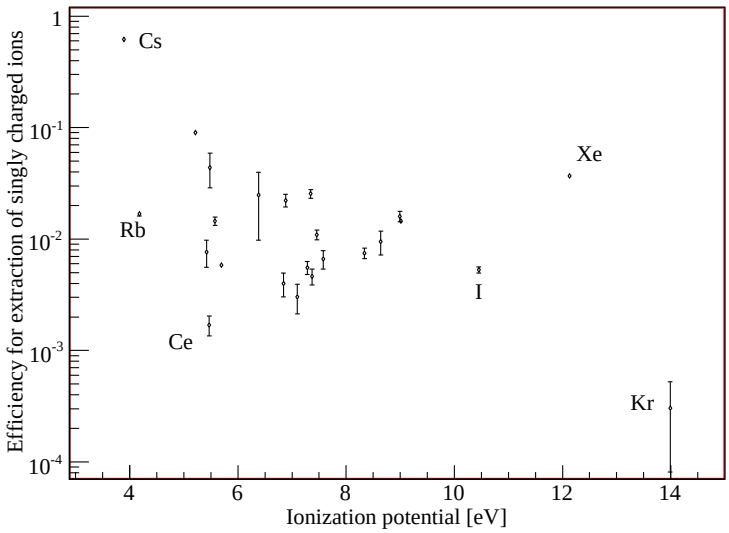

Figure 4.21: Efficiency for extraction of fission fragments as singly-charged ions from ^{252}Cf in 500 mbar Ar as function of the ionization potential.

Conclusions and outlook

A spontaneous fission ^{252}Cf source was used to characterize the gas cell for stopping of energetic fission products. The selective laser enhancement allows easy and reliable

identification of isotopes that are overwhelmed by more abundant ones. The behavior of different ions and atoms in weekly-ionized argon plasma was investigated. As a following stage the influence of electrical field will also be studied.

This work was supported by the European Commission within the Sixth Framework Programme through I3-EURONS (contract no. RII3-CT-2004-506065), BriX-IUAP P6/23, FWO-Vlaanderen (Belgium) and GOA/ 2004/03.

4.2.2 Additional processes and suppression of the Ar^+ ions on-line

In order to identify the origin of some ions, it is interesting to study their time of arrival with respect to a given parameter. Considering the long time required to evacuate the gas cell, of the order of 100 ms, in comparison to the arrival of the accelerated beam, one can identify where in the gas cell the ions are created, or where they are lost. A typical time profile of that kind is shown in Fig. 4.22 in the case of $^{40}Ar^+$ ions coming from the buffer gas atoms ionised by the primary cyclotron beam ($^{58}Ni^{10+}$, 185 MeV) after the injection of a 10 ms pulse at $2.8 \cdot 10^8$ pps [Fac04a].

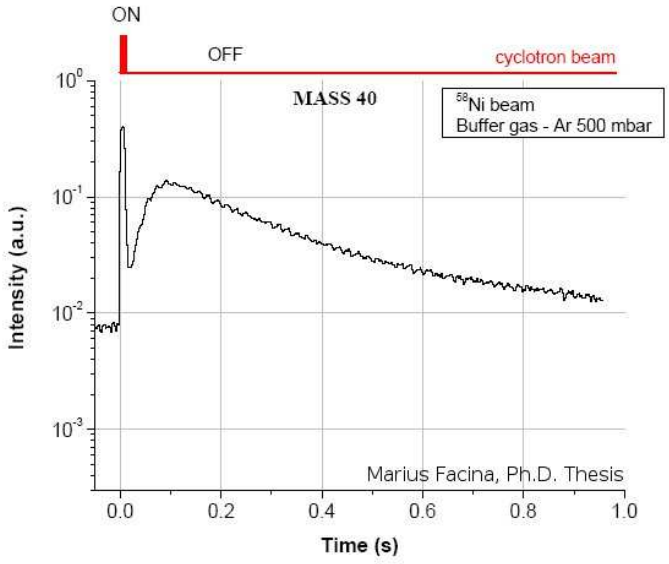

Figure 4.22: Time profile of $^{40}Ar^+$ ions coming from ionised buffer gas elements in synchronisation with the cyclotron beam ($^{58}Ni^{10+}$, 185 MeV) after a 10 ms beam pulse at $2.8 \cdot 10^8$ pps [Fac04a].

While the slow component peaking at 100 ms is understood to originate from the ions drifting through the gas cell from the primary beam irradiation area, the instantaneous component proved to be harder to explain. The only particles that can penetrate the gas so rapidly are photons; it was therefore suggested that photons coming from the slowing down of the primary beam are responsible for the re-ionisation of the buffer gas in the vicinity of the gas catcher exit nozzle. In order to suppress those unwanted ions and especially the electrons that would be associated with this ionisation process (and could contribute to recombination with other ions of interest), a new gas cell was designed, the *dual-chamber* gas cell, discussed in section 4.2.3, where the exit region is optically shielded from the main chamber using two different chambers connected with a short channel.

Using this new gas cell, the fast component of the Ar^+ time profile should be suppressed. The time profile obtained is shown in Fig. 4.23. As the fast component

remains, two options are suggested: either the original assumption was wrong or the photons manage to reach the exit region. As several reflections would be necessary to transport the photons to the exit hole and as the expected photon flux is orders of magnitude too small to provide a sizeable effect, other processes are investigated.

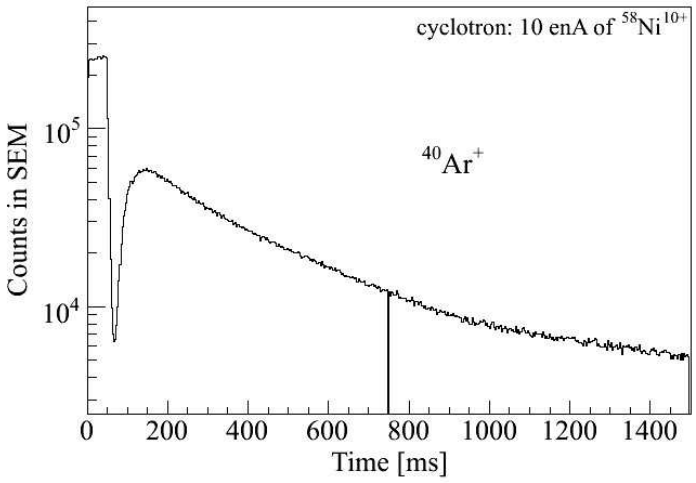

Figure 4.23: Time profile of Ar^+ ions coming from ionised buffer gas elements in synchronisation with the cyclotron beam using the dual-chamber gas cell.

In order to generate such a fast signal, the only place where the ions can be created is actually outside the gas cell in the chamber surrounding the gas cell and the SPIG. As the pressure inside the gas cell is high, the background pressure in the surrounding chamber (see Fig. 3.10) is $\approx 10^{-2}$ mbar. The incoming primary beam can therefore ionise argon atoms outside the gas cell. Those ions are then attracted by the negative potential applied on the SPIG rods, as discussed in section 3.2.2. The trajectory of those ions has been simulated, ignoring the RF pseudo-potential and the gas flow, using the SimIon code [Sim]. The results are shown in Fig. 4.24.

In this first approximation, it can be seen that the Ar^+ ions can penetrate the SPIG structure. The action of the radially-confining pseudo potential together with the longitudinal push of the gas jet are the final ingredients yielding the fast component to the Ar^+ time profiles in Fig. 4.22 and 4.23.

This new hypothesis has been verified using metal plates outside the gas cell and a mesh around the SPIG rods to collect or repel those ions. The effect of those electrodes on the total mass-separated $^{40}Ar^+$ and $^{58}Ni^+$ signals is shown in Fig. 4.25. While the Ar^+ signal is clearly suppressed, little effect is seen on the Ni^+ ions of interest. Indeed, Ni^+ only comes out of the gas cell a certain time after the Ni^+ cylotron pulse. For further use of the gas cell, a tube has been placed around the primary beam path to ensure that no ions can reach the secondary beam path.

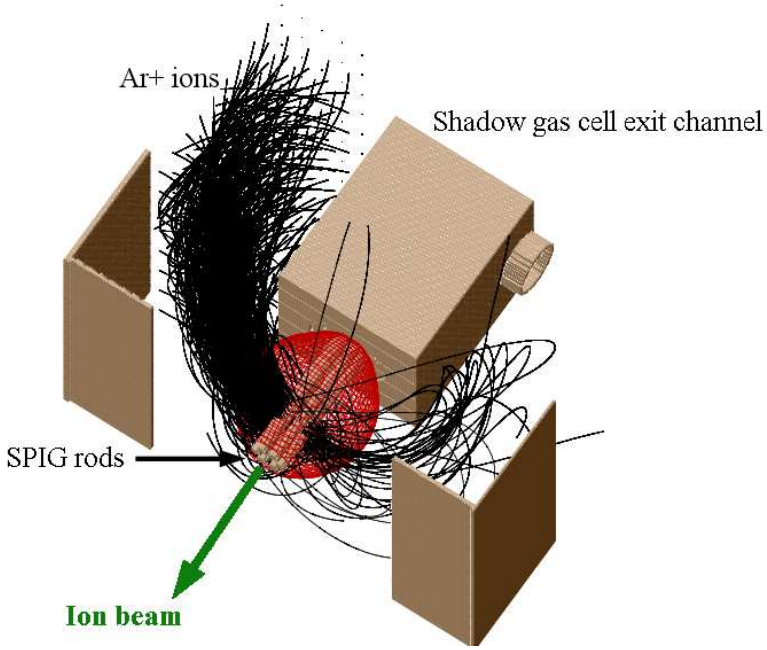

Figure 4.24: SimIon simulation of the Ar^+ ions outside the gas cell attracted by the static potential of the SPIG rods, disregarding the effects of the gas flow or of the radio-frequency pseudo-potential. The argon ions are represented in black; the equipotential lines of the SPIG rods are displayed in red. The argon ions start at rest from the edge of the picture. This figure only displays a very small portion of the gas cell, which corresponds to the exit channel.

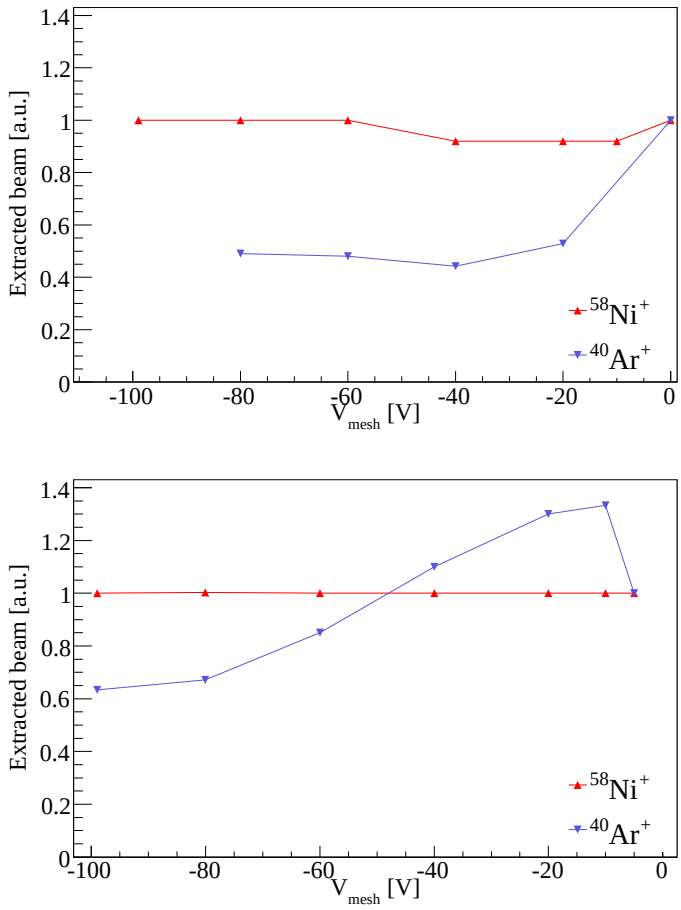

Figure 4.25: Effect of the collector plates (top) and of the mesh (bottom) on the $^{40}Ar^{+}$ and $^{58}Ni^{+}$ signals.

4.2.3 Dual-chamber gas cell: towards better control

Paper III

Yu. Kudryavtsev, T.E. Cocolios *et al.*, *Nuclear Instruments and Methods in Nuclear Physics Research B*267(2009)2908 – 2917.

In order to suppress the surviving ions as well as the re-ionised contaminants by means of electrical fields inside the gas catcher, the dual-chamber gas cell has been designed. It consists of a gas cell catcher where the volumes for thermalising the recoils and re-ionising the element of interest are optically disconnected. Both volumes are connected by a channel and the atoms travel with the gas flow across this channel from one volume to the next.

The first, and largest, volume houses the thin target and the filaments for isotope production. It is also the volume from which the gas enters the cell. The second volume, much smaller in size, is used to irradiate the atoms with the laser beams. Since the charge density in that second volume is much smaller than in the first volume, or than in the conventional gas catcher, electric fields may be applied. An Ion Collector (IC) can therefore be used to collect the remaining ions surviving the thermalisation processes.

The performances of this new gas catcher have been investigated with stable nickel and radioactive rhodium isotopes in off-line and on-line conditions, sending the lasers either along or across the ionisation volume. The most striking results are the general great improvement in selectivity using the IC, the constant efficiency in spite of the intense incoming primary beam, but also the limits of this technique for β^--decaying isotopes with half-lives in the 100 ms range that stick to the SPIG rods from where they decay; the daughter products are then slowed down by the background buffer gas and caught as single ions by the confining pseudo-potential of the radio-frequency structure; those ions are out of reach of the IC potential.

A later experimental test with this gas cell has shown that β^+-decaying isotopes can suffer from the same limitation, e.g. in the study of the neutron-deficient $_{50}$Sn and $_{49}$In isotopes. The In isotopes can be produced both directly and from the decay of the Sn isotopes while Sn has no precursor in the reaction used; Sn is therefore not subject to the SPIG decay effect. A SPIG with a reduced surface area is under development to overcome this limiting factor.

Dual chamber laser ion source at LISOL

Yu. Kudryavtsev, T.E. Cocolios, J. Gentens, M. Huyse, O. Ivanov, D. Pauwels, T. Sonoda, P. Van den Bergh, P. Van Duppen
Instituut voor Kern- en Stralingsfysica, Katholieke Universiteit Leuven, B-3001 Leuven, Belgium

Abstract

A new type of gas cell for the resonance ionization laser ion source at the Leuven Isotope Separator On Line (LISOL) has been developed and tested under off-line and on-line conditions. Two-step selective laser ionization is applied to produce purified beams of radioactive isotopes. The selectivity of the ion source has been increased by more than one order of magnitude by separation of the stopping and laser ionization regions. This allows the use of electrical fields for further ion purification.

Laser ion source, ion guide, resonance laser ionization
29.25, 32.80.Fb, 42.62.-b, 52.70.La

Introduction

For the production of short-lived radioactive ion beams often high-pressure noble gases are used as a stopping media for the nuclear reaction products: the ion guide technique that was pioneered in the early 1980s at the University of Jyväskylä [33, 34] and the ion catcher technique implemented recently at in-flight radioactive beam facilities [35, 36, 37, 38, 39]. In both methods one tries to avoid the recombination of the stopped recoil ions. In the ion guide method, this is achieved by a fast evacuation of the ions from the cell by the gas flow through the exit hole. In the gas catcher method, which is mainly designed for in-flight separators, DC and RF electrical fields are used to prevent the ions from touching the walls of the gas cell and to move them towards the exit hole where the motion is taken over by the gas flow. Furthermore, the electrical fields separate the ions and electrons created during the stopping process and reduce the ion recombination. The high intensity of the incoming beam can cause space-charge effects and reduce the efficiency [40, 41, 42]. Mainly because of its small recombination coefficient, only helium is used.

Opposite to the above mentioned methods, the operational principle of the laser ion source is based on an element-selective resonance multi-step laser ionization of neutral atoms that after production in a nuclear reaction are thermalized and neutralized in a buffer gas where a weakly-ionized plasma is created by the primary beam, the recoil ions and the radioactivity. This method was developed at K.U. Leuven in the early 1990s [43, 44, 45], and is used since then at the Leuven Isotope Separator On Line (LISOL) facility (Belgium) to produce short-lived radioactive isotopes. Recently, it has been implemented at the IGISOL facility (Finland) [46, 47]. For completeness, we note that laser ionization spectroscopy in a gas cell has been developed as well [48]. Depending on the nuclear reaction different types of gas cells have been used for proton-induced fission and light- and heavy-ion-induced fusion evaporation. In these experiments helium or argon at 500 mbar pressure as a buffer gas are typically used, however argon is preferentially used because of the larger recombination coefficient and the larger stopping power for energetic recoils. In both fission and fusion gas cells the stopping/thermalizing and laser ionization zones are not separated physically [49, 50]: stopping and laser ionization happens in the same gas cell. As a result the primary accelerator beam, recoils and radioactivity influence the plasma conditions in the laser ionization zone and the ions created by resonant laser ionization (laser/photo ions) at a distance of a few cm from the primary beam path recombine fast (on a ms time scale), see e.g. Fig. 4 in [50]. Furthermore, unwanted ions are present and create an isobaric background for the experiments [51]. To reduce the recombination of laser ions, the survival of non-resonantly-produced ions and the creation of unwanted ions by different processes (see further), a pulsed beam mode in anti-phase with the mass separator time gate was used. In this way the mass-separated ion beam was only transported to the detection set-up when the primary beam was not present [45].

There are several sources of non-selective ionization in the laser ionization zone; these are ions scattering off the primary beam creating a flux of energetic ions in

the laser ionization zone and hard UV and x-ray radiation from the target/window material and from the buffer gas. The nuclear reaction products, especially in the case of fission, can also contribute to the weakly-ionized plasma and unwanted ion creation in this zone. When the primary beam passes through the gas it transfers most of its energy to atoms via inelastic collisions. This energy is dissipated in the gas via the emission of δ-electrons and photons. The δ-electrons with energy up to a few keV have a short range in the gas (less than 1 mm) but they cause excitation of inner electrons of the buffer gas atoms. This excitation results in vacancy cascades with emission of Auger electrons and fluorescent photons. The keV energy photons can initiate further excitation and ionization [52, 53]. The probability of emitting fluorescent photons is higher for heavier atoms. In case of argon gas about 12% of the deposited energy in the excitation of K-shell electrons goes to fluorescence and the rest to Auger electron emission [54]. The gas cell windows, made of molybdenum, give 76% of excitation energy in the x-ray region. The vacancies in the K and L shells cause also an electron-shake-off process that leads to the creation of multi-charged ions (with maximum 4+ state for argon) [55] that emit hard UV radiation. Most of the energy is deposited in the beam path but the scattered ions, the photons and energetic reaction products ionize the gas at larger distance from the point of initial ionization and a low-density plasma is created far from the beam path. This causes recombination of laser-produced ions, thus reducing the ion source efficiency, and the creation of unwanted ions. Collection of the unwanted ions prior to laser ionization using electrical fields is prevented due to the space-charge effect present in the gas cell [40, 50].

In this article we present a new gas cell with separated stopping- and laser-ionization chambers. In this design the laser ionization zone is not in direct view from the accelerator beam path and the trajectories of recoils. This should allow us to avoid recombination of laser-produced ions, to use the accelerator beam in DC mode and to collect not-neutralized ions before laser ionization using electrical fields.

Experimental setup

Dual chamber gas cell The dual chamber gas cell for proton-induced fission is shown in Fig. 4.26. It consists of stopping and ionization chambers that are connected via an elbow channel. The stopped recoils are brought from the stopping volume to the laser ionization volume by the gas flow. The noble gas, purified down to the ppb level in a getter-based purifier, enters the gas cell via the ring slit that homogeneously distributes the gas across the cell. The inner diameter of the stopping chamber is 4 cm and its length is 6 cm. The accelerator beam enters the cell through a molybdenum foil of 4 μm in thickness. The target is installed on the tilted surface of the insert that is fixed in the stopping chamber. The angle between the target surface and the incoming accelerator beam can be changed. This angle equals to 16° for proton-induced fission of uranium-238 and 35° for heavy-ion-induced fusion-evaporation reactions. The shape of the insert guarantees a turbulent free homogeneous gas flow towards the elbow. This is confirmed by gas flow simulations

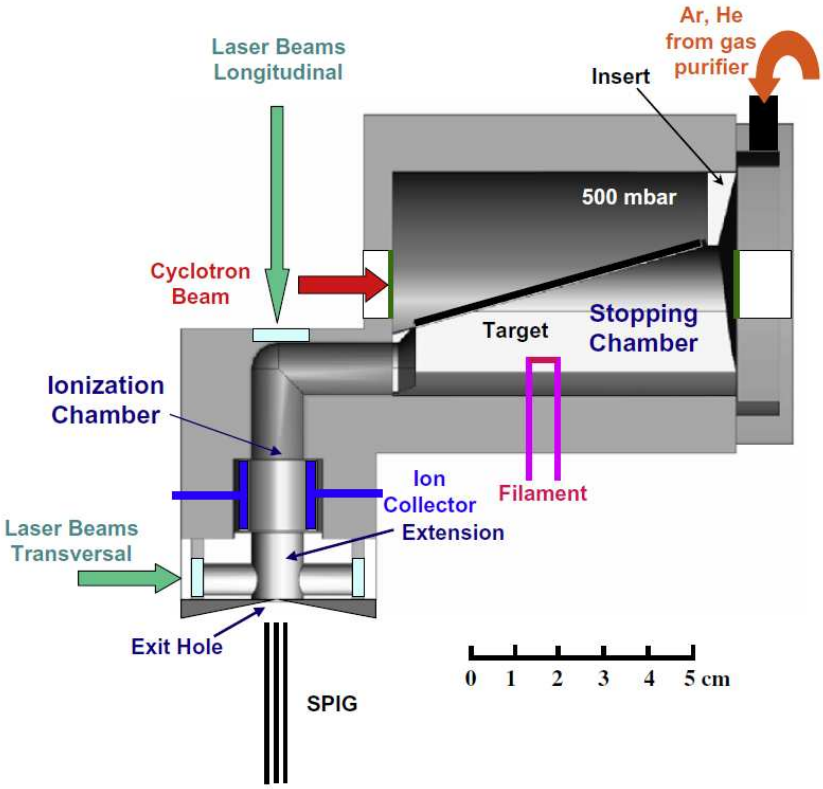

Figure 4.26: A schematic drawing of the dual chamber laser ion source gas cell.

as presented in Page 82.

The laser beams enter the ionization chamber (30 mm long and 10 mm in diameter) longitudinally through a quartz window and ionize atoms along the chamber axis, Fig.4.26. This laser beam path can be used to monitor the ion behavior in the ionization chamber. Atoms of stable nickel or cobalt isotopes can be produced inside the gas cell by resistive heating of corresponding filaments. An additional extension of 12 mm in length allows transverse laser beam entrance near the exit hole region. In this case an ion collector, located upstream, can be used to collect non-neutralized ions that come from the stopping chamber without collecting the laser-produced ions. The ion collector plates are shaped according to ring electrodes with an inner diameter of 11 mm. The evacuation time of the laser-ionized volume (both longitudinal and transverse) at the exit hole diameter of 0.5 mm is bigger than the time between two subsequent laser pulses of 5 ms guaranteeing that all atoms have been irradiated by laser light. Ions leaving the gas cell are captured by a SextuPole Ion Guide (SPIG) and transported towards the mass separator.

Sextupole ion guide The ions coming out of the cell have essentially the jet velocity of the carrier gas. The RF voltage applied to the SPIG rods provides radial confinement of the ions. A DC voltage up to 300 V of either polarity (+ or −) can

be applied between the gas cell and SPIG rods. In normal running conditions the SPIG rods are negatively biased relative to the gas cell. In this case molecular ions that can be formed inside the gas cell after laser ionization are dissociated if the voltage is large enough [56, 57]. In the case of a positive polarity, the ions from the gas cell are repelled. However in the longitudinal ionization mode part of the laser beam intensity goes through the exit hole and can ionize atoms outside the gas cell; only those ions created inside the SPIG are then transported towards the mass separator. This is the so-called LIST mode (Laser Ion Source Trap) proposed for a hot cavity in [58]. The results of our studies on the LIST mode, coupling a gas cell with an RF ion guide, combined with laser ionization in the RF structure and showing the possibility to do laser spectroscopy free of pressure broadening are presented in a separate paper [59].

Detection After mass separation, the radioactive ions are implanted into the movable tape of a tape station. Two high-purity germanium γ detectors and three scintillation β detectors surround the implantation point. Stable ions are detected by a secondary electron multiplier. An ion counting system and a digital oscilloscope were used to acquire ion time profiles after laser ionization. More details can be found in [57, 60].

Laser system Two-step two-color schemes are used for the resonance laser ionization of stable and radioactive atoms. The first step laser excites atoms into an intermediate state followed by a transition into an autoionizing state by the second step laser. The laser system consists of two dye lasers pumped by two excimer XeCl lasers with a maximum pulse repetition rate of 200 Hz [44]. The first step laser radiation is frequency doubled in a second-harmonic generator. The laser beams of the first and second steps are overlapped at very small angle in the ionization chamber of the gas cell located 15 m away from the laser system. The diameters of the laser beams are about $4 - 6$ mm. The laser pulse widths and bandwidths are equal to 15 ns and 0.15 cm^{-1}, respectively.

Evacuation properties of the gas cell

Important parameters influencing the efficiency of the gas cell are its evacuation time and diffusion losses towards the walls of the atoms thermalized in the buffer gas. Those were studied by measuring the ion time profiles and by calculation of the flow pattern and trajectories of atoms and ions in the cell.

Ion time profiles Fig. 4.27 shows the laser ion time profiles of stable cobalt ions produced in the ionization chamber without extension, longitudinally, using helium and argon as buffer gas. The laser ionization of the continuous flow of cobalt atoms takes place at $t = 0$. The evacuation time from the elbow region in the case of argon equals about 35 ms, which is 3.5 times longer than in the case of helium, 10 ms. This ratio reflects the difference in the conductance of the exit hole of 0.5 mm in diameter

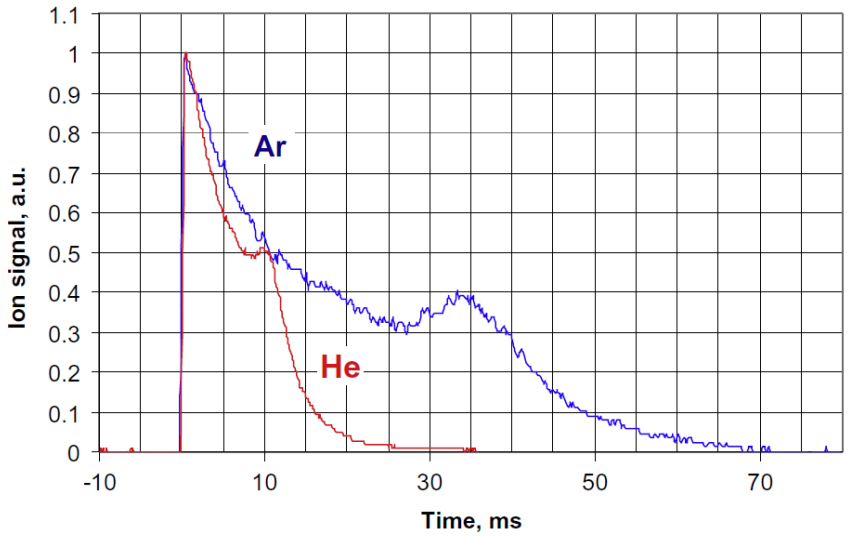

Figure 4.27: Time profiles of cobalt ions after a single laser pulse for longitudinal ionization in the gas cell without extension with helium and argon (500 mbar) as buffer gas.

for argon and helium, 35 and 112 cm^3/s, respectively. The ion time distribution is a measure of the spatial distribution of the cobalt atoms in the laser beam path at the moment of laser ionization. The bump in the argon time profile at 35 ms (10 ms in helium) reflects a higher cobalt atom density in the elbow region, see Page 82.

The information about the evacuation time from the stopping chamber of the gas cell can be obtained if atoms are injected into the cell during a short time. We applied the same technique as explained in [40, 50] using an accelerated 185 MeV ^{58}Ni beam that is stopped in the gas cell, evacuated to the laser ionization zone, resonantly ionized, mass-separated and detected. Fig. 4.28(a) shows the ion time profile of nickel atoms from the cell at different argon pressure after injection of a 50 ms long pulse of 185 MeV ^{58}Ni beam at $t = 0$ with a beam intensity of 0.25 pnA measured in a DC mode. In this measurement the insert was not inside the stopping chamber and the lasers were running at 100 Hz. At 480 mbar, the nickel beam is stopped approximately in the center of the cell, 30 mm from the entrance window and the maximum of the mass-separated ion signal is observed at 320 ms. Note that the ion signal is resonant and only ^{58}Ni ions are present on mass 58. If the pressure is reduced, the beam is stopped further away from the entrance window and the evacuation time and diffusion losses increase. At 400 mbar 92% (relative to 480 mbar) of the ions are extracted and mass-separated. At 300 mbar the maximum of the ion signal is at 600 ms and only 57% of the ions are extracted and mass-separated compared to 480 mbar. If the pressure is reduced further down to 200 mbar the ion signal drops to 11% compared to 480 mbar (not shown in Fig.4.28(a)). Fig. 4.28(b) shows the calculated evacuation time profiles at 480, 400 and 300 mbar of argon that will be discussed in the next paragraph. It is interesting to note that the evacuation

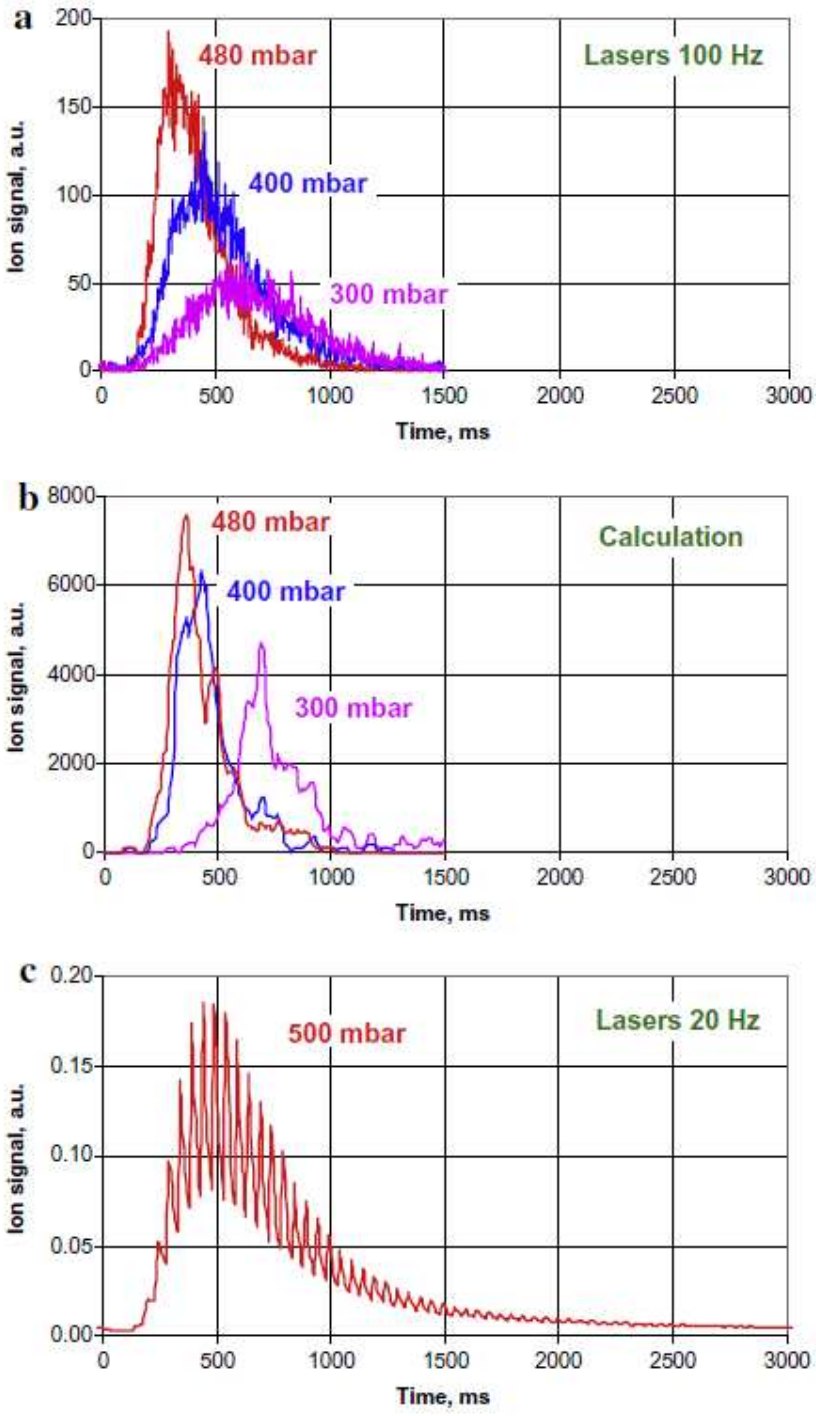

Figure 4.28: The evacuation time profile of nickel atoms after injection of a 50 ms pulse of 185 MeV ^{58}Ni beam at $t = 0$ ms, $I_{DC} = 0.25$ pnA) in argon from: (a) the dual chamber gas cell at different argon pressure and laser repetition rate 100 Hz, (b) the calculated evacuation time profiles from the dual chamber gas cell at 480, 400 and 300 mbar, (c) the standard LISOL gas cell at 500 mbar of argon and laser repetition rate 20 Hz [48].

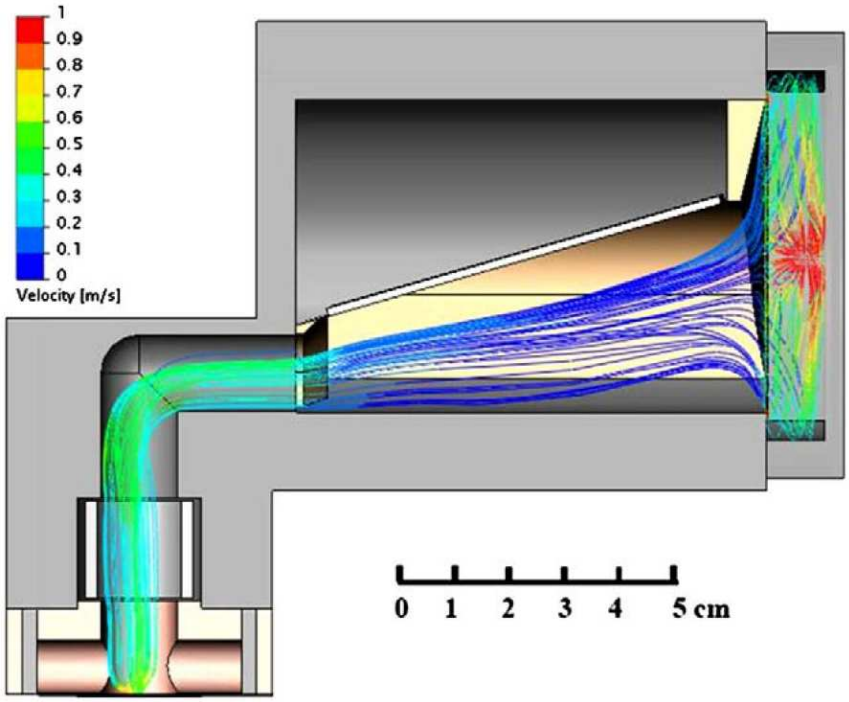

Figure 4.29: Gas flow simulation in the dual chamber cell with an insert for the fission target and with an extension for transverse laser ionization.

time profile of the standard LISOL gas cell (Fig. 4.28(c)) is longer than in the dual chamber gas cell as the extra delay from the ionization chamber is compensated by a better match between the effective stopping volume and the gas flow. In both the dual chamber gas cell and the standard LISOL gas cell, the arrival of the first ions occurs at approximately similar times (150 ms).

Gas flow simulation The gas flow simulations were performed by using the COSMOS-Floworks 2006 program [61]. It takes into account the exact dimensions of the gas cell including the ring slit for the gas entrance, the target holder and the ion collector. Fig. 4.29 shows gas flow trajectories in the cell including the fission target and with the extension for the transverse laser ionization. The flow is laminar without turbulences. The elbow causes the flow lines in the ionization chamber to be closer to the left-hand side of the cell. As a consequence, the overlap of the laser beams (diameter $4-6$ mm) with the flow of atoms along the ionization chamber is not complete. The good overlap with the flow of atoms in the elbow region explains the bump at longer times in the shape of the cobalt ion time profiles (at 10 ms and 35 ms for helium and argon, respectively) as shown in Fig. 4.27.

The evacuation time and the diffusion losses of nuclear reaction products were calculated using the real target geometry. The initial distribution of fission products in the cell was calculated for fission recoils from the 10 μm uranium-238 target in 500

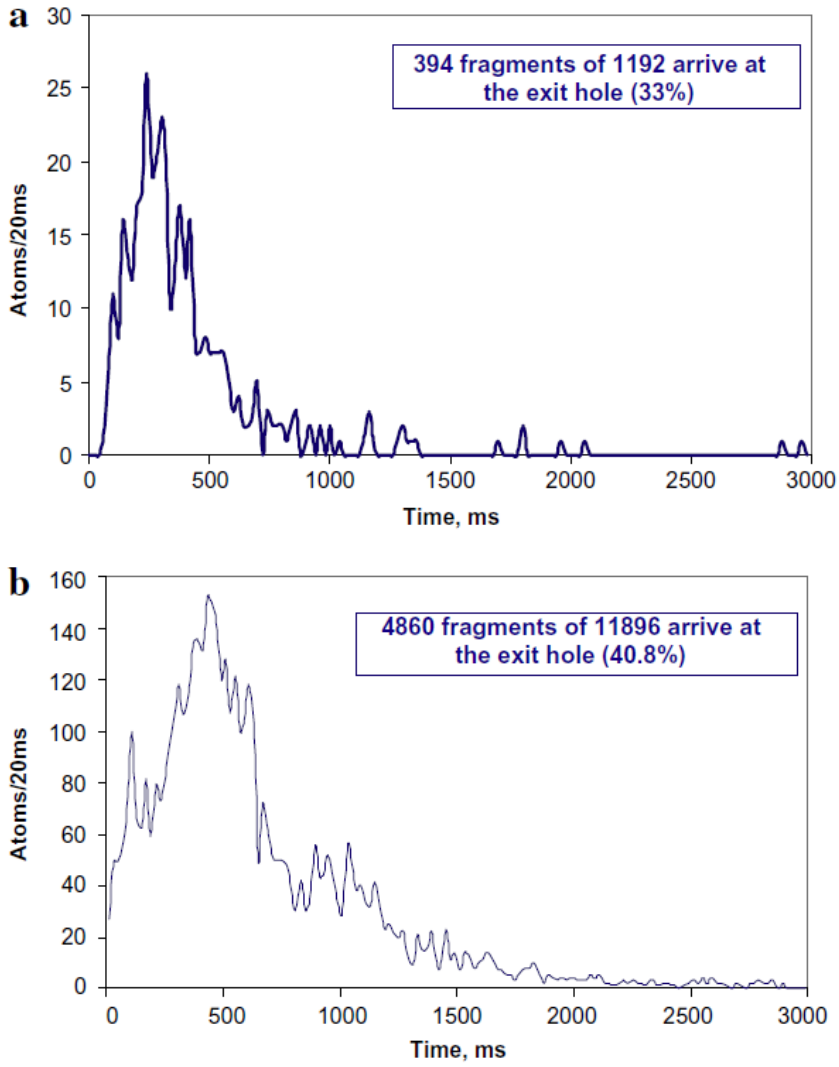

Figure 4.30: The simulated evacuation time profile of fission products for the 0.5 mm exit hole from (a) the dual chamber gas cell, (b) the standard LISOL fission gas cell [48].

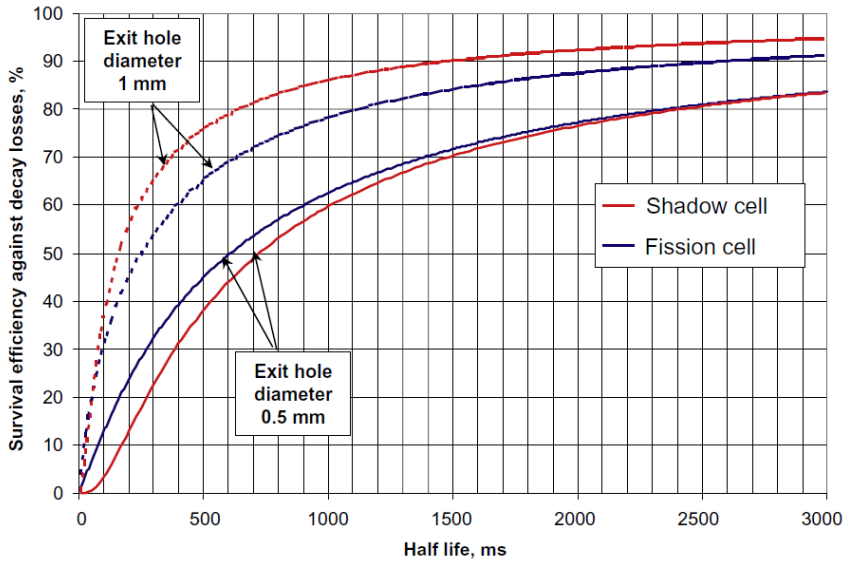

Figure 4.31: Survival efficiency against radioactive decay losses as a function of the half life of the isotope for the dual chamber- and the standard LISOL fission gas cells for 0.5 mm and 1 mm exit hole.

mbar argon. The trajectories of 1192 fragments were calculated using a macroscopic simulation including diffusion losses. Fig. 4.30(a) shows the simulated evacuation time profile of all recoils that survive the diffusion and arrive to the exit hole. A total of 394 atoms were found at the exit hole resulting in a transport efficiency of 33%. The first atoms arrive after 60 ms and within 600 ms most of the atoms are evacuated from the cell. For comparison, in Fig. 4.30(b) the time distribution of the fission products escaping from the standard fission gas cell [49] is shown. Note the presence of atoms at very short times, which is due to the fact that in the standard cell part of the fission recoils are stopped very close to the exit hole. The diffusion losses in this cell are less in comparison to the one in the shadow cell. The simulation shows that 40.8% of the recoils stopped in the gas cell after fission are transported to the exit hole.

The delay in evacuation of the recoils from the gas cell can cause an additional reduction of the total ion source efficiency due to radioactive decay inside the cell during the transport to the exit hole. This effect was calculated as a function of the half life of the studied isotope for the dual chamber cell and for the standard fission cell for an exit hole diameter of 0.5 mm and of 1 mm. The results are shown in Fig. 4.31. It is obvious that the survival efficiency of both cells is larger in the case of a 1 mm exit hole compared to 0.5 mm because of a faster gas flow through the exit hole. Within the calculated range of half-lives (up to 3 s) the dual chamber cell with a 0.5 mm exit hole has a lower efficiency. This is again related to the delay time in the elbow region and ionization chamber. However this delay is reduced by a factor of four by increasing the exit hole diameter up to 1 mm; the efficiency of the

shadow cell is then larger compared to that of the standard fission cell for isotopes with half-lives larger than about 40 ms.

The gas flow simulation allows to explain reasonably well the experimental results. In the previous section (Page 79), Fig. 4.28(a) and (b) show experimental and calculated time profiles of the evacuated nickel ions after the pulsed injection of the 185 MeV ^{58}Ni beam into the gas cell at different argon pressures. The initial position of the stopped ions was calculated using the SRIM code. Then the trajectory of each ion was calculated using the flow data. The evacuation time is the time elapsed between the creation of the ion and the moment of successful arrival of this ion at the exit hole. The injection time of 50 ms was taken into account. The calculated efficiency, defined as the number of nickel atoms/ions transported to the exit hole versus the number of incoming nickel ions, equals 68%, 61%, 49% and 14% at 480, 400, 300 and 200 mbar, respectively. The increasing loss with decreasing pressure is due to diffusion to the walls of the gas cell but the strong reduction between 300 and 200 mbar is mainly due to incomplete stopping in the gas. The relative efficiency at 400, 300 and 200, relative to the one at 480 mbar equals 90%, 72%, and 21% respectively. These values can be compared with the experimental values of 92%, 57% and 11% presented in the previous section (Page 79) (see Fig. 4.28).

Laser ionization

The concept of the dual chamber gas cell was investigated by using longitudinal and transverse laser ionization of stable atoms evaporated from a filament in off-line and on-line conditions as well as radioactive isotopes produced in fusion-evaporation and fission reactions.

Longitudinal laser ionization

Off-line test An important element of the gas cell is the ion collector (IC) (see Fig. 4.26). Its performances were tested off-line by longitudinal laser ionization of stable nickel atoms evaporated from the filament. Time profiles of the mass-separated nickel ions at different voltages applied to the ion collector are shown in Fig. 4.32. The voltage pulses (5 ms long) of different polarities but equal amplitude are applied to the opposite electrodes 10 ms after the laser pulse. This measurement is performed in the cell without extension. If the amplitude of the pulse is more than 24 V, essentially all ions in the time interval between 15 and 33 ms are collected. This time interval corresponds to ions located in the IC region when the voltage pulse was applied. When the IC pulse is made 10 ms longer the ions produced in the elbow region are also collected. In case of a DC voltage on the ion collector, only ions produced very close to the exit hole survive the collection because of the weak electrical field in this region.

On-line test The performance of the ion collector was also tested in the presence of a 1 eμA 265 MeV $^{40}Ar^{11+}$ beam in the cell with extension at 500 mbar of

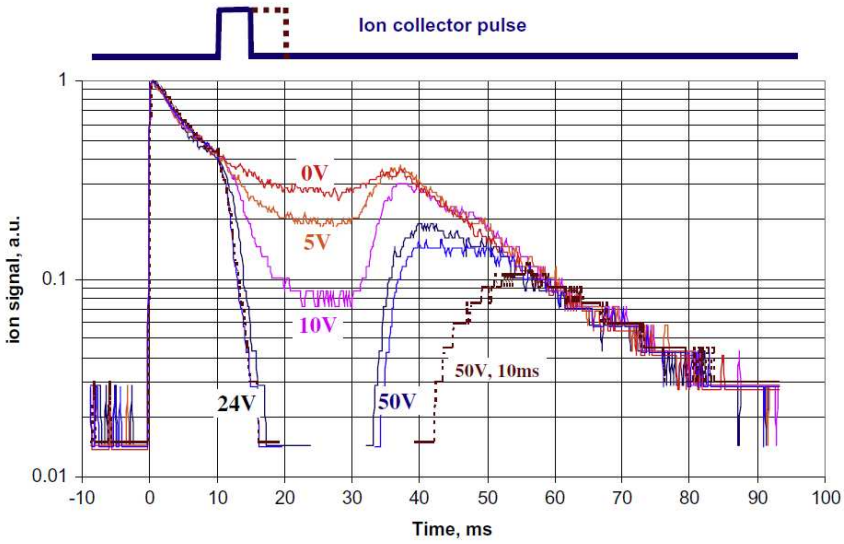

Figure 4.32: Time profiles of the mass-separated nickel ions after a single laser pulse for longitudinal ionization in the gas cell without extension for different amplitudes of electrical pulses (5 ms long) applied to the ion collector (IC) with delay of 10 ms. The dashed line shows the effect of an increase in pulse length from 5 to 10 ms at 50V.

argon as the buffer gas. In this case, in the stopping volume, about $3 \cdot 10^{17}$ ion-electron pairs$\cdot s^{-1} \cdot cm^{-3}$ are created in the cyclotron beam path, see eq. 1 and Table 1 in [50], resulting in a plasma density of about $5 \cdot 10^{11}$ ions$\cdot cm^{-3}$ in this region. This is extremely high for applying any electrical field for the ion collection [40]. However in the laser ionization chamber, the plasma conditions are completely different and the ion collector can be used for purification. Fig. 4.33 shows time profiles of stable nickel atoms after longitudinal laser ionization in 500 mbar of argon with a laser repetition rate of 5 Hz (a laser pulse every 200 ms). The time distribution of the ion signal without cyclotron beam (the end of the signal is defined when the flat part in the range $30 - 50$ ms drops by a factor of 2) equals to 76 ms, which corresponds to the evacuation time of ions from the ionization chamber with extension. If the cyclotron beam is switched ON the length of the signal is shorter ($\sim$ 63 ms). The reason for the shorter pulse is the neutralization of the laser-produced ions in the elbow region, which are in a direct view from the cyclotron beam path. The neutralization is due to the processes discussed in the introduction. Note that the amplitude of the ion signal from the rest of the ionization chamber stays almost the same indicating that the shielding effect indeed works. At longer times (> 100 ms), the signal does not decrease further but saturates and even crosses the curve of laser ions without cyclotron beam, indicating their beam-related non-resonant character. If the ion collector is switched ON (applied DC voltage of 40 V) the nickel ion signal dramatically decreases after 15 ms and drops by three orders of magnitude at 60 ms.

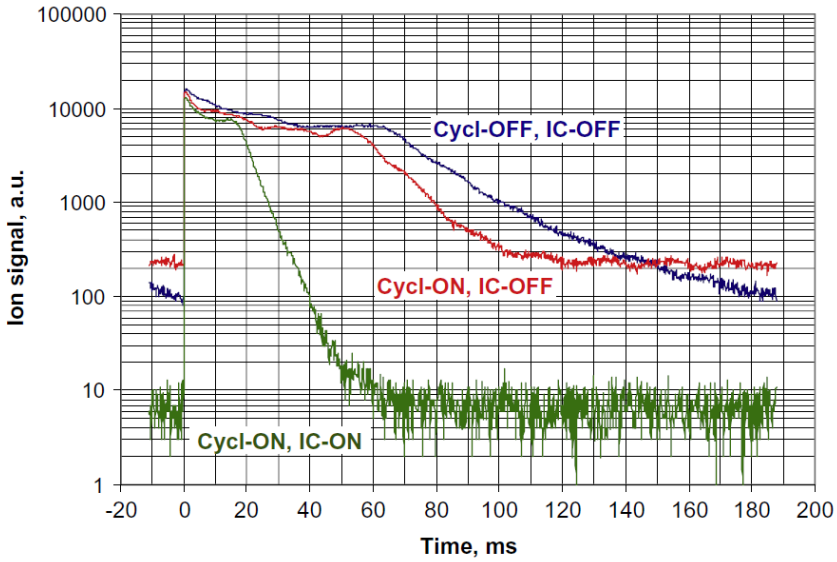

Figure 4.33: Time profiles of nickel ions after a single laser pulse for longitudinal ionization in the gas cell with extension. Note that the curves are not normalized to each other. The exit hole diameter is 0.5 mm and the argon pressure is 500 mbar.

It is important to note that the ion time profile at $0 < t < 15$ ms is only weakly influenced by the presence of the cyclotron beam and the IC.

Transverse laser ionization When using transverse laser ionization the cyclotron beam and ion collector can run in DC mode. In this case the laser pulse repetition rate should be high enough: the evacuation time of the laser-irradiated volume should be more than the time between two subsequent laser pulses. The time profiles of transversely laser produced nickel ions at different laser repetition rates are shown in Fig. 4.34. The lasers are triggered at $t = 1$ ms. At low pulse repetition rate of 20 Hz one observes a time profile with a FWHM of 5.5 ms decreasing to the noise level before the next laser pulse is fired. When increasing the repetition rate to 100 Hz, a pulse structure is still present indicating that not all atoms have been ionized. At 200 Hz saturation is almost reached. This is supported by Fig. 4.35 where the ion count rate as a function of the laser pulse repetition rate is shown for transverse laser ionization. The time profiles were taken with the ion collector ON and OFF and no influence of the IC voltage was observed. This is in agreement with the time profile of the ion signal with longitudinal laser ionization and ion collector ON (Fig. 4.33), where the nickel ions are not collected during the first 15 ms.

Fig. 4.35 shows also the ion count rate as a function of the laser pulse repetition rate for the longitudinal laser ionization with ion collector ON. Since the signal with longitudinal ionization (20 ms) is longer than with the transverse one (5.5 ms), the saturation in Fig. 4.35 is observed at lower (50 Hz) repetition rate. However the saturation level is less because the ions produced in the upstream region of

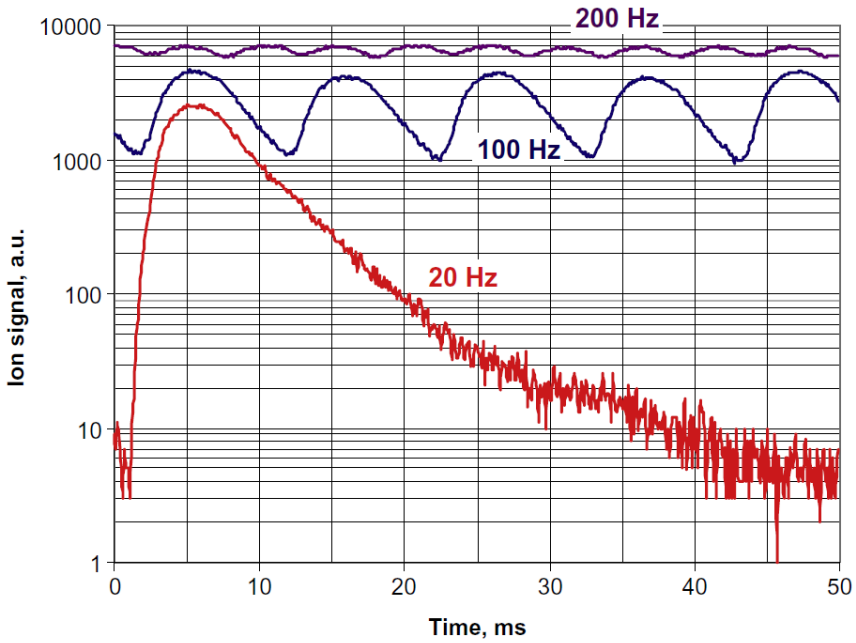

Figure 4.34: Time profiles of nickel ions after transverse laser ionization at different laser repetition rates. The exit hole diameter is 0.5 mm and the argon pressure is 500 mbar.

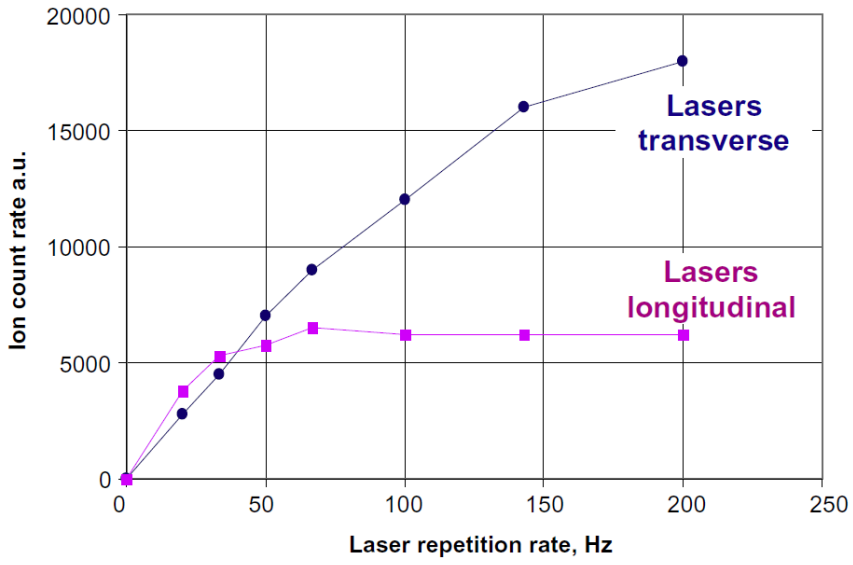

Figure 4.35: Ion count rate of stable nickel ions as a function of the laser repetition rate for transverse and longitudinal ionization in the chamber with extension.

the ionization chamber are collected. The presence of the cyclotron beam does not change the time profiles and the saturation curves. The influence of the ion collector on the laser selectivity of stable ^{58}Ni in the presence of the 265 MeV $^{40}Ar^{11+}$ beam was tested with lasers running at 200 Hz. The laser selectivity, defined as the ratio of the ^{58}Ni count rate with lasers ON to the count rate with lasers OFF, equals to 155 without the IC voltage and increases up to 7500 at the IC voltage of 40 V. This shows that the ion collector can be used to improve the selectivity of the laser ion source for radioactive isotopes and that the dual camber gas cell can be used under DC primary beam conditions.

Heavy-ion-induced fusion-evaporation reaction The dual chamber gas cell was tested in on-line conditions using radioactive ^{94}Rh isotopes produced by impinging a ^{40}Ar beam on a ^{58}Ni target. Fig.4.36(a) shows a β-gated γ spectrum with transverse lasers tuned in resonance to rhodium when the ion collector is ON. Only rhodium γ lines are present; the total ^{94}Rh yield equals 12600(850) at/μC. A similar spectrum and yield of 13600(650) at/μC are observed if the IC is OFF. Yields of 14670(100) at/μC and 14690(100) at/μC have been deduced from counting the number of β particles without IC and with IC, respectively. The slightly larger yields obtained in the case of β counting is due to contributions from the decay of long-lived daughter isotopes. As no significant difference in yield with and without IC is observed it can be concluded that the ion collector does not collect laser-ionized radioactive rhodium isotopes produced in heavy-ion fusion reaction. Fig. 4.36(b) shows the spectrum on mass 94 when the lasers are OFF and IC is OFF. Very weak γ lines belonging to ^{94}Rh are present in the spectrum since some ions survive neutralization and reach the exit hole. A laser selectivity for ^{94}Rh of 500 could be deduced. The selectivity for this radioactive isotope is three times larger than for the stable nickel isotope on mass 58, see previous section on Page 87. This can be explained by the presence of background molecular ions at mass 58. If the IC voltage is applied no γ lines are observed, Fig.4.36(c). The total selectivity has been determined from counting the number of β particles and was more than 2200. This increase in selectivity of the dual chamber gas cell ion source opens new possibilities to perform spectroscopy studies of neutron-deficient isotopes in the $N = Z$ region. Even though the cross section to produce these $N = Z$ nuclei in heavy-ion fusion evaporation reactions is expected to be very low and should be compensated by high primary beam intensities, a high selectivity is essential as the production channels for less exotic isobaric contaminants is orders of magnitude higher.

Proton-induced fission reaction A striking difference in selectivity of the standard laser ion source for different β^--decaying states within the same isotope, produced in a proton-induced fission of uranium was observed. The laser selectivity changed from 200 for ^{112m}Rh to $3-4$ for ^{112g}Rh [62]. This was explained as due to different ways the β^--decaying states were populated; directly in the fission reaction or through β^- decay. In the dual chamber gas cell, the ion collector can be used as an additional tool to understand the different selectivity for high- and low-spin

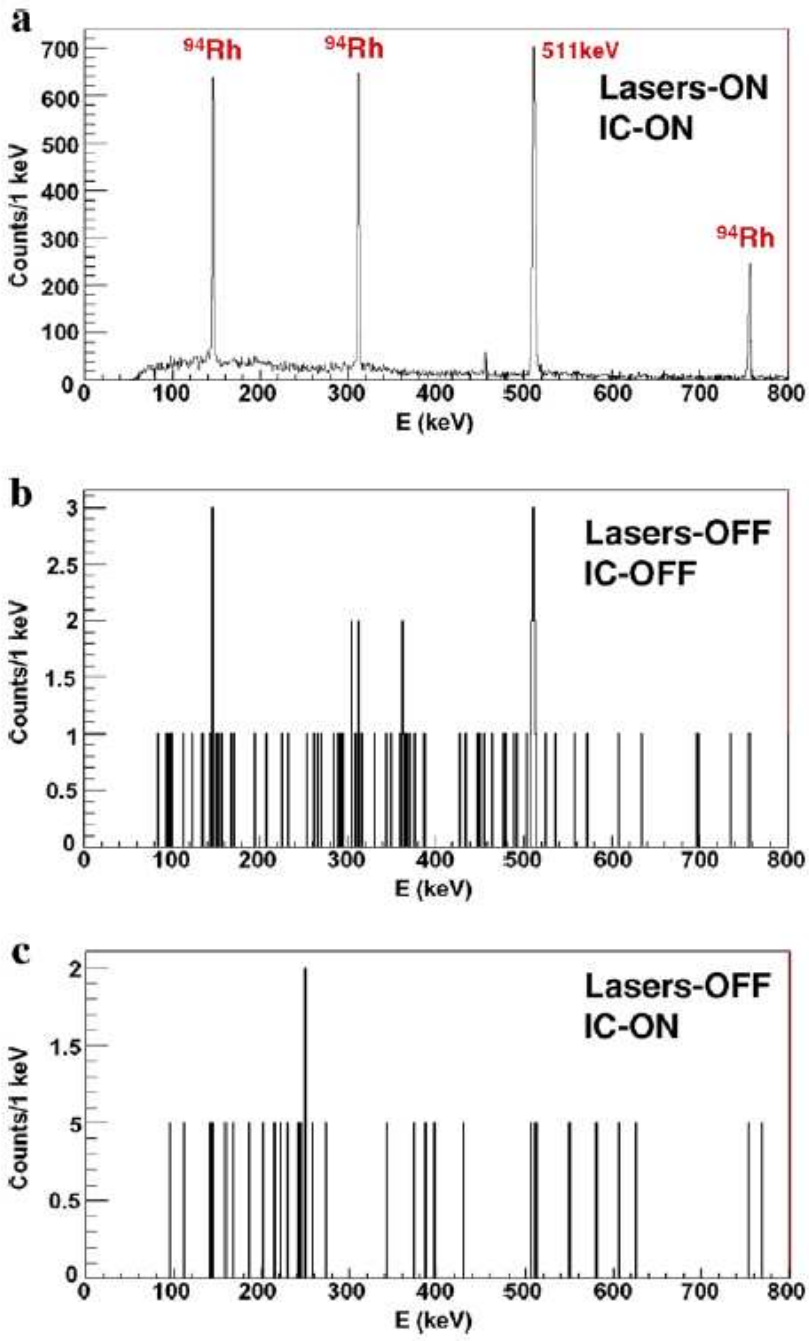

Figure 4.36: β-gated γ spectrum obtained at mass 94: (a) with lasers tuned in resonance to rhodium isotopes and IC - ON, (b) Lasers OFF and IC - OFF, (c) Lasers OFF and IC - ON. The measuring time is 300 s. The ^{94}Rh atoms were produced in the ^{40}Ar + ^{58}Ni heavy-ion fusion-evaporation reaction.

isomers. Radioactive neutron-rich ^{112}Rh isotopes were laser ionized in the same way as neutron-deficient ^{94}Rh isotopes described in the previous paragraph. Fig. 4.37(a) shows a β-gated γ spectrum with transverse lasers tuned in resonance to rhodium atoms when the ion collector is OFF. As in the case of ^{94}Rh, the ion collector mode (ON or OFF) has almost no influence on the laser-produced ions. Transitions only present in the decay of the high-spin isomer are denoted by m while the ones present in both decays are denoted by m+g. In the present set-up, laser radiation ionizes the ground- or metastable nuclear isomer state with equal efficiency as the isomer shift is much smaller compared to the total laser line width. The half-lives of both isomers ($T_{1/2}(^{112m}\mathrm{Rh}) = 6.8$ s $T_{1/2}(^{112g}\mathrm{Rh}) = 2.1$ s), are much longer than the evacuation time of the gas cell, so the decay losses inside the cell can be neglected. The inset in Fig. 4.37(a) shows a simplified decay scheme of the mass 112 chain. Next to direct feeding in the fission reaction, also feeding through the β^--decaying parent nucleus (^{112}Ru, $T_{1/2} = 1.75$ s) can occur and only the low-spin ground state of ^{112g}Rh receives feeding from the even-even mass ^{112}Ru ($I = 0^+$) nucleus. Fig. 4.37(b) shows the spectrum accumulated at mass 112 when the lasers are OFF and the IC is OFF. The γ lines belonging to the high-spin isomer (^{112m}Rh) are reduced by a factor of 25 while γ lines belonging to the decay of ^{112g}Rh are only reduced by a factor of 2.3 (note that the 349 keV line intensity in Fig. 4.37(a) stems for 33% and 87% from the ground state and high-spin isomer, respectively). If the IC voltage is applied all γ lines of the high-spin isomer disappear, Fig. 4.37(c), however the intensity of the lines fed by the ^{112g}Rh is only slightly reduced. The selectivity for the ^{112m}Rh is estimated to be above 1000 and the selectivity for ^{112g}Rh is increased from 2.3 to 3.1.

The different behavior of isotopes whether or not receiving feeding from parent nuclei can be explained by the fact that these parent nuclei stick to the inner surface of the gas cell and/or to the SPIG rods and subsequently decay. The majority of all fission products is neutralized in the stopping chamber and passes through the ion collector in the laser ionization chamber. Some of them are deposited in the exit hole region or on the SPIG rods instead of being pumped away. Their β decay can detach the daughter nucleus from these surfaces and leaves the nucleus in an ionized state, mostly in a 1+ state. These ions can then be further transported by the gas flow in the cell or outside the cell by a combination of the buffer gas and the electrical fields applied. From the experiments described below we can conclude that the main contribution to the non-resonant production of such daughter nuclei comes from the rods of the RF ion guide. Fig. 4.38(a) shows the calculated distribution of atoms from the gas jet that hit the SPIG rods for a distance between the cell and the rods of 1.5 mm. Most of the atoms are deposited in the beginning of the RF structure. If the SPIG is displaced further, the relative amount in the beginning is increased. Fig. 4.38(b) shows the calculated argon pressure along the central line of the SPIG for a gas cell pressure of 500 mbar and an exit hole diameter of 0.5 mm. The energy of the recoiling daughter ions after a β^- decay depends on the Q-value. In the ^{112}Ru-^{112g}Rh decay the Q_β-value is 3.95 MeV [63] and the maximum recoil energy of ^{112g}Rh ions is 94 eV, which corresponds to a range of 2 mm in argon at a pressure of 1 mbar.

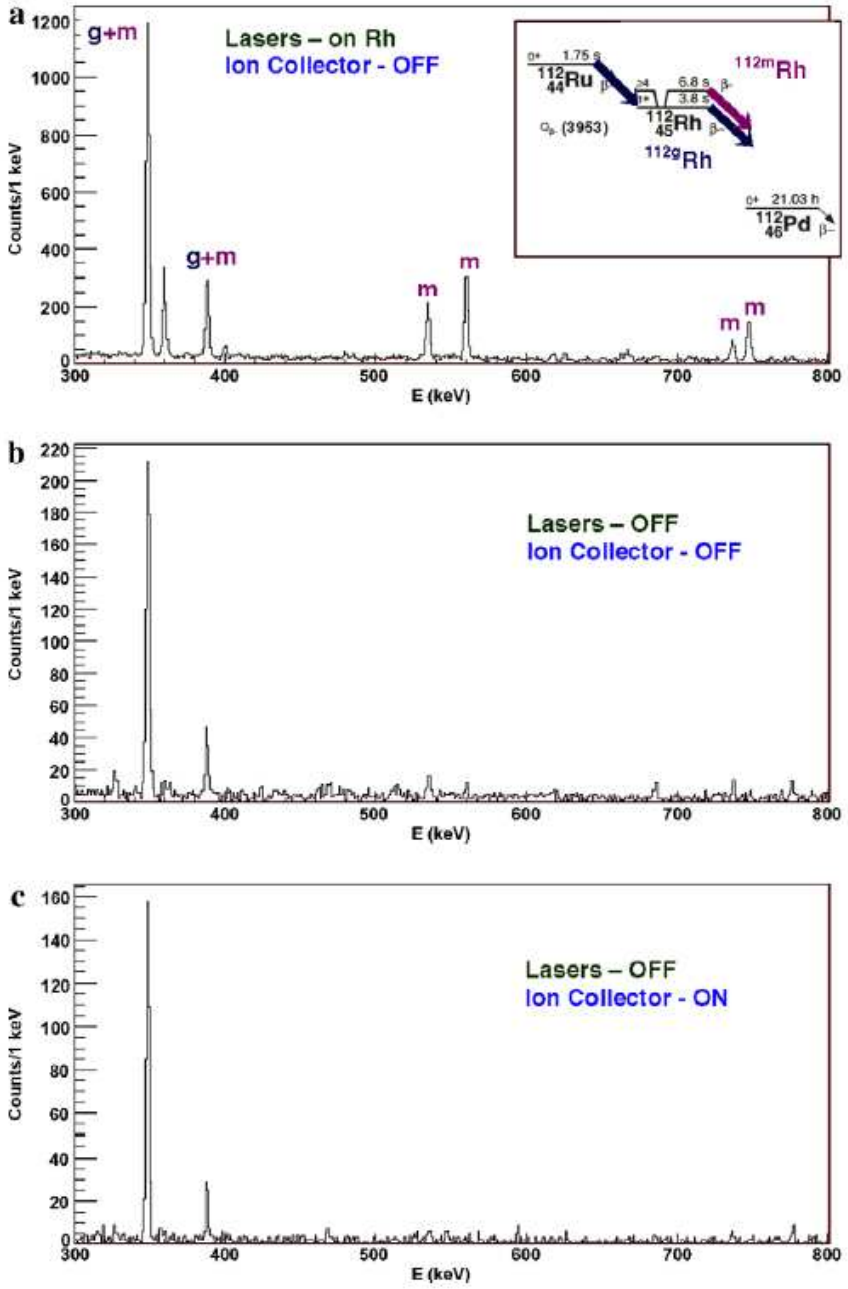

Figure 4.37: β-gated γ spectrum on mass 112: (a) with lasers tuned in resonance to rhodium isotopes and IC OFF, (b) Lasers OFF and IC OFF, (c) Lasers OFF and IC ON, inset decay chain at mass $A = 112$. The ^{112}Rh atoms were produced in the proton-induced fission of ^{238}U.

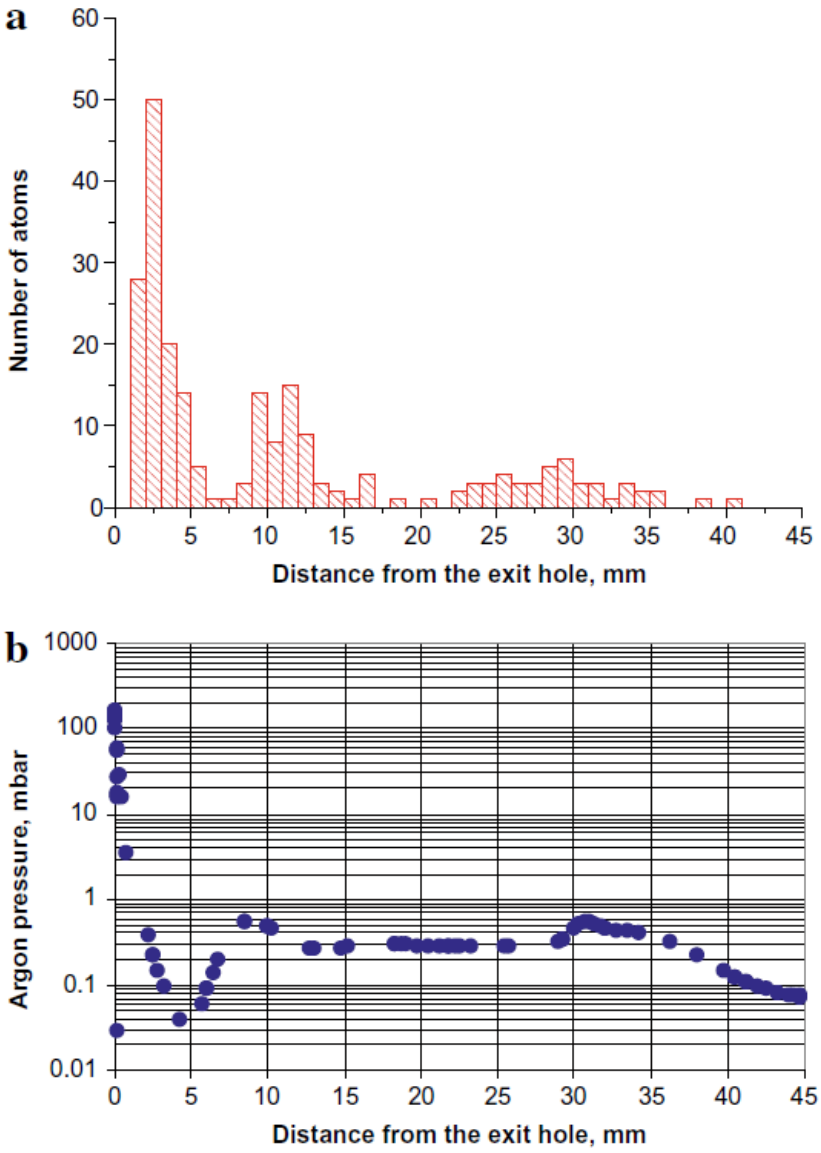

Figure 4.38: (a) Calculated distribution of atoms hitting the SPIG rods from an argon gas jet; (b) calculated argon gas pressure on the axis of the SPIG for an exit hole diameter of 0.5 mm and a gas cell pressure of 500 mbar.

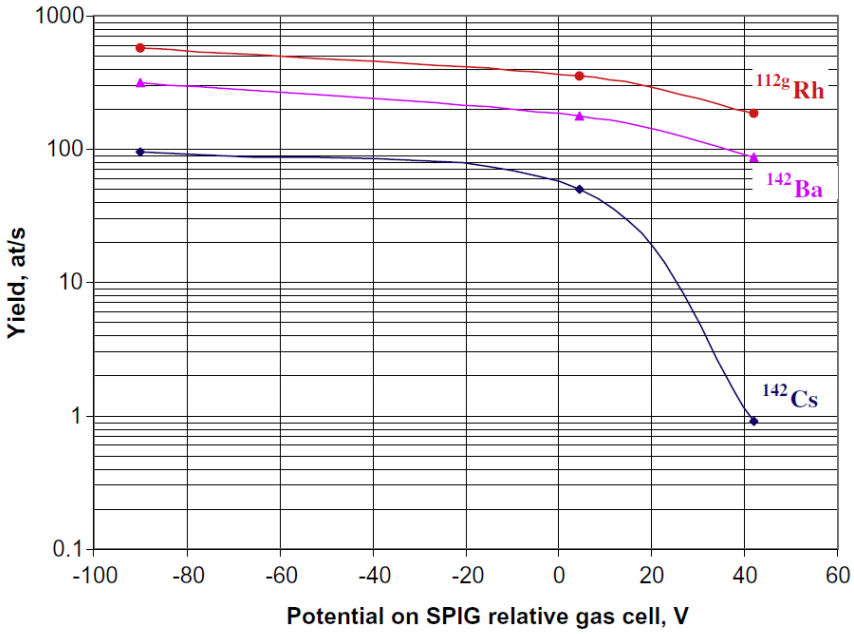

Figure 4.39: Yield of ^{112}Rh, ^{142}Ba and ^{142}Cs isotopes produced in the proton-induced fission of ^{238}U as a function of the SPIG rods potential relative to the gas cell.

Also, the depth of the potential well created by the RF field of the SPIG is about 100 eV. Thus the recoiling ^{112}Rh ions can be easily confined by the RF structure and then can get a longitudinal velocity due to collisions with argon atoms from the jet. The charge state distribution after β^- decay for different isotopes displays a typical yield around 80% for the single-charge state and around 10% for the double-charge state [64] and makes it a very efficient ionization process. In order to measure the importance of the latter discussed process versus the deposition of mother nuclei inside the gas cell, a measurement of the mass-separated yield of different isotopes were performed for a series of fission products as a function of the applied voltage between the exit hole and the SPIG. Fig. 4.39 shows the yields (with lasers OFF) of different isotopes as a function of the potential on the SPIG rods relative to the gas cell. By applying a positive potential ($>$ 30 V in case of argon), the ions created in the gas cell and between the cell and the rods are not transported through the SPIG [59]. For stable nickel ions created in the ionization chamber, the reduction factor at a SPIG potential of 42 V is more than 1000. The reduction factor for laser-produced ^{112m}Rh was determined to be more than 100. However, for ^{112g}Rh, the reduction is only 2 times, (Fig. 4.39). A similar small reduction of factor 2 is observed for ^{142}Ba, which has ^{142}Cs as a parent nucleus with a Q_β-value of 7.3 MeV and a lifetime of 1.7 s. These ions can only come from the β^- decay of atoms sticking to the SPIG rods. A completely different situation is observed for the yield of ^{142}Cs isotopes, which drops 55 times when applying 40 V. This can be explained by the fact that the mother nucleus for ^{142}Cs is ^{142}Xe, which is a gaseous element that does not stick to

the SPIG rods. We observed the sticking effect in our previous work [57], where we measured the ion-source efficiency using long-lived radioactive ^{57}Co evaporated from a resistively heated filament. About 30% of the evaporated atoms were found on the SPIG rods. The sticking of radioactive isotopes in atomic or molecular form to the RF structure and consequent decay leading to the production of unwanted isotopes can limit the selectivity of the LIST method for neutron-rich nuclei, coupled either to a gas cell or a hot cavity. If the energy of the recoiling ions is small, they can be captured in the radial direction by the RF field without stopping in a low-pressure gas. A way to reduce this effect is the reduction of the RF structure surface.

Conclusions

Results obtained with a new type of gas cell whereby the stopping volume of the nuclear reaction products including the primary beam path are separated from the laser ionization volume have been presented. In this dual chamber gas cell concept the direct ionization near the exit hole through hard x rays is blocked and enables the use of electrical fields inside the gas cell. This leads to a strong increase of the selectivity. A laser selectivity of least 2200 has been achieved for exotic nuclei produced in fusion-evaporation reactions opening up new possibilities for e.g. spectroscopy studies in $N = Z$ region. However, for isotopes produced in fission reactions, which have strong feeding from the β^--decaying mother nuclei, the selectivity is limited because of the deposition of radioactive mother atoms on the rods of the RF ion guide.

Acknowledgements

The authors wish to thank to the cyclotron group at CRC Louvain-La-Neuve for running the accelerator. This work was supported by FWO-Vlaanderen (Belgium), GOA/2004/03 (BOF-K.U.Leuven), the 'Interuniversity Attraction Poles Programme - Belgian State - Belgian Science Policy' (BriX network P6/23) and by the European Commission within the Sixth Framework Programme through I3-EURONS (Contract RII3-CT-2004-506065).

4.2.4 Gas catcher Laser Ion Source Trap

Paper IV

T. Sonoda, T.E. Cocolios *et al.*, *Nuclear Instruments and Methods in Nuclear Physics Research B*267(2009)2918 – 2926.

In order to achieve even greater purity, the Laser Ion Source Trap (LIST) concept has been proposed, first for ISOL facilities [Bla03] and then for gas catchers as well [Moo05, Kar07, Kes08]. As described in section 2.2.3, it consists in geometrically disconnecting the atomisation from the ionisation. In the dual-chamber gas cell approach, only the thermalisation is isolated from the other processes. In order to achieve the LIST, the ionisation needs to take place beyond the gas cell.

The idea is then to use the gas cell to produce an atom jet that can be subsequently ionised by the lasers. In order to suppress the contamination from the surviving ions, either a potential is applied on the SPIG rods to repell the ions or the use of the IC is made. The jet atoms are finally ionised in the SPIG.

The properties of this approach are studied with different gas catchers, using ionisation either along or across the SPIG. The time profile of incoming Co^+ ions reveals that the LIST conditions are indeed met.

The beam properties are further studied from the line shape analysis of the resonance of the laser ionised nickel isotopes. Reduction in the Doppler and pressure broadenings of those resonances indicates that the conditions met in the LIST are suitable for in-source laser spectroscopy. The conditions for in-source laser spectroscopy in a gas catcher are then compared to those of the hot-target ISOL technique for copper. The LIST at the exit of a gas catcher would eventually offer the best compromise between resolution and sensitivity for laser spectroscopy.

The isotope shift of the stable $^{58,60-62,64}$Ni isotopes has been investigated but the mass shift remains too important with respect to the field shift and the achieved resolution is still insufficient to extract changes in the mean square charge radius in this region of the nuclear chart. This method remains attractive for the study of heavier isotopes, like bismuth, or for the study of the electromagnetic moments of isotopes with broad hyperfine structures, like copper.

The current setup is limited by structural constraints (no window in the separator magnet) and by the laser system (low repetition rate) but this study opens the way for the next-generation facilities (S^3, PALIS, ...).

The Laser Ion Source Trap (LIST) coupled to a gas cell catcher

T. Sonoda, T.E. Cocolios, J. Gentens, M. Huyse, O. Ivanov, Yu. Kudryavtsev, D. Pauwels, P. Van den Bergh, P. Van Duppen
Instituut voor Kern- en Stralingsfysica, Katholieke Universiteit Leuven, B-3001 Leuven, Belgium

Abstract

The proof of principle of the Laser Ion Source Trap (LIST) coupled to a gas cell catcher system has been demonstrated at the Leuven Isotope Separator On Line (LISOL). The experiments were carried out by using the modified gas-cell-based laser ion source and the SextuPole Ion Guide (SPIG). Element-selective resonance laser ionization of neutral atoms was taking place inside the cold jet expanding out of the gas cell catcher. The laser path was oriented in longitudinal as well as transverse geometries with respect to the atoms flow. The enhancement of beam purity and the feasibility for in-source laser spectroscopy were investigated in off-line and on-line conditions.

Laser ion source, Gas jet, Resonance ionization, Laser spectroscopy
29.25.Rm, 29.25.Ni, 41.85.Ar

Introduction

The laser ion source at the Leuven Isotope Separator On Line (LISOL) facility provides highly-purified beams of exotic nuclei produced in different types of nuclear reactions [65, 66, 67, 68, 69, 70, 71]. The operational principle of the laser ion source is based on element-selective multi-step laser ionization of nuclear reaction products which are thermalized and neutralized inside a high-pressure noble gas. The essential part of the laser ion source is the gas cell, which is filled with typically 0.5 bar Ar gas and is placed on the cyclotron beam axis, whereby most ions from the reaction products are neutralized. The neutralized atoms are transported by a gas flow towards the exit hole of the cell, where the atoms are re-ionized by laser radiations. The highly-purified beams are thus realized by separation by Z via laser ionization and by A/q at the mass separator. In many cases, however, the mass-separated beam contains in addition to the isotope of interest, small amounts of isobaric or doubly-charged ion contaminants that survive the neutralization or charge-exchange processes inside the gas cell. For studies of $\beta-\gamma$ and $\gamma-\gamma$ spectroscopy, such contaminants are unwanted background even if those yields are limited. In order to remove such contaminants, two different approaches are under investigation at LISOL: "the dual-chamber laser ion source" [72] and the Laser Ion Source Trap "LIST". The dual-chamber laser ion source is the subject of a separate publication [72] and only the LIST coupled to a gas catcher is discussed here.

The LIST was originally proposed to improve the quality of the ion beam from a hot cavity laser ion source [73]. This method is also being developed at Jyväskylä [74, 75], where the LIST is coupled to the IGISOL gas cell catcher [76]. The concept of the LIST method coupled to a gas cell catcher is shown in Fig. 4.40. The reaction products are thermalized and stopped in the buffer gas, subsequently neutralized and finally flushed out of the gas cell in a supersonic gas jet. The resonance ionization from the laser beams takes place in the gas jet leaving the gas cell and the photo-ions are captured in the RF-field of the SextuPole Ion Guide (SPIG) [77, 78, 79, 80] located immediately after the gas cell. In order to suppress unwanted ions, a positive DC voltage is applied on the SPIG rods to prevent the surviving ions that escape the gas cell from entering the SPIG. Only the ions that are resonantly ionized by the lasers close to the entrance of or inside the SPIG are sent through the mass separator. The purity of the beam can be further improved by applying a time gate after each laser pulse. In this way, unwanted ions can be further suppressed yielding extreme purity of the final beam.

The beam-quality improvements reached with the LIST open new possibilities such as in-source laser spectroscopy. For precise laser-spectroscopic studies, the width of the measured resonant spectral line should be as close as possible to the natural line width. The experimental width is a convolution of many effects adding to the intrinsic laser linewidth, including mainly the pressure broadening from collisions with the buffer gas, the power broadening from the lasers and the Doppler broadening due to the atomic velocity distribution. In the LIST case, the isolated atomic beams are obtained by supersonic adiabatic expansion in vacuum, which reduces the Doppler

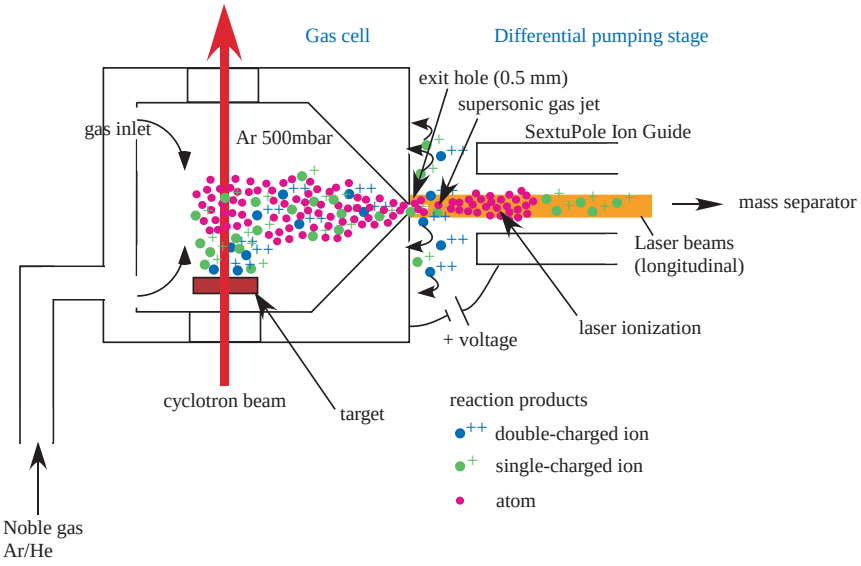

Figure 4.40: The concept of the LIST method coupled to a gas cell catcher.

broadening substantially. Additionally, the gas density in the ionization region is too low to significantly contribute to the pressure broadening of the spectral line. While in some cases elements with large hyperfine structure or large isotope shift can be studied inside the gas cell [81, 82], the LIST condition creates a suitable environment for laser spectroscopy on a wider range of nuclei, complementary to standard ISOL systems making use of solid or liquid target/catcher systems. In those cases, the release properties can seriously reduce the efficiency for certain elements or for short-living nuclei. Here, the time restriction from the decay losses is only the evacuation time of the gas cell. Short-lived isotopes, with half-lives down to 100 ms, are suitable candidates for laser spectroscopy.

In the present work, we studied the LIST performances in off-line and on-line conditions. The laser beams are sent either by a longitudinal or a transverse path with respect to the gas jet outside the cell. In the off-line conditions, laser beams ionize stable Co, Ni or Cu atoms evaporated from a filament located inside the cell. The suppression effect of unwanted ions is shown by monitoring the time profile on the arrival of mass-separated ions while applying different repeller voltages. Frequency scans of the first step laser for stable ^{58}Ni and ^{63}Cu in the gas cell and in the jet have been performed to compare the resonant linewidth in the different conditions. The evolution of the pressure broadening and the pressure shift in argon as a function of the argon pressure in the cell for the resonant 232.003 nm nickel line and the resonant 244.164 nm copper line were evaluated. As a demonstration, the isotope shifts of ^{58,60,62,64}Ni have been measured in the jet. In online condition, neutron-deficient Rh isotopes produced in fusion-evaporation reaction were successfully ionized in the LIST.

Experimental set-up

Two different gas cells were used for the LIST experiment. The experimental set-ups are shown in Figs. 4.41 and 4.42 according to the cell type. The first cell, which is a single-chamber gas cell, is shown in Fig. 4.41. It was originally used for heavy ion-induced fusion-evaporation and proton-induced fission reactions in on-line LISOL experiments [70]. In the present test, it was used only for off-line measurements. The diameter of the exit hole was 1 mm and the gas pressure in the cell was fixed at 150 mbar of argon and 200 mbar of helium, respectively.

The second cell is the dual-chamber gas cell, shown in Fig. 4.42. A detailed description of this gas cell can be found in [72]. Its main feature is the separation in two volumes: one for thermalizing the reaction products and the other for laser re-ionization. Due to a lower charge density in the re-ionization volume, electrical fields inside the gas cell can be applied using a potential V_{ic} on the ion collector plates (Fig. 4.42). The diameter of the exit hole was 0.5 mm and the pressure of the cell can be increased up to 500 mbar for argon and 1000 mbar for helium. The maximum pressure in both cells thus depends on the size of the exit hole and the pumping capacity outside the cell. The dual-chamber gas cell was used for both off-line and on-line experiments. In the on-line test, an accelerated beam from the cyclotron impinged on a target which was tilted by 35° with respect to the beam direction. The reaction products recoiling out from the target are thermalized inside the stopping volume and then move to the re-ionization volume by a gas flow.

The SPIG is located at the differential pumping region in front of the exit hole of the cell. This technique was originally proposed for the ion transportation from the low- to high-vacuum regions while maintaining the beam quality [77]. The distance between the gas cell and the SPIG is adjustable. The six rods of the SPIG have a diameter of 1.5 mm, the length of the rods is 126 mm and the diameter of the inner circle of the ion guide is 3 mm. The voltage configuration consists of three parameters: SPIG V_{rf} (radio-frequency, typically 300 Vpp, 4.7 MHz), SPIG V_{dc} (superimposed to SPIG V_{rf} before being applied to the SPIG rods), and SPIG-end V_{se}. In order to see the laser ions which are produced inside the SPIG, a positive potential was applied to SPIG V_{dc} repelling unwanted ions coming from the gas cell. The SPIG-end V_{se} was given a negative or zero voltage. The acceleration voltage on the isotope separator is typically set at 40 kV.

The optical system has been thoroughly described in [66]. It consists of two tunable dye lasers pumped by two XeCl excimer lasers. The maximum laser pulse repetition rate is 200 Hz. Two-colour, two-step schemes are used to ionize atoms through auto-ionizing states. Two laser paths to the LIST were used either in the longitudinal (LIST_L) or in the transverse (LIST_T) direction with respect to the atom beam. In the LIST_L, the lasers are introduced from the backside of the cell and pass through the exit hole and the SPIG. In the LIST_T, the lasers come across the gas jet between the exit hole of the cell and the SPIG, perpendicular to the gas jet. The single-chamber gas cell was only tested with the LIST_L, while the dual-chamber gas cell was studied with both geometries. For atomic spectroscopy studies, the intrinsic

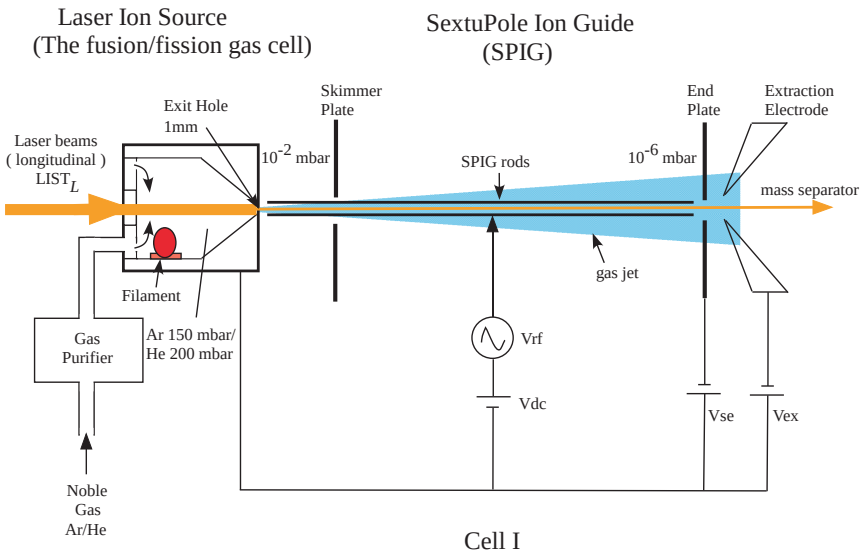

Figure 4.41: A top view of the single-chamber gas cell together with the SPIG in the LIST experiment.

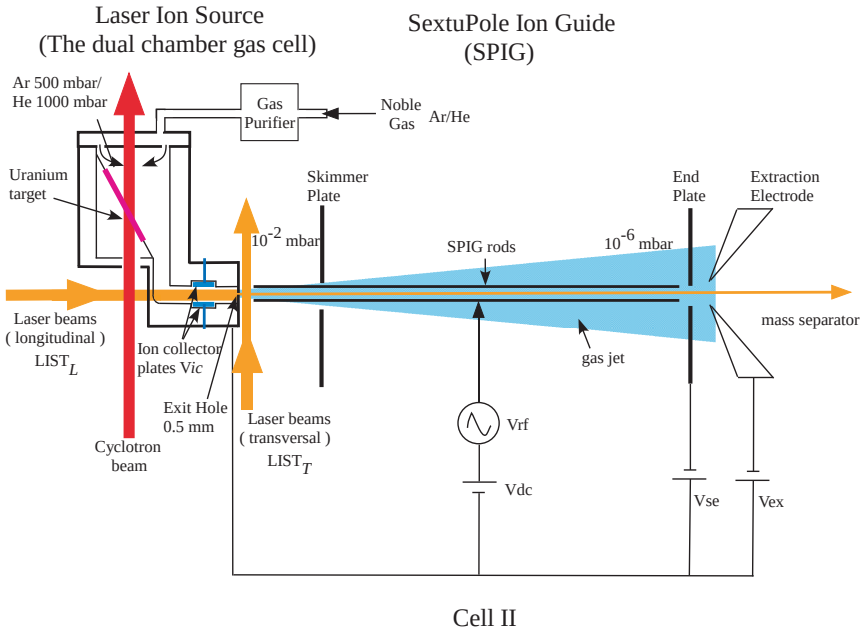

Figure 4.42: A top view of the dual-chamber gas cell [72] together with the SPIG in the LIST experiment.

bandwidth of the first-step laser has been minimized to 1.6 GHz with etalon, starting from 4.5 GHz in the second harmonic without etalon.

A fraction of the laser beams is deflected into a reference cell, where an atomic beam of the investigated element is produced from a resistively-heated crucible. The pressure in the reference cell is 10^{-6} mbar. The laser beams ionize the atoms in a crossed-beam geometry and the obtained ions are accelerated towards a secondary electron multiplier. This setup is used to perform laser spectroscopy in vacuum. Furthermore, the wavelength of the first step transition is consistently monitored by a Lambdameter LM-007.

In the present study, there are a number of limitations. First, when the lasers are sent through the gas cell (LIST$_L$), the ionization region where the laser beams and the jet atoms overlap is restricted due to a limited laser-spot size determined by the diameter of the gas cell exit hole. This can be solved by sending the lasers from the other end through the isotope separator and the acceleration electrodes [74]; it is however, not possible with the current setup, as the dipole magnet has no window. The size of the exit hole being 1 mm or 0.5 mm in diameter, the ionization region will also be a cylinder of that dimension. This value is more than six times smaller than the original laser-spot size and reduces greatly the overlap of the laser beam with the plume of atoms and thus the ionization efficiency. This limitation is not fully avoided even if sending the lasers in transverse geometry, where also the size of the expanding jet is larger than the laser cross section.

Moreover, our present laser system is not ideal for the LIST as the maximum repetition rate of the pulsed lasers is 200 Hz. If the overlapped length in laser photons and jet atoms, in the longitudinal mode, is 50 mm and the jet velocity is 500 m/s, then 10 kHz repetition rate is required for at least one encounter between the laser photons and the atoms. Therefore the present setup reaches only up to 1/50 of the LIST capability. This is even worse in the transverse mode. Additionally, the laser bandwidth after frequency doubling is 1.6 GHz, which is considered wide for laser spectroscopy. Due to those limitations, the present work represents a feasibility study and not yet a report on a full-fetched facility. However, since this is expected to be a linear behavior, one can scale the measured efficiencies with this reduction factor of 50 in duty cycle to estimate the performance of the LIST mode.

Results and discussion

The different approaches used in this work are detailed in Table 4.6. The section is then divided according to the type of laser path used in the LIST: longitudinal (LIST$_L$) or transverse (LIST$_T$).

LIST using longitudinal laser ionization - LIST$_L$

Suppression of unwanted ions with the repeller voltage In order to suppress unwanted ions coming from inside the cell, a positive potential was applied

Table 4.6: Experimental conditions for the gas cell, the longitudinal LIST$_L$ and the transverse LIST$_T$. Two voltage configurations, SPIG V_{dc} and (Ion Collector) IC V_{ic}, are adjusted for the different conditions.

	SPIG V_{dc} [V]	IC V_{ic} [V]	Laser path
Gas cell	−210	0	Longitudinal
LIST$_L$	+46	0	Longitudinal
LIST$_T$	0	±40	Transverse

to SPIG V_{dc} with respect to the cell. Fig. 4.43 shows the result of time-profile measurements of stable cobalt ions ($^{59}Co^{1+}$) with different SPIG V_{dc} voltages. The gas cell "Cell I", shown in Fig. 4.41, was used. The mass-separated ions were counted by the Secondary Electron Multiplier (SEM) located one meter downstream from the focal plane at the end of the mass separator. The laser pulse was fired at $t = 1$ ms longitudinally through the gas cell filled with Ar at pressure 150 mbar and passed through the 1 mm exit hole into the SPIG. The laser-repetition rate was 1 Hz, avoiding effects from previous pulses. The SPIG-end V_{se} was fixed at −40 V, the distance between the SPIG and the exit of the cell was 2 mm.

In Fig. 4.43, when the repeller voltage is 0 V, the majority of the signal is made by ions ionized inside the gas cell from which they are continuously evacuated. When applying a positive SPIG V_{dc} voltage, most photo-ions from the gas cell are prevented from entering the SPIG. However even at 26 V, ions from the gas cell are still entering the SPIG due to the continuous collisions with the jet atoms. By increasing the voltage further, the ions coming from inside the cell are finally suppressed from entering the SPIG. Consequently, the remaining signal in the time profile comes from ions which are ionized only outside the gas cell and captured by the SPIG. Some counts also appear at $t = 1$ ms in Fig. 4.43, produced by scattered laser photons entering the SEM. This contributes a few counts in total SEM signals. The background of SEM without any lasers was nearly zero. The delay between the laser pulse and the start of an ion pulse was 100 μs, from which $\sim$ 20 μs correspond to the time of flight of the ions through the separator; the remaining 80 μs correspond to the transport time through the SPIG. The signals left over at longer time with the highest voltage ($V_{dc} = 46$ V) are ions that are delayed in the SPIG. The width of the remaining peak was about 88 μs in Full Width at Half Maximum (FWHM).

Similar results were also observed with He as the buffer gas at a pressure 200 mbar. The suppression voltage needed to observe the ion signal from the LIST mode was about 20 V.

Wavelength scans and the velocity evaluation of the gas jet One of the interests in the LIST mode is to study the feasibility of laser spectroscopy inside the gas jet for exotic nuclei. Therefore the resonant linewidth of a specific element has to be evaluated in the gas jet and compared to other conditions. The laser ion source at LISOL allowed for direct comparison of the resonant linewidth for stable

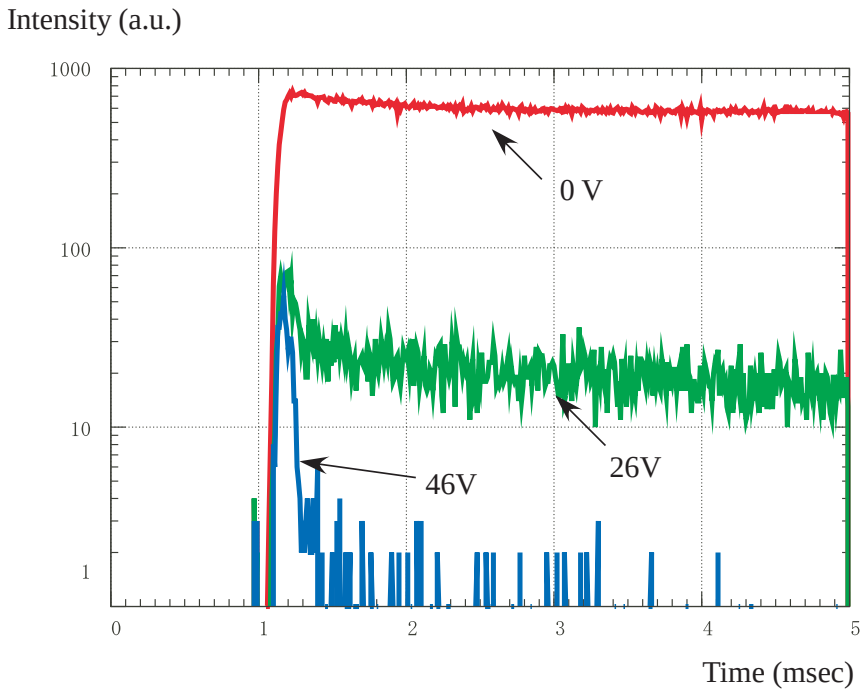

Figure 4.43: The time profile of Cobalt ions ($^{59}Co^{1+}$) transported via the SPIG and mass-separated. The laser pulse was fired at $t = 1$ ms. Different SPIG V_{dc} voltages were used as indicated in the figure. The voltage polarity was applied positively to suppress ions from the gas cell. The delay between the laser pulse and the start of an ion pulse is 100 μs (For interpretation of the references to colours in this figure, the reader is referred to the web version of this paper.).

isotopes in the following three circumstances: (1) inside the reference cell (vacuum, 10^{-6} mbar), (2) inside the gas cell (He or Ar with a few hundreds mbar), (3) inside the gas jet (LIST$_L$/LIST$_T$). Frequency scans of the first step laser for stable ^{58}Ni have been performed and the resonant linewidth at those different locations is extracted. The partial atomic level scheme of Ni is given in Fig. 4.44. An efficient ionization path is used, starting from the $^3F_4$ ground state via a transition at $\lambda_1 = 232.003$ nm to the $^3G_5$ intermediate level at 43090 cm^{-1}, followed by a transition at $\lambda_2 = 537.84$ nm to an auto-ionizing state.

Fig. 4.45 shows the resonance of the first step transition under the three different conditions. In this measurement, the Cell I configuration (Fig. 4.41) was used with 200 mbar of helium as the buffer gas. The SPIG V_{dc} voltage was kept at +46 V in the LIST mode. The result clearly shows a displacement of the resonance centroid acquired in the jet from that acquired in the reference cell or the gas cell. This displacement is caused by the Doppler shift of the moving atoms in the jet while they are ionized inside the SPIG. From this measurement, the jet velocity was deduced to be $\sim$ 1663 m/s using the displacement $(\nu' - \nu) = +7.2$ GHz, where ν' is the resonance frequency of atoms in the jet and ν is the resonance frequency for atoms

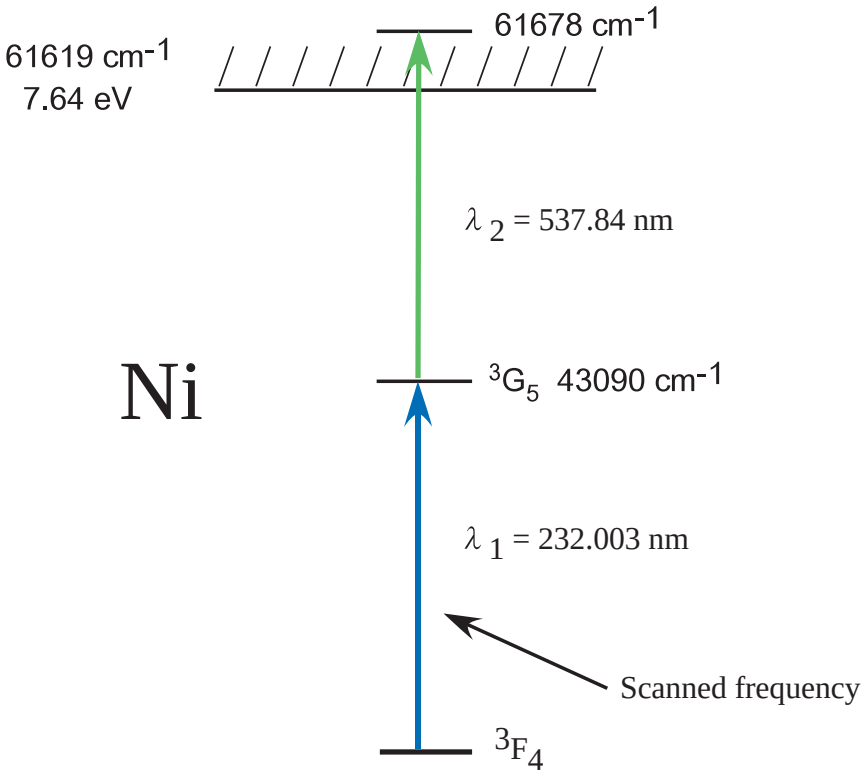

Figure 4.44: Partial atomic level diagram of Ni. Next to the wavelength, the log-ft (transition strength) is listed [83].

in the reference cell.

Table 4.7: Comparison of the linewidth of Ni in different locations using He 200 mbar as the buffer gas based on the data in Fig.4.45.

Ionization place	centroid (cm^{-1})	FWHM (cm^{-1}/GHz)
Reference cell	43089.636	0.101(5)/3.03(15)
Gas cell	43089.646(15)	0.211(33)/6.33(99)
LIST$_L$	43089.875(14)	0.135(6)/4.05(18)

Table 4.7 shows the values of the centroid and the Full Width at Half Maximum (FWHM) of the resonance peak in those different locations. There are four components which should be convoluted in this resonance line. The first component is the intrinsic band width of the laser ($\Delta_{laser} \approx 1.6$ GHz Gaussian FWHM in this setup). The second component is a laser power broadening Γ_{power} (Lorentzian FWHM). This was a very important source of broadening; the laser power was therefore adjusted to a value as low as possible in all three cases while still allowing sufficient ionization to perform the measurement. The two other components are the Doppler broadening $\Delta_{Doppler}$

(Gaussian FWHM) from the atom velocity distribution and the pressure broadening $\Gamma_{pressure}$ (Lorentzian FWHM) from the surrounding gas. This last component grows linearly with the pressure as

$$\Gamma_{pressure} = \text{constant} \cdot \text{Pressure}, \tag{4.1}$$

where the constant depends on the atomic transition of interest. The overall resonance line is therefore a Voigt profile where the Gaussian and the Lorentzian contributions are given by

$$\Delta = \sqrt{\Delta^2_{laser} + \Delta^2_{Doppler}} \text{ and} \tag{4.2}$$
$$\Gamma = \Gamma_{power} + \Gamma_{pressure}. \tag{4.3}$$

The total FWHM is then given empirically by [84]:

$$\text{FWHM} = 0.5346 \cdot \Gamma + \sqrt{0.2166 \cdot \Gamma^2 + \Delta^2}. \tag{4.4}$$

In the wavelength scan for the evaporated atoms in the reference cell, the pressure broadening is negligible as high vacuum is reached inside the reference cell: $\Gamma \approx \Gamma_{power}$. This contrasts strongly with the gas cell where the pressure broadening is typically dominant contribution for the width of a resonance peak, that depends on the type of element, electron transition and the amount of gas pressure. This pressure effect is evaluated by the resonance linewidth when the pressure is systematically changed. Additional remark in the case of the reference cell, the ionization is performed in a crossed-beam geometry, thus probing the atomic beam in a direction where the velocity is perpendicular; the Doppler broadening is thus negligible: $\Delta \approx \Delta_{laser}$. As for the Doppler broadening in the case of the gas cell, the velocity of the atoms in the gas is subjected to a Maxwell-Boltzmann distribution. The velocity range depends on the mass, with a wider distribution for lighter masses. In the case of Ni, a simple calculation yields a velocity range of FWHM$\approx$ 300 m/s in 200 mbar He as a buffer gas. This value broadens the peak by $\Delta_{Doppler} \approx 2$ GHz.

In the case of ionization in the SPIG, the jet conditions are the most important. As the pressure in the entrance of the SPIG is already low, the pressure broadening is reduced substantially. The main contribution to the FWHM is therefore the Doppler broadening in addition to an intrinsic band width and a power broadening of the laser.

Pressure broadening of the nickel resonance line in argon In the gas cell with an exit hole diameter of 1 mm, the maximum argon pressure of 150 mbar is limited by the pumping capacity of the system. With an exit hole of 0.5 mm, the gas pressure can be increased up to 500 mbar. At this pressure, the broadening and the shift of the nickel resonant line are large enough to be measured with the existing laser bandwidth. Fig.4.46 shows the wavelength scans of the first step laser in the three different locations. The deduced FWHM values are given in Table 4.8 in

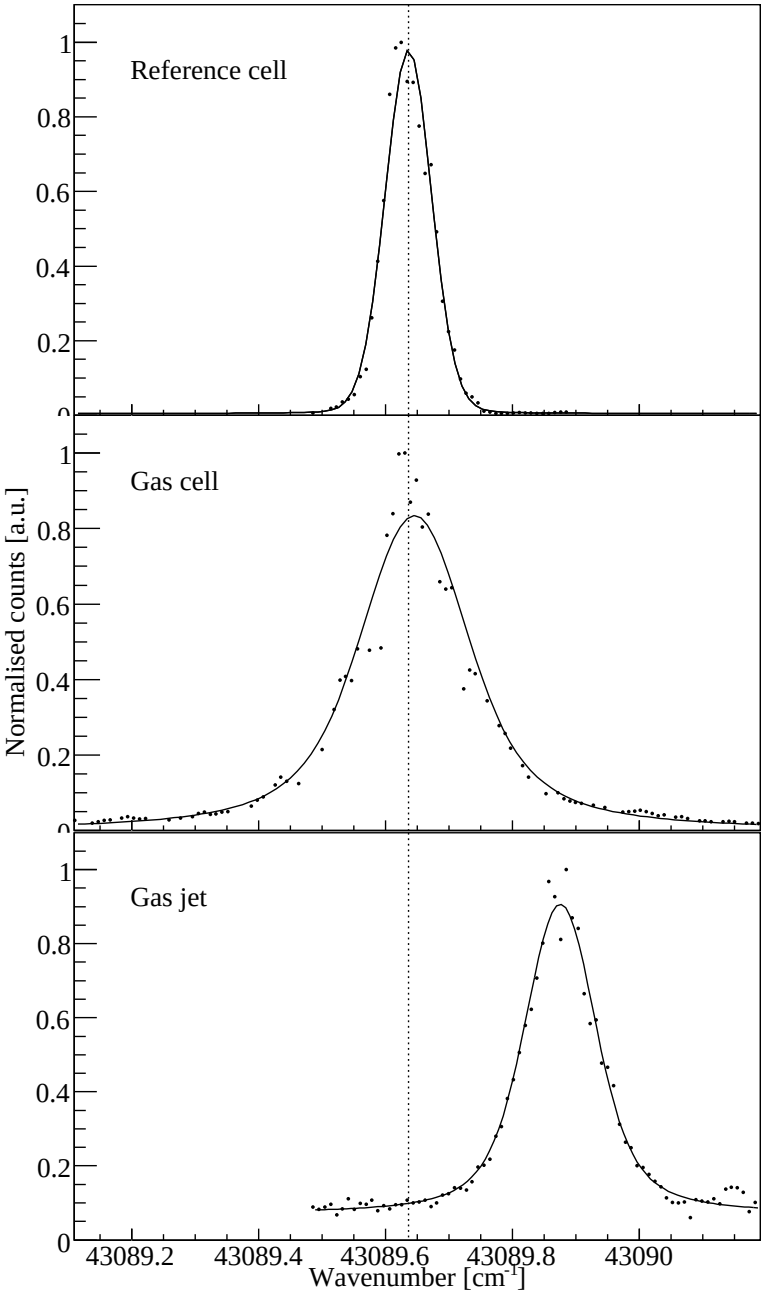

Figure 4.45: Scan of the first step transition of Ni in three different locations: in the reference cell (top), in the gas cell (middle), in the LIST$_L$ (bottom), using 200 mbar helium as the buffer gas. A Doppler shift of 7.2 GHz is observed when ionizing in the jet, which corresponds to an atom velocity of 1663 m/s. The solid line represents the best fit of a Voigt profile through the data points.

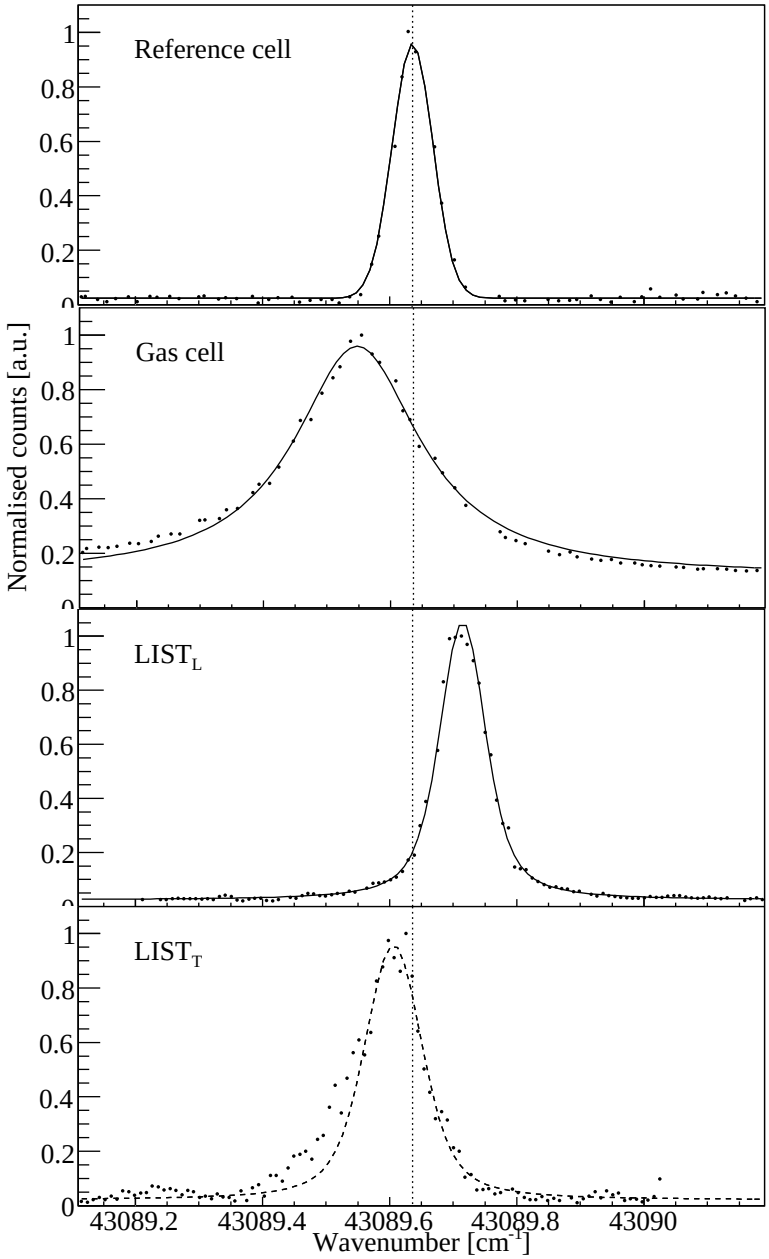

Figure 4.46: The resonant linewidths of the first step transition of Ni in three different locations: in the reference cell (top), in the gas cell (second from the top), and in the gas jet with the lasers in the longitudinal LIST$_L$ (second from the bottom), and with the lasers in the transverse LIST$_T$ (bottom). The gas cell was filled with 500 mbar of argon as the buffer gas. The solid line is the best fit of a Voigt profile through the data point. The dashed line is the best fit through the high-frequency half of the asymmetric resonance in the LIST$_T$; the asymmetry is due to the high pressure gradient in the region close to the exit nozzle.

the same form as in Table 4.7. The width of the resonance in the reference cell and in the jet (LIST$_L$) are the same around ~ 2 GHz. The signal from the gas cell filled with 500 mbar argon is, however, much broader (~ 6 GHz) and red-shifted by 2.5 GHz relative to the resonance in the reference cell. Similarly to the case where He was used, the jet velocity was deduced by the displacement of the SPIG resonance peak and resulted in ≈ 550 m/s.

Table 4.8: Comparison of the linewidth of Ni in different locations using 500 mbar of Ar as the buffer gas based on the data in Fig. 4.46. Most of the uncertainty comes from systematic effects of the laser power fluctuations and laser modes; it has been estimated to 0.005 cm^{-1} based on the fluctuations observed on the spectra of Fig. 4.46.

Ionization place	centroid (cm^{-1})	FWHM (cm^{-1}/GHz)
Reference cell	43089.636	0.064(5)/1.92(15)
Gas cell	43089.551(5)	0.215(5)/6.45(15)
LIST$_L$	43089.715(5)	0.087(7)/2.61(21)
LIST$_T$	43089.606(33)	0.108(15)/3.24(45)

Performing similar comparisons at different argon pressures gives the evolution of both the pressure broadening and the pressure shift. The results are shown in Figs. 4.47 and 4.48 for the resonant 232.003 nm nickel line and the resonant 244.164 nm copper line. A pressure broadening of 11.3(6) MHz per mbar and a pressure shift of $-5.5(3)$ MHz per mbar can be extracted for nickel; in the case of copper, a pressure broadening of 5.4 MHz per mbar is found and a pressure shift of $-1.9(1)$ MHz per mbar. The difference between nickel and copper highlights the importance of the electronic transition studied.

LIST using transverse laser ionization - LIST$_T$

Suppression of unwanted ions with the collector plates (ion collector) The repeller voltage to suppress unwanted ions used in the longitudinal geometry cannot be used in the transverse geometry as the ions produced between the gas cell and the SPIG would all be repelled. Instead, a voltage (V_{ic}) is applied to the ion collector inside the laser ionization chamber, as described in [72].

This method can only be used with the dual-chamber gas cell pictured in Fig. 4.42. A voltage difference from -40 V to $+40$ V is applied across the plates to collect the ions surviving the neutralization processes in the gas catcher and only an atom beam exits the cell. The ions are then produced between the gas cell exit and the SPIG, placed at a distance of 3 mm, and at the entrance of the SPIG, since the laser spot size is 5 mm.

The performance of the ion collector depends on several parameters such as the collection efficiency of the ions and the ion production rate is discussed in [72].

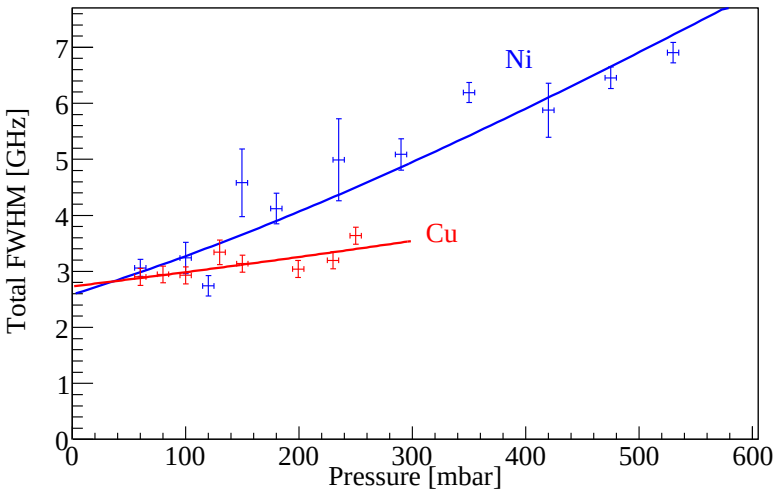

Figure 4.47: The evolution of the pressure broadening in argon as a function of the argon pressure in the cell for the resonant 232.003 nm nickel line and the resonant 244.164 nm copper line. Some data points are the average of several measurements. The solid lines are the best fits according to Eqs. 4.1 and 4.4.

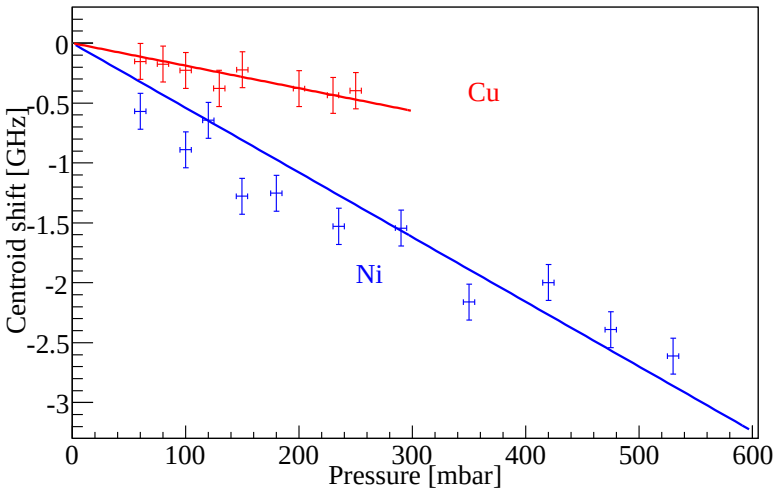

Figure 4.48: The evolution of the pressure shift in argon as a function of the argon pressure in the cell for the resonant 232.003 nm nickel line and the resonant 244.164 nm copper line. Some data points are the average of several measurements. The solid lines are linear best fits going through the origin.

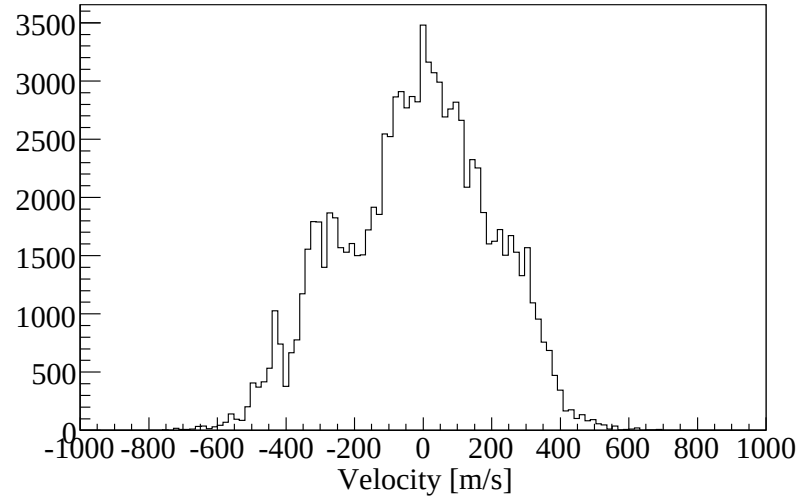

Figure 4.49: Simulated velocity distribution in the direction perpendicular to the atom jet in the area covered by the lasers between the gas cell and the SPIG. The buffer gas in the gas cell is Ar at 500 mbar. This distribution contributes to the total broadening of the optical resonance by 750 MHz.

Overlap between the laser and atom beams Compared to the longitudinal mode inside the gas cell and based on a laser repetition rate of 200 Hz, a laser spot size of 5 mm and a supersonic velocity in the Ar gas jet of 560 m/s, a reduction factor of 560 in duty factor is expected in this transverse mode. This assumes that both the laser excitation and ionization steps are saturated. Experimentally, a reduction factor of 300(10) has been measured with $^{58}Ni^{+}$ ions from a filament, probably due to a larger laser-spot size than in the previous estimate.

Another important parameter concerning the overlap of the two beams in this geometry is the velocity distribution of the atoms. With the increased distance between the gas cell exit and the SPIG, the atom beam diverges strongly; a simulated velocity distribution in the transverse direction is shown in Fig. 4.49. Such a distribution translates into a Gaussian profile in the optical resonance with a FWHM of 12 GHz. Convoluted with the laser lineshape, this contributes to the total broadening of the optical resonance; in the case of a gas catcher filled with 500 mbar of Ar, the estimated increase in broadening is 750 MHz.

Wavelength scans and the environmental conditions The optical resonance using the LIST$_T$ is shown at the bottom of Fig. 4.46. Its properties appear in Table 4.8.

The broader FWHM in the LIST$_T$ can be partially explained by the transverse velocity distribution previously discussed. However, some effects from the gas pressure could still play a role as there could be a pressure gradient close to the exit nozzle. This pressure gradient is also responsible for the asymmetry and the shift of the

resonance in the LIST$_T$.

On-line measurement The LIST$_T$ was used on-line with radioactive neutron-deficient ^{94}Rh isotopes produced in the ^{58}Ni(^{40}Ar, 1p3n)^{94}Rh reaction. In this heavy-ion reaction and using longitudinal ionization in the gas cell, the 70.6 s (4^+) low-spin ground state is produced with 900(100) ions per μC while the 25.8 s (8^+) high-spin isomer, more favored, is produced with 6000(100) ions per μC. The γ spectra in the different conditions are shown in Fig. 4.50.

By comparing longitudinal ionization inside the gas catcher to transverse ionization in the LIST$_t$, a reduction factor in efficiency of at least 700 is extracted from the β-decay rates. This is more than in the case of stable ^{58}Ni although it is of a similar order of magnitude. This could be due to the difference in the laser effective spot size between those elements.

On the other hand, the difference between the LIST mode with and without laser ionization is striking. The peaks are not visible anymore once the lasers are blocked while they are still clear with the laser ionization. Although the limited statistics only allows the extraction of a lower limit on the selectivity of 4, the real value that can be expected is much larger.

In case of the neutron-rich isotopes produced in the proton-induced fission of ^{238}U, another source of contamination is present through the deposits of neutral radioactive isotopes on the RF structure of the SPIG [72]. The subsequent β^- decay of these neutron-rich nuclei leaves the daughter nuclei in an ionic state, yielding possibly in the capture by the pseudo-potential of the SPIG. This could be a limit of applicability of the LIST concept for the neutron-rich isotopes.

Laser spectroscopy in and around a gas catcher Laser spectroscopy in ion-sources has been already performed in both hot cavity ion sources [85] and gas catchers [81]. The resolving power of each technique can be compared by analyzing the resonance linewidth in their respective type of ion source. In the case of in-source laser spectroscopy with a hot cavity [86, 87, 88], the resonance linewidth is the combination of the laser bandwidth with the Doppler broadening from the hot atomizer temperature (typically 2500 K); in the case of in-gas-cell-laser spectroscopy, the Doppler contribution is limited to that of room temperature (300 K) but the pressure broadening plays an important role. A simulation of the respective contributions in case of the copper transition at 244.164 nm is shown in Fig. 4.51. Even at pressures as high as 500 mbar of Ar, the resolution for laser spectroscopy in a gas cell is better than with a hot cavity.

The resolution of both systems remains however limited. This limit is mostly lifted when working in the LIST mode with the gas cell as the ions are cold and not under the influence of the pressure anymore. In Fig. 4.51, the present resolution with the LIST mode is given when the typical inherent laser bandwidth of 1.6 GHz is assumed. The resolution is dominated by the laser bandwidth. A laser with a narrower bandwidth could improve the resolution although the velocity distribution in the gas jet has to be taken into account (e.g. Fig. 4.49). The reduction of the

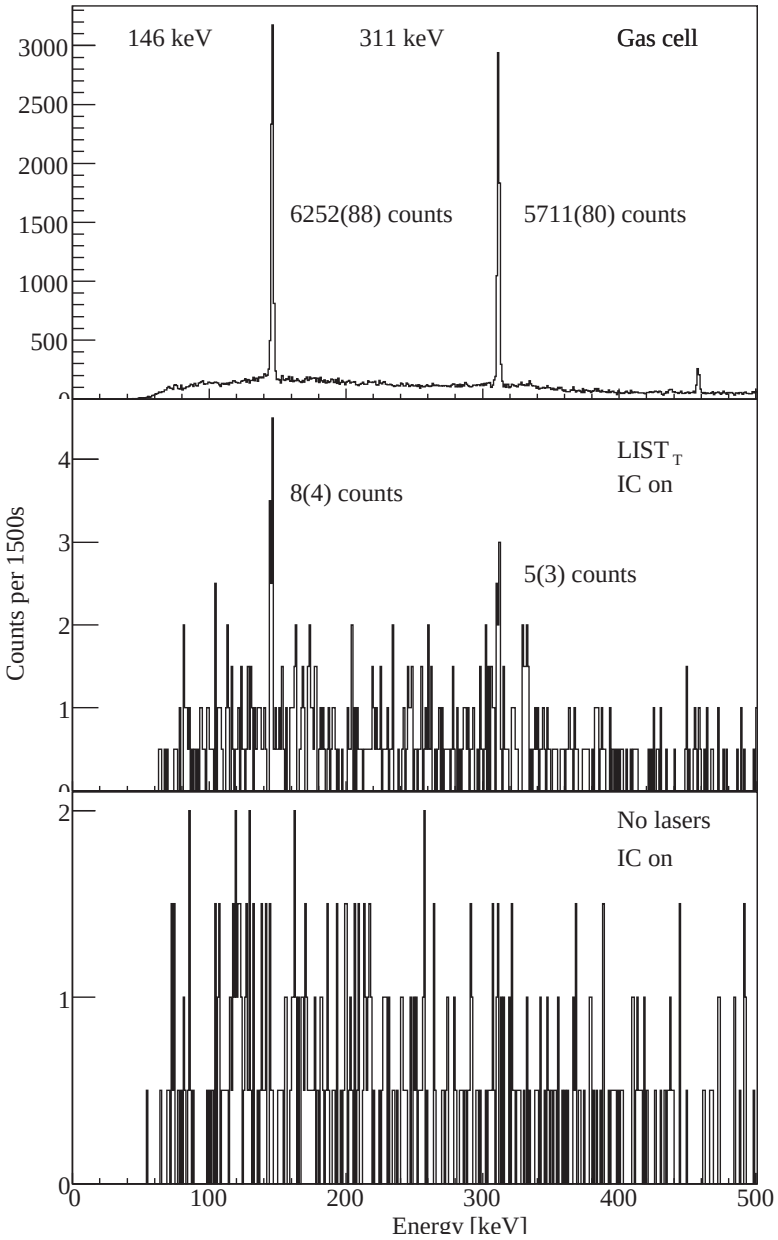

Figure 4.50: γ spectra in the decay of ^{94}Rh from 0 to 500 keV. From top to bottom: longitudinal ionization inside the gas catcher; ionization in the LIST$_T$; background in the LIST mode without laser ionization. The spectra are normalized to a measurement time of 1500 s.

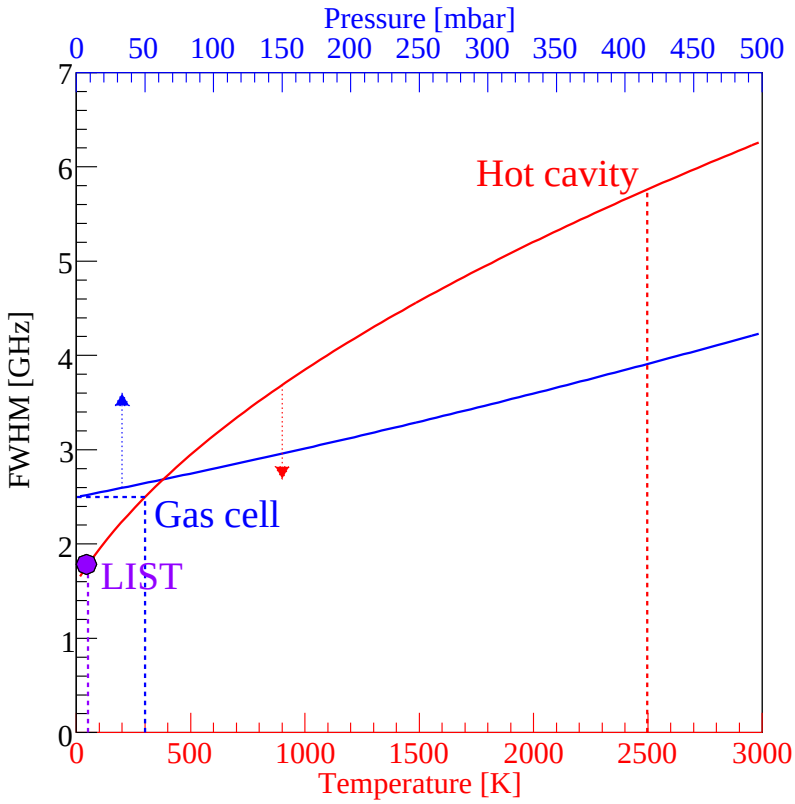

Figure 4.51: Simulated resonance linewidth of the copper transition at 244.164 nm for in-source laser spectroscopy with a hot cavity as a function of the atomizer temperature and for in-gas-cell laser spectroscopy at room temperature (with $\Delta_{Doppler}(300\text{K})$) as a function of the gas cell pressure for the typical working range of LISOL. A typical inherent laser bandwidth of 1.6 GHz is assumed in both cases. The typical running temperature for the hot cavity (ISOLDE, 2500 K [86, 87, 88]) and for the gas cell are shown with dashed lines. The LIST operating mode is also shown (low temperature and low pressure) and the resolution is dominated by the total laser bandwidth.

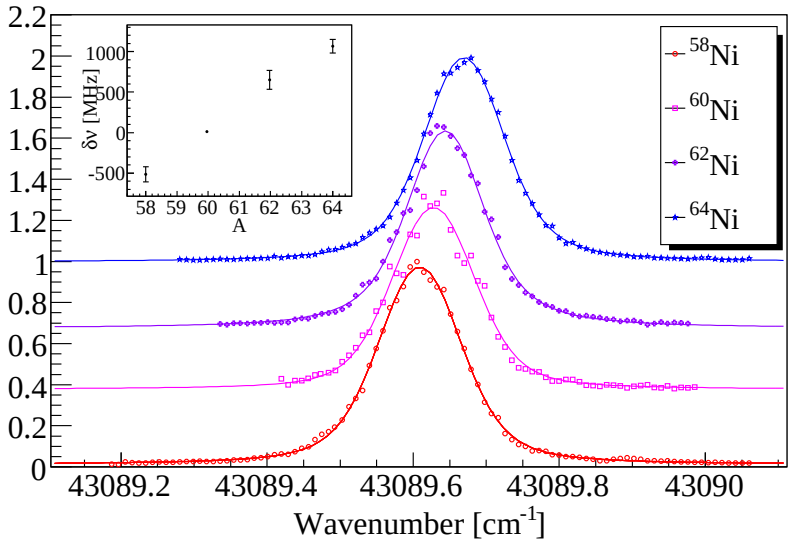

Figure 4.52: Wavelength scan of the first step resonant transition in Ni at mass $A = 58, 60, 62, 64$ with He as the buffer gas in the LIST$_L$. SPIG $V_{dc} = 20$ V, SPIG position was 0.75 mm from the gas cell. Inset: isotope shift of the even-A nickel isotopes.

resonance linewidth in the LIST$_L$ opens the possibility of further laser spectroscopic studies at LISOL. This is demonstrated by measuring the isotope shift of ^{58,60,62,64}Ni with either He or Ar as the buffer gas. Fig. 4.52 shows the result of the wavelength scans of the first step resonant transition for Ni at mass $A = 58, 60, 62, 64$ in He. Although the linewidth of the transition is still wide, mainly because of the laser bandwidth and power, the isotope shift of Ni was observed.

In order to relate the isotope shift to the changes in the mean-square charge radius, the electronic F-factor in the Field Shift (FS) and the Specific Mass Shift (SMS) have to be known. When isotope shifts have been measured for the same isotopes using different transitions, it is possible to extract a relative measurement of those parameters using a King plot. However, the uncertainty in our measurement is large in comparison with the limited contribution to the isotope shift of the nuclear effects. The linear relation yielding the relative information can therefore not be extracted. The extraction of the changes in the mean-square charge radius is thus impossible with our current setup in this mass range.

The Normal Mass Mhift (NMS), one of the last contributions to the isotope shift, is indeed $\delta\nu \approx 350$ MHz per two mass units, see the inset in Fig. 4.52. This effect dominates the isotope shift and the FS, related to the changes in the mean-square charge radius, is buried underneath. The NMS and SMS become rapidly smaller as A increases while the FS increases with increasing Z; laser spectroscopy can therefore still be possible to determine the changes in the mean-square charge radius in heavier isotopic chains. Elements with large hyperfine parameters, like copper and bismuth, are good candidates for in-source laser spectroscopy to determine nuclear magnetic

dipole moments [86, 88, 89].

Conclusion

The LIST coupled to a gas cell catcher has been studied at LISOL. The operational novelty of this method is relying on element-selective resonant laser ionization of neutral atoms which is taking place inside the supersonic cold jet expanding out of the gas cell catcher. In this paper, some systematic studies have been performed with two different laser geometries, either longitudinal (LIST_L) or transverse (LIST_T) with respect to the gas jet outside the cell. In the LIST_L, a suppression voltage was applied on the SPIG V_{dc}. It follows that only photo-ions created inside the SPIG are sent to the mass separator; all other ions produced inside the cell are repelled. The needed suppression voltage was then found to be about 20 V in He and 50 V in Ar, respectively. In the LIST_T, an ion collector voltage was utilized inside the gas cell. The suppression capability has been firstly demonstrated with neutron-deficient ^{94}Rh isotopes produced in fusion-evaporation reactions. Although statistics was limited due to restrictions on the setup, this result shows that high selectivity is achievable.

Another aspect arising from the LIST is the feasibility for in-source laser spectroscopy after a gas cell. This possibility is opened by the extremely low density and low temperature inside the jet which makes the velocity distribution of the atoms nearly uniform, resulting in small pressure and Doppler broadenings. The resonance linewidth for the Ni isotopes at different locations was compared in terms of individual effects contributing into one FWHM. In these results, it can be found that the gas jet as an environment for laser spectroscopy is much more comparable to that of vacuum conditions, while inside the gas cell, the pressure is a crucial parameter for determining the resonance width. The broadening was evaluated to be 11.3 MHz/mbar for Ni and 5.4 MHz/mbar for Cu in Ar gas pressures between 60 and 530 mbar. In addition, the jet velocity for the two types of buffer gas has been evaluated as 1663 m/s for He and 550 m/s for Ar from the displacement of the resonance peak in the LIST_L. The possibility for isotope shift measurements with the stable even-A nickel isotopes was also demonstrated. For actual measurements of changes in the charge radius or magnetic moments of atomic nuclei, the FWHM of the resonance peak in the jet should be minimized for satisfying the demanded accuracy in either longitudinal or transverse approach. In the current setup, using a suitable laser system whose fundamental linewidth is typically 100 MHz, a resolution of the order of at best 1 GHz can be obtained due to the Doppler broadening inside the gas jet. However, a dedicated optimization of the gas jet should allow to further improve this resolution. Elements with large hyperfine parameters are still good candidates for ionization laser spectroscopy. Additionally this method will show a strong advantage for elements with slow release times or low release efficiencies in conventional ISOL systems as the gas flow transports all elements and decay losses can be minimized by fast evacuation of the cell volume. Spectroscopy inside the gas cell is also achievable for isotopes displaying large hyperfine structures or isotope shift; care should therefore be taken in choosing the appropriate conditions maxi-

mizing the production (higher pressures) while minimizing the resonance linewidth (lower pressures).

Certainly, for future applications of the LIST combined with a gas cell, the overlap efficiency between the laser photons and the jet atoms is a determining factor. The efficiency comprises two parameters: the time overlap and the geometrical overlap. For the enhancement of the former part, a high repetition laser system is needed to achieve at least one photon-atom encounter. Then the expected repetition rate depends on the ionization length which is related to the geometrical overlap. If the jet is collimated enough, for example, for 10 cm without expansion, the needed repetition rate is 5 kHz for one encounter (for a jet velocity of 500 m/s). Pulsed lasers satisfying such a repetition rate are now commercially available. For getting such a narrow jet, some special nozzle for the exit hole of the cell or specific pressure outside of the cell will be necessary [90, 91]. Finally, one should consider the losses associated to photo-ions produced in the gas cell and then repelled; such losses also appear in the vicinity of the exit hole when applying the suppression voltage between the SPIG and the cell exit hole. It can be minimized by sending the lasers from the other end of the beam line through the isotope separator and acceleration electrodes. Alternatively using the transverse approach with suppression voltage inside the cell is also suitable though a very high repetition laser is then needed.

Acknowledgements

We would like to thank the accelerator group at Louvain-La-Neuve for running and maintaining the accelerator. This work was supported by FWO-Vlaanderen (Belgium), GOA/2004/03 (BOF-K.U.Leuven), the Interuniversity Attraction Poles Programme Belgian State Belgian Science Policy (BriX network P6/23), and by the European Commission within the Sixth Framework Programme through I3-EURONS (Contract RII3-CT-2004-506065).

Chapter 5

The magicity at $N = Z = 28$ investigated by in-gas-cell laser spectroscopy

5.1 In the vicinity of $N = Z = 28$

As introduced in section 1.2, 28 is the first magic number arising from the spin-orbit addition to the nuclear potential. As such, the study of the behaviour of the nuclei with $N = 28$ and $Z = 28$ is crucial to understand the shell model of the nucleus. A few recent studies and their conclusions will be introduced in this section.

5.1.1 The $N = 28$ isotones

Nuclei ranging from $^{41}_{13}$Al to $^{60}_{32}$Ge have been observed along the $N = 28$ magic shell closure, crossing the $Z = 20$ and $Z = 28$ shell closures at $^{48}_{20}Ca_{28}$ and $^{56}_{28}Ni_{28}$. Fig. 5.1 shows the systematics of the energy level of the first 2^+ excited state $E(2^+)$, of the transition probabilities B(E2:$0^+ \rightarrow 2^+$) and of the difference in the 2-proton separation energy δ_{2p} across this isotonic chain [nnd, For01, Gad03, Bas07, Aud03]. The main features are the high excitation energies and the high changes in the separation energies at $Z = 20$ and $Z = 28$, characteristic of magic shell closures. The interpretation of the transition probabilities is less conclusive, especially at $Z = 28$ since the systematics are incomplete.

Those isotones are also under investigation to study the shell closure at $N = 28$ itself. Recently, the measurement of the energy level of the first 2^+ excited state in $^{42}_{14}Si_{28}$ [Bas07] has highlighted how fragile the shell closure at $N = 28$ is away from the valley of β-stability. Evidence of shell erosion has also been identified from the measurement of the g-factor of $^{43}_{16}S_{27}$ [Gau09]. Many of the heavier isotones are stable elements, in a region well-described by the shell model of the nucleus. Finally, the heaviest isotopes, beyond $Z = 28$, are very exotic and have not been thoroughly studied.

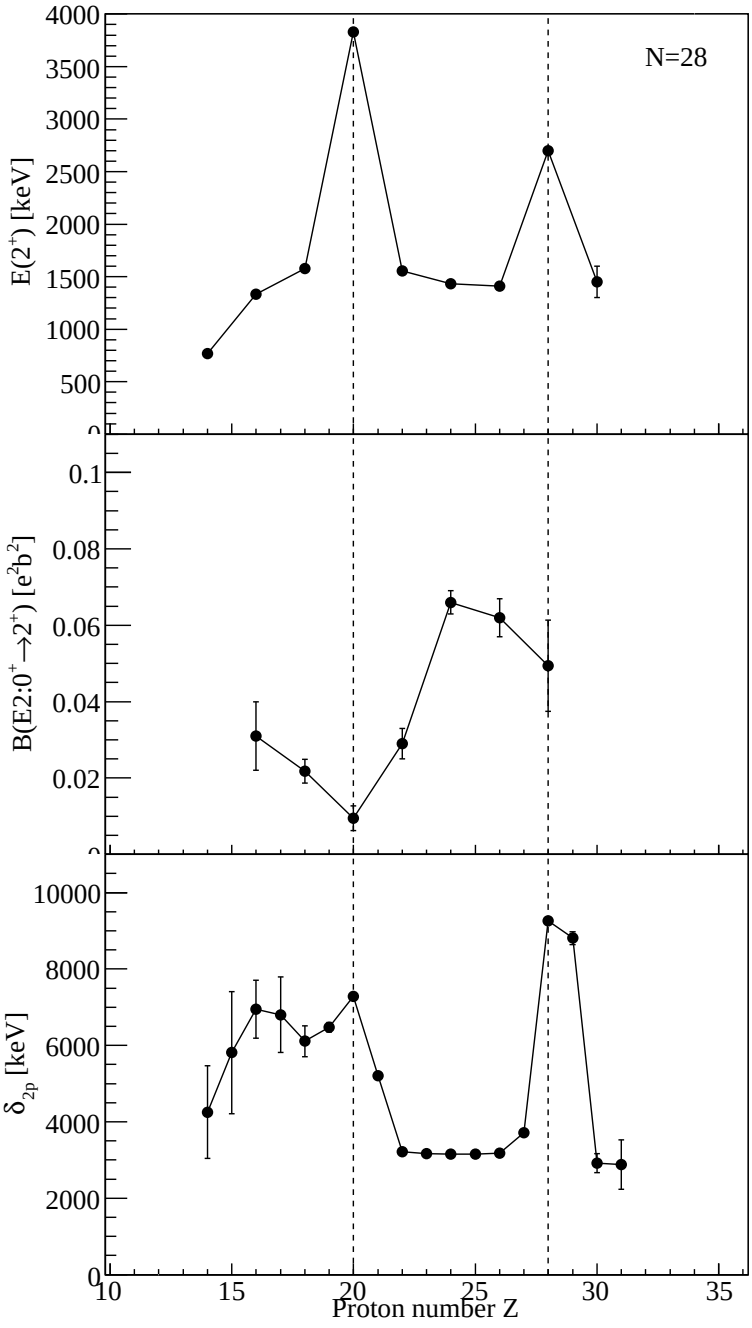

Figure 5.1: From top to bottom: systematic energy level of the first 2^+ excited state in the $N = 28-$even Z isotones; systematic transition probablity B(E2:$0^+ \rightarrow 2^+$) in the $N = 28-$even Z isotones; changes in the 2-proton separation energy in the $N = 28$ isotones.

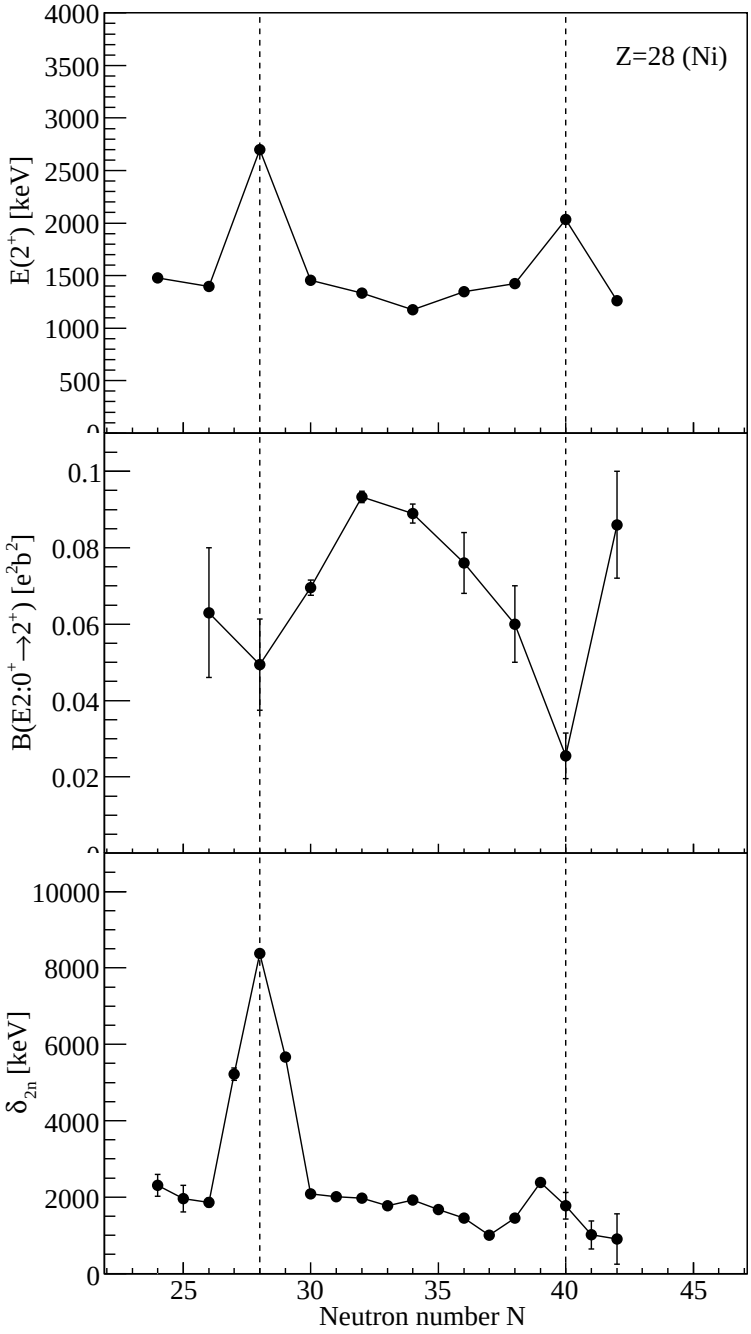

Figure 5.2: From top to bottom: systematic energy level of the first 2^+ excited state in the even-N $_{28}$Ni isotopes; systematic transition probablity B(E2:$0^+ \rightarrow 2^+$) in the even-N $_{28}$Ni isotopes; changes in the 2-neutron separation energy in the $_{28}$Ni isotopes.

5.1.2 The $Z = 28$ isotopes

The $Z = 28$ isotopes, also known as the 'nickel' isotopes, range across the nuclear chart from $^{48}_{28}Ni_{20}$ at the $N = 20$ closed shell to $^{78}_{28}Ni_{50}$ at the $N = 50$ closed shell, crossing the $N = 28$ shell and $N = 40$ sub-shell closures at $^{56}_{28}Ni_{28}$ and $^{68}_{28}Ni_{40}$, respectively. Fig. 5.2 shows the systematics of the energy level of the first 2^+ excited state $E(2^+)$, of the transition probabilities B(E2:$0^+ \rightarrow 2^+$) and of the difference in the 2-neutron separation energy δ_{2n} across this isotopic chain [nnd, Yur04, Sor02, Per06, Aud03]. Similarly to the $N = 28$ isotones, the excitation energy of the first 2^+ excited state shows the characteristic behaviour interpreted as magicity at $N = 28$ and $N = 40$; the other two observables bring however confusing messages.

Indeed, the sharp peak in the changes of the 2-neutron separation energy at $N = 28$ is a typical feature of magicity but this does not translate clearly in the transition probabilities which remain flat in this region without peaking down [Yur04]. This observation is reversed at $N = 40$, a shell closure issued from the harmonic oscillator potential, where the transition probabilities peak down while the changes in the separation energy remain flat; the behaviour of the transition probabilities is interpreted as coming from the parity change across the $N = 40$ shell closure, from the pf-orbitals to the $g_{9/2}$-orbital, rather than as a display of magicity [Sor02, Bre08].

5.1.3 $^{56}_{28}Ni_{28}$

Located where the two shell closures with 28 nucleons meet, the nucleus $^{56}_{28}Ni_{28}$ should be an anchor point for the shell model of the nucleus. In that respect, it has been the subject of extensive experimental and theoretical studies, as well as the isotopes in its vicinity [Sem96, Lis03, Hon04]. All those studies conclude on the fact that the ^{56}Ni nucleus is a very soft core for shell-model calculations. Indeed, the study of the excited energy levels in the $_{29}$Cu isotopes in the direct vicinity of ^{56}Ni can only be explained if excitations from the core are allowed [Lis03].

5.1.4 Magnetic dipole moments of the copper isotopes

In order to probe the stability of the core for the neighbouring nuclei, the magnetic dipole moment is a powerful tool that reveals information on the single-particle configuration of the ground state of a nucleus. The $_{29}$Cu isotopes, with a single proton outside the $Z = 28$ shell closure in the $\pi p_{3/2}$ shell, are of particular interest. For the study of the monopole migration of the $\pi f_{5/2}$ on the neutron-rich side of the nuclear chart, extensive work has been performed with high-resolution collinear fast-beam laser spectroscopy at ISOLDE [Fla09, Vin10]; the most neutron-deficient isotopes are, however, beyond the reach of that facility. Other techniques have been used to study those isotopes, like Nuclear Magnetic Resonance on Oriented Nuclei (NRM/ON) for ^{59}Cu [Gol04], β-NMR for ^{57}Cu [Min06] or in-source laser spectroscopy at ISOLDE for $^{58-59}$Cu [Sto08a]. None of those measurements, however, could determine an accurate value of the sign and magnitude of the magnetic moment. The case of ^{59}Cu, with the highest confidence, requires an independent precision confirmation as the

NRM/ON measurement technique could have suffered from systematic uncertainties related to the iron sample where it was implanted. In the case of ^{57}Cu, a large discrepancy between the theoretical predictions and the β-NMR measurement could not be explained and further investigation with another technique was required.

In this chapter, the precision measurement of the magnetic dipole moment of $^{57-59}$Cu by in-gas-cell resonant ionisation spectroscopy is reported.

5.2 In-gas-cell laser spectroscopy of the cupper isotopes

The neutron-deficient $^{57-59}$Cu isotopes have been investigated at LISOL with in-gas-cell resonant laser ionisation spectroscopy from fusion-evaporation of protons or ^{3}He on a natural nickel thin target using the dual-chamber gas cell (see section 4.2.3). The stable ^{63,65}Cu were evaporated from a filament at the same time to allow a simultaneous measurement of a reference and a radioactive isotope.

The measurement of the activity (for the radioactive isotopes) or of the beam intensity (for the stable isotopes) with respect to the frequency of the first laser yields the resonance spectrum with four components, typical of the $J = 1/2 \rightarrow 1/2$ atomic transition studied. Preliminary work with this transition on the effects of pressure is presented in section 4.2.4.

For each acquired spectrum, the hyperfine parameter of the atomic ground and first excited states are extracted[1], together with the isotope shift between the reference and radioactive isotopes. Those can also be used to discuss the spin assignment for the radioactive isotopes. The magnetic dipole moments can then be extracted relative to that of ^{63}Cu. Finally, the possibility of extracting changes in the mean-square charge radii from the isotope shifts is investigated. This work is the first on-line research that combines in-gas-cell laser spectroscopy and isotope separation on-line. It is therefore of great importance for the gas-cell-based RIB facilities (IGISOL, S^3, PALIS, LaSpec, SHIPTRAP, ...).

5.2.1 First look into the magnetic dipole moment of the neutron-deficient, even$-N$, ^{57,59}Cu isotopes

Paper V
T.E. Cocolios *et al.*, *Physical Review Letters* 103(2009)102501.

The hyperfine parameters of the atomic ground-state of ^{59,63,65}Cu, which have been extensively studied [Lut78, Sto08a, Fla09, Vin10], are found in our measurements to be in very good agreement with the previously measured values, confirming that both the technique is accurate and the precision reported is valid. Using those, the magnetic dipole moments for ^{57,59,65}Cu are extracted. ^{59,65}Cu are again in good

[1]The special case of ^{58}Cu is discussed in section 5.2.2

agreement with the previously known values [Gol04, Lut78]. The measurement of the magnetic dipole moment of ^{57}Cu is, however, very different from the literature value [Min06].

Very good agreement with the recent calculations using the GXPF1 interaction [Hon04, Sto08b], based on a $^{40}_{20}\mathrm{Ca}_{20}$ core and the full pf-shell, is found. Many other theoretical and phenomenological approaches are also discussed, like the calculations using the FDP6 interaction [Sem96], the use of mirror nuclei [Buc83] or corrections to the Schmidt moment [Tow87], also found to be in very good agreement with the new measured magnetic moment. This shows that the shell-model can perform well and predicts as well the softness of the $^{56}_{28}\mathrm{Ni}_{28}$ core and its influence on its neighbouring isotopes.

Magnetic dipole moment of ^{57,59}Cu measured by in-gas-cell laser spectroscopy

T.E. Cocolios, A.N. Andreyev, B. Bastin, N. Bree, J. Büscher, J. Elseviers, J. Gentens, M. Huyse, Yu. Kudryavtsev, D. Pauwels, P. Van den Bergh, P. Van Duppen
Instituut voor Kern- en Stralingsfysica, Katholieke Universiteit Leuven, B-3001 Leuven, Belgium

T. Sonoda
RIKEN, Wako, Saitama 305-0198, Japan

Abstract

For the first time, in-gas-cell laser spectroscopy study of the ^{57,59,63,65}Cu isotopes has been performed using the 244.164 nm optical transition from the atomic ground state of copper. The nuclear magnetic dipole moments for ^{57,59,65}Cu relative to that of ^{63}Cu have been extracted. The new value for ^{57}Cu of $\mu(^{57}Cu) = +2.582(7)\mu_N$ is in strong disagreement with the previous literature value but in good agreement with recent theoretical and systematic predictions.

Electromagnetic moments, $39 \leq A \leq 89$, Laser spectroscopy
21.10.Ky, 27.40, 27.50, 42.62.Fi

With more than 3000 nuclei known so far, the present nuclear chart offers a vast landscape to study mesoscopic systems. Many of these nuclei cannot be described by *ab initio* calculations and theory uses models based on a fundamental or phenomenological approach in order to describe observables of yet unobserved isotopes. The confrontation of experimental data with the theoretical predictions allows for fine tuning of theory and furthermore for discovering new aspects of the interactions at work in the atomic nucleus. This is especially the case when studying isotopes with extreme proton-to-neutron ratios. In nuclear structure, the identification of the magic numbers $2, 8, 20, 28, 50, 82, 126$ [92] is the foundation for the shell model of the nucleus. While these magic numbers are well established in nuclei close to the valley of β-stability, their universality is strongly questioned [93].

Of special interest is the magic number 28 as it is the smallest magic number issued from the spin-orbit interaction added to the nuclear potential. Both the $N = 28$ isotones [94, 95] and the nickel ($Z = 28$) isotopes [96, 97] are under intensive investigation to probe their magic character. With $N = Z = 28$, ^{56}Ni is expected to be doubly magic. While it displays a high 2_1^+ excited state in comparison to the other nickel isotopes [96] and a sudden change in the two-neutron and two-proton separation energies [98], both characteristic of a doubly magic nucleus, the evolution of the transition strength $B(E2)$ and the behavior of the nuclei in the vicinity point towards particle excitations across the shell gaps and a breaking of this magic core [99, 100, 101].

The nuclear magnetic dipole moment is a very sensitive tool to study the nuclear structure in the vicinity of magic nuclei. Indeed, the odd-A $_{29}$Cu isotopes can be described as a single proton coupled to an even-A $_{28}$Ni core and their magnetic dipole moment should in principle be defined by the former particle only. The copper isotopes have therefore been extensively studied [102, 103, 104, 105, 106, 107]. The magnetic moments from $N = 30$ up to $N = 40$ depart strongly from the Schmidt moment of a single proton in the $1p_{3/2}$ orbital [104]; this trend continues while approaching $N = 28$. This motivated further studies towards ^{57}Cu [105, 106]. Recent shell model calculations using the GXPF1 interaction [101, 107] give a good description of the magnetic moment of the copper isotopes from $N = 40$ to 30 but failed to reproduce the value of ^{57}Cu [105], the isotope closest to the doubly magic ^{56}Ni.

Indeed, the β-NRM measurement reported in [105], made at an in-flight facility, came as a surprise. A magnetic moment $|\mu(^{57}\text{Cu})| = 2.00(5)\mu_N$ was measured, compared to a predicted value of $2.489\mu_N$ [101, 105, 107], pointing towards a more significant shell breaking around ^{56}Ni compared to what was included in the model. Other calculations [108, 104] suggested similarly large values for $\mu(^{57}\text{Cu})$. Note however that the β-NMR resonance from which the $\mu(^{57}\text{Cu})$ is extracted (Fig. 1 in [105]) is limited to a single point and has not yet been reproduced. This called therefore for verification using a different radioactive ion beam technique, *e.g.* laser spectroscopy at an ISOL facility [106]. From an experimental point of view, this is a challenging task as the production rate of the $T_z = -1/2$ ^{57}Cu isotope is small and its half-life is short ($T_{1/2} = 199$ ms). The in-source laser spectroscopy of radioactive copper isotopes, as developed in high-temperature ISOL target ion source systems [103, 106],

is a very sensitive technique but can suffer from significant delay losses. In contrast to this, laser ionisation spectroscopy in a buffer gas cell coupled to an on-line isotope separator allows the study of short-lived isotopes [109] providing higher sensitivity and accuracy compared to the high-temperature systems thanks to the smaller total laser line width. In this letter, we report about the first successful measurement of the magnetic dipole moment of ^{57}Cu using in-gas-cell laser spectroscopy.

The experiment was performed at the Leuven Isotope Separator On-Line (LISOL) facility of the Centre de Recherche du Cyclotron (CRC), Louvain-La-Neuve (Belgium). Beams of ^{3}He (25 MeV, 2 μA) or protons (30 MeV, 2 μA) impinged on a thin natural nickel target (thickness 5 μm) placed in the LISOL dual chamber gas cell [110]. The radioactive isotopes are produced through the reactions ^{58}Ni(p,2n)^{57}Cu, ^{60}Ni(p,2n)^{59}Cu and ^{58}Ni(^{3}He,pn)^{59}Cu. The radioactive recoils are stopped and thermalised in 130 mbar of argon. Stable ^{63,65}Cu atoms are also produced by the resistive heating of a natural copper filament inside the gas cell.

The atoms are brought towards the ionization chamber of the gas cell by the gas flow where they are ionised to a Cu^{+} state using a resonant two-step two-color laser ionization process [110, 111]. The ions exit the gas cell via a 1 mm exit hole and are caught by a radio-frequency sextupole ion guide before being accelerated to an energy of 40 keV. The beam is further separated according to the isotope mass-to-charge ratio by a dipole magnet. Typical production rates are about 6 ions$\cdot s^{-1}$ for ^{57}Cu and $1.7\cdot10^{4}$ or $1.7\cdot10^{5}$ ions$\cdot s^{-1}$ for ^{59}Cu using protons or ^{3}He, respectively. While scanning the laser frequency, two beams are extracted and counted simultaneously at two different detection stations, ^{57,63}Cu or ^{59,65}Cu, respectively. After mass separation, the radioactive isotopes (^{57,59}Cu) are implanted in a tape station and counted via their respective β decay using three plastic detectors (efficiency 50% [112]) while the stable isotopes (^{63,65}Cu,) are simultaneously counted by a secondary electron multiplier placed after the collector chamber of the mass separator.

The laser spectroscopy is performed by scanning the frequency of the first step laser across the transition from the $3d^{10}4s\ ^{2}S_{1/2}$ atomic ground state to the $3d^{9}4s4p\ ^{4}P_{1/2}$ atomic excited state at 244.164 nm; the ionization scheme is shown in Fig. 5.3. The resonances are identified by counting the number of ions extracted as a function of the applied laser frequency. The interaction of the nuclear spin $I = 3/2^{-}$, for all isotopes, and the electronic total angular momentum $J = 1/2$, for both atomic levels, yields two sub-levels with quantum numbers $F = 1, 2$ for each atomic level; the resulting hyperfine structure has four components, as visible in Fig. 5.4. The electronic angular momenta $J_1, J_2 = 1/2$ restrict the sensitivity of this transition to the magnetic dipole moment. This study can therefore not extract any information on the electric quadrupole moment of the copper isotopes ground states. The large splitting in both atomic levels allows for the independent extraction of the hyperfine parameter A_{hf} for each atomic level, unlike [106] where only one parameter can be fitted.

Each of the isotopes has been measured repeatedly to ensure the reproducibility of the data. In total, 34 independent measurements are available for ^{59}Cu and ^{65}Cu, 68 for ^{57}Cu and 106 for ^{63}Cu. The hyperfine parameters extracted for every run

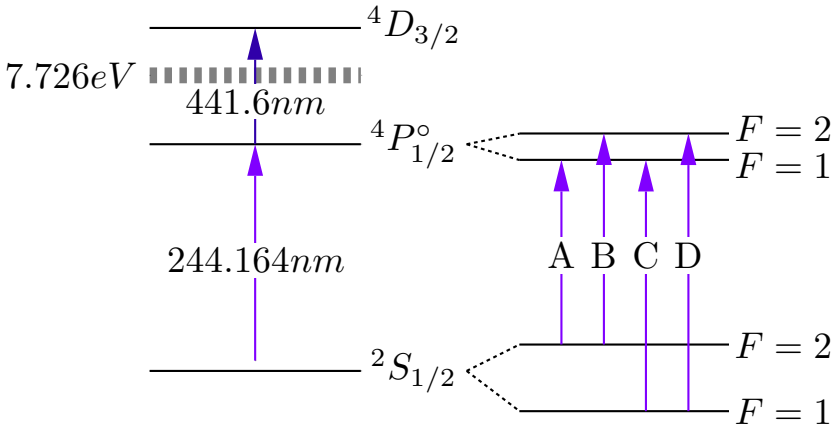

Figure 5.3: Laser ionization scheme of copper used in this work. The right part shows the hyperfine splittings and transitions. The thick dashed line is the ionization potential.

are consistent to each other and no systematic drift in these parameters has been observed, as shown in Fig. 5.5. The average value over all the measurements for each of those parameters is shown in Table 5.1. Off-line, the pressure dependence of the resonance line width and of the center of gravity position were investigated in details and are reported in [109].

The hyperfine parameters for the atomic ground state of ^{63,65}Cu are known with good accuracy [113] (see table 5.1). The results from this work, $A_{hf:gs} = 5.858(10)$ GHz and 6.288(17) GHz, respectively, are fully consistent with those. Moreover, as shown in Fig. 5.5 and as expected in the absence of hyperfine anomaly, the ratio of the two hyperfine parameters remains constant for all isotopes. A nine-fold increase in accuracy is observed for the hyperfine parameter $A_{hf:gs}$ of ^{59}Cu as given by the present in-gas-cell laser spectroscopy measurement with respect to the high-temperature in-source laser spectroscopy work [106]. This is due to the improved total resonance line width (3.5 GHz vs. 4.5 GHz), the larger separation of the hyperfine levels of the $3d^9 4s4p\ ^4P_{1/2}$ level compared to the $3d^{10}4p\ ^2P_{1/2}$ level, and the high number of independent measurements. Supported by the good agreement on the stable isotopes, the consistency of the ratio of the two hyperfine parameters and based on the precise knowledge of the magnetic moment of ^{63}Cu [114, 115], the moments of ^{57,59,65}Cu are extracted, as detailed in [106], from both atomic levels. The results are given in Table 5.1. The signs are determined based on the ordering of the peaks considering the relative intensity of the $F = 1 \rightarrow 1$ transition (labeled C), much lower with respect to the others, as seen in Fig. 5.4.

Good agreement is found with previous moment measurements of the ^{59,65}Cu isotopes. The measured moment of the lightest isotope ^{57}Cu ($\mu = +2.582(7)\mu_N$) displays, however, a major difference with the literature value ($|\mu| = 2.00(5)\mu_N$) [105]. A careful inspection of our running conditions and of our analysis has been

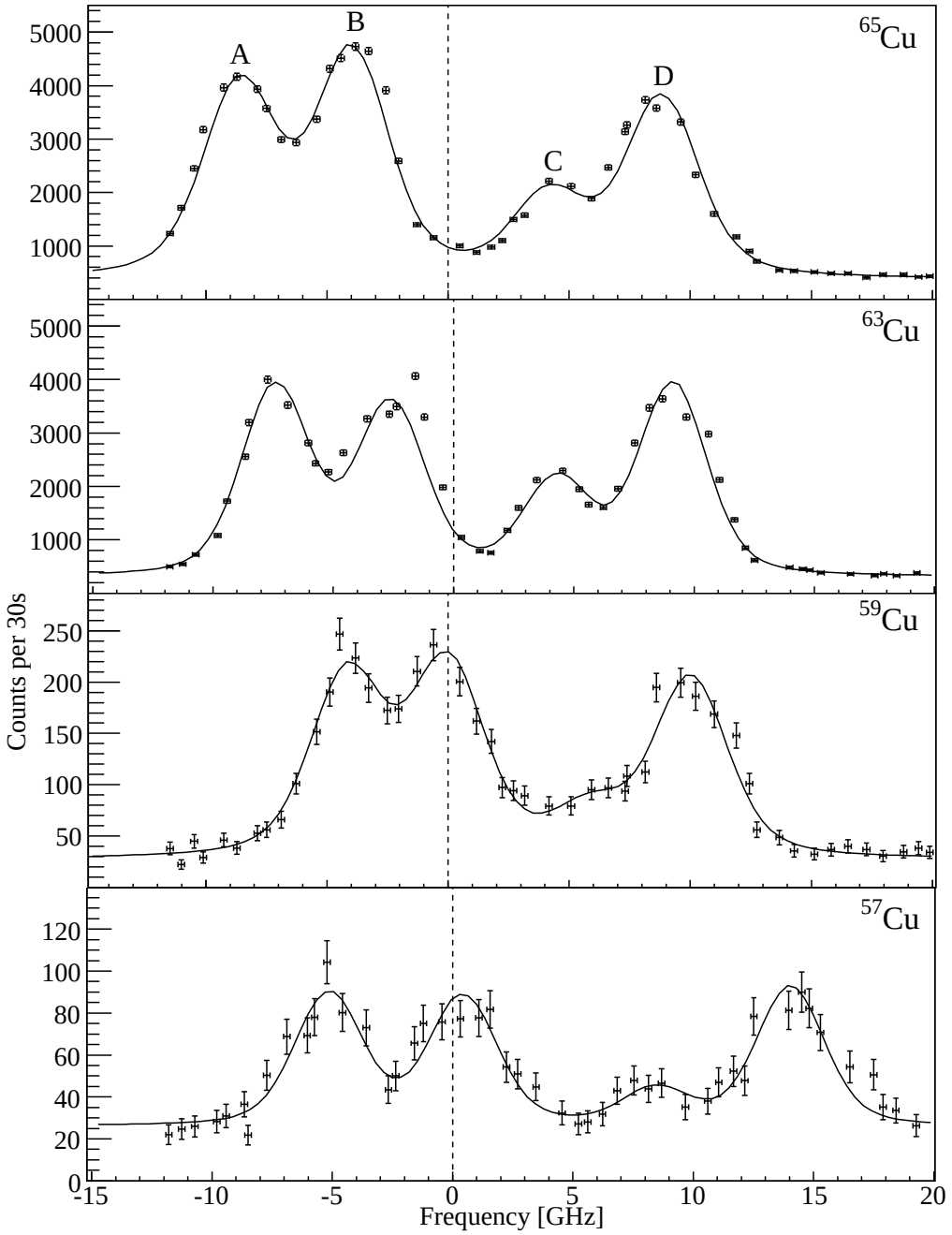

Figure 5.4: Typical examples of the single hyperfine spectra of ^{57,59,63,65}Cu. Each point is sampled for 30 seconds. ^{57}Cu and ^{63}Cu are measured simultaneously; so are ^{59}Cu and ^{65}Cu. The frequency axis is centered at the center of gravity of ^{63}Cu. The lines are the best fits of four Voigt profiles on top of a constant background, with free amplitudes for each peak, a common full width at half maximum and relative positions constrained by a linear combination of the transition center of gravity and the two hyperfine parameters.

Table 5.1: Measured hyperfine parameters $A_{hf:exp}$ for the atomic ground (gs) and excited (es) states and the deduced moments μ_{exp} using ^{63}Cu as the reference isotope. The literature values $A_{hf:lit:gs}$ [106, 113], μ_{lit} [114, 104, 115, 105] and theoretical calculations using GXPF1 [101, 107] are given for comparison; no literature is available on the atomic excited hyperfine parameter.

A	I	$A_{hf:exp:gs}$ [GHz]	$A_{hf:lit:gs}$ [GHz]	$A_{hf:exp:es}$ [GHz]	μ_{exp} [μ_N]	μ_{lit} [μ_N]	μ_{GXPF1} [μ_N]
57	$3/2^-$	6.785(15)	-	2.834(16)	+2.582(7)	2.00(5)	2.489
59	$3/2^-$	5.033(10)	4.87(9)	2.069(8)	+1.910(4)	+1.891(9)	1.886
63	$3/2^-$	5.858(10)	5.866908706(20)	2.432(8)	-	2.2273602(13)	2.251
65	$3/2^-$	6.288(17)	6.284389972(60)	2.588(15)	+2.387(7)	2.3818(3)	2.398

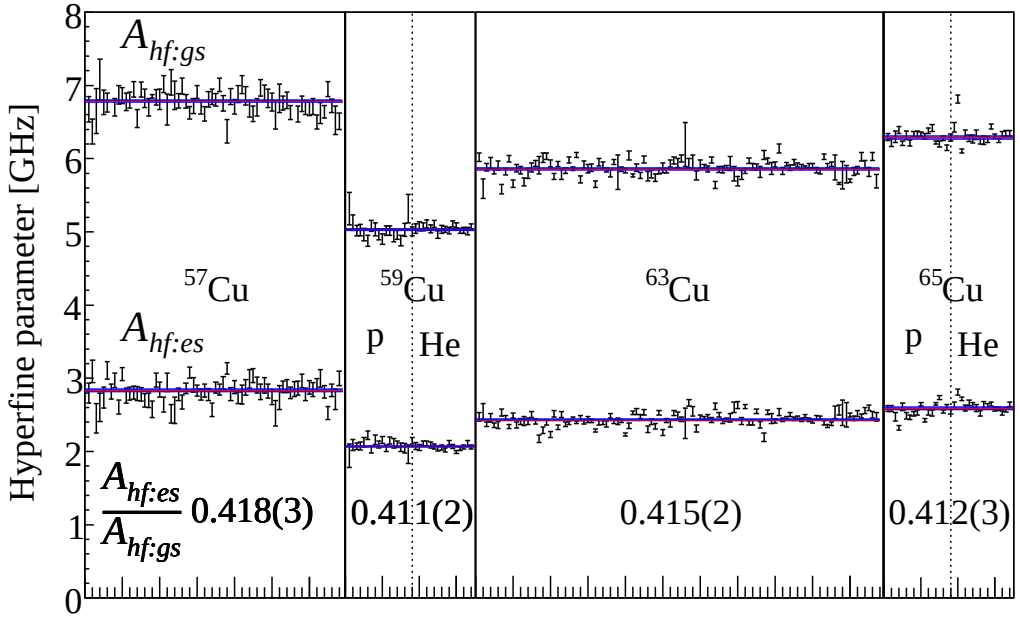

Figure 5.5: Systematic extracted hyperfine parameters A_{hf} for ^{57,59,63,65}Cu for the atomic ground state ($A_{hf:gs}$) and the atomic excited state ($A_{hf:es}$). For ^{59,65}Cu, data using both reactions are presented, identified by the primary beam used, proton (p) or ^{3}He (He) respectively. The solid lines are the averages through the points.

performed. Moreover, the systematic measurement of ^{63}Cu, the high reproducibility of the spectra, and the good agreement of each measured isotope with the established literature values confirm the accuracy of the method. The literature value in [105] is therefore questioned.

All the magnetic moments of the copper isotopes depart strongly from the Schmidt value $\mu_{Schmidt} = +3.79\mu_N$ of a single proton in a $1p_{3/2}$ orbital. In the case of the semi-magic ^{69}Cu$_{40}$ nucleus, the difference between the Schmidt moment and the experimental moment is very well reproduced by the shell-model calculation from Towner [116, 104] ($\mu = +2.87(13)\mu_N$). ^{68}Ni was taken as a closed-shell core but including effects of core polarisation, meson exchange current, Δ-isobars and relativistic corrections in perturbation theory. The same calculations for ^{57}Cu$_{28}$ using ^{56}Ni as the core give $\mu = +2.40(18)\mu_N$ and reproduce the new measured value.

Theoretical studies considering a ^{40}Ca core and the full fp-shell valence space are also in agreement with the dipole moment of ^{57}Cu as measured in this Letter, predicting a magnetic moment of $\mu = +2.48\mu_N$ using the FPD6 interaction [108] or $\mu = +2.489\mu_N$ using the GXPF1 interaction (with effective g factors $g_s^{eff} = 0.9g_s^{free}$, $g_l^{free} = 1.1$ for protons and $g_l^{free} = -0.1$ for neutrons) [101, 107]. The moments of the isotopes between $N = 28$ and $N = 40$ have also been extracted with the latter interaction and reproduce the experimental data accurately (see Fig. 5.6).

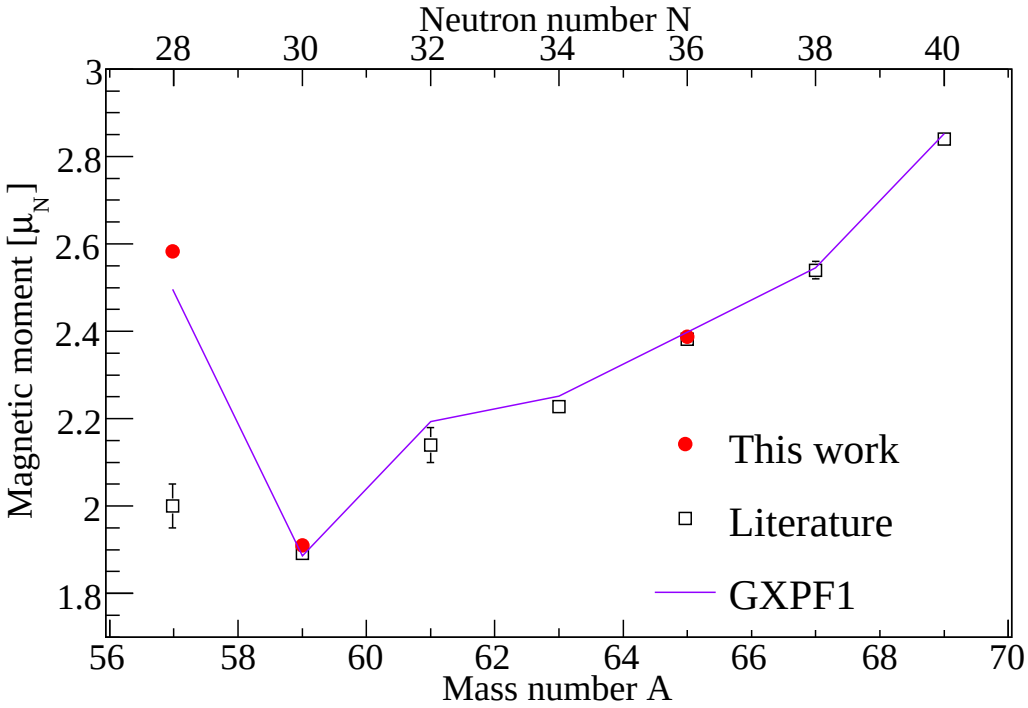

Figure 5.6: Ground state nuclear magnetic dipole moments of the odd-A copper isotopes. The full circles are the moments published in this Letter, the full squares are the experimental values from the literature [102, 104, 105, 114, 115]. Theoretical calculations using the GXPF1 interaction, a ^{40}Ca core and the full fp-shell valence space [101, 107] is shown with a solid line. The Schmidt value $\mu_{Schmidt} = +3.79\mu_N$ falls out of the range of the figure.

The new value for the magnetic dipole moment of ^{57}Cu can also be used together with the one of its mirror partner ^{57}Ni ($-0.7975(14)\mu_N$ [117]) to extract the isoscalar spin expectation value $\langle \sum \sigma_Z \rangle = 0.75(2)$ according to the formalism described in [105]. This quantity reflects the contribution from the nucleon spin to the magnetic moment. Our value is in strong disagreement with the value of $-0.78(13)$ from [105]. However, it is in reasonable agreement with the calculated values 0.71 using the FPD6 interaction [108] and 0.51 using the GXPF1 interaction [101, 105]. The departure of this value from 1 is an extra indication of a non-pure $p_{3/2}$ nuclear configuration (see Fig. 3 in [105]).

Moreover, the dipole moments of ^{57}Cu can be estimated based on its respective mirror nucleus ^{57}Ni [118, 119]. The phenomenologically deduced moment $\mu = +2.49(3)\mu_N$ is again in agreement with our measurement. The magnetic moment of ^{57}Cu and ^{57}Ni can also be combined to calculate the magnetic dipole moment of ^{58}Cu according to the additivity rule [106]. The value of $\mu = +0.595(2)\mu_N$ is in agreement with the experimental value $+0.52(8)\mu_N$ [106].

Our work brings out how well the GXPF1 interaction describes the structure near

^{56}Ni as proven by the very sensitive reproduction of the magnetic dipole moment of the chain $^{57-69}$Cu. There is indeed no need for a more significant shell breaking than introduced in [101], unlike stated previously in [105].

To conclude, we have reported the first on-line magnetic moment measurement of an exotic isotope using in-gas-cell resonant ionization laser spectroscopy coupled to a mass separator. The system is proven to be very stable, has a superior accuracy compared to high-temperature in-source laser spectroscopy due to a lower total resonance line width. Furthermore, it allows laser spectroscopy measurements of short-lived radioactive isotopes and of isotopes from refractory elements that are not possible using high-temperature target-ion source systems. This new technique opens therefore exciting possibilities for the future radioactive ion beam facilities across the world making use of the gas-cell technology (e.g. GANIL, NSCL, RIKEN).

The hyperfine parameter of the $3d^9 4s4p\ ^4P_{1/2}$ level in copper has been measured for the first time. Moreover, the known magnetic moments for ^{59}Cu and ^{65}Cu are well reproduced. The discrepancy with the β-NRM measurement of ^{57}Cu questions, however, the correctness of the value published in [105]. Finally, a good agreement of the new measurement with recent theoretical calculations and with the prediction from the mirror nucleus ^{57}Ni is found.

Besides, other isotopes displaying large hyperfine splittings are very well suited for this type of measurement. The neutron-deficient silver, indium and tin isotopes, approaching $N = 50$, are expected to possess large magnetic dipole moments. They are therefore ideal to probe this shell closure. The in-gas-cell laser spectroscopy technique can also be improved by reducing the resonance line width further, performing the laser spectroscopy in a Laser Ion Source Trap (LIST [120]) as recently shown in [109].

We thank the CRC team, Louvain-La-Neuve (Belgium). This work was supported by FWO-Vlaanderen (Belgium), GOA/2004/03 (BOF-K.U.Leuven), the 'IUAP - Belgian State - Belgian Science Policy' - (BriX network P6/23) and by the European Commission within the Sixth Framework Programme through I3-EURONS (Contract RII3-CT-2004-506065).

5.2.2 Deeper look into the magnetic dipole moment of the neutron-deficient $^{57-59}$Cu isotopes and discussion on the isotope shifts

Paper VI
T.E. Cocolios *et al.*, *Physical Review C*83(2010)014314.

This publication reports extensively on the detailed analysis of the in-gas-cell laser spectroscopy of $^{57-59,63,65}$Cu isotopes. The effects of the pressure on the hyperfine parameters and on the isotope shifts are investigated and found to be negligible due to the relative nature of those measurements, either between energy sub-levels or between isotopes under the same conditions. The drift of the wavemeter absolute frequency reading is similarly negligible. Furthermore, no effect can be attributed to the position of the second step of the ionisation scheme. Finally, the high number of repetitions of the measurement further confirms the final high precision of the measurement. The specificity of the analysis of the collapsed structure of ^{58}Cu is also discussed. A discussion on the spin assignments for the radioactive isotopes, based on the comparison to the Schmidt moments and on the number of observed transitions, yields that spins $I = 0$ for ^{58}Cu and $I = \frac{1}{2}$ for ^{57,59}Cu can be fully rejected and that $I = \frac{3}{2}$ is the most likely spin assignment for ^{57,59}Cu, hereby confirming the known spin assignments.

The magnetic dipole moment of the even-N ^{57,59,63,65}Cu are well reproduced by the calculations using the GXPF1 interaction [Hon04, Sto08b]. The agreement with the even-A ^{58}Cu is, however, poorer, as can be systematically observed for the heavier copper isotopes [Sto08a, Vin10]; the g-factors of the copper isotopes up to ^{64}Cu are compared to the empirical g-factors for a single neutron in the $\nu p_{3/2}$ or $\nu f_{5/2}$ orbital coupled to a single proton in the $\pi p_{3/2}$ orbital, using the neighbouring odd-A isotopes as single-particle moments. The new input from ^{57}Cu provides a good agreement with the other $\nu p_{3/2} \otimes \pi p_{3/2}$ empirical g-factors; the value for ^{58}Cu, although not falling directly on this value, points towards a pure $\nu p_{3/2} \otimes \pi p_{3/2}$ configuration.

The magnetic dipole moments of ^{57,58,59}Cu

T.E. Cocolios, A.N. Andreyev, B. Bastin, N. Bree, J. Büscher, J. Elseviers, J. Gentens, M. Huyse, Yu. Kudryavtsev, D. Pauwels, P. Van den Bergh, P. Van Duppen
Instituut voor Kern- en Stralingsfysica, Katholieke Universiteit Leuven, B-3001 Leuven, Belgium

T. Sonoda
RIKEN, Wako, Saitama 305-0198, Japan

Abstract

In-gas-cell laser spectroscopy of the isotopes ^{57,58,59,63,65}Cu has been performed at the LISOL facility using the 244.164-nm optical transition from the atomic ground state of copper. A detailed discussion on the hyperfine structure of ^{63}Cu is presented. The magnetic dipole moments of the isotopes ^{57,58,59,65}Cu are extracted based on that of ^{63}Cu. The new value $\mu = +0.479(13)\mu_N$ is proposed for ^{58}Cu, consistent with that of a $\pi p_{3/2} \otimes \nu p_{3/2}$ ground-state configuration. Spin assignments for the radioactive isotopes ^{57,58,59}Cu are confirmed. The isotope shifts between the different isotopes are also given and discussed.

Electromagnetic moments, $39 \leq A \leq 89$, Laser spectroscopy
21.10.Ky, 27.40, 27.50, 42.62.Fi

Introduction

Magic numbers are the cornerstones of the shell model of the nucleus. While those are well established for the stable nuclei, their persistence away from the valley of β stability is questioned. The magic number 28 is the first to arise from the addition of the spin-orbit term to the nuclear potential. This is why nuclei in the vicinity of $N = 28$ [121, 122] and of nickel ($Z = 28$) [123, 124] are under current investigation to probe the magic nature of these shell closures far from stability. With $N = Z = 28$, ^{56}Ni is expected to be doubly magic. Indeed, it presents a high excitation energy for the 2_1^+ excited state in comparison to the other nickel isotopes [123] and a sudden change in the two-neutron and two-proton separation energies [125]. However, the evolution of the $B(E2)$ does not drop as sharply as expected for a doubly magic nucleus [126]. Moreover, the properties of the neighboring nuclei cannot be explained by simply coupling particles and/or holes to the ^{56}Ni core but require excitations of this core [127, 128].

The study of the nuclear magnetic dipole moments in the vicinity of that nucleus is essential to further the understanding of the different processes at play. Of special interest is the copper isotopic chain ($Z = 29$), which consists, in the frame of the shell model, of a single proton added to the nickel core. For the odd-A copper isotopes, the magnetic dipole moment is then governed by the single proton while in the case of the even-A odd-odd copper isotopes, the coupling of the proton and a neutron should be responsible for the magnetic dipole moment. Extensive studies on the copper isotopic chain have therefore been performed [129, 130, 131, 132, 133, 134] and are still current [135, 136].

The nuclear dipole moments of the odd-A copper isotopes have been found to depart strongly from the Schmidt value +3.79 μ_N. This difference increases significantly while going from $N = 40$ down to $N = 30$ [131] but the trend breaks for the $N = 28$ isotope ^{57}Cu as it rises to a higher value, yet not sufficiently to be explained by the shell-model calculations [132]. This discrepancy pointed toward a larger breaking of the core than anticipated. This last isotope was studied using the β-NMR technique at a fragmentation facility but the resonance, seen in Fig. 1 of Ref. [132], was of limited quality. Further confirmation of this result using a different method was therefore necessary, e.g, via in-source laser spectroscopy [133]. The new result reported in Ref. [135] disagrees with the literature value and is much closer to the shell-model calculations [128, 133]. In this article, more details on the analysis of the results reported in Ref. [135] will be given, together with new data obtained for the isotope ^{58}Cu.

Using laser spectroscopy, it is possible to study the influence of the nucleus on atomic transitions by means of laser radiation. Through the interaction between the electron angular momentum and the nucleus electromagnetic moments, the degeneracy of the atomic levels can be lifted, giving rise to a new set of states, the hyperfine levels, with quantum number F such that

$$|I - J| \leq F \leq I + J, \tag{5.1}$$

where I is the nuclear spin and J is the electron angular momentum. The change in

energy ΔE of a given hyperfine level with respect to the degenerate energy level is then given by

$$\Delta E = \frac{A_{hf}}{2} \cdot K + \frac{B_{hf}}{2} \cdot \frac{3K(K+1) - 2I(I+1)2J(J+1)}{2I(2I-1)2J(2J-1)}, \tag{5.2}$$

where A_{hf} and B_{hf} are called the dipole and quadrupole hyperfine parameters, respectively, and $K = F(F+1) - I(I+1) - J(J+1)$. The magnetic dipole moment μ enters in the dipole hyperfine parameter

$$A_{hf} = \frac{\mu \cdot H_0}{IJ}. \tag{5.3}$$

H_0 is the magnetic field at the position of the nucleus generated by the electron motion. This parameter is specific to the transition studied and remains independent of the isotope. One can then measure the different transitions, deduce the hyperfine parameters and, in the absence of hyperfine anomaly, extract the moment of one isotope given that of another isotope [137]. The specific case of copper will be discussed in the section on analysis and discussion.

For the copper isotopes, high-precision in-flight laser spectroscopy has been performed down to the $N = 32$ isotope ^{61}Cu [138]. The study of the more exotic nuclei on the neutron-deficient side requires higher sensitivity to cope with the reduced beam intensities. In-source spectroscopy is ideally suited for this type of sensitive measurement [139]. The hot cavity target and ion source, however, can suffer from large decay losses due to the diffusion and effusion processes from the target to the atomizer [140]. As a consequence, the short-lived $T_{1/2} = 199$ ms isotope ^{57}Cu is presently beyond reach of the hot-target facilities [133].

Gas catchers, on the other hand, suffer less from such limitations as the nuclear reaction products recoil directly out of the target and can be used for laser spectroscopy studies [141]. We report here on such study on the stable isotopes ^{63,65}Cu and on the neutron-deficient isotopes ^{57,58,59}Cu. We detail the systematic study of the stable ^{63}Cu, which was used to assert the reliability of the in-gas-cell laser spectroscopy technique, used for the first time at an on-line mass separator. The hyperfine structure of the odd-A isotopes ^{57,59,63,65}Cu as well as that of ^{58}Cu are analysed and presented. The magnetic dipole moments are extracted and that of ^{58}Cu is discussed. The spin assignments for those isotopes are confirmed. Finally, the isotope shifts are extracted and the possibility of determining changes in the mean-square charge radius is discussed.

Experimental details

Production and spectroscopy The experiment was performed online at the Leuven Isotope Separator On-Line (LISOL) facility in the Centre de Recherche du Cyclotron (Cyclotron Research Center, CRC), Louvain-La-Neuve (Belgium). The CYCLONE110 cyclotron provided beams of ^{3}He (25 MeV, 2 μA) and protons (30 MeV, 2 μA). Those beams impinged on a thin (thickness 5 μm) natural nickel target

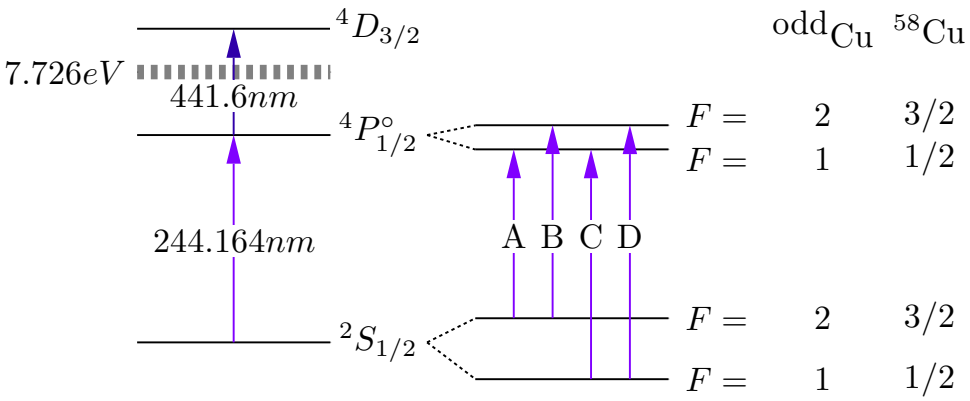

Figure 5.7: Laser ionization scheme of copper used in this work. The right part shows the hyperfine splittings and transitions. The thick dashed line is the ionization potential. The labels A,B,C,D will be used to label the different transitions in Figs. 5.8 and 5.12.

(68% ^{58}Ni, 26% ^{60}Ni). The isotopes of interest are produced in the dual chamber laser ion source [142]. The radioactive isotopes $^{57-59}$Cu are produced from the nuclear reactions ^{58}Ni$(p,2n)^{57}$Cu, ^{58}Ni$(p,n)^{58}$Cu, ^{60}Ni$(p,3n)^{58}$Cu, ^{60}Ni$(p,2n)^{59}$Cu and ^{58}Ni(^{3}He,pn)^{59}Cu. Finally, the stable isotopes ^{63,65}Cu are produced from the resistive heating of a natural copper filament.

The recoils are thermalized and neutralized in 130 mbar of argon. The atoms are transported from the stopping chamber to the ionization chamber by the gas flow. In the latter volume, they are irradiated by laser light to be ionized to a Cu^+ state in a two-step two-color resonant process [142, 143] shown in Fig. 5.7. One of the valence electrons is brought from the $3d^{10}4s\ ^2S_{1/2}$ ground state to the $3d^9 4s4p\ ^4P^\circ_{1/2}$ excited state at 40943.73 cm^{-1} via a transition at 244.164 nm; this electron is further excited to the $3d^9 4s5s\ ^4D_{3/2}$ autoionizing state at 63584.57 cm^{-1} beyond the ionization potential.

The ions leave the gas cell through a 1-mm exit hole in the supersonic jet made by the argon buffer gas. They are caught by the pseudopotential of a radiofrequency sextupole ion guide, accelerated to an energy of 40 keV and finally separated according to their mass-to-charge ratio in a dipole magnet.

The stable isotopes ^{63,65}Cu are counted in a secondary electron multiplier placed after the collector chamber of the mass separator. The radioactive isotopes $^{57-59}$Cu are implanted on a mylar tape and counted via their respective β decay using three plastic detectors (efficiency 50% [144]). The mylar tape is frequently moved to remove the longer-lived activity and present a fresh sample for further measurement. A feature of the dipole magnet is to allow the simultaneous detection of multiple beams. During the online study of the radioactive nuclei, a stable isotope ion beam is measured at the same time to monitor the behavior of the ion source and to minimize systematic effects; ^{63}Cu was used as a reference for ^{57,58}Cu while ^{65}Cu was used

for ^{59}Cu.

The laser system has been thoroughly described in Ref. [145]. It consists of two tuneable dye lasers pumped by two XeCl excimer lasers. The maximum repetition rate is 200 Hz. The first step dye laser is frequency doubled to reach the UV transition at 244.164 nm. The energy reached per pulse for this transition is 100 μJ; the energy reached per pulse for the second step is 1 mJ. The laser spectroscopy is performed by scanning the laser frequency of the first step of the ionization process from the $^2S_{1/2}$ state to the $^4P^\circ_{1/2}$ state across a range of 35 GHz and by observing the number of ions produced as a function of the applied frequency. The linewidth of this laser is minimized by using an etalon in the oscillator. A FWHM of $\Delta \approx 1.6$ GHz is reached for the second harmonic UV beam. The laser frequency at each step is recorded with a Lambdameter LM-007. Typical resonance spectra can be seen in Fig. 5.8.

Systematic study of ^{63}Cu In order to assert the reliability of the in-gas-cell laser spectroscopy technique, used for the first time at an online mass separator, several effects have been systematically studied. In this section, we report on our findings regarding the effect of the gas cell pressure, the influence of the ionization transition and the systematic fluctuations of the wavemeter. It is concluded that no systematic uncertainties have to be added by any of these effects. The fluctuations in the relative intensities of each component is also discussed.

Pressure effects A systematic study of the effects of the pressure on the laser spectra has been performed. The gas cell pressure is the main source of broadening of the line, as discussed in Ref. [141]. A pressure broadening of 5.4 MHz·mbar^{-1} has been measured, as well as an overal pressure shift of -1.9 MHz·mbar^{-1}. The hyperfine structure of ^{63}Cu was measured at different pressures ranging from 60 to 250 mbar. The extracted hyperfine parameter for the atomic ground state is shown as a function of the pressure in Fig. 5.9. No influence of the pressure can be seen on this parameter. All the peaks are therefore shifted by a similar amount. A similar effect is expected on the isotope shift between two isotopes.

Influence of the ionization transition Laser scanning of the ionization transition has been performed from each hyperfine sub-level of the atomic excited state by setting the first-transition laser to excite the valence electron into either the $F = 1$ or the $F = 2$ level. The scans of the ionizing transition are shown in Fig. 5.10.

The resonance spectrum to the autoionizing level is the same for both hyperfine levels. Its width is above 150 GHz and therefore covers the large splitting (20 GHz) of the excited state completely in spite of the smaller laser bandwidth (5 GHz). The position of the maximum is the same for both cases within our accuracy and no systematic effect can be attributed to the ionizing transition. Finally, hyperfine spectra of ^{63}Cu were acquired at different frequencies for the ionizing transition. No changes in the structure could be observed.

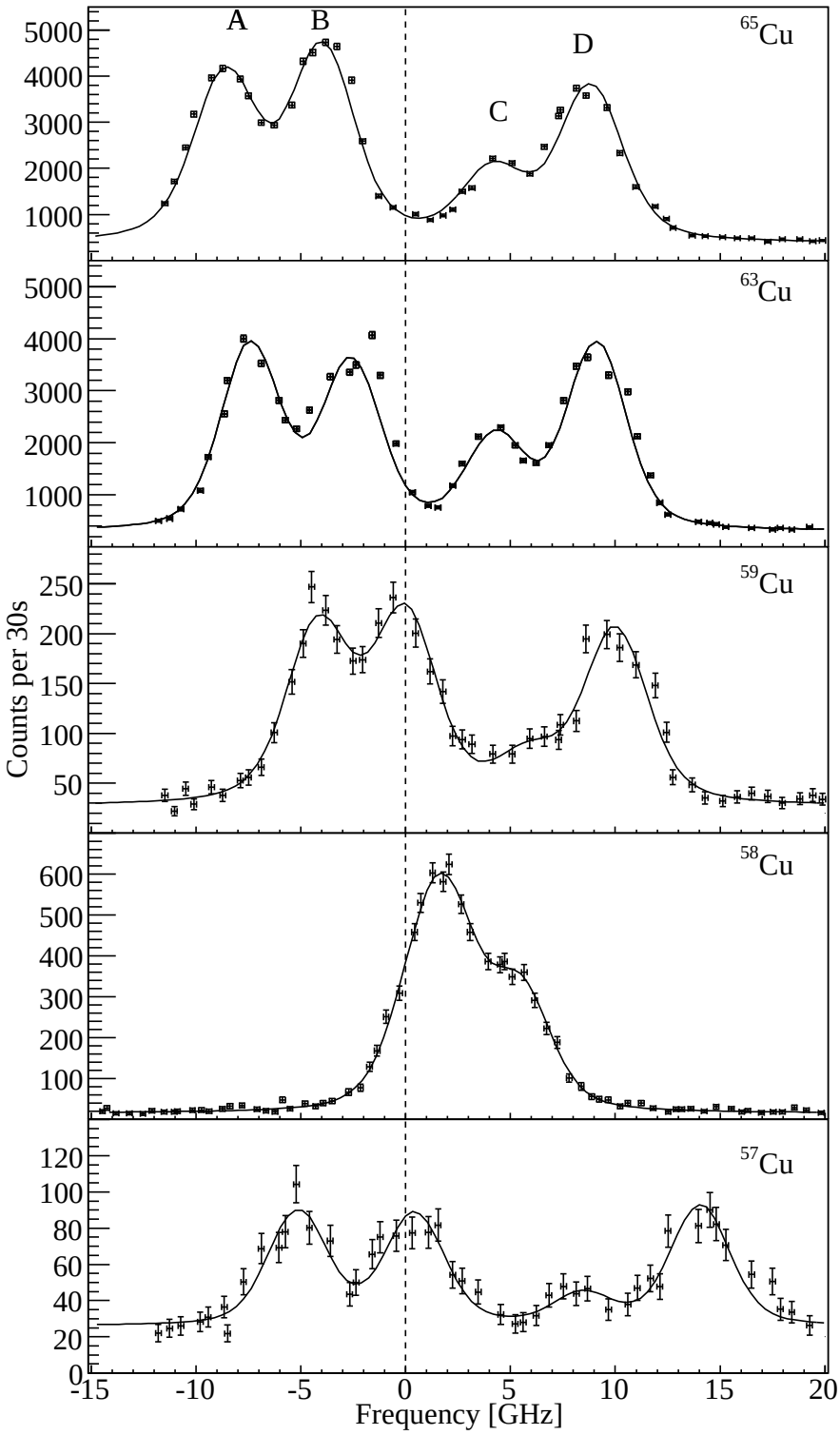

Figure 5.8: Typical examples of the single hyperfine spectra of ^{57,58,59,63,65}Cu (bottom to top). Each point is sampled for 30 seconds. ^{57}Cu and ^{63}Cu are measured simultaneously; so are ^{58}Cu and ^{63}Cu or ^{59}Cu and ^{65}Cu. The frequency axis is centered at the center of gravity of ^{63}Cu. A,B,C,D are labels for each hyperfine transition as described in Fig. 5.7

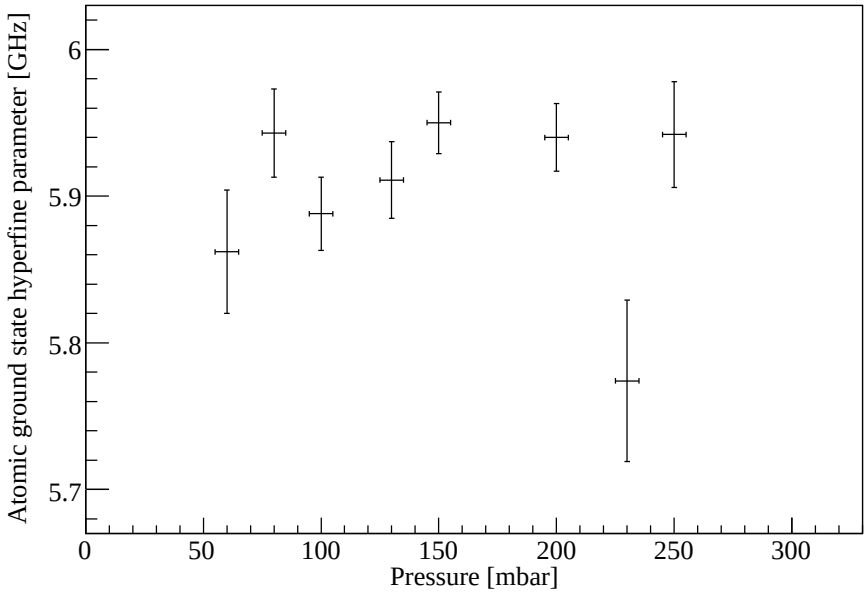

Figure 5.9: Effect of the pressure on the hyperfine parameter $A_{hs:gs}$ of the atomic ground state of ^{63}Cu.

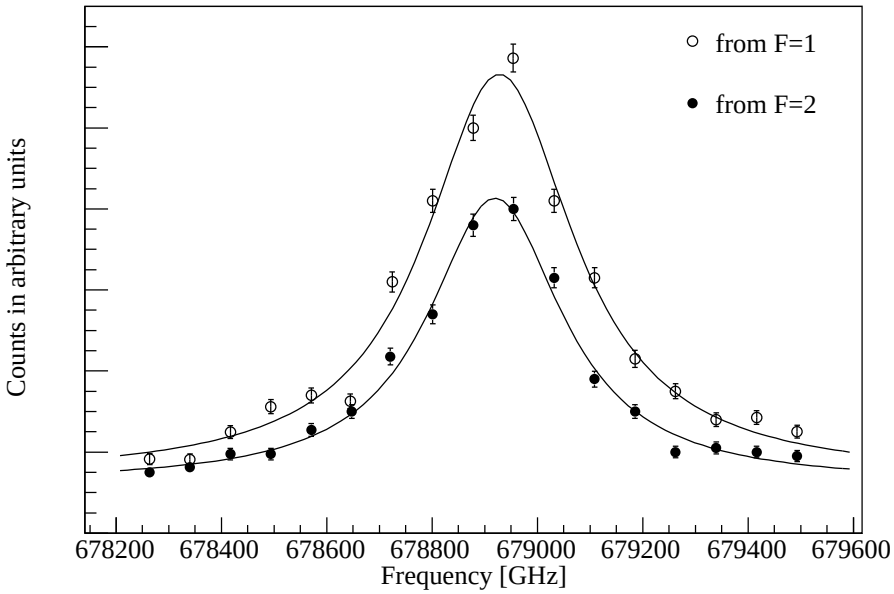

Figure 5.10: Spectroscopy of the ionization transition in ^{63}Cu while populating either the $F = 1$ (open circles) or the $F = 2$ (full circles) hyperfine level of the intermediate excited state.

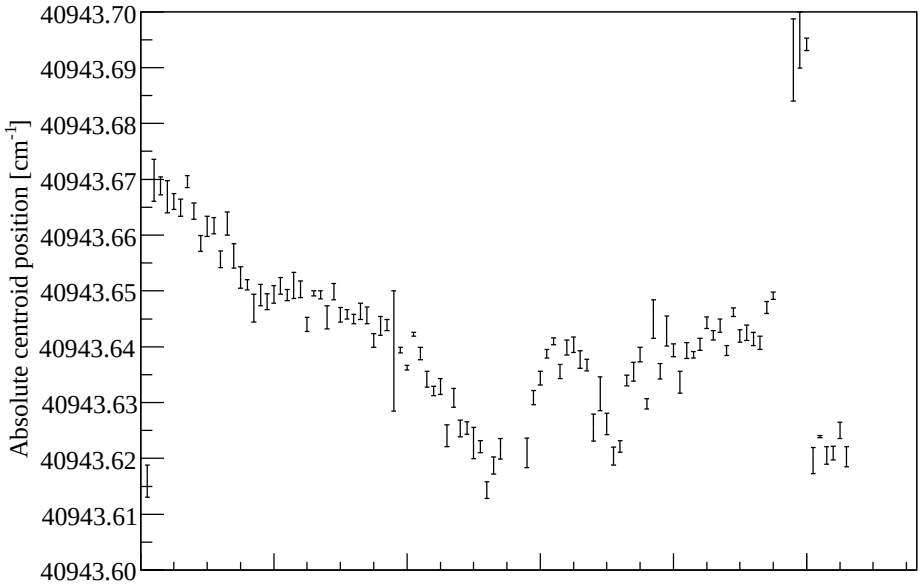

Figure 5.11: Evolution of the center of gravity of ^{63}Cu in the course of the experiment. The x axis represents the consequent order of the different runs, spanning a time of 7 days.

Systematic fluctuations The online experiment was performed over a period of seven days. Many beam and environmental parameters fluctuate on an hourly or daily basis, possibly affecting the result. It was not possible to monitor all of those parameters and only cumulative effects can be seen on the spectra.

First, the absolute laser frequency is measured for each step. The analysis of the hyperfine spectra returns therefore the absolute transition frequency. Fig. 5.11 shows the evolution of that absolute transition frequency for ^{63}Cu in the course of the experiment. Fluctuations of up to 1 GHz per day have been observed. The fluctuations are, however, occuring over a time scale much larger than the scan time and the reading is considered accurate within a single scan. This drift is due to thermal expansion of mechanical pieces in the laser laboratory as the temperature of this room changes. Note, however, that the hyperfine parameter is extracted from the difference in the position of the different peaks, which is independent of the absolute peak position. Similarly, the isotope shift between any two isotopes is the difference in absolute frequency and this systematic shift cancels out in the analysis.

Large fluctuations of the relative intensities of the hyperfine peaks have also been observed, as shown in Fig. 5.12. As a consequence, the relative intensities cannot be relied on for the determination of nuclear spins. The relative intensity of the different components in in-source laser ionization spectroscopy has been described thoroughly in Ref. [146]. The lack of information on the ionizing transition used in this experi-

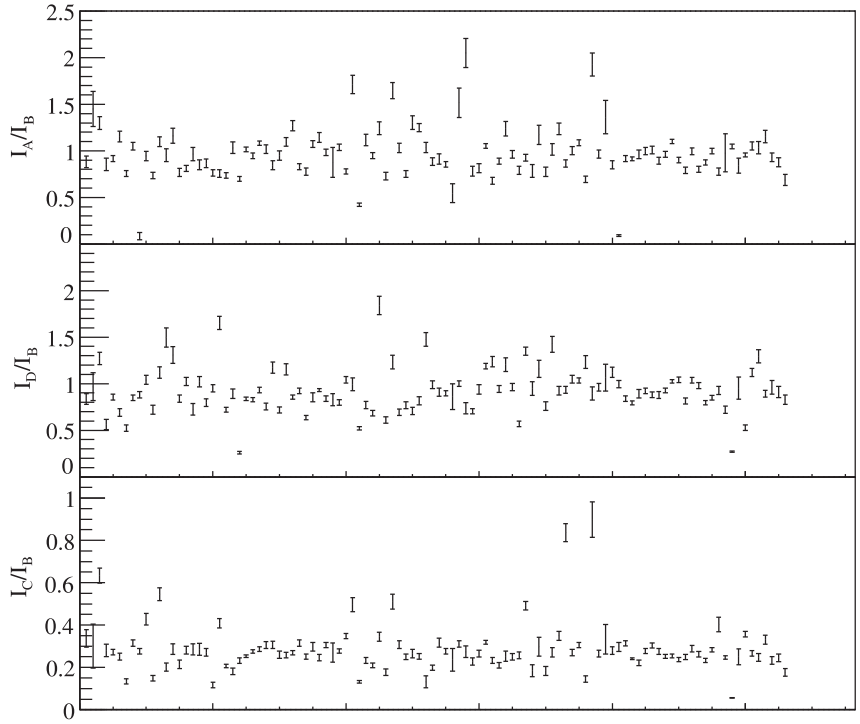

Figure 5.12: Evolution of the relative intensity of the C (bottom), D (middle) and A (top) transitions of the hyperfine spectrum of ^{63}Cu with respect to the B transition in the course of the experiment. The labels are given according to Fig. 5.7 The x axis represents the consequent order of the different runs, spanning a time of 7 days.

ment does not allow for the full calculation to be performed. Moreover, fluctuations of the gas pressure and of the chamber temperature can affect the population distribution. Nevertheless, the peak labeled C in Fig. 5.8 is systematically smaller than the other three and can therefore be attributed to the $F = 1 \rightarrow 1$ transition. Based on this, one can still determine the sign of the hyperfine parameters and, hence, that of the moments.

Analysis and Discussion

Odd-A isotopes

Data analysis The laser spectroscopy is performed on a $J = \frac{1}{2} \rightarrow \frac{1}{2}$ atomic transition. With the chosen transition, for any nuclear spin $I > \frac{1}{2}$, four transitions are expected. If $I = 0$, no hyperfine structure can be seen; if $I = \frac{1}{2}$, only three transitions can occur as $F = 0 \rightarrow 0$ is a forbidden transition. The appearance of four peaks in the hyperfine spectra of ^{57,59,63,65}Cu is a confirmation that the spin of those odd-A isotopes is at least $\frac{3}{2}$. For the rest of the work, the known spin $I = \frac{3}{2}$

for ^{57,59,63,65}Cu is used.

As seen in eq. 5.2, if either $I = \frac{1}{2}$ or $J = \frac{1}{2}$, the scaling factor in front of the hyperfine parameter B diverges and no quadrupole moment can be measured. Thus, the study can only give information on the magnetic dipole moment μ. The position of each peak (ν_i) is then given by a linear combination of the center of gravity of the transition, ν_0, and the hyperfine parameters of the atomic ground state, $A_{hf:gs}$, and the excited state, $A_{hf:es}$:

$$\nu_i = \nu_0 + \frac{A_{hf:es}}{2} \cdot K_{i:es} - \frac{A_{hf:gs}}{2} \cdot K_{i:gs}, \tag{5.4}$$

where $K_i = -\frac{5}{2}$ or $K_i = \frac{3}{2}$, depending on the hyperfine levels. The position of the four peaks is therefore defined by three parameters only.

In each run, two isotopes are always measured in parallel, namely ^{57,63}Cu or ^{59,65}Cu. For each run, the line shape, thoroughly described in Ref. [141], is determined from the stable spectrum and applied to the radioactive isotope. The typical line width is 3.5 GHz. As mentioned previously, the relative intensities cannot be relied on and the amplitude of each component is left unconstrained.

During the experiment, 106 independent measurements have been performed on ^{63}Cu, 68 on ^{57}Cu and 34 on ^{59,65}Cu. The extracted hyperfine parameters $A_{hf:gs}$ and $A_{hf:es}$ for the atomic ground and excited states, respectively, are shown in Fig. 5.13. As discussed in the study of ^{63}Cu, the hyperfine parameters do not suffer from any drift and accurate averages can be extracted. The averages are given in Ref. [135] and in Table 5.2.

The correlation between the hyperfine parameters of each atomic level for a given isotope is also investigated. This investigation is shown in Fig. 5.14. The two hyperfine parameters for each isotope are distributed in a circular scatter and are not correlated in the data analysis. They therefore offer two independent measurements of the magnetic dipole moment. The ratio of the two parameters, represented by the line accross Fig. 5.14 and given in Table 5.2, are constant from one isotope to the next, as expected in the absence of hyperfine anomaly. Indeed, this effect is expected to be too small to be observed with the limited resolution of the in-source technique [150]. The average of the ratio is 0.414(2).

Magnetic dipole moments Based on eq. 5.3, the magnetic dipole moments are extracted for each atomic level separately, relative to ^{63}Cu, according to the following

$$\mu = \mu_{63} \cdot \frac{A_{hf}}{A_{hf:63}} \cdot \frac{I}{I_{63}}. \tag{5.5}$$

The calculated moments are then averaged within each isotope for the two atomic levels. The results, using a spin $I = \frac{3}{2}$ for each isotope, are given in Table 5.2. A spin assignment $I = \frac{5}{2}$ for ^{57,59}Cu has also been investigated and yielded unphysical moments, larger than the Schmidt limit. This further confirms the spin assignment $I = \frac{3}{2}$.

Table 5.2: Measured hyperfine parameters $A_{hf:exp}$ for the atomic ground (gs) and excited (es) states (except for ^{58}Cu), their ratio, and the deduced moments μ_{exp} using ^{63}Cu as the reference isotope. The literature values $A_{hf:lit:gs}$ [133, 147], μ_{lit} [148, 131, 149, 132] and theoretical calculations using GXPF1 [128, 134] are given for comparison; the atomic excited hyperfine parameter has no prior measurement.

A	I	$A_{hf:exp:gs}$ [GHz]	$A_{hf:lit:gs}$ [GHz]	$A_{hf:exp:es}$ [GHz]	$\frac{A_{hf:exp:es}}{A_{hf:exp:gs}}$	μ_{exp} [μ_N]	μ_{lit} [μ_N]	μ_{GXPF1} [μ_N]
57	$3/2^-$	6.785(15)		2.834(16)	0.418(3)	+2.582(7)	2.00(5)	2.489
58	1^+	1.891(52)	2.11(57)			+0.479(13)	+0.52(8)	0.600
59	$3/2^-$	5.033(10)	4.87(9)	2.069(8)	0.411(2)	+1.910(4)	+1.891(9)	1.886
63	$3/2^-$	5.858(10)	5.866908706(20)	2.432(8)	0.415(2)		2.2273602(13)	2.251
65	$3/2^-$	6.288(17)	6.284389972(60)	2.588(15)	0.412(3)	+2.387(7)	2.3818(3)	2.398

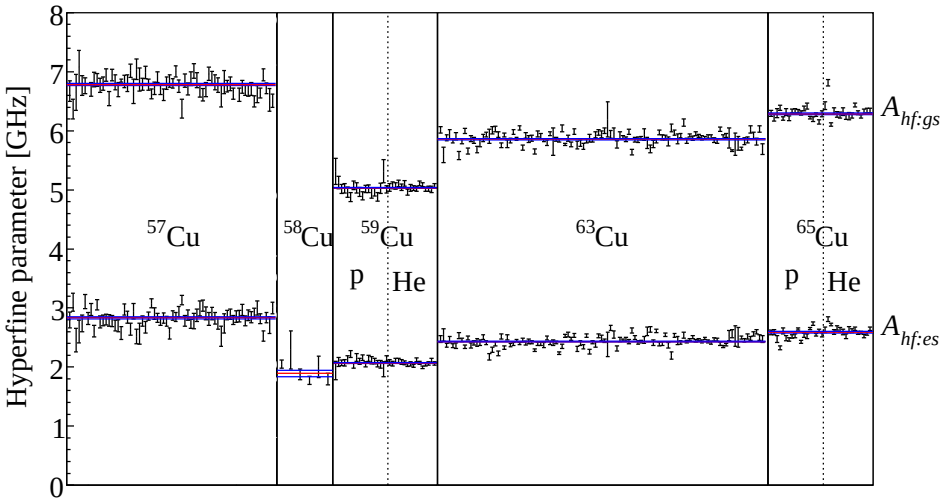

Figure 5.13: Systematic extracted hyperfine parameters A_{hf} of ^{57,58,59,63,65}Cu for the atomic ground state ($A_{hf:gs}$) and of ^{57,59,63,65}Cu for the atomic excited state ($A_{hf:es}$). In the case of ^{59,65}Cu, data using both reactions are presented, identified by the primary beam used, proton (p) or ^{3}He (He) respectively. The x axis represents the succession of experimental runs. The solid lines are the averages through the points.

The implication of the measurement of those dipole moments has been discussed in Ref. [135]. The measured dipole moments for ^{59,65}Cu are in good agreement with the previous measurements while that of ^{57}Cu ($\mu = +2.582(7)\mu_N$) is in disagreement with that presented in Ref. [132] ($\mu = 2.00(5)\mu_N$). Since our measurement has been repeated many times and since the systematic effects have been thoroughly investigated, the result in Ref. [132] is strongly questioned. Finally, the magnetic moments of the neutron-deficient copper isotopes are very well reproduced by the shell-model calculation using the FPD6 interaction [151] or the GXPF1 interaction [128, 134].

Odd-odd isotope ^{58}Cu

Data analysis Six measurements of the hyperfine structure of ^{58}Cu have been performed. Due to its small magnetic dipole moment, the hyperfine structure of ^{58}Cu is collapsed. A structure can, however, be seen, confirming that the spin is not 0. A spin $I = 1$ is used. The four peaks cannot be resolved, unlike in the case of the odd-A isotopes (see Fig. 5.8). Further constraints are therefore required in order to fit the hyperfine spectrum properly, for example, using a similar approach to that described in Ref. [133].

In order to reduce the number of free parameters, the ratio of the two hyperfine

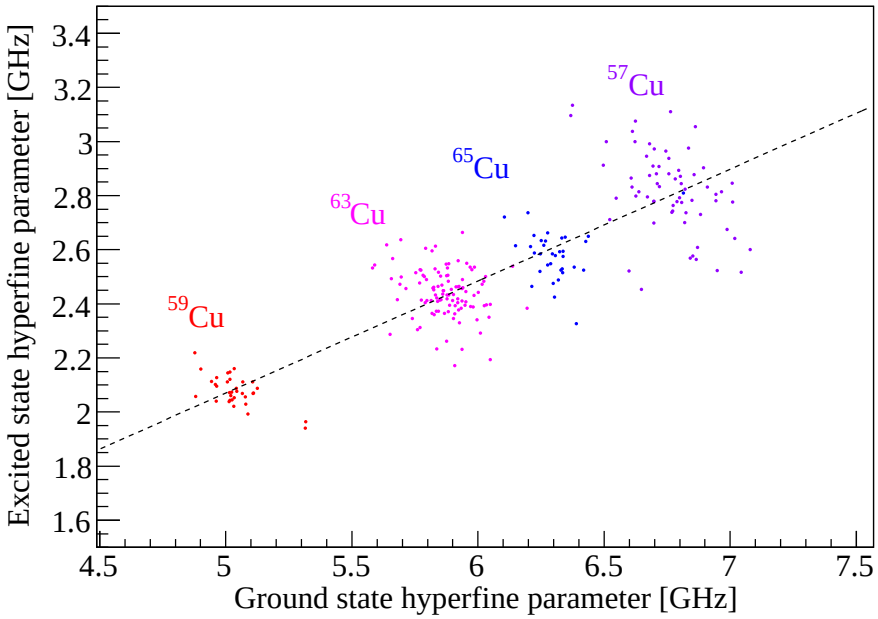

Figure 5.14: Distribution of the atomic excited state hyperfine parameter $A_{hf:es}$ as a function of that of the atomic ground state $A_{hf:gs}$ for ^{57,59,63,65}Cu. The dotted line is the average of the ratio over the four isotopes.

parameters is used:

$$A_{hf:es} = 0.414 \cdot A_{hf:gs}. \tag{5.6}$$

As a result, only one parameter can be extracted from the analysis of the hyperfine spectrum and the precision on the determination of the magnetic dipole moment is less than in the odd-A case.

The difference with the work from Ref. [133] is that the calculated relative intensities cannot be relied on, as discussed before on ^{63}Cu. The only limit is that no peak can disappear totally from the hyperfine spectrum.

The spectra are then fitted similarly to those of ^{57}Cu, using four Voigt profiles with the line-shape parameters from ^{63}Cu, for which the position is determined by combining equations 5.4 and 5.6. The systematic extracted values are shown in Fig. 5.13. The average is given in Table 5.2. In spite of the limited resolution, the hyperfine parameter of the atomic ground state is found to be $A_{hf:gs} = +1.891(52)$ GHz, in agreement with the hot cavity result 2.11(57) GHz but with 10 times higher precision.

Magnetic dipole moment Similarly to the odd-A copper isotopes, the magnetic dipole moment of ^{58}Cu can be extracted based on that of ^{63}Cu. Using $I = 1$ for ^{58}Cu, a magnetic dipole moment $\mu(^{58}\text{Cu}) = +0.479(13)\ \mu_N$ is found. It is in reasonable agreement with the shell-model calculation using the GXPF1 interaction 0.60 μ_N [128, 133] and with the Schmidt value +0.627 μ_N. The latter can be understood as the large discrepancy between the Schmidt value for the single proton ($\mu_S(\pi p_{3/2}) = +3.79\mu_N$, $\mu(^{57}\text{Cu}) = +2.582(7)\mu_N$) and for the single neutron ($\mu_S(\nu p_{3/2}) = -1.913\mu_N$, $\mu(^{57}\text{Ni}) = -0.7975(14)\mu_N$ [152]) cancel out.

The empirical moment can be calculated from the additivity of the g factors of ^{57}Ni (g_{Ni}) and ^{57}Cu (g_{Cu}) as [153]

$$\mu(^{58}\text{Cu}) = I_{58} \cdot \Big(\frac{g_{\text{Cu}} + g_{\text{Ni}}}{2} + \frac{g_{\text{Cu}} - g_{\text{Ni}}}{2} \times \frac{I_{\text{Cu}}(I_{\text{Cu}}+1) - I_{\text{Ni}}(I_{\text{Ni}}+1)}{I_{58}(I_{58}+1)}\Big). \tag{5.7}$$

This equation can be greatly simplified since $I_{\text{Cu}} = I_{\text{Ni}} = I_{57} = \frac{3}{2}$. It becomes

$$\mu(^{58}\text{Cu}) = \frac{I_{58}}{I_{57}} \cdot \frac{\mu(^{57}\text{Cu}) + \mu(^{57}\text{Ni})}{2}, \tag{5.8}$$

where $\mu(^{57}\text{Cu}) = +2.582(7)\ \mu_N$ and $\mu(^{57}\text{Ni}) = -0.7975(14)\ \mu_n$ [152]. It gives a value of $+0.595(2)\ \mu_N$, also in reasonable agreement with our result.

Moreover, if one looks at the systematic of the g factors of the 1^+ and 2^+ states in the even-A copper isotopic chain, it can be seen that the additivity rule gives a qualitative indication of the purity of the proton-neutron configuration. Fig. 5.15 compares the experimental g factors of the 1^+ and 2^+ neutron-deficient odd-odd copper isotopes to the empirical values. From this comparison, one can conclude that the $\pi p_{3/2} \otimes \nu p_{3/2}$ configuration dominates in the ground state of ^{58,60}Cu while it is the $\pi p_{3/2} \otimes \nu f_{5/2}$ configuration that dominates in the ground state of ^{62,64}Cu.

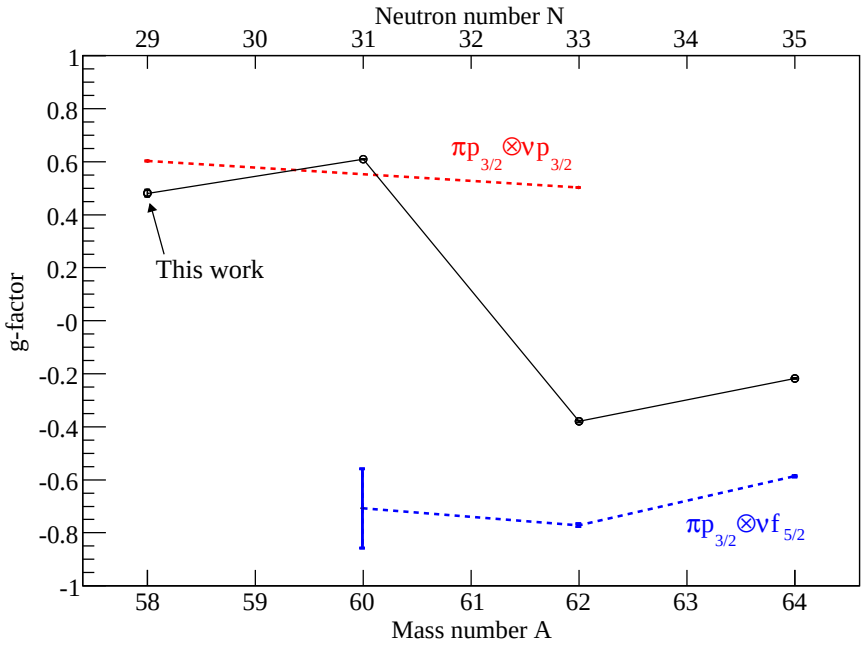

Figure 5.15: Systematic g factors of the $1^+, 2^+$ state in odd-odd neutron-deficient copper isotopes. The colored dashed lines show the empirical g factors based on the additivity rule using the neighboring nickel (or zinc) and copper isotopes [149].

Table 5.3: Isotope shift in GHz of the copper isotopes using the $3d^{10}4s\ ^2S_{1/2}$ to $3d^9 4s4p\ ^4P^\circ_{1/2}$ transition at 224.164 nm.

$^{57-63}$Cu	$^{58-63}$Cu	$^{59-65}$Cu	$^{63-65}$Cu
3.449(20)	3.137(180)	3.206(17)	0.977(21)

Isotope shifts Since two isotopes are always measured in parallel, the isotope shift can be extracted in each run free from the systematic drift discussed in the analysis of ^{63}Cu. The isotope shift is taken as the difference between the center of gravity of each hyperfine structure, extracted as described above. In that way, the isotope shift in the couples $^{57-63}$Cu, $^{58-63}$Cu and $^{59-65}$Cu are extracted. In the case of $^{63-65}$Cu, an extrapolation of the drift of the center of gravity in ^{63}Cu is necessary. The drift is assumed to be linear in time in the course of the measurement of ^{65}Cu. Similarly to the hyperfine parameters, the isotope shift extracted for each run are shown in Fig. 5.16. The average values are given in Table 5.3 and shown in Fig. 5.17.

The isotope shifts between the four heaviest isotopes ^{58,59,63,65}Cu have been measured previously using a different transition ($3d^{10}4s\ ^2S_{1/2}$ to $3d^{10}4p\ ^2P_{1/2}$ at 327.4 nm [154, 133]), allowing a comparison of the two transitions following the method of King [155]. The King plot is, however not conclusive, due to the large contribution

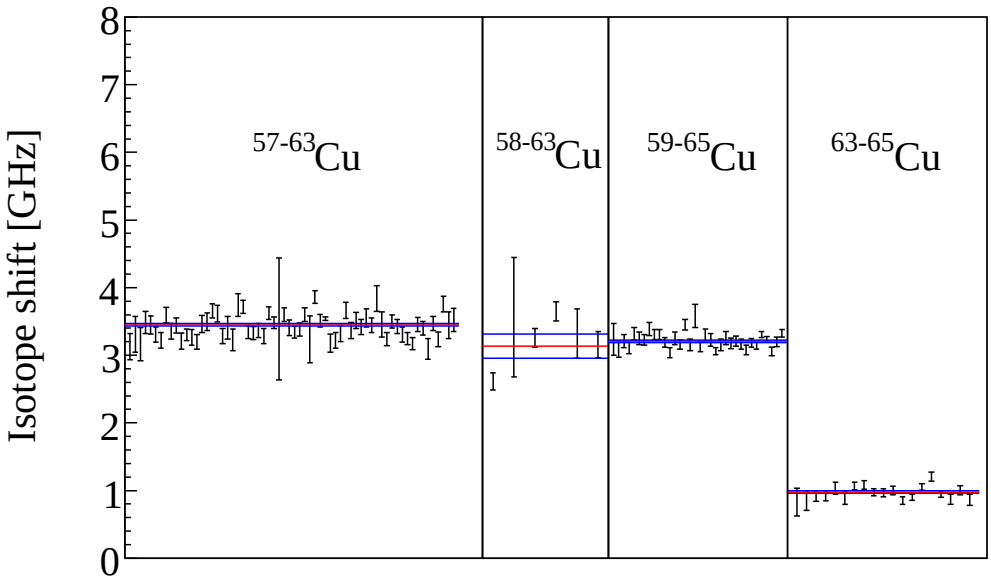

Figure 5.16: Systematic extracted isotope shift for the couples $^{57-63}$Cu, $^{58-63}$Cu, $^{59-65}$Cu and $^{63-65}$Cu. The x axis represents the succession of experimental runs. The solid lines are the averages through the points.

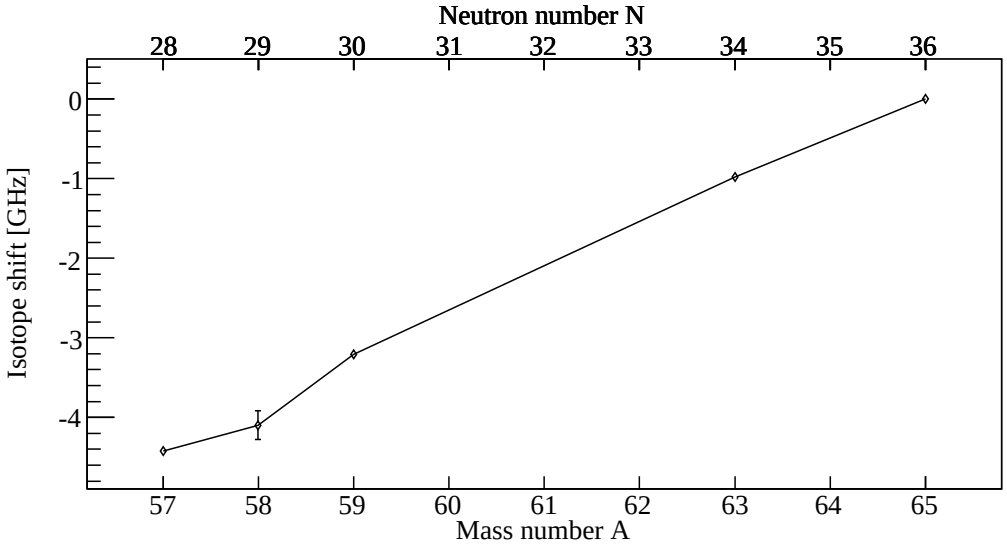

Figure 5.17: Evolution of the isotope shift of copper in this work using the $3d^{10}4s\ ^2S_{1/2}$ to $3d^9 4s4p\ ^4P^\circ_{1/2}$ transition at 224.164 nm from $A = 57$ to $A = 65$.

from the mass shift in the mass region of interest and the limited resolution of the in-source spectroscopy work, both here and in the work from Ref. [133]. No changes in the mean-square charge radius of copper can therefore be extracted.

Conclusion

In-gas-cell resonant ionization laser spectroscopy has been performed for the first time at an online mass separator facility. The hyperfine structure of ^{57,58,59,63,65}Cu has been measured using for the first time the $^2S_{1/2}$ to $^4P^\circ_{1/2}$ transition at 224.164 nm. A systematic study of this transition on ^{63}Cu has shown that all systematic effects that can be attributed to the experimental setup cancel out in the data analysis. The magnetic dipole hyperfine parameter of the $3d^9 4s4p\ ^4P^\circ_{1/2}$ state has been measured for the first time in ^{57,59,63,65}Cu and its ratio to the ground-state magnetic dipole hyperfine parameter is 0.414(2). This is also the first laser spectroscopy measurement of the semimagic $N = 28$ isotope ^{57}Cu.

The magnetic dipole moments of ^{57,58,59,65}Cu are extracted based on that of ^{63}Cu. A new value of +2.582(7) μ_N is found for ^{57}Cu, in large disagreement with the previous literature value but in reasonable agreement with the shell-model calculations. A new value of +0.479(13) μ_N is presented for ^{58}Cu, in agreement with the previous literature value but more precise. The latter magnetic moment is consistent with a dominant $\pi p_{3/2} \otimes \nu p_{3/2}$ configuration, as expected in the vicinity of the closed-core nucleus ^{56}Ni. Although no direct confirmation of the spin assignment is possible with the studied transition, the nuclear spin of the different isotopes is strongly supported by this work, as any other spin assignment yields unphysical magnetic moments. Spins 0 for ^{58}Cu and $\frac{1}{2}$ for ^{57,59}Cu are firmly ruled out.

The isotope shifts between all five isotopes have been extracted. This mass region is however dominated by the mass shift and the resolution is insufficient to extract accurate information on the changes in the mean-square charge radii. Higher-precision in-source techniques, like the Laser Ion Source Trap (LIST) [156] coupled to a gas cell [141] or the use of two-photon excitation or saturation spectroscopy [157] in a hot cavity, would yield the required accuracy for that type of study while maintaining the high sensitivity.

Acknowledgments Fruitful discussions with G. Neyens and N. Severijns are greatfully acknowledged. We thank the CRC team, Louvain-La-Neuve (Belgium), for providing the primary beams. This work was supported by FWO-Vlaanderen (Belgium), GOA/2004/03 (BOF-K.U.Leuven), the IUAP - Belgian State Belgian Science Policy - (BriX network P6/23) and by the European Commission within the Sixth Framework Programme through I3-EURONS (Contract RII3-CT-2004-506065).

Chapter 6

Shape coexistence in the polonium isotopes

6.1 Review around $Z = 82$

^{208}Pb is the heaviest even-Z, even-N stable nucleus of the nuclear chart. As an element, lead is also one of the most dense materials, recognised for its high bulk mass. When one is asked about comparing 1 kg of feathers to 1 kg of lead, one should not worry so much about the weight but rather about how big a bag is needed for the feathers.

^{208}Pb is also recognised for its magic character. Indeed, with $Z = 82$ protons and $N = 126$ neutrons, this isotope is doubly magic. The energy of its first 2^+ excited state is so high (> 4 MeV) that it is not even the first excited state. The first excited state is indeed a 3^- state that has been attributed to octupole degrees of freedom [Gil66]. Fig. 6.1 and 6.2 show the systematics of the energy level of the first 2^+ excited state $E(2^+)$ and the difference in the 2-neutron, or 2-protron, separation energy δ_{2n}, respectively δ_{2p}, for the lead ($Z = 82$) isotopes and the $N = 126$ isotones, respectively. Note that the $B(E2)$ transition matrix elements have not been as extensively studied as in the case of Ni, for which more extended information is available. Nonetheless, the two figures presented illustrate well the magicity of $^{208}_{82}\mathrm{Pb}_{126}$.

It has however been evidenced with the discussion on $Z = 28$ in Chapter 5, that the persistence of a magic number far from the valley of β stability can be questioned. $Z = 82$ is no stranger to this quest and the neutron-deficient isotopes around lead have been thoroughly investigated [Jul01].

In the region around mid-shell between $N = 82$ and $N = 126$ ($N = 104$), deformed structures based on particle-hole excitations, as described in section 1.3.2, are found at low excitation energy, giving rise to the phenomenon called shape coexistence. The most extreme case is that of ^{186}Pb, which first two excited states have spin and parity $I^\pi = 0^+$ [And00], leading to three different shapes within an energy span of less than 700 keV.

The proximity of those states can result in a mixing of the different shapes with

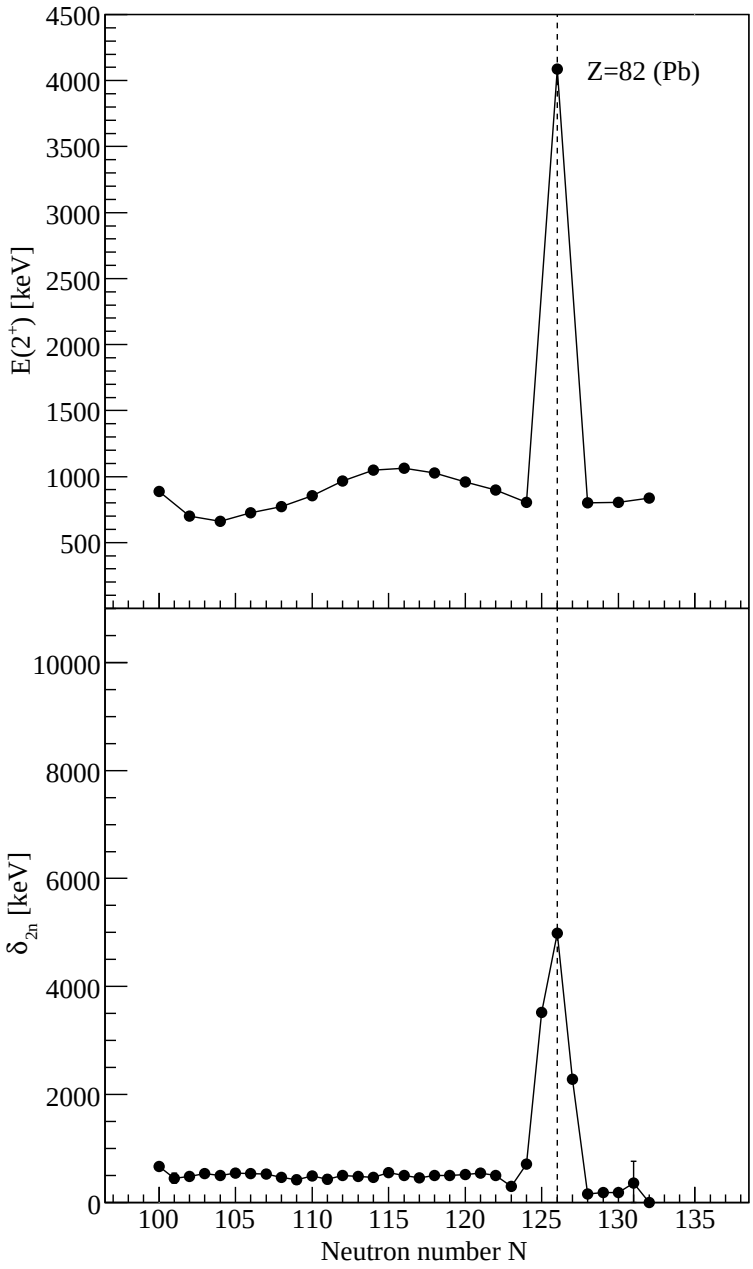

Figure 6.1: From top to bottom: systematic energy level of the first 2^+ excited state in the even-N $_{82}$Pb isotopes; changes in the 2-neutron separation energy in the $_{82}$Pb isotopes.

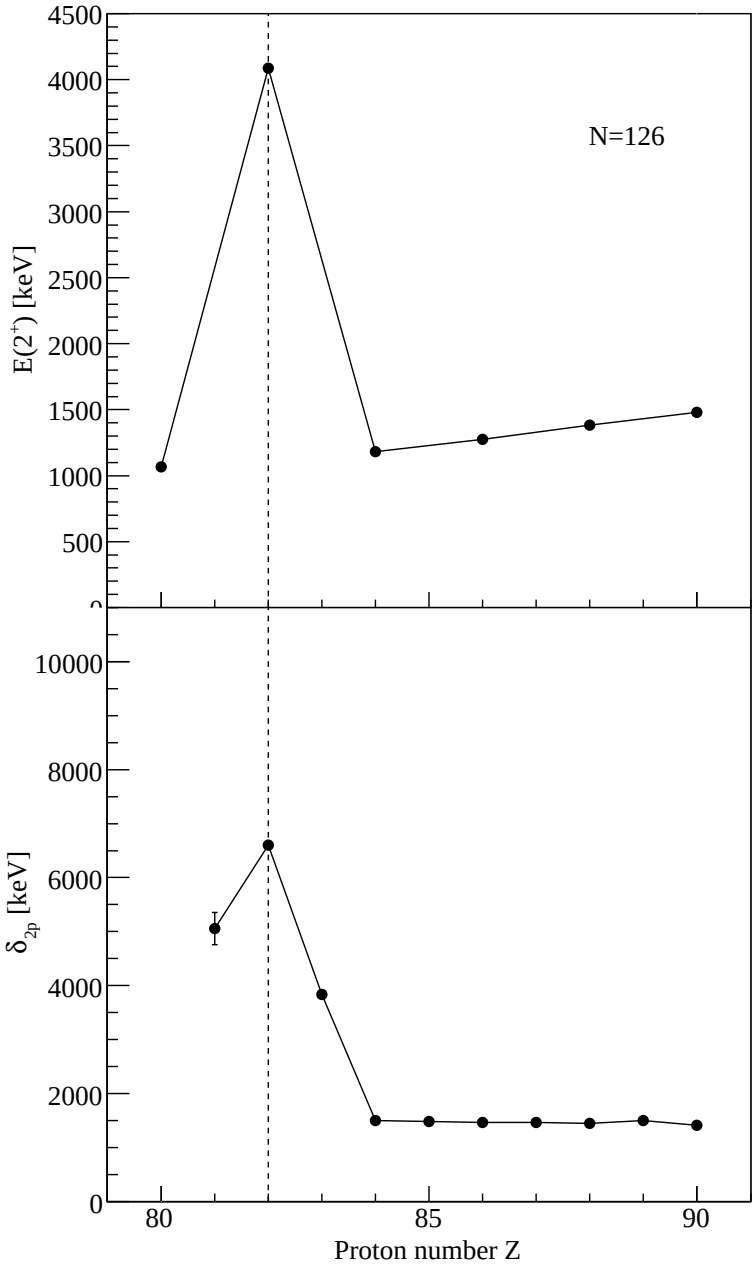

Figure 6.2: From top to bottom: systematic energy level of the first 2^+ excited state in the even-Z $N = 126$ isotones; changes in the 2-proton separation energy in the $N = 126$ isotones.

one another. In the case of the ground state of the lead isotopes, the measurement of the changes in the mean-square charge radii concluded however that the ground state of those isotopes remains spherical across the mid-shell [DW04, De 07, Sel09].

With $Z = 84$, the polonium isotopes have two protons outside of the magic $Z = 82$ shell closure. In the mid-shell region, evidences of shape coexistence have been identified, first in the study of the α decay of the radon and polonium isotopes [Wau92, Wau93, Bij95], and more recently in the study of the first excited state lifetime [Gra08]. The intrusion of a prolate band even results in a well-deformed ground state beyond $N = 104$ [Hel96, Vel03, And06]. In order to determine the extent to which the shape of the ground state of those isotopes is affected by the coexistence, the changes in the mean-square charge radii have been investigated experimentally.

6.2 Laser spectroscopy of the polonium isotopes $^{192-210,216,218}$Po

The ground-state properties of the polonium isotopic chain have been studied at ISOLDE by means of in-source resonant ionisation laser spectroscopy using the RILIS. The polonium atoms were produced in the proton-induced fission of ^{238}U or in the decay of $^{206-211}$At, ^{224}Ra and ^{222}Rn, as detailed in section 4.1.3. The polonium isotopes have been studied from ^{191}Po up to ^{218}Po. Isotopes with half-lives ranging from $T_{1/2} = 33$ ms (^{192}Po) up to $T_{1/2} = 102$ years (^{209}Po) have been investigated, with count rates as low as 0.02 ion·s^{-1} for ^{191}Po and 0.3 ion·s^{-1} for ^{192}Po, as observed at the detection setup.

The measurement of the activity (for the shorter-lived isotopes) or of the beam intensity (for the longer-lived isotopes) with respect to the frequency of the second resonant step laser around 843.38 nm, as seen in the ionisation scheme presented in section 4.1.1, yields the laser resonance spectrum. The even-Z, even-N isotopes, with a spin $I^\pi = 0^+$, do not display any hyperfine structure. The odd-A isotopes, however, have a complex structure as the nuclear spins are non-zero (typically $I^\pi = \frac{3}{2}^-, \frac{13}{2}^+$) and couple to the $J = 2$ atomic levels.

No preliminary knowledge is available on this $J = 2 \rightarrow 2$ atomic transition and large-scale atomic calculations have to be relied on to extract the nuclear information of interest.

6.2.1 Laser spectroscopy of the even-A polonium isotopes $^{192-210,216,218}$Po

Paper VII
T.E. Cocolios, W. Dexters, M.D. Seliverstov *et al.*, in preparation for publication as a letter.

The isotope shifts in the even-A polonium isotopes $^{192-210,216,218}$Po are presented.

For the isotopes overlapping with the previous data from the 255.8 nm atomic transition [Kow91], a linear relation is found between the modified isotope shifts in the King plot.

Large-scale atomic calculations [Fri02] have been performed using the GRASP-92 [Par96] and RATIP [Fri01] packages. The electronic F-factors and the SMS constants K_{SMS} have been extracted for both transitions, for this work and for the previous studies. The agreement on the F-factors is very good but a systematic shift in specific mass shift is observed, resulting in a large systematic uncertainty on the charge radii.

The changes in the mean-square charge radii are then extracted using those calculated atomic parameters. The charge radii are found to deviate strongly from the spherical Finite Range Droplet Model [Mye83] from ^{198}Po towards the more neutron-deficient isotopes. This deviation sets in at the same neutron number $N = 114$ than in mercury or platinum but with a much larger magnitude. The deformed FRDM [Möl95] does not reproduce this early departure. Extracting the deformation parameter $|\beta_2|$ from the $\delta\langle r^2\rangle_{exp}$ gives for ^{194}Po a value that matches the $|\beta_2|$ extracted from the transition probability $B(E2)$ in ^{194}Po [Gra08].

The Beyond Mean Field calculations using the Skyrme Sly4 interaction [Ben06, Gra08] reproduce partially this strong departure but fail to reproduce its magnitude at ^{192}Po.

Shape evolution of the nuclear ground-state of the even-even polonium isotopes

T.E. Cocolios, W. Dexters, M.D. Seliverstov, A.N. Andreyev, B. Bastin, J. Büscher, I.G. Darby, M. Huyse, M. Keupers, Yu. Kudryavtsev, P. Van Duppen, M. Venhart
Instituut voor Kern- en Stralingsfysica, Katholieke Universiteit Leuven, B-3001 Leuven, Belgium

S. Antalic
Department of Physics and Biophysics, Comenius University, Bratislava 84248, Slovakia

A. Barzakh, D. Fedorov, P. Molkanov
Petersburg Nuclear Physics Institute, 188350 Gatchina, Russia

M. Bender
Centre d'Etudes Nucléaires de Bordeaux Gradignan, F-33175 Gradignan, France

V.N. Fedosseev, B.A. Marsh, J. Van de Walle
CERN, Ch-1211 Geneva 23, Switzerland

K.T. Flanagan, E. Mané
Department of Physics, University of Manchester, Manchester, M60 1AD, United Kingdom

S. Franchoo, I. Stefan
Institut de Physique Nucléaire d'Orsay, F-91406 Orsay, France

P.-H. Heenen
Service de Physique Nucléaire Théorique, Université Libre de Bruxelles, B-1050 Bruxelles, Belgium

K. Heyde
Vakgroep Subatomaire en Stralingsfysica, University of Gent, B-9000 Gent, Belgium

G. Huber
Institut für Physik, Johannes Gutenberg Universität, D-55099 Mainz, Germany

U. Köster
Institut Laue-Langevin, F-38042 Grenoble, France

R.D. Page
Oliver Lodge Laboratory, University of Liverpool, Liverpool, L69 7ZE, United Kingdom

M.A. Sjoedin
KTH - Royal Institute of Technology, SE-10044 Stockholm, Sweden

J.L. Wood
School of Physics, Georgia Institute of Technology, Atlanta, GA 30332-0430, United States of America

S. Zemlyanoy
Joint Institute of Nuclear Research, 141980 Dubna, Moscow Region, Russia

Abstract

In-source resonant ionization laser spectroscopy of the even-A polonium isotopes $^{192-210,216-218}$Po has been performed using the $6p^3 7s\ ^5S_2$ to $6p^3 7p\ ^5P_2$ transition in the polonium atom at 843.38 nm. The comparison of the isotope shifts in $^{200-210}$Po with a previous data set allow to test recent large-scale atomic calculations and assert the accuracy of the calculated atomic parameters. The changes in the mean-square charge radii are extracted relative to ^{208}Po and compared to nuclear models. A large departure from sphericity is observed for $A \leq 196$, reproduced by Beyond Mean Field calculations but not by two-level mixing calculations. A kink is observed beyond $N = 126$ of a comparable magnitude to that observed in the neighboring nuclei.

Charge distribution, $190 \leq A \leq 219$, Radioactive beams, Calculations and mathematical techniques in atomic and molecular physics
21.10.Ft, 27.80.+w, 29.38.-c, 31.15.-p

The atomic nucleus is a unique medium to study mesoscopic systems with interacting fermions of different length scales. The interplay of the strongly-interacting nucleons within the nucleus leads to a subtle mix of individual and collective behaviors. The electronic cloud is also the result of the balance between the electromagnetic forces at play in the atom. Those two bodies span very different scales, yet their interactions can reveal important informations [158].

In heavy nuclei, the large number of particles is a challenge for accurate descriptions of the atom or of the nucleus. Laser spectroscopy can be used to probe the atomic structure, as well as the effects of the nucleus on it. This technique requires, however, specific conditions to be met, concerning the intensity of the atom source, as well as its purity. For the heaviest elements, limited production rates and purity are challenges that need to be overcome.

In nuclei around $Z = 82$, the stabilizing effect of the closed-proton-shell configuration on the nuclear structure is established [159]. Nonetheless, particle excitations accross that shell closure give rise to deformed structures at low energy [160]. As the neutron shells are depleted from $N = 126$ towards the more neutron-deficient region, the increased number of valence neutrons gives rise to increased proton-neutron interactions. The shape-coexistence phenomenon is enhanced and eventually peaks at the neutron mid-shell $N = 104$ [161], as evidenced by the triple shape coexistence of spherical, oblate and prolate 0^+ states at low energy in ^{186}Pb [162]. However, shape coexistence does not systematically imply a large mixing of the different configurations, as observed in the study of the shape of the ground state of the neutron-deficient lead isotopes [163, 164].

With $Z = 84$, the polonium isotopes exhibit signs of shape coexistence as they approach mid-shell [165]. Around $N = 104$, the intrusion of prolate bands at low energy eventually result in a well-deformed ground-state [166, 167, 168]. An observable that is very sensitive to the nuclear shape is the charge distribution. The changes in the mean-square charge radii of the polonium isotopes, $\delta\langle r^2\rangle$, have therefore been studied by means of in-source resonant ionization laser spectroscopy.

As there is no stable isotope of polonium, the study of the atomic structure of polonium is limited [169, 170]. Knowledge of the atomic transitions are seldom and the previous laser spectroscopy study [170] had to rely on the predictions of the spherical Finite Range Droplet Model (FRDM) [171] as a starting point for the extraction of the $\delta\langle r^2\rangle$. Prior to the present study, new ionization schemes for polonium were investigated and a selective and sensitive atomic transition for laser spectroscopic studies was found [172]. In the last 20 years, the progress and developments in the field of atomic structure theory have resulted in the ability to compute large-scale calculations for open-shell atoms [173]. Such computations, by means of the Grasp-92 [174] and Ratip [175] packages, have been performed to determine the necessary electronic input for the analysis of the laser spectroscopy data.

In this Letter, we report on the measurement of the isotope shift of the neutron-deficient, even-A polonium isotopes from ^{210}Po down to the short-lived ($T_{1/2} = 33$ ms) ^{192}Po and of the neutron-rich even-A polonium isotopes $^{216-218}$Po. The results of the large-scale atomic calculations are discussed based on the experimental data. The

$\delta\langle r^2\rangle$ are extracted and discussed in terms of macroscopic and microscopic models.

The polonium isotopes have been produced at the CERN ISOLDE facility in the proton-induced spallation reaction of ^{238}U. Beams of $^{194-204}$Po were produced in a first experiment (Run I, 2007) and beams of $^{192-210,216-218}$Po were produced in a second experiment (Run II, 2009). Those isotopes span a range of half-lives from 33 ms in ^{192}Po to 102 years in ^{209}Po. This demonstrates the versatility of the in-source laser spectroscopy technique. In Run I, 10 isotopes and 4 isomers were studied in over a week while, in Run II, 12 isotopes and 3 isomers were investigated in the course of a week. This shows that in-source laser spectroscopy is a very effective means of studying the ground-state properties of those isotopes. Moreover, the study of long chains of isotopes within a single experimental campain reduces the possibility of systematic effects from one experiment to another.

The proton beam from the CERN PS-Booster (1.4 GeV, 1.4 μA on average) impinged on a UC_x target (50 g·cm^{-2}) in a repeated sequence of pulses separated by periods of 1.2 s. Recoiling nuclei diffused out of the target matrix and effused to the atomizer kept at high temperature ($\approx$ 2300 K). The atoms were then resonantly ionized by a three-step three-color laser ionization scheme [172]. Atomic electrons were promoted, using Cu-vapour- (Run I) or Nd:YAG- (Run II) pumped dye lasers, from the $6p^4\ ^3P_2$ atomic ground state to the $6p^3 7s\ ^5S_2$ atomic excited state via a transition at 255.8 nm, then to the higher-lying $6p^3 7p\ ^5P_2$ atomic excited state via a transition at 843.38 nm, and finally beyond the ionization potential into the continuum with the green light from the primary laser (510.6 nm for the Cu-vappor lasers and 532 nm for the Nd:YAG laser). The ionized beams of polonium were then accelerated to an energy of 50 keV and separated according to the mass-to-charge ratio of the different isotopes through a dipole magnet. Although the laser ionization process is Z-selective, contamination can occur through surface ionization of elements with a low ionization potential, such as francium. From $A > 204$ on, the francium yields become so overwhelming that a direct measurement becomes extremely difficult. However, once the target was sufficiently irradiated, a large number of long-living isotopes are present in the target which, once the proton beam is turned off and the short-living francium isotopes have decayed away, can act as precursors of the desired polonium isotopes. The isotopes $^{206-210}$Po were obtained in this way in the β^+/EC decay of the isobaric astatine nuclei while the isotopes ^{216,218}Po were produced in the α decay of ^{224}Ra and ^{222}Rn, respectively.

The α-decaying isotopes $^{192-196,216-218}$Po were implanted in thin C foils (20 μg·cm^{-2}) mounted on a rotating wheel while the α decay was observed using Si detectors. The total solid angle covered by the detectors was 20% of 4π (Run I, [164]), and 66% of 4π (Run II, [176]). The β-decaying isotopes $^{200-204}$Po were implanted in the mylar tape of the ISOLDE tape station and studied using a single coaxial HPGe detector. The longer-lived isotopes $^{206-210}$Po benefited from high yields and the beam current was directly monitored in a Faraday cup.

The laser spectroscopy was performed by scanning the laser at 843.38 nm from the first to the second excited state of the ionization scheme and monitoring the yields as a function of the applied frequency. The obtained frequency scans are shown in

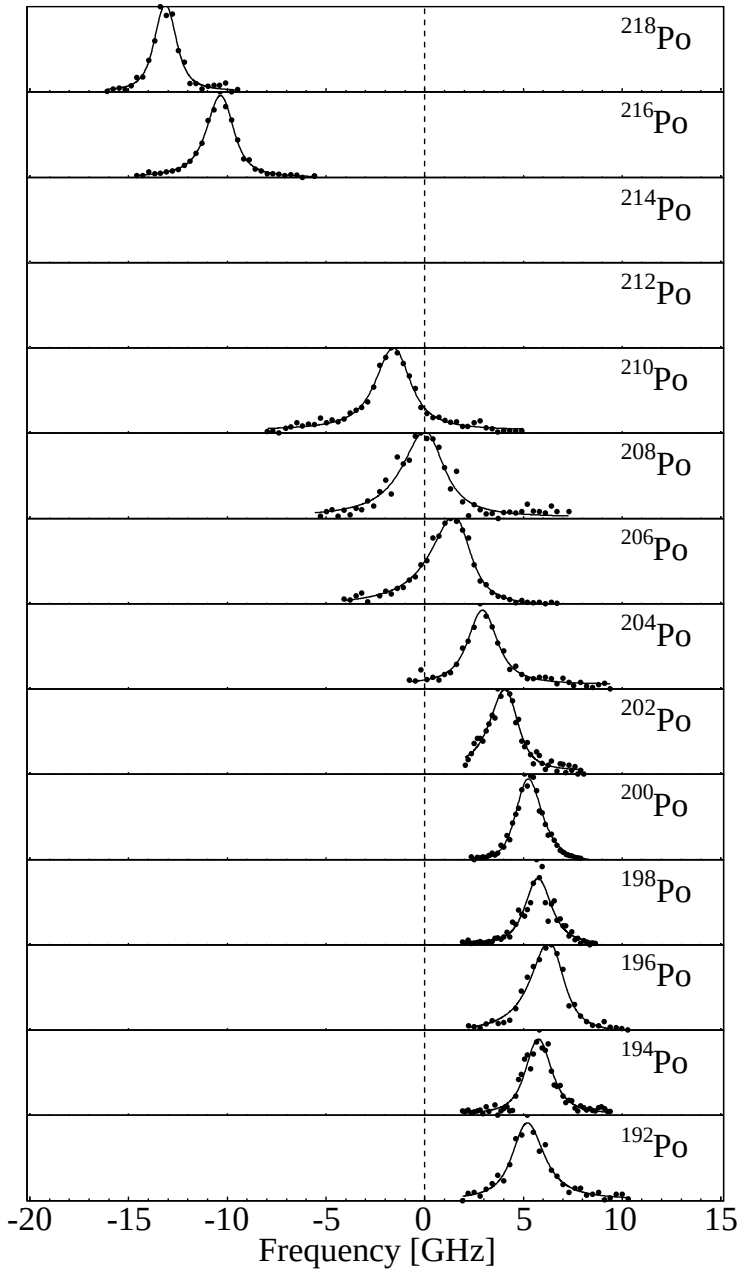

Figure 6.3: From top to bottom: laser scan of the 843.38 nm transition between the $6p^3 7s\ ^5S_2$ and $6p^3 7p\ ^5P_2$ atomic excited states in even-A Po-I for $A = 218$ down to $A = 192$.

Table 6.1: Isotope shifts $\delta\nu_{exp}^{A,208}$ and changes in the mean-square charge radii $\delta\langle r^2\rangle_{exp}^{A,208}$ of the polonium isotopes with respect to ^{208}Po. The first error on the $\delta\langle r^2\rangle_{exp}^{A,208}$ stems from the isotope shift measurements, while the second error is the systematic uncertainty originating from the SMS.

Mass	$\delta\nu_{exp}^{A,208}$ [GHz]	$\delta\langle r^2\rangle_{exp}^{A,208}$ [fm^2]
218	−13.155(96)	1.081(8)(42)
216	−10.451(81)	0.859(7)(34)
210	−1.631(75)	0.131(6)(8)
208	0	0
206	1.412(85)	−0.113(7)(8)
204	2.789(78)	−0.222(7)(17)
202	4.095(117)	−0.326(10)(25)
200	5.199(72)	−0.412(6)(34)
198	5.942(143)	−0.468(12)(42)
196	6.104(60)	−0.474(5)(51)
194	5.732(134)	−0.435(11)(59)
192	5.067(162)	−0.371(14)(68)

Fig. 6.3. The line profile of the resonance is a deformed Voigt profile. For Run I, the data is analysed as described in Ref. [177]. For Run II, the assymetry is introduced by using a different Lorentzian width parameter on each side of the resonance. The position of each resonance ν is determined and the isotope shifts $\delta\nu_{exp}^{A,208}$ are then deduced with respect to ^{208}Po. The isotope shifts are presented in Table 6.1.

Thanks to a large overlap between this data set and that using the 255.8 nm transition [170], the two transitions could be compared by plotting modified isotope shifts with respect to each other according to the formalism of King [178]. The King plot is shown in Fig. 6.4. The slope of this graph is the ratio of the two electronic factors while the y intercept is a linear combination of the SMS contributions to each isotope shift. The line given by the results of the large-scale atomic calculations is shown as well. The comparison of the experimental data to these calculations yields $\chi^2_\nu = 7$. An offset in the SMS contribution, but with the same F-factors, yields a much better agreement with $\chi^2_\nu = 0.79$. This confirms the precision of the calculations of the F-factors but raises some questions on the SMS contributions. A systematic uncertainty on the SMS of ± 0.05 GHz·u^{-1} is therefore introduced. The electronic parameters are shown in Table 6.2.

The $\delta\langle r^2\rangle$ are then extracted using those parameters and a 0.911(4) correction for higher moments [179]. The experimental values are given in Table 6.1 and shown in Fig. 6.5. The $\delta\langle r^2\rangle$ are first compared to the predictions from the spherical FRDM [171] and show a large deviation from sphericity starting from ^{198}Po, which occurs earlier than in the $Z \leq 82$ elements. This large deviation in $^{194-198}$Po can not be explained by the FRDM-calculated static deformation, as shown when comparing with

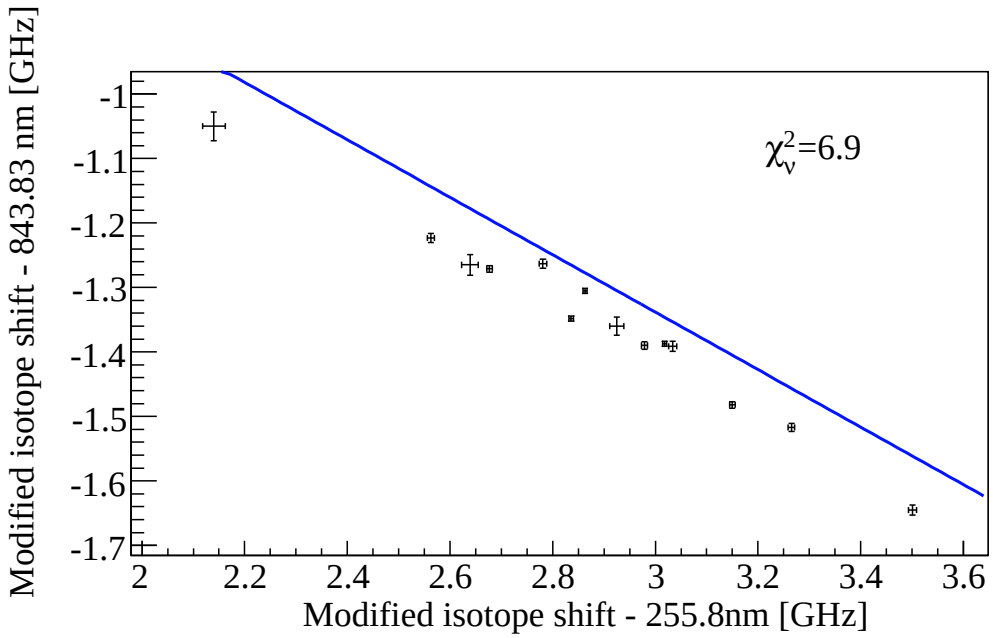

Figure 6.4: King plot between the transitions at 255.8 nm [170] (x axis) and at 843.83 nm (present work, y axis) for $^{200-210}$Po. The line is the calculated relation from the large-scale atomic calculation. A value of $\chi^2_\nu = 6.9$ is found in comparing the calculations to the experimental data.

Table 6.2: Calculated atomic electronic factor F and SMS constant K_{SMS} of the 255.8 nm and 843.83 nm transitions.

Transition [nm]	F [GHz/fm^2]	K_{SMS} [GHz]
255.8	29.140	226
843.38	−12.976	−151

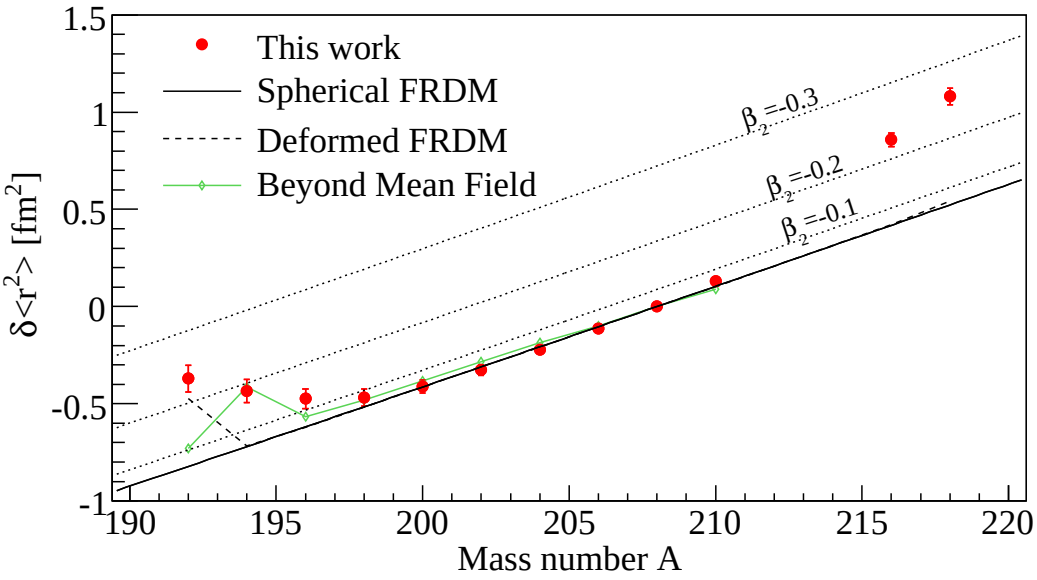

Figure 6.5: Changes in the mean-square charge radii $\delta\langle r^2\rangle$ for the even-A polonium isotopes $^{192-210,216-218}$Po, using ^{208}Po as a reference. The solid line represents the spherical FRDM [171], the dotted line represents the deformed FRDM [180] and the colored line with diamonds represents the Beyond Mean Field calculation with the SLy4 interaction [181].

the axially symmetric deformed FRDM [180]. Indeed, only ^{192}Po is reproduced by this approach.

The previous approach can be reversed and the deformation parameter $|\beta_2|$ may be extracted for the neutron-deficient polonium isotopes. The values obtained by comparing the $\delta\langle r^2\rangle_{exp}$ to the FRDM are listed in Table 6.3. Experimentally, those may also be extracted from the transition matrix elements $B(E2)$. For ^{194}Po, the value of $|\beta_2| = 0.186(^{20}_{21})$ e^{2}b^2 from the $\delta\langle r^2\rangle_{exp}$ is in good agreement with the value $|\beta_2| = 0.170(30)$ e^{2}b^2 from lifetime measurement studies [165].

The deformation parameter may also be compared to two-level mixing calculations [182]. Since the lead isotopes do not show any noticeable mixing, the calculations are greatly simplified. The mixing parameters can be extracted from the energy systematics as well as from the α decay of polonium to lead. Both yield consistent results [183]. The probability of the deformed component of the wavefunction in the ground state of the even-A polonium isotopes is given in Table 6.3. The reduced mixing in the ground state between ^{192}Po (58%) and ^{194}Po (32%) follows nicely the trend deduced for the $|\beta_2|$ from the $\delta\langle r^2\rangle_{exp}$. This is however not the case for ^{196,198}Po, as the deviation from sphericity shows a much smoother evolution with the $|\beta_2|$ than in the two-level mixing calculations.

The $\delta\langle r^2\rangle$ have also been calculated using the Beyond Mean Field approach [181]

Table 6.3: Deformation parameter $|\beta_2|$ extracted from the $\delta\langle r^2\rangle_{exp}$ and contribution of the deformed wave function to the ground state in a two-level mixing model based on the α-decay hindrance factors [182, 183].

Mass	$\lvert\beta_2\rvert$ [e^{2}b^2]	Mixing [%]
200	$0.013(^{51}_{13})$	0
198	$0.075(^{29}_{53})$	1
196	$0.131(^{26}_{22})$	2
194	$0.186(^{21}_{20})$	32
192	$0.237(^{20}_{19})$	57

and are shown in Fig. 6.5. From these calculations, it is concluded that the ground state is made of wave functions having different axial quadrupole deformation. The resulting wave function is spread over many configurations and the nuclei are soft. The idea of sphericity and deformation becomes then more complex. It remains possible to define a mean deformation from the average of the individual components deformation, weighted to their respective contribution in the collective wave function. The deformation for the isotopes $^{192-210}$Po averages finally to a spherical mean value and only more neutron-deficient isotopes start to display a clear prolate deformation. The calculated $\delta\langle r^2\rangle$ are in fair agreement with the experimental trend. The deviation from sphericity is nicely reproduced but a surprising deviation in the case of ^{192}Po is observed. The origin of this deviation is not yet understoood. These calculations clearly confirm that, unlike in the lead case, the different shapes mix in the ground state.

Finally, the neutron-rich isotopes $^{216-218}$Po show a clear break from the trend of the polonium isotopes below $N = 126$. The magnitude of this kink is similar to what is observed in the neutron-rich neighboring lead ($Z = 82$) [184], bismuth ($Z = 83$) [185] and heavier isotopes. This effect has only been marginally reproduced by Relativistic Mean Field calculations [186].

In conclusion, in-source resonant ionization laser spectroscopy has been performed on the polonium isotopes from the very neutron-deficient ^{192}Po to the very neutron-rich ^{218}Po. The overlap with the previous data set available in the literature has allowed to test the large scale atomic calculations and those tests have asserted the accuracy of those calculations for the electronic F-factors. The changes in the mean-square charge radii of the even-A polonium isotopes $^{192-210,216-218}$Po have been extracted and compared to recent results and calculations. The coexistence of the different shapes at low excitation energies yield to a very soft nature of the most neutron-deficient polonium nuclei. The early departure from sphericity leads eventually to a well-defined prolate ground state for the even more neutron-deficient isotopes.

We would like to thank the ISOLDE collaboration for providing excellent beams. This work was supported by FWO-Vlaanderen (Belgium), by GOA/2004/03 (BOF-

K.U.Leuven), by the IUAP - Belgian State Belgian Science Policy - (BriX network P6/23), by the European Commission within the Sixth Framework Programme through I3-EURONS (Contract RII3-CT-2004-506065), by the U.K. Science and Technology Facilities Council, and by the Slovak Research and Development Agency (Contract No. APVV-20-006205).

Table 6.4: Experimental (^{194}Po [Gra08]) and phenomenological transition probabilities $B(E2)$ for the even-A polonium isotopes $^{192-200}$Po based on the Grodzins rule. Deformation parameter $|\beta_2|_{B(E2)}$ extracted from those $B(E2)$ and $|\beta_2|_{r^2}$ from the $\delta\langle r^2\rangle_{exp}$.

Mass	$B(E2)$ [W.u.]	$\lvert\beta_2\rvert_{B(E2)}$ [e^{2}b^2]	$\lvert\beta_2\rvert_{r^2}$ [e^{2}b^2]
192	110(24)	0.188(44)	$0.237(^{20}_{19})$
194	90(20)	0.170(30)	$0.186(^{21}_{20})$
196	62(14)	0.141(33)	$0.131(^{26}_{22})$
198	48(11)	0.124(29)	$0.075(^{29}_{53})$
200	43(10)	0.118(28)	$0.013(^{51}_{13})$

6.2.2 Grodzins rule

The transition probabilities $B(E2)$ in polonium have not yet been thoroughly studied and the knowledge is limited to the two isotopes ^{194,210}Po [Gra08, Ell73]. It is however possible to predict the transition probabilities in the other isotopes based on the energy of the first excited 2^+ state using Gordzins' rule [Ram01]. It states that the product $E(2^+)\cdot B(E2)$ should be constant for a given isotopic chain.

The Grodzins' rule, or its extension to exotic nuclei [Hab], assumes deformed isotopes and it is thus only applicable to the lightest polonium isotopes. Table 6.4 compares the deduced $B(E2)$ values using the Grodzins' rule, normalised to the experimental $B(E2)$ value for ^{194}Po [Gra08]. Using these $B(E2)$values, the deformation parameter $|\beta_2|$ can be deduced according to [Ram01]

$$|\beta_2| = \frac{4\pi}{3ZR_C^2}\sqrt{\frac{B(E2)}{e^2}}. \tag{6.1}$$

Table 6.4 compares the deduced $|\beta_2|$ values applying the Grodzins' rule with the values obtained from $\delta\langle r^2\rangle_{exp}$ in $^{192-200}$Po. The agreement is fair for $A \leq 198$, showing that the energy of the first excited 2^+ state gives a good indication of the collectivity in the ground state of these neutron-deficient polonium isotopes. The same exercise for the heavier polonium isotopes fails, confirming the lack of collectivity in those isotopes.

6.3 Polonium amongst others

The $\delta\langle r^2\rangle$ of polonium may also be compared to those of the neighbouring even-Z nuclei. In Fig 6.6, the systematic $\delta\langle r^2\rangle$ of $_{78}$Pt [Le 99], $_{80}$Hg [Ulm86], $_{82}$Pb [Ans86, Din87, Dut91, De 07], $_{84}$Po [Kow91], $_{86}$Rn and $_{88}$Ra [Fri05] are shown.

On the neutron-deficient part of the systematics, the difference with the lead ($Z = 82$) isotopes is striking as those remain very close to the spherical FRDM while

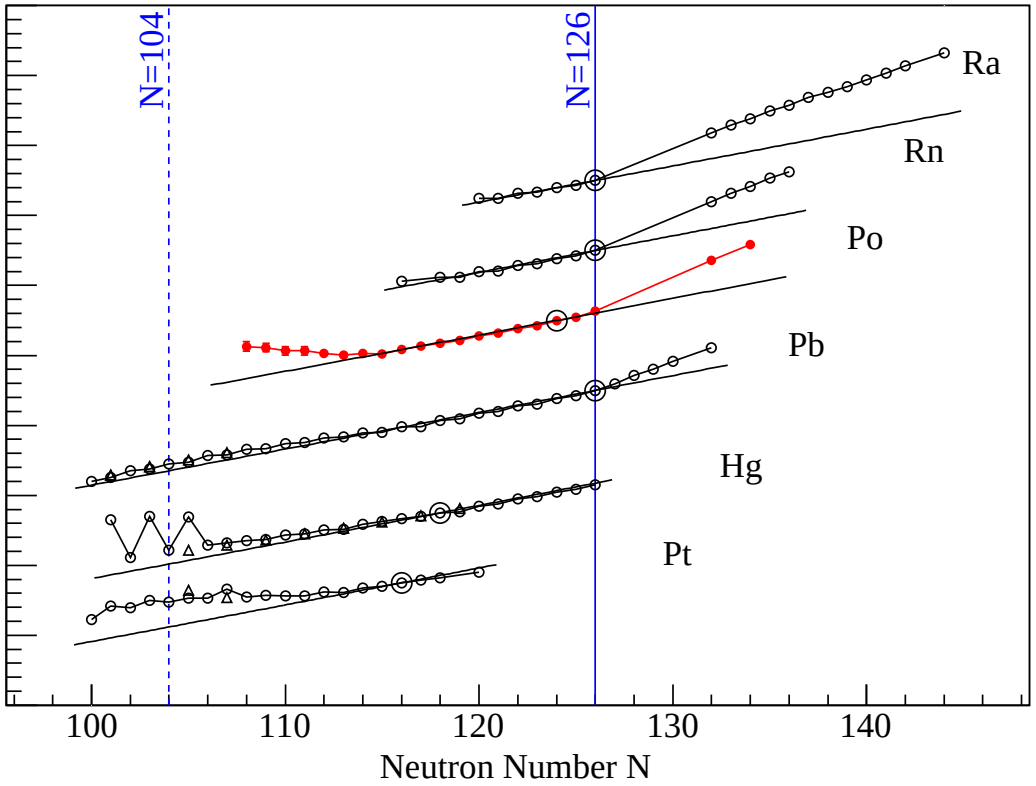

Figure 6.6: Systematics in the $\delta\langle r^2\rangle$ for the even-Z isotopes $_{78}$Pt [Le 99], $_{80}$Hg [Ulm86], $_{82}$Pb [Ans86, Din87, Dut91, De 07], $_{84}$Po [Kow91], $_{86}$Rn and $_{88}$Ra [Fri05]. The large circles indicate the reference isotope for each chain. One large division represents 1 fm^2. The shift between each isotopic chain is arbitrary.

the polonium isotopes depart from this trend for $N < 116$. Similarly, the platinum ($Z = 78$) and the mercury ($Z = 80$) isotopes depart from the spherical FRDM for $N < 116$, although the magnitude of the deformation is not as important as in the polonium case. The main feature of the mercury isotopes is the large isomer shift in the very neutron-deficient isotopes around the mid-shell $N = 104$. The $\delta\langle r^2\rangle$ for polonium in this region could however not be measured in the course of this study. The half-lives of those isotopes are indeed too short to allow for the radioactive recoils to efficiently diffuse out of the thick target matrix before decaying. The yields are therefore extremely small.

The similarities and discrepancies between the different isotopic chains can be enhanced by comparing relative $\delta\langle r^2\rangle$ according to the formalism introduced in [Hul61] and thoroughly described in [Cam95]. The relative $\delta\langle r^2\rangle^{N,124}$ are normalised within each isotope to $\delta\langle r^2\rangle^{122,124}$. One can then compare two isotopic chains with each other. A typical example is shown in Fig. 6.7 (top) between the lead and mercury isotopes. One can see that, apart from the large isomer shift of the most neutron-deficient mercury isotopes, the $\delta\langle r^2\rangle$ scale with one another remarkably well.

The polonium isotopes are compared to their neighbouring even-Z platinum, mercury, lead and radon isotopes (see Fig. 6.7). It can be seen that the behaviour of the polonium isotopes between $N = 126$ and $N = 116$ is again remarkably similar to that of the other isotopes. For $N < 114$, however, the polonium isotopes depart much more drastically from the systematic trend, even from the deformed platinum isotopes. Note that in the polonium and platinum cases, it is assumed that multi-particle-multi-hole excitations through the $Z = 82$ shell gap cause the onset of collectivity [Woo92, Bij95]. It appears therefore as a surprise that, in spite of a larger number of active protons in the platinum case compared to polonium, the effects are bigger in the latter. This might however be due to specific occupation of the nuclear levels in polonium, where both the protons and the neutrons are occupying similar orbitals for N, Z between 82 and 126. No data on the radon isotopes are available in that region and their behaviour can unfortunately not be compared.

It would be interesting to complete these figures with the odd-A isotopes to verify weather the fine details in the odd-even staggering are reproduced as well. The hyperfine structure of those isotopes is however not fully resolved in the data and the analysis is still ungoing. A preliminary analysis confirms however that the odd-A isotopes follow a similar trend as the even-A isotopes down to ^{193}Po.

On the neutron-rich side of the systematics, the kink beyond $N = 126$ in polonium is similar to what is observed in the lead ($Z = 82$), radon ($Z = 86$) and radium ($Z = 88$) isotopes. It seems, however, that it does not scale as the $\delta\langle r^2\rangle$ do below $N = 126$. A more comprehensive discussion on those isotopes goes beyond the scope of this thesis and can be found in [Dex10].

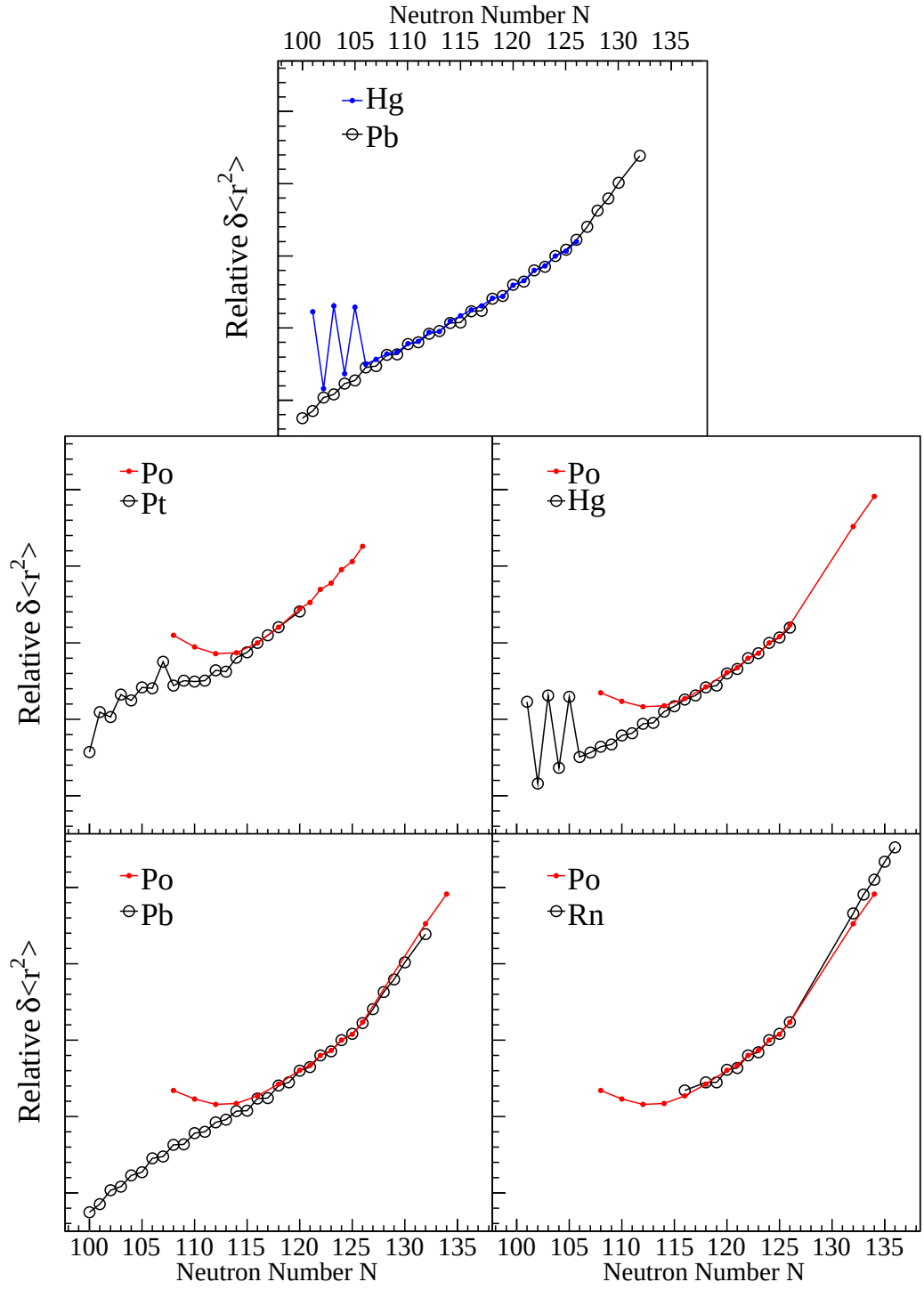

Figure 6.7: Relative $\delta\langle r^2\rangle$ for the even-Z isotopes $_{78}$Pt [Le 99], $_{80}$Hg [Ulm86], $_{82}$Pb [Ans86, Din87, Dut91, De 07], $_{84}$Po [Kow91], and $_{86}$Rn [Fri05]. The relative $\delta\langle r^2\rangle^{N,124}$ are normalised within each isotope to $\delta\langle r^2\rangle^{122,124}$. The scale on the y axis is therefore arbitrary.

Chapter 7

Conclusions and Outlook

In this work, many nuclear properties have been explored by means of resonant ionisation laser spectroscopy. This technique now shows a wide range of applications, from the selective production of radioactive ion beams to the study of the nuclear moments and shapes, as well at hot-target ISOL facilities as in gas-cell based facilities. The recent developments have allowed two main results to be found. The measurement of the magnetic dipole moment of the neutron-deficient copper isotopes has proven that the shell-model calculations in that region of the nuclear chart were accurate. The changes in the mean-square charge radii of the even-A polonium isotopes present a strong deviation from the spherical FRDM, much stronger than in the neighbouring elements, and provides further evidence of the swift onset of collectivity close to mid-shell $N = 104$.

Many developments have been undertaken for the improvement of the resonant ionisation selectivity. At the hot-target ISOL facility ISOLDE, several resonant ionisation schemes have been studied for polonium ($Z = 84$). As it does not possess any stable isotope, this study was performed on-line.

At the gas-cell-based facility LISOL, the origin of non-resonantly-produced ions has been investigated with a ^{252}Cf source in off-line conditions, concluding on a possible connection between the ionisation potential and the survival efficiency of the elements. A new gas cell, with separated volumes for catching the reaction recoils and for ionising the atoms of interest, has been characterised. The use of electric fields inside that gas cell have resulted in a substantial improvement in selectivity. It also allowed to identify an additional process responsible for the production of non-resonantly-produced ions: neutral radioactive atoms are deposited on the surface of the SPIG and the recoils from their decay are captured back in the pseudo-potential of this ion guide and re-introduced in the beam. Reducing the surface area of the SPIG would likely reduce the importance of this effect. New structures for the SPIG are currently under design in collaboration with Prof. M. Wada, Dr. T. Sonoda and Dr. A. Takamine from RIKEN (Japan).

The use of a laser ion source trap LIST coupled to a gas catcher has also been investigated at LISOL. This technique has been confirmed to work experimentally for the first time with a gas catcher. The improvements in the resolution of the laser scan

opens also the door for greater precision in in-source laser spectroscopy. The current setup suffers however from the limited repetition rate of the laser system, insufficient to irradiate all the atoms leaving the gas cell. Moreover, the ions produced in the LIST do not all have sufficient momentum along the beam direction to efficiently be extracted from the SPIG. A dragging field of a few Volts would result in a reduced extraction time and an overall improvement in extraction efficiency. Developments in this direction are also under consideration. The plume of the supersonic jet coming from the gas cell aperture is also not the most appropriate for this application. Indeed, a large divergence of the supersonic jet has been observed, resulting in the loss of many atoms. A new gas cell nozzle, inspired from the exhaust of a rocket engine, could provide a better emittance for the atom beam. The development of such a nozzle is currently being researched at the IGISOL facility of the University of Jyväskylä.

All these developments benefitted greatly to the scientific research program. At the LISOL facility, the magnetic dipole moments of the neutron-deficient isotopes $^{57-59}$Cu isotopes have been measured by in-gas-cell resonant ionisation laser spectroscopy. The moment of ^{57}Cu is found to be in disagreement with the previous literature value but in much better agreement with the shell model predictions. The isotope shifts were also extracted but the resolution was not sufficient to extract accurate field shifts as the mass shift contribution dominates in this light nuclei. A new research program has also started, reaching towards the $N = Z = 50$ nucleus ^{100}Sn. The $_{47}$Ag, $_{49}$In and $_{50}$Sn isotopes, produced in heavy-ion fusion-evaporation reactions are currently being investigated as possible candidates for in-gas-cell resonant ionisation laser spectroscopy at LISOL and, for the more neutron-deficient isotopes, at the S^3 facility in GANIL.

At the hot-target ISOL facility ISOLDE, the evolution of the shape of the polonium isotopes $^{191-204,206-211,216,218}$Po has been probed by in-source laser spectroscopy with the RILIS. The isotope shifts in $^{200,202,204,206-210}$Po have been compared to the previous study on those isotopes with a different atomic transition and the resulting King plot has brought the confirmation that the latest large-scale atomic calculations are accurate enough for the extraction of the nuclear information. The changes in the mean-square charge radii for the even-A isotopes $^{192-210,216-218}$Po have been extracted and compared to various models, confirming that the shape of the neutron-deficient polonium ground states is very much influenced by the intrusion of deformed configurations. The odd-A isotopes have also been measured, however they present an unresolved hyperfine structure and this requires further analysis. This analysis should provide information on the magnetic dipole moments as well as on the electric quadrupole moments.

The study of the transition probably $B(E2)$ of the neutron-deficient even-A polonium isotopes $^{196-202}$Po is currently on-going at REX-ISOLDE using the MINIBALL germanium array. It will provide collective effect information on those transitional isotopes. With HIE-ISOLDE, it will also be possible to perform transfer reactions on those nuclei. Po(d, p) reactions can provide information on the single particle nature of the excited levels while the Po(t, p) reactions can provide information on the

pairing in those isotopes.

Finally, it becomes evident that it is only by combining different techniques, from nuclear decay (α, β, ...), to ground state properties (masses, charge distributions, ...), to nuclear excitations and reactions (Coulomb excitation, transfer reactions, ...), that a comprehensive picture of a region of the nuclear chart can be unveiled.

Appendix A

Layout of the electronic logic for IS456

In the logic of a radioactive ion beam experiment, many parameters are intricate to each other, between the ion beam production and transport, the detection system and the data acquisition. There is always one parameter ruling over the others to guarantee the smooth running of the experiment.

In the study of the polonium isotopes at CERN ISOLDE, the radioactive ion beam structure is made by the PS-Booster supercycle (see Fig. 3.1 for details). The detection setup is either the Windmill or the ISOLDE tape station[1]. The difficulty, however, comes from the laser system, which is both a part of the radioactive ion beam production and a measuring device.

In order to lift the conflict between the different time structures of those three entities, an additional layer is used. The system is controlled and coordinated externally by a set of clocks that tie together the supercycle, the lasers and the windmill.

In this appendix, the electronic logic behind the key parts of that system are described in the frame of Run I from experiment IS456 (2007, see section 6.2.1). For the details of the logic behind Run II, see [Dex10]. This description wil ffocus on the measurements with the Windmill setup (see section 3.3.2). In a first part, the acquisition validation is described, then the acquisition sequence, and finally the change between two laser frequencies.

A.1 Acquisition validation

The measurement is performed in integral units of supercycle in order to guarantee that the irradiation of the target is similar for each laser frequency step. An initial trigger for the acquisition validation is therefore the signal that announces the start of a supercycle. This signal was measured to arrive 535 ms ahead of the first proton bunch of the supercycle. A delay to that signal was therefore introduced.

[1]The Faraday cup measurements were performed off-line with a different logic controlled only by the lasers.

The lasers require time to stabilise after the frequency has been changed. A signal was sent by the lasers once the required stability had been achieved. This signal constituted another trigger for the start of the acquisition phase.

The data acquisition system provided a signal when it was operational and ready to record data. This signal was also introduced as a trigger for the start of the acquisition.

Finally, a free running clock was used to give the user an additional control over the trigger of the experiment. This 'Happy clock' was also a trigger for the acquisition.

Those four signal were brought together by means of successive & gates that would provide a high signal when all the conditions were met for the start of the acquisition (supercycle timing, laser stabilisation, acquisition ready, 'Happy' user).

A.2 Acquisition sequence

A.2.1 Acquisition timing

The acquisition validation signal starts the main clocks of the acquisition logic, master to the logic. Three clocks are started simultaneously.

The first clock controls the implantation. The separator is allowed to send beam to the experimental setup only while this clock counts. It goes for an integral number of supercycles. This signal is brought together to an & gate in the ISOLDE control room where an additional condition is placed on the beam gate with regards to the proton impact (see e.g. section 4.1.3).

The second clock controls the acquisition system. It opens the buffer for the data acquisition system to accept the incoming information. This clock works also in integral units of supercycle and counts for at least as much as the first clock. For longer-lived isotopes, it counted longer that the first clock.

The third clock controls the rotation of the windmill. It counts for an integral number of supercycles bigger than the other two clocks, but shortened to account for the windmill spinning time. When this clock comes to an end, the windmill rotates and presents a fresh foil to the radioactive ion beam.

When using the ISOLDE tape station, a similar logic was followed but with short ISOLDE-controlled beam gates and ISOLDE-controlled tape motion.

A.2.2 Detector logic

The α, β and γ radiations were recorded with the devices introduced in section 3.3. The energy information was registered by the analog-to-digital converter of the data acquisition system while the timing information provided a logic gate for the data acquisition system.

For isotopes with limited production yields, the buffer of the data acquisition system could not be filled within a single laser frequency step and an additional pulser at ~ 100 Hz was used to fill that buffer.

A.2.3 Laser veto

When the Cu-vapour lasers fire, a strong electromagnetic pulse is released through the experimental hall. This signal, at a frequency of 11 kHz, was picked up by the cables and the pre-amplifiers of the detection logic. It resulted in the broadening of the resolution of our detection system.

In order to veto events coming in coincidence with this electromagnetic wave, the firing signal from the lasers was sent to the acquisition timing. The length of cable required to transport the signal could not allow for a prompt veto but the repetitive nature of the signal allowed to use the current signal as a precursor for the following pulse. A delay clock with timing 84 ms was used.

The duration of the noise on the detector logic was measured to be 6 ms long. During this period, the acquisition was blocked, resulting in a 7% loss in acquisition time.

This effect was not observed with the Nd:YAG lasers (Run II).

A.3 Frequency change

Once the three main clocks of the acquisition timing come to an end, the laser frequency step measurement is complete. The windmill is rotated, triggered by the windmill delay clock and the lasers are told to increment to the next laser frequency by the beam gate clock.

A clock that has ran its course can only restart once the counter is reset. The clocks are therefore only reset by the windmill rotation clock completion, in order to ensure that no acquisition can start until the setup is ready.

The frequency has been measured by a wavemeter and averaged over the length of the measurement. It is then sent to a file on the computer network that can be accessed by the data acquisition system for recording with the data.

The acquisition of the following laser frequency step may then start when the acquisition validation permits it. A complete layout of the electronic logic is shown on page 180.

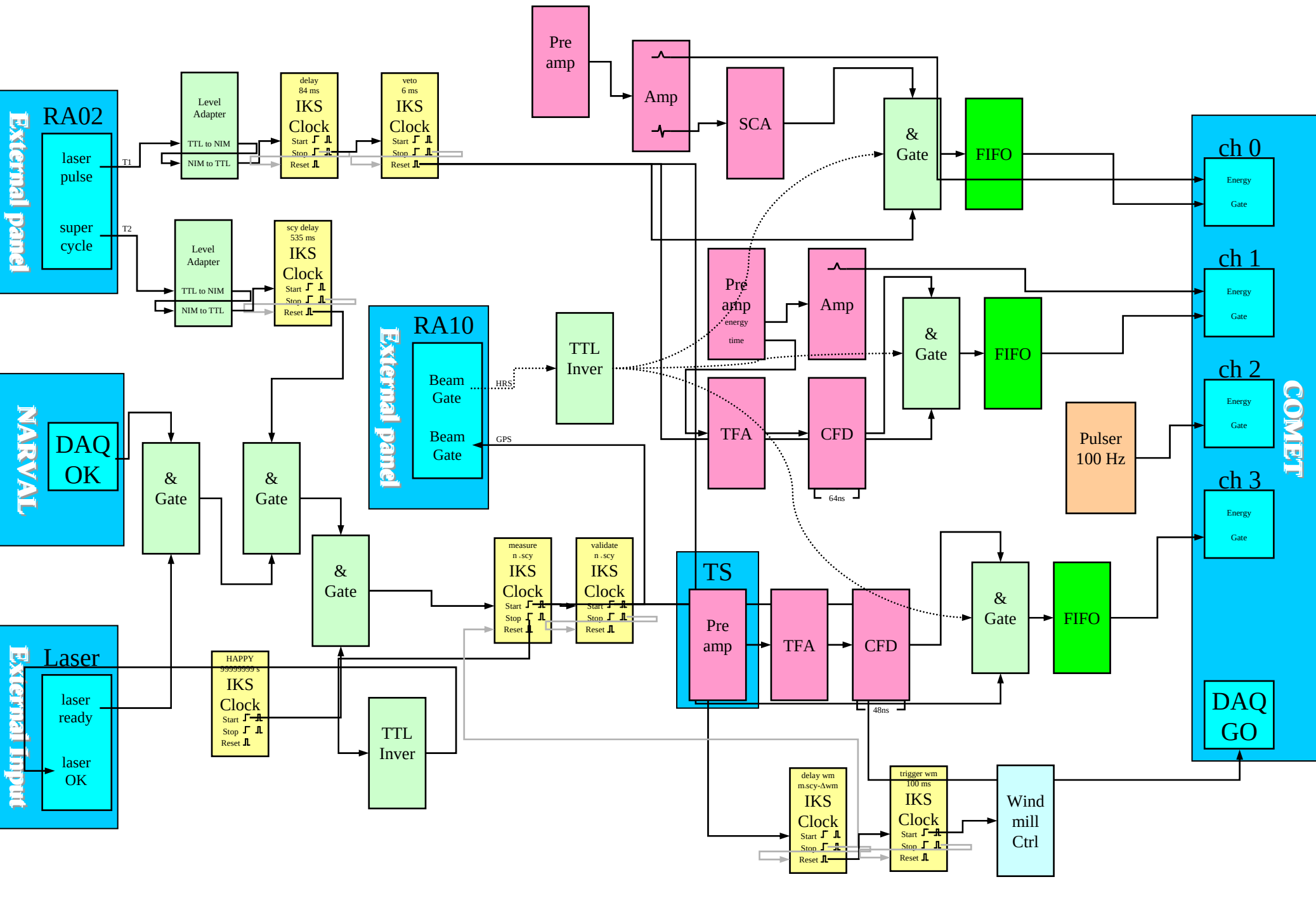
External panel
RA02
laser pulse
super cycle
T1
T2
Level Adapter
TTL to NIM
NIM to TTL
delay 84 ms
IKS Clock
Start
Stop
Reset
veto 6 ms
scy delay 535 ms
Pre amp
Amp
SCA
& Gate
FIFO
ch 0
ch 1
ch 2
ch 3
Energy
Gate
COMET
NARVAL
DAQ OK
External panel
RA10
Beam Gate
HRS
GPS
TTL Inver
Pre amp
energy
time
TFA
CFD
64ns
Pulser 100 Hz
External Input
Laser
laser ready
laser OK
HAPPY 99999999 s
measure n .scy
validate n .scy
TS
48ns
DAQ GO
delay wm m.scy-Δwm
trigger wm 100 ms
Wind mill Ctrl

Appendix B

New decay information

In the course of the study of the neutron-deficient polonium isotopes at CERN ISOLDE, isomeric beams of polonium were produced with higher intensities than previously available. In somecases higher amount of data could be collected and, through the production of isomeric beams, in a similar fashion to the copper isotopes [Ste07, Van04], a clear distinction between the low-spin and high-spin isomers of the odd-A isotopes could be achieved. Thanks to these improved conditions, new nuclear decay information on the neutron-deficient odd-A isotopes ^{195,199}Po are available.

B.1 Serendipity in the α decay of ^{195}Po

In the course of Run I, a shoulder was observed on the high-energy side of the α-decay energy spectrum of ^{195}Po. The possibility of a new α-decay line was considered, especially as this one showed a response to the laser scan consistent with an α particle emitted from the high-spin isomer in ^{195}Po.

This nuclei was therefore investigated further in the course of Run II with a higher solid angle for α-particle detection and a γ detector for possible coincidences. The lasers were used in broad-band mode to maximise production and acquire a high amount of data on that nucleus.

Paper VIII
T.E. Cocolios, *et al.*, in preparation for publication in *Physical Review C*.

The shoulder was proven to be arising from the summing of the energy of an electron in the internal decay of ^{195m}Tl with the energy of the α particles.

However, the data revealed new information on the fine structure decay of the low-spin isomer ^{195}Po^{ls} to ^{191}Pb^{ls}. The conversion coefficient in the decay of the 597 keV level in ^{191}Pb^{ls} could be estimated for the first time and confirmed an $E0$ component to the decay of that excited state. New branching ratios and hindrance factors in the α decay of the mother and daughter nuclei comfirmed the spin assignment of $I = \frac{3}{2}$ for the low-spin isomers in both ^{191}Pb and ^{195}Po.

Furthermore, a new level at 214.5 keV has been identified in the fine structure decay of the low-spin ^{195}Po^{ls}. The large hindrance factor and the observation of that state in the β^+/EC decay of ^{191}Bi ($I = (\frac{9}{2})$) only permit a spin assignment $I = \frac{5}{2}$. This level is therefore proposed as arising from the $\nu f_{5/2}^{-1}$ configuration.

By reporting also on the 1980 measurements of the β^+/EC decay of ^{193}Bi, the systematic of the lowest $I = \frac{5}{2}$ level in the odd-A neutron-deficient lead isotopes has been extended. The systematic of the neutron single energy levels $\nu p_{1/2}$, $\nu p_{3/2}$, $\nu f_{5/2}$, and $\nu i_{13/2}$ in neutron-deficient odd-A lead isotopes is finally presented.

Intruder configuration and single particle levels in ^{191}Pb

T.E. Cocolios, A.N. Andreyev, B. Bastin, J. Büscher, I.G. Darby, W. Dexters, M. Huyse, M. Keupers, Yu. Kudryavtsev, M.D. Seliverstov, P. Van Duppen, M. Venhart
Instituut voor Kern- en Stralingsfysica, Katholieke Universiteit Leuven, B-3001 Leuven, Belgium

S. Antalic
Department of Physics and Biophysics, Comenius University, Bratislava 84248, Slovakia

A. Barzakh, D. Fedorov, P. Molkanov
Petersburg Nuclear Physics Institute, 188350 Gatchina, Russia

V.N. Fedosseev, B.A. Marsh, J. Van de Walle
CERN, Ch-1211 Geneva 23, Switzerland

K.T. Flanagan, E.Mané
Department of Physics, University of Manchester, Manchester, M60 1AD, United Kingdom

S. Franchoo, I. Stefan
Institut de Physique Nucléaire d'Orsay, F-91406 Orsay, France

G. Huber
Institut für Physik, Johannes Gutenberg Universität, D-55099 Mainz, Germany

U. Köster
Institut Laue-Langevin, F-38042 Grenoble, France

R.D. Page
Oliver Lodge Laboratory, University of Liverpool, Liverpool, L69 7ZE, United Kingdom

M.A. Sjoedin
KTH - Royal Institute of Technology, SE-10044 Stockholm, Sweden

S. Zemlyanoy
Joint Institute of Nuclear Research, 141980 Dubna, Moscow Region, Russia

Abstract

The α decay of ^{195}Po has been studied at CERN ISOLDE using beams of resonantly laser-ionized polonium. Fine structures in the α decay of the low-spin and high-spin isomers have been fully resolved. The α and γ energies have been determined with greater precision than previously available. Identification of the parent state is made possible via isomer selection based on narrow-band laser frequency scanning. Branching ratios in the decay of ^{195}Po and ^{191}Pb have been examined. The conversion coefficient in the decay of the α-populated 597 keV excited state in ^{191}Pb has been determined for the first time. New branching ratio measurements have been performed in the decay of the low-spin isomer ^{191}Pb. The small Hindrance Factor is consistent with an unhindered decay. This observation confirms a $I^\pi = \frac{3}{2}^{(-)}$ spin assignment for this isomer and the excited state at 597 keV. A new state at 214.8(5) keV has been found in ^{191}Pb. A $I^\pi = \frac{5}{2}^{(-)}$ spin assignment is proposed based on the large Hindrance Factor in the α decay feeding this state and its observation in the β decay of ^{191}Bi in LISOL. The systematic single-particle energy levels for the $\nu p_{1/2}$, $\nu p_{3/2}$, $\nu f_{5/2}$ and $\nu i_{13/2}$ in the odd-A isotopes $^{191-207}$Pb are presented.

Internal conversion, α decay, $190 \leq A \leq 219$, Radioactive beams, Fine and hyperfine structure
23.20.Nx, 23.60.+e, 27.80.+w, 29.38.-c, 32.10.Fn

Introduction

Shape coexistence in the region of neutron-deficient lead isotopes is important and extensive studies of this phenomenon have been performed, both on the experimental and theoretical fronts [187, 188, 189, 190, 191, 192, 193, 194, 195, 196, 197, 198, 199, 200, 201]. With 109 neutrons, ^{191}Pb is located in the heart of this region. The study of the fine structures in the α decay of the low spin ($\frac{3}{2}^-$) and high spin ($\frac{13}{2}^+$) isomers of ^{195}Po have already been studied in a previous experiment using the gas-filled separator RITU [193]. However, limitations in the production mechanism and measuring conditions prevented the determination of the conversion coefficient of the decay of the 597 keV level, strongly populated by the ^{195}Po^{ls} fine structure α decay. The observation of an $E0$ component to the decay would indicate that both states are of similar spin and parity. This could confirm the shape-coexistence nature of this state, as suggested in Ref. [193]. Complementary to the α-decay studies, the β decay of neutron-deficient $I^\pi = (\frac{9}{2}^-)$ ^{191,193}Bi isotopes provides information on higher spin states.

The ground state properties of the polonium isotopes have been studied in a campaign of experiments at CERN ISOLDE (Run I in 2007 for $^{193-200,202,204}$Po and Run II in 2009 for $^{191-192,195,196,201,203,206-211,216,218}$Po). In this study, the fine structure in the α decay of ^{195}Po has been revisited. The relevant parts of the decay chain at mass 195 are shown in Fig. B.1.

The β decay of the neutron-deficient ^{191,193}Bi isotopes has been performed in CRC LISOL as part of a wider survey of the neutron-deficient bismuth isotopes [202, 203, 204, 205, 206]. This latter study populates the higher spin states in the daughter ^{191,193}Pb nuclei. Comparing the two decays allows the unambiguous determination of the spin of several energy levels in ^{191}Pb.

Fine structure α decay of ^{195}Po at ISOLDE and evidence of shape coexistence in ^{191}Pb

The proton beam from the CERN PS-Booster (1.4 GeV, 1.4 μA on average) impinged on a UC_x target (50 g·cm^{-2}) in a repeated sequence of pulses separated in periods of 1.2 s referred to as the supercycle. Nuclei produced in the spallation reaction diffused out of the target matrix and effused to the RILIS ion source cavity kept at high temperature ($\approx$ 2300 K). The atoms were then irradiated with three different laser beams to resonantly excite a valence electron from the polonium atom beyond its ionization potential and thus create a Po^+ ion [208]. The ions were then extracted from the ion source cavity, accelerated by DC field to an energy of 50 keV and separated according to the mass-to-charge ratio in the dipole magnet of the ISOLDE General Purpose Separator. Note that elements with a low ionization potential, such as thallium, may also be ionized upon contact with the hot surface of the atomizer. Isobaric contaminants may therefore be present in the mass-separated beam.

The ions were implanted in one of ten carbon foils (20 μg·cm^{-2}) mounted on a rotating wheel. The foil at the implantation point was surrounded by two Si detectors, a circular detector at the back of the foil (active area 300 mm^2, thickness

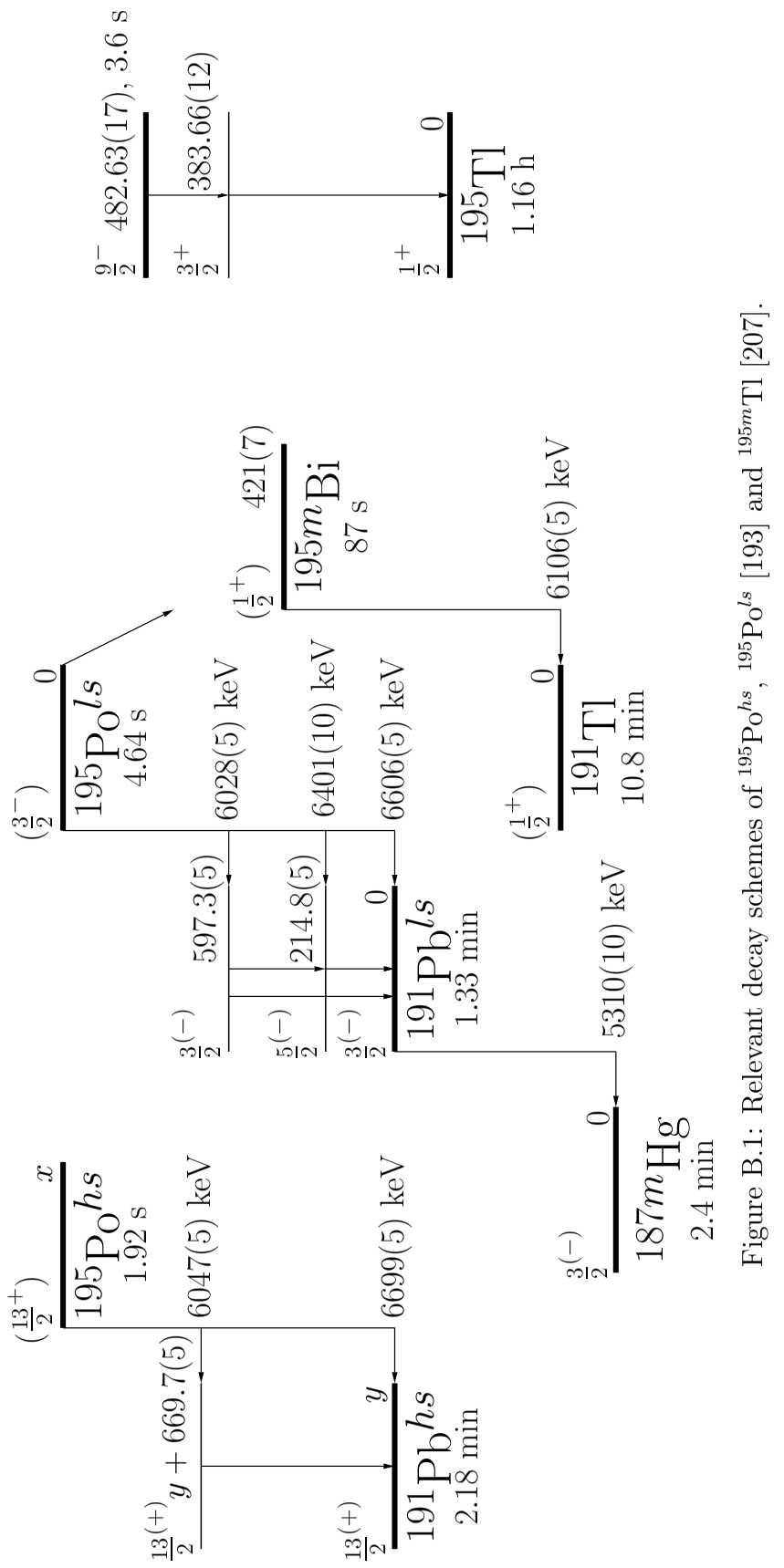

Figure B.1: Relevant decay schemes of ^{195}Po^{hs}, ^{195}Po^{ls} [193] and ^{195m}Tl [207].

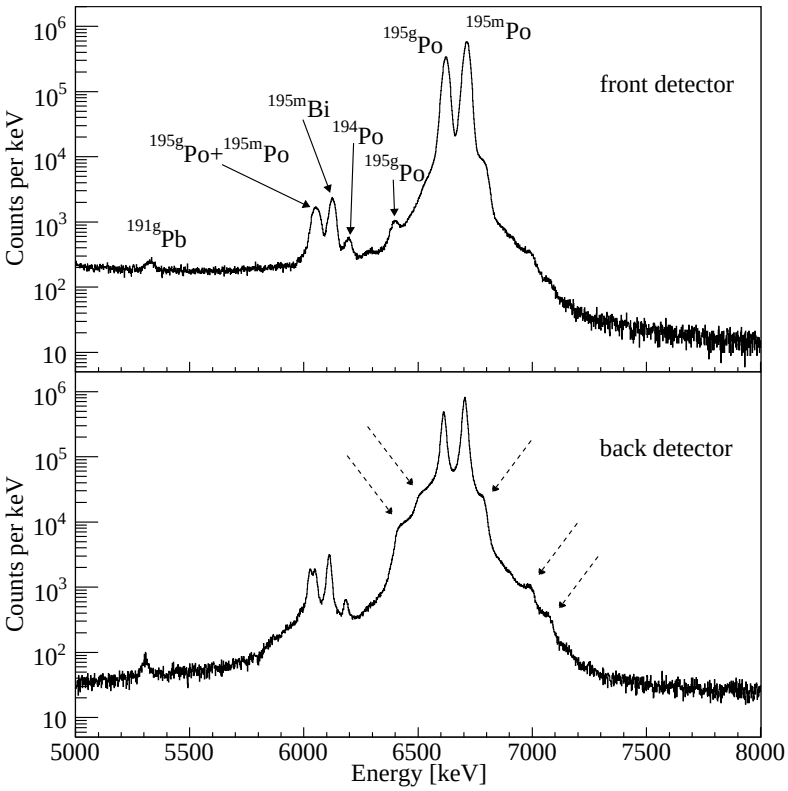

Figure B.2: α-particle energy spectra measured at mass number 195 while ionizing polonium (Run II) using the front detector (top) and the back detector (bottom) over a period of 5 hours. The peaks are labeled on the top spectrum with their assignments. The low- and high-energy shoulders of the two main α lines, indicated by dashed arrows on the bottom spectrum, are discussed in the text.

300 μm) and an annular detector at the front of the foil (active area 450 mm^2, thickness 300 μm) that let the ion beam through. The total covered solid angle was 66% of 4π. The energy resolution (Full Width at Half Maximum - FWHM) of those detectors for α particles with $E_\alpha = 5.5$ MeV was 20 keV and 30 keV, respectively. A HPGe detector was placed behind the back detector outside the vacuum chamber. Its energy resolution (FWHM) for γ radiation was 4.3 keV at $E_\gamma = 1.3$ MeV. The wheel was rotated regularly (one motion every second PS-Booster supercycle) to remove the relatively long-lived bismuth and lead activity.

The non-gated α-particle energy spectra are shown in Fig. B.2. The spectra show only α particles emitted in the decay of the polonium isotopes ^{194,195}Po and of their daughters ^{191}Pb and ^{195m}Bi. The presence of ^{194}Po in the beam originates from the tail of the mass line of that isotope. No ^{195}Tl contribution can be directly observed in this spectrum as it is a pure β^+/EC-decaying isotope. A very intense γ-ray transition at 384 keV, coming from the internal decay of ^{195m}Tl [207], is however observed in

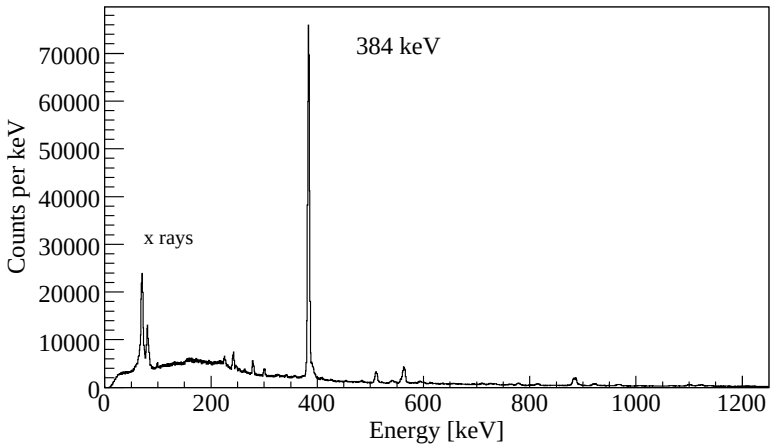

Figure B.3: γ-ray energy spectrum measured at mass number 195 while ionizing polonium (Run II). A broad gate is put on the Si detectors to discard the events coming from the foils that are not at the implantation position. The 384 keV γ line is in coincidence with the electrons emitted by the fully-converted 99 keV transition (see Fig. B.1). The γ rays that are not labeled are all attributed to the β decay of ^{195g}Tl.

the γ-ray energy spectrum shown in Fig. B.3.

Several features are observed in the α spectra in Fig. B.2. First, low-energy tails of the α peaks are observed, mostly visible on the two main transitions at $E_\alpha = 6606$ keV and $E_\alpha = 6699$ keV. These tails can be explained by the energy loss of the emitted α particles through the carbon foil. Indeed, at a beam energy of 50 keV, the polonium isotopes are implanted at a calculated depth of 25 nm [209] compared to the 90 nm thickness of the foil. This tail has a cut-off due to the limited angle range covered by the detectors and allowed by the foil mount geometry; this cut-off is visible as a shoulder for the two main peaks in Fig. B.2 at an energy of 6400 keV and 6500 keV, respectively.

A high-energy tail is also present, corresponding to the random summing of an α particle, for example from the decay of ^{195}Po, with that of an electron or positron, for example from the β decay of ^{195}Tl. The cut-off of the β-summing for the two main peaks in Fig. B.2 can be seen at an energy of 7000 keV and 7100 keV, respectively.

Another feature of this spectrum, which is seen in Fig. B.2 at 6790 keV, is a broad shoulder on top of the high-energy β-summing. This extra shoulder has been identified thanks to α-γ coincidences. Fig. B.4 shows the energy of the α particles as a function of the α-γ time difference for events in coincidence with a gate on the 384 keV γ-ray transition from the internal decay of ^{195m}Tl (see Fig. B.1). $E_\gamma = 384$ keV and corresponds to the electron emitted by the fully-converted transition at 99 keV in the decay of ^{195m}Tl. Two broad bands at an α energy of 6606 keV and 6699 keV are due to the random coincidences with the 384 keV transition. Both bands

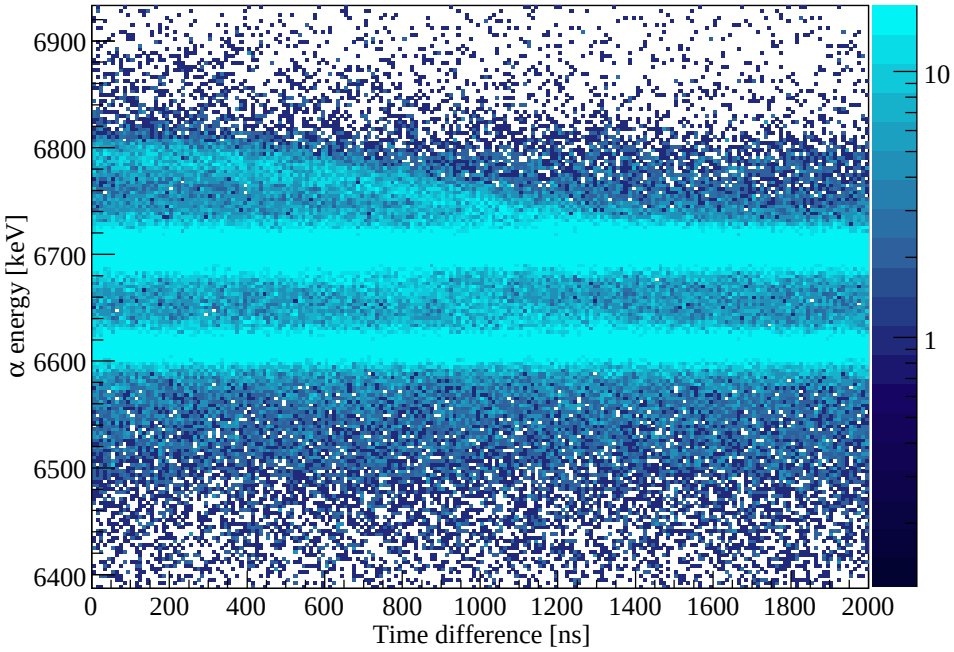

Figure B.4: (Color online) Energy of the α particles as a function of the α-γ time difference for events in coincidence with the γ-ray transition at 384 keV from the internal decay of ^{195m}Tl (Run II). The y axis shows the energy recorded in the Si detector while the x-axis shows the time difference between the Si detector and the Ge detector.

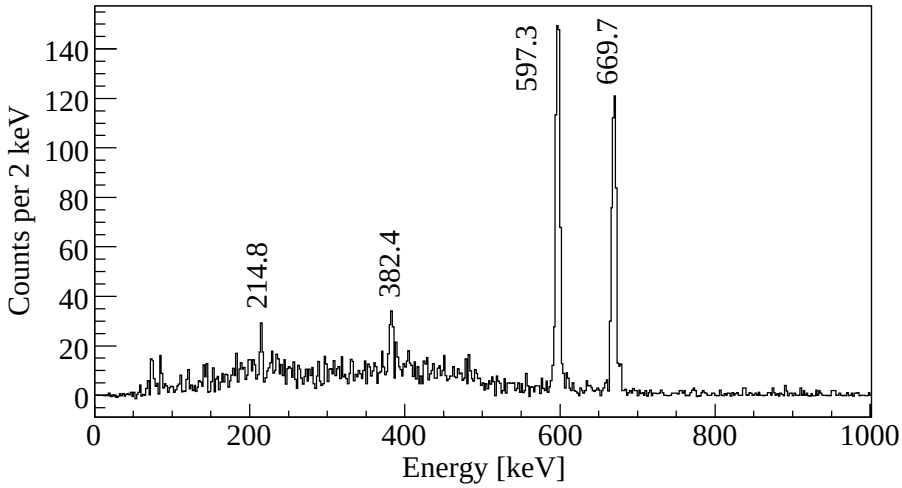

Figure B.5: Background-subtracted random-subtracted γ-ray energy spectrum in coincidence with the two α-particles around 6050 keV from the fine structures in the decay of ^{195}Po (Run II). The γ rays are labeled according to their energy.

show a sideband that seems to vanish at $\approx$ 1200 ns. This is attributable to the true coincidence between the 384 keV γ ray and the fully-converted transition at 99 keV in the decay of ^{195m}Tl. The energy of the electron emitted by the latter sums up with the energy of the α particles randomly. However, if the time difference between the detected electron and the α particle exceeds 1200 ns, the energy of the electron and of the α particle do not sum anymore as it is beyond the integration time of the acquisition electronics (1000 ns for this detector).

The fine structure decays of ^{195}Po have also been investigated using the coincidence data. The γ-ray energy spectrum in prompt coincidence with the two unresolved α-decay peaks identified around E_α = 6050 keV is shown in Fig. B.5. Two transitions at 597.3(5) keV and 669.7(5) keV, already known from previous studies [193], can be seen, as well as the x rays emitted together with the conversion electrons of those two transitions. Two additional transitions at 214.8(5) keV and 382.4(5) keV are identified for the first time. Those two energies add up to 597.2(7) keV and are therefore consistent with a cascade that decays from the 597 keV level. The γ ray observed in the excited ^{191}Pb nucleus are listed in Table B.3.

The energy of the α particle populating each state can be determined by gating on the γ-ray transitions separately to produce γ-gated α spectra. Those are shown in Fig. B.6. The two α decays around 6050 keV can then be clearly identified as an α decay at E_α = 6028(5) keV in coincidence with the γ-ray transition at E_γ = 597.3 keV and another at E_α = 6047(5) keV in coincidence with E_γ = 669.7 keV, respectively. In the case of the cascade, the 6028 keV α decay is identified in both cases while an additional α decay is observed at an energy E_α = 6401(10) keV in coincidence with the 215 keV γ-ray transition. The order of the cascade of γ-ray

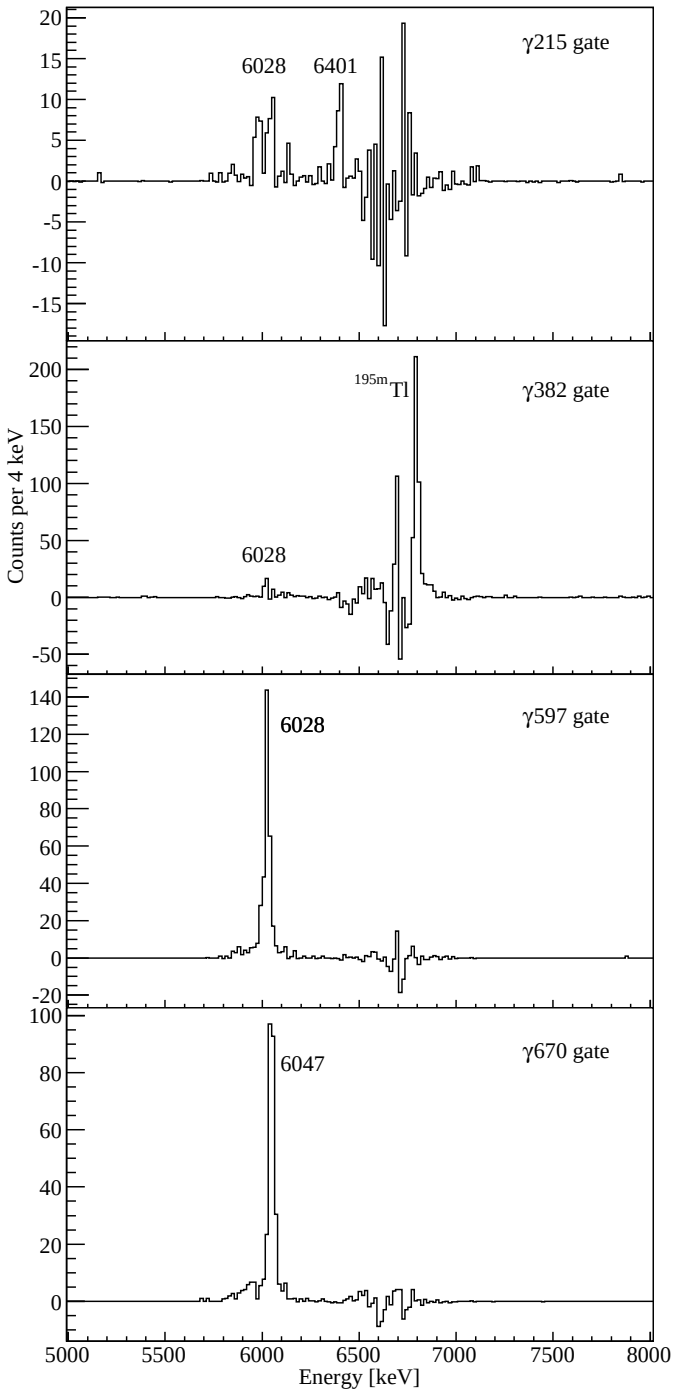

Figure B.6: From top to bottom: background-substracted, random-substracted γ-gated α spectra in coincidence with the γ-ray transitions at 214.8 keV (top), 382.4 keV, 597.3 keV and 669.7 keV (bottom) (Run II). The α-particle energies are labeled on the spectra. The summed α-electron energies can also be seen in coincidence with the 382.4 keV gate because of the proximity of the 383.66 keV γ-ray from the internal decay of ^{195m}Tl.

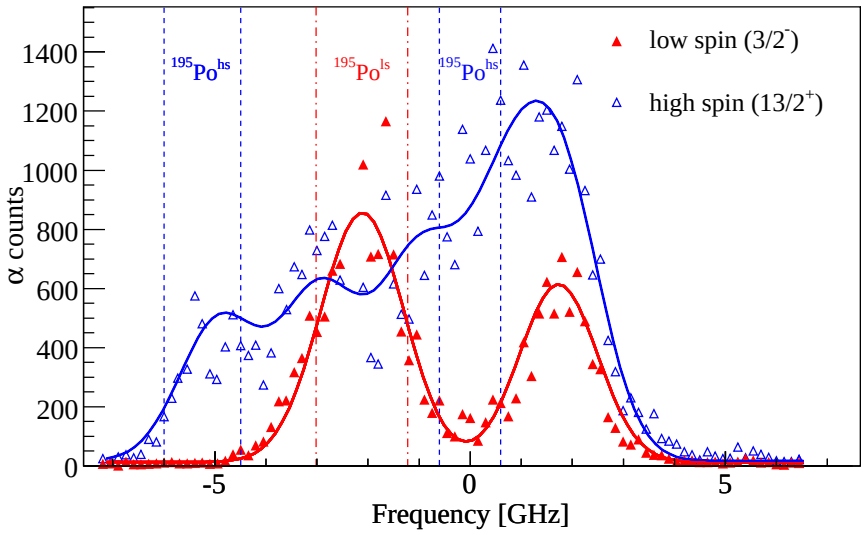

Figure B.7: Hyperfine structure of ^{195}Po^{ls} (red full triangles) and ^{195}Po^{hs} (blue open triangles) using the atomic transition at 843.38 nm from the ionization scheme of polonium (Run I). The range used to study ^{195}Po^{ls} is limited by the red dot-dashed lines while those for ^{195}Po^{hs} are limited by the blue dashed lines.

transitions from the 597 keV level is then ordered as going through a level at 214.8(5) keV, as shown in Fig. B.1.

The assignment of each component to the decay of the low- or high-spin isomer of ^{195}Po has been discussed in Ref. [193] in terms of Q_α value, from which it was concluded that the fine structure component $6028-597.3$ keV comes from the decay of the low-spin ^{195}Po^{ls} isomer while the $6047-669.7$ keV component comes from the decay of the high-spin ^{195}Po^{hs} isomer. Using the different atomic hyperfine profiles of the two nuclear states in ^{195}Po, it is also possible to enhance the production of one of the isomers over the other. The use of such isomeric beams has already been demonstrated for other elements [210, 211]. The hyperfine spectra for both nuclear states using the second transition of the ionization scheme at 843.38 nm, as described in Ref. [208], is shown in Fig. B.7 together with the regions enhancing the production of each isomer with respect to the other. The α-particle energy spectra for each laser frequency range are shown in Fig. B.8. The enhancement can be seen in the main α transitions as well as on the two peaks around $E_\alpha = 6050$ keV, confirming the assignment of each component. The transitions, their assignment and energies are summarized in Table B.1.

Based on the content of each transition, precise relative intensities can be extracted (see Table B.1). The partial information available in Ref. [193] can also be used to extract the conversion coefficient of the transition at 597.3 keV in two ways. First, the relative intensity of the 6028 keV α-decay line of ^{195}Po^{ls}, $b_\alpha = 0.32(1)$, mea-

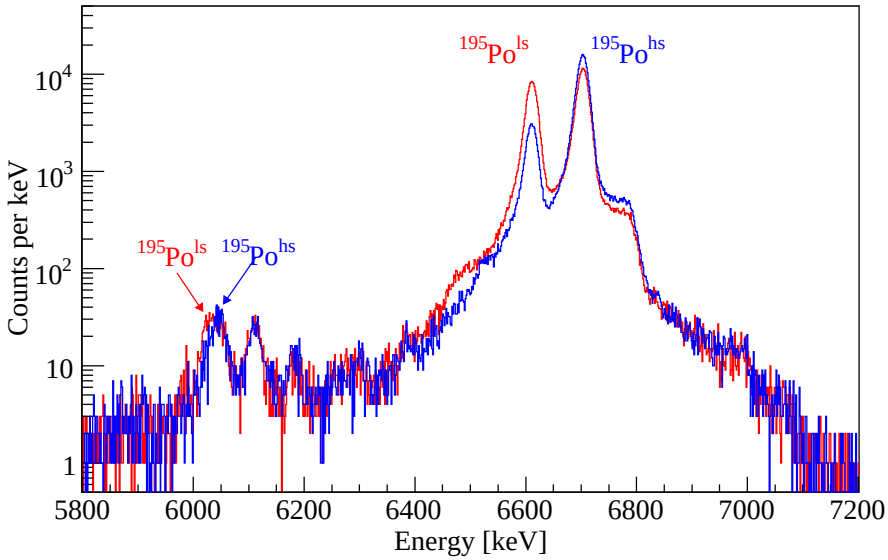

Figure B.8: Laser frequency-gated α-particle energy spectra of ^{195}Po using the ranges indicated in Fig. B.7 (Run I). In the red spectrum, the production of ^{195}Po^{ls} is enhanced while in the blue spectrum, that of ^{195}Po^{hs} is enhanced.

Table B.1: Properties of the fine structure decay of ^{195}Po^{ls} and ^{195}Po^{hs}: α-particle energy E_α and intensity I_α, Hindrance Factor HF, excitation energy in the daughter nucleus E_γ and conversion coefficient α of the decay of that excited level

Isotope	E_α [keV]	I_α [%]	HF	E_γ [keV]	α
^{195}Po^{ls}	6606(5) [212]	99.56(1)	1.64(14)	0	
	6401(10)	0.125(5)	125(14)	214.8(5)	
	6028(5)	0.32(1)	2.14(20)	597.3(5)	0.57(24)
^{195}Po^{hs}	6699(5) [212]	99.82(1)	1.95(60)	0	
	6047(5)	0.18(1)	2.45(75)	669.7(5)	0.8(3) [193]

Table B.2: Branching ratios in the decay of ^{195}Po^{ls} and ^{191}Pb^{ls} from this work and in the literature.

Isotope	b_α [%]	b_α^{lit} [%]
^{195}Po^{ls}	93.5(35)	63(25) [212]
^{191}Pb^{ls}	0.056(6)	0.013(5) [215]

sured in this study, can be compared with the known contribution from the α-γ chain, $b_{\alpha\gamma} = 0.17(5)$, given in Ref. [193], yielding a conversion coefficient $\alpha = 0.88(56)$. The second approach is to rescale the known value of $\alpha = 0.8(3)$ in ^{195}Po^{hs} from Ref. [193] by comparing the α branching ratios and γ intensities in the decay of ^{195}Po^{ls,hs}, yielding a value of $\alpha = 0.50(27)$. Averaging between those two independent estimates, a conversion coefficient of 0.57(24) is found compared to the calculated values $\alpha_{tot}(E2) = 0.019$, $\alpha_{tot}(M1) = 0.068$ and $\alpha_{tot}(E1) = 0.007$. This shows that the transition has a large $E0$ contribution, confirming the similar spin assignment for the low-spin isomer and the 597.3 keV level in ^{191}Pb. It is therefore a good candidate for shape coexistence as stated in Ref. [193]. Moreover, the spin assignment of $\frac{13}{2}^{(+)}$ for the 669.7 keV level in ^{191m}Pb is also confirmed by combining the spin assignment from Ref. [213] with the identification of an $E0$ component in its decay [193].

Considering further the content of the different α-decay transitions identified in Fig. B.2, the different lifetimes, and the fraction of the beam that recoils out of the carbon foil after emitting an α particle [214], accurate branching ratios can be extracted. The α branching ratio for ^{191}Pb^{ls} is found to be $b_\alpha = 0.056(6)\%$. For ^{195}Po^{ls}, the branching ratios in the decay of the low-spin ^{195m}Bi have to be considered. Although the precision is limited [203], the fraction of ^{195}Po^{ls} that β-decays is small enough that a good accuracy for b_α can still be reached. A value of $b_\alpha = 93.5(35)\%$ is found, assuming that the β decay of ^{195}Po^{ls} only populates the $I = (\frac{1}{2}^+)$ state in ^{195}Bi. Those values are consistent with the previous literature values [212, 215], as shown in Table B.2, and benefit from a larger amount of data. No new branching ratios could be determined in the decay of ^{195}Po^{hs} or ^{191}Pb^{hs} as the α decays of the high-spin ^{195}Bi and ^{191}Pb^{hs} are not observed.

Using the formalism of Rasmussen [216], Hindrance Factors (HF) in the decay of ^{195}Po with respect to ^{194,196}Po [212], assuming no change in angular momentum ($\Delta L = 0$), are calculated and given in Table B.1. All HF in the main component and in the fine structure decay of ^{195}Po^{ls} and ^{195}Po^{hs} are low $(1-3)$. This means that the α decay is unhindered and that the spin of the mother and daughter states are the same. The conclusions presented in Ref. [193] are thus all confirmed. The high HF of the 6401 keV α decay, however, indicates a change in spin or configuration between ^{195}Po^{ls} and the 215 keV excited level in ^{191}Pb^{ls}. Finally, the HF of ^{191}Pb^{ls} with respect to ^{190,192}Pb [217] shows also a small value of 0.42(8), consistent with an unhindered decay to the $I^\pi = \frac{3}{2}^-$ isomer ^{187m}Hg [218]. This offers an experimental confirmation, according to the $\Delta L = 0$ α-decay strong rule, that the spin assignment of the ^{191}Pb^{ls} isomer is indeed $I^\pi = \frac{3}{2}^-$, and thus similarly for the excited state at

597.3 keV and for the ^{195}Po^{ls} isomer.

β decay of ^{191,193}Bi in LISOL and migration of the $\nu f_{5/2}$ single-particle energy level in neutron-deficient lead isotopes

The α and β decays of the neutron-deficient $^{192-196}$Bi isotopes have been studied at the CRC LISOL facility in the years 1980 [202, 203, 204, 205, 206]. The radioactive nuclei were produced in fusion-evaporation reactions using ^{14}N, ^{16}O and ^{20}Ne beams on natural Ir (37.3% ^{191}Ir, 62.7% ^{193}Ir), natural Re (37.4% ^{187}Re, 62.6% ^{187}Re) and ^{181}Ta targets, respectively. The radioactive recoils were subsequently ionized in a plasma ion source, mass separated and implanted in an aluminized mylar tape. Single γ-ray energy spectra were recorded with two Ge detectors with 20% efficiency at 1.3 MeV.

The lists of observed γ-ray energies for ^{191,193}Bi are given in Table B.3. For ^{193}Bi, relative efficiencies I_γ are also given. By matching the summed energies of several γ-ray transitions with existing γ-ray energies, possible cross-over transitions in the decay of some excited levels are proposed. Note that true summing in the detector alone cannot explain the observed relative intensities and that those transitions are therefore real.

Since the 214.8 keV γ ray is populated by the α decay of the low-spin $I^\pi = (\frac{3}{2}^-)$ ^{195}Po^{ls} isotope as well as by the β decay of the high-spin $I^\pi = (\frac{9}{2}^-)$ ^{191}Bi isotope, only a spin assignment of $I = \frac{5}{2}^{(-)}$ is possible. This is also supported by the high HF measured in the α-decay study (see Table B.1). This would correspond to a neutron hole in the $\nu f_{5/2}$ orbital and completes the systematic single-particle energy levels in the neutron-deficient odd-A lead isotopes.

From the study of the decay of the isotopes ^{195,197}Bi [205, 206], it has been observed that the transition with the most intensity to the low-spin isomer in the lead daughter isotope is the decay of the $\frac{5}{2}^-$ excited state to the $\frac{3}{2}^-$ state. The same observation is made for the decay of ^{191}Bi. Based on the confirmation of the spin of ^{191}Pb^{ls} as $\frac{3}{2}^-$, and by comparing the relative intensities of the different transitions presented in Table B.3, the 174.5 keV level in ^{193}Pb is also a good candidate for the $\nu(f_{5/2})^{-1}$ configuration. The systematic neutron single-particle energy levels for the $\nu p_{1/2}$, $\nu p_{3/2}$, $\nu f_{5/2}$ and $\nu i_{13/2}$ orbitals in the neutron-deficient odd-A isotopes $^{191-207}$Pb are presented in Fig. B.9.

Conclusion

In conclusion, using resonant laser ionization, high yields of ^{195}Po were achieved. The study of the α decay of the low-spin and high-spin isomers in coincidence with the lasers has allowed to extract α-particle and γ-ray energies, branching ratios and conversion coefficients with better precision. Hindrance Factors confirm the spin assignments $I = \frac{3}{2}$ for the low-spin isomers ^{191}Pb^{ls} and ^{195}Po^{ls}. The conversion coefficient in the fine structure decay of ^{195}Po^{ls} is measured for the first time, confirming the spin assignment $I = \frac{3}{2}$ for the 597 keV energy level in ^{191}Pb and its shape coex-

Table B.3: List of γ-ray energies E_γ and relative intensities I_γ observed in the excited structure of ^{191,193}Pb from the α decay of ^{195}Po and the β decay of ^{191,193}Bi. The proposed cross-over transitions in ^{193}Pb are based on summed γ-ray energies matching an observed γ-ray energy with too large relative intensity to be attributed to summing effects in the detector.

Isotope	E_γ [keV]	I_γ [%][1]	Origin	Coincident γ-ray
^{191}Pb	214.8(5)	4.3(10)	α, β	382.4
	382.4(5)	10.6(21)	α	214.8
	597.3(5)	100	α	
	669.7(5)		α, β	
	708.26		β	
	820.2		β	
	954.7		β	
	1082.3		β	
	1117.71		β	
Isotope	E_γ [keV]	I_γ [%][2]	Possible cross-over	
^{193}Pb	174.5	100		
	196.8	5.4		
	290.6	7.8		
	320.1	7.7		
	354	8.7		
	505.9	5.2		
	554.2	38		
	621.2	9.2		
	681.1	48		
	687.2	12.4		
	711.1	48.8		
	739.1	13.5		
	750.1	6.3	$196.8 + 554.2$	
	818.5	14.2	$196.8 + 621.2$	
	861.8	20	$174.5 + 687.6$	
	873.9	29.4	$320.1 + 554.2$	
	995.7	23.8		
	1022.3	12.8		
	1049.1	9.9	$174.5 + 873.9$	
	1116.1	8.4		
	1124.7	5.2		
	1171.6	10.1	$174.5 + 995.7$	
			$354 + 818.5$	
	1630.6	0.4	$505.9 + 1124.7$	

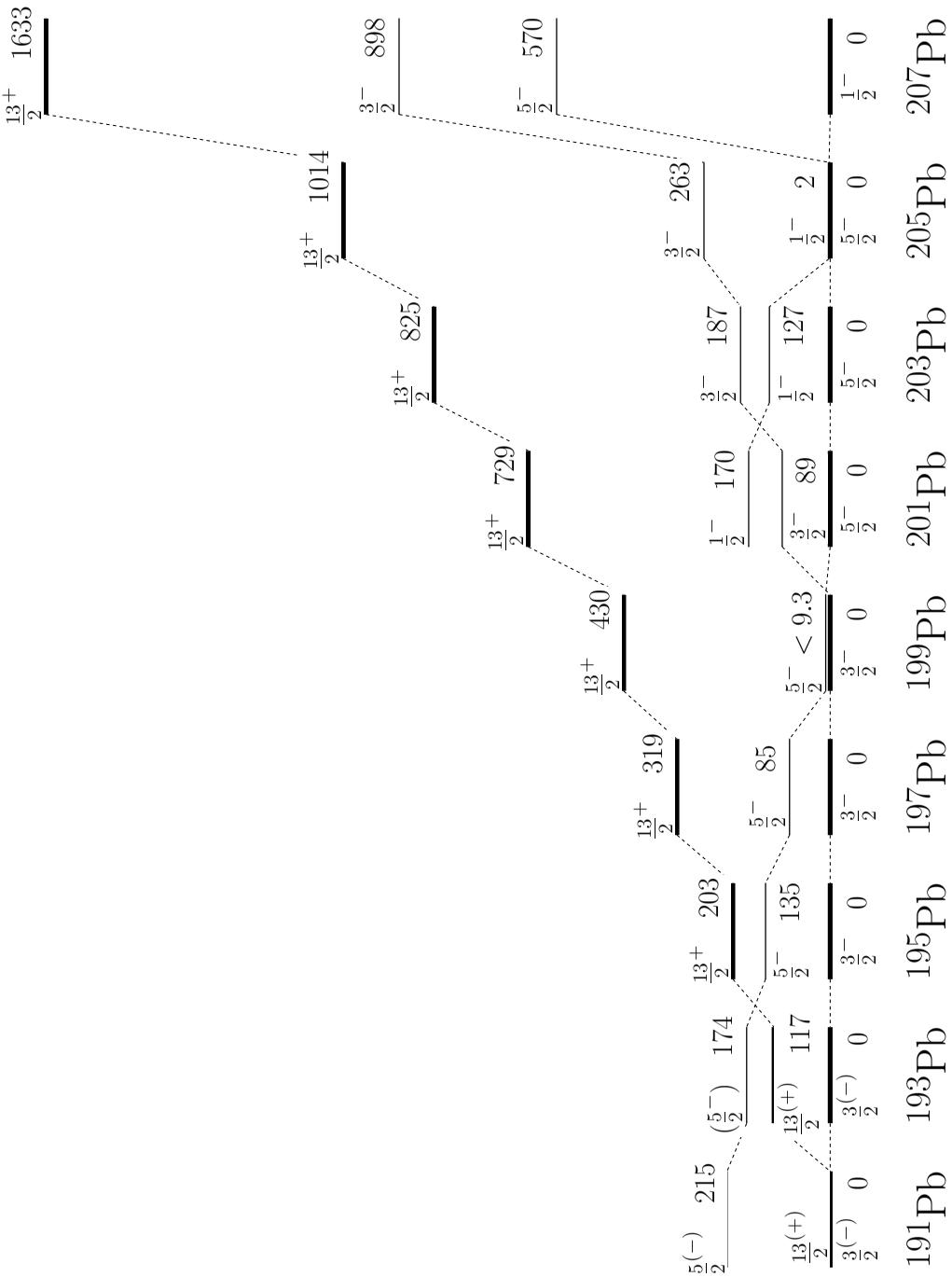

Figure B.9: Systematic neutron single-particle energy levels of $\nu p_{1/2}$, $\nu p_{3/2}$, $\nu f_{5/2}$ and $\nu i_{13/2}$ orbitals in neutron-deficient odd-A Pb isotopes. This completes the previous systematics presented in Ref. [205].

istence nature. A new level is found at 214.8 keV and is also observed in the β decay of ^{191}Bi, allowing a spin assignment of only $I = \frac{5}{2}$. It is a good candidate for the $\nu(f_{5/2})^{-1}$ level and completes the systematics of the neutron single-particle energy levels in the neutron-deficient lead isotopes down to ^{191}Pb.

Acknowledgments

We would like to thank the ISOLDE collaboration and the CRC team for providing excellent beams. This work was supported by FWO-Vlaanderen (Belgium), GOA/2004/03 (BOF-K.U.Leuven), by the IUAP - Belgian State Belgian Science Policy - (BriX network P6/23), by the European Commission within the Sixth Framework Programme through I3-EURONS (Contract RII3-CT-2004-506065), by the U.K. Science and Technology Facilities Council, and by the Slovak Research and Development Agency (Contract No. APVV-20-006205).

B.2 β^+/EC decay of ^{199}Po

In this section, some observation on the γ-rays emitted after the β^+/EC decay of ^{199}Po to ^{199}Bi are presented. As the setup did not allow to study coincidences, no level scheme can be built. Many discrepancies with the literature are however highlighted.

The β^+/EC decay of the isotope ^{199}Po is a nice illustration of the cold war: everyone wants it, everyone does it, everyone claims something different and in the end, no one seems to get it right. The leve structure of ^{199}Bi was indeed studied at CERN ISOLDE in the α decay of ^{203}Rn, At [Jon71], at the Joint Institute for Nuclear Research (JINR), Dubna (Russia), in the fusion-evaporation of ^{10}Be on ^{197}Au [Kor76], and at the UNiversity Isotope Separator at Oak Ridge (UNISOR) facility, Oak Ridge (TN, USA), in the fusion-evaporation of ^{14}N on natural Ir [Sto85]. In the latter work, the discrepancies between the three approaches have been thoroughly highlighted. The main source of difficulties arises from the fact that the ground state and the isomer have similar half-lives ($T_{1/2} = 5,47$ min & 4.17 min) and that the purity is limited.

The study presented in [Sto85] is the first that produces a mass-separated beam of ^{199}Po to study the β^+/EC decay independently from other polonium isotopes or from other decay modes (α decay of ^{203}At in [Jon71]). The reaction used in that study should also populate more strongly the high-spin isomer ^{199m}Po while the α decay of ^{203}Rn in [Jon71] should in contrary populate more the low-spin ground state ^{199g}Po. Based on those assumptions, the origin of the different lines was proposed.

Resonant laser ionisation offers high beam intensities and high selectivity. It is also possible to identify each isomer according to its hyperfine structure. In the study of the ground state properties of the neutron-deficient polonium isotopes at CERN ISOLDE, discussed in chapter 6, intense beams of mass-separated ^{199}Po were produced. The background conditions were optimal with only a possible contamination of ^{199}Tl ($T_{1/2} = 7.42$ h). The beams were implanted at the ISOLDE tape station and measured with a single HPGe crystal.

The hyperfine structure of the two isomers was measured by scanning the laser frequency of the second resonant transition of the laser ionisation scheme, as detailed in section 6.2. Following the intensity of a γ-ray attributable to a pure decay from one of the two isomers yields the hyperfine spectrum. The hyperfine spectra following the 246 keV (^{199g}Po) and 1002 keV (^{199m}Po) γ-ray transitions is shown in Fig. B.10.

By selecting a specific frequency range, it is possible to enhance the production of one of the two isomers over the other. The ranges selected for ^{199g}Po and ^{199m}Po are shown in Fig. B.10. Note that although it is possible to produce a very clean beam of ^{199m}Po, it is more difficult to do so for ^{199g}Po as it does not have a maximum outside of the the hyperfine structure of ^{199m}Po. It is however possible to produce a pure spectrum of either ^{199g}Po or ^{199m}Po by a linear combination of the spectra produced in those two ranges. Those purified β^+/EC decay spectra are shown in Fig. B.11.

The two spectra are normalised to a background line for better display (from the

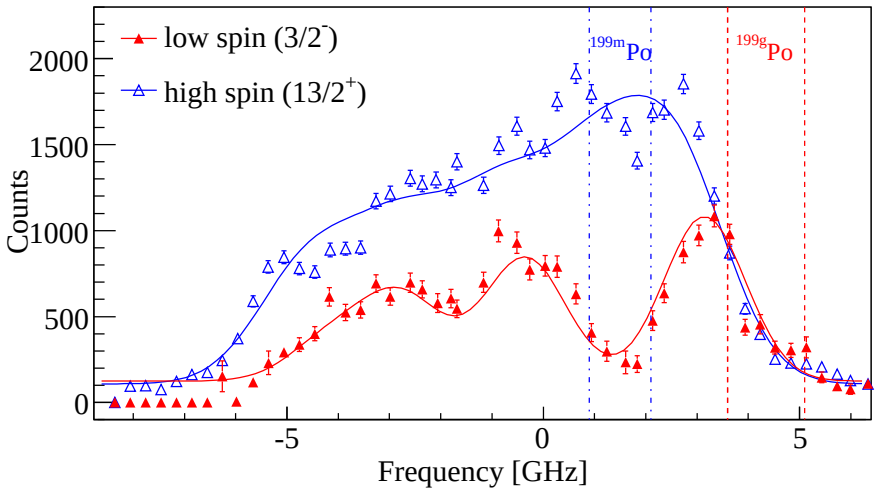

Figure B.10: Hyperfine structure spectra of the 246 keV (^{199g}Po, full red triangles) and 1002 keV (^{199m}Po, open blue triangles) γ-ray transitions. The range of frequencies enhancing the production of ^{199g}Po is delimited by the red dashed lines while that for ^{199m}Po is delimited by the blue dot-dashed lines.

β^- decay of ^{140}La ($T_{1/2}$ = 40.3 h), implanted in the tape station the week prior to the experiment). Many transitions appear to be clearly of pure origin, like that at 880 keV (^{199g}Po) or that at 1034 keV (^{199m}Po), as suggested in [Sto85]. There are, however, some disagreements, as seen, for example, in the 846 keV transition, clearly present in both γ-ray energy spectra. The lists of observed γ-rays for ^{199g,m}Po and the relative intensities are given in Tables B.4 and B.5.

As the setup was limited to a single HPGe crystal, no coincidences could be studied. It is however possible to try and find cross-over transitions by summing γ-ray energies to match an exisiting transition. Note that this could also be an evidence of summing effects in the detector. The transitions matching by summation are listed in Table B.6.

It might be interesting, in light of the discrepancies noted here, to perform a thorough nuclear decay study of that isotope with a more appropriate setup.

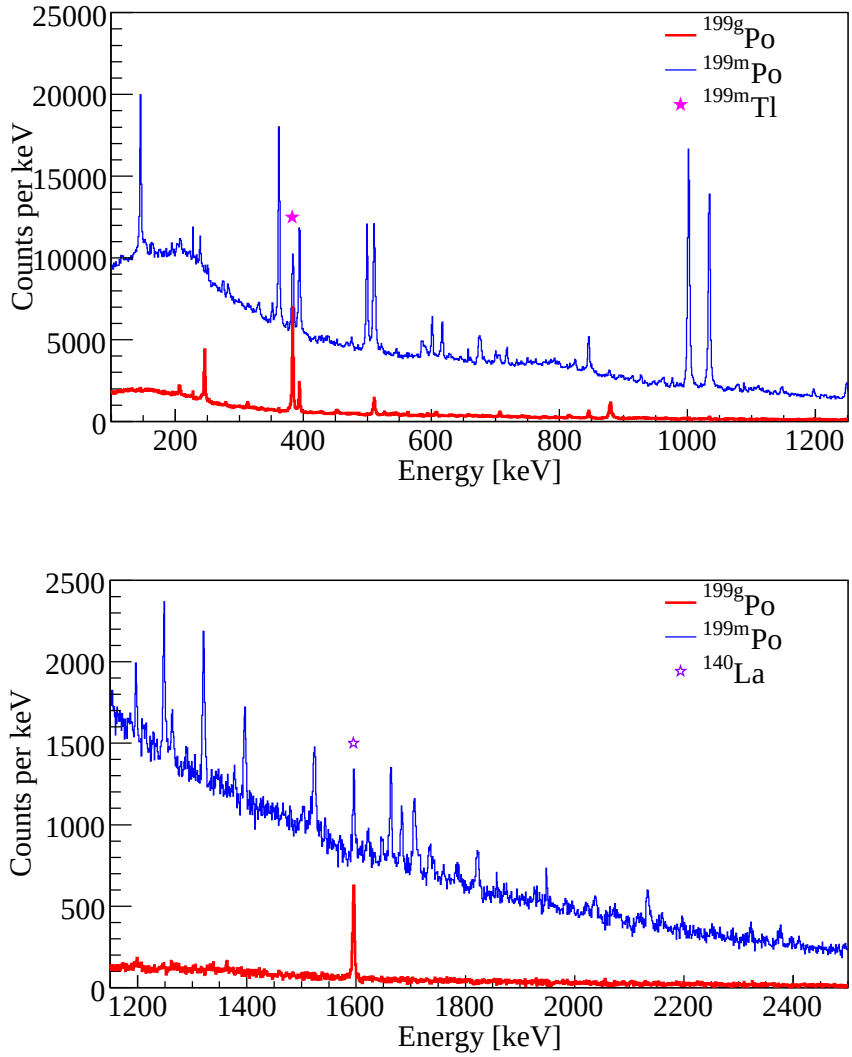

Figure B.11: γ-ray spectra of purified ^{199g}Po (thick red line) and ^{199m}Po (thin blue line) obtained by a linear combination of the spectra obtained at the two ranges hilighted in Fig. B.10. Both spectra are normalised to the background line at 1596 keV (^{140}La) for better display.

Table B.4: List of γ-ray transitions in ^{199g}Po and their intensities in this work and the previous studies [Jon71, Kor76, Sto85].

This work		[Sto85]		[Kor76]		[Jon71]	
E_γ [keV]	I_γ	E_γ [keV]	I_γ	E_γ [keV]	I_γ		
^{199g}Po							
206.83(9)	17.9(14)	206.7	18			206.6	18.9
245.88(2)	100	246.0	100	246.0	100	245.9	100
278.76(17)	6.7(6)						
313.07(11)	13.4(11)						
393.95(3)	94.2(72)	394.2					
452.69(17)	17.6(15)	452.5	14.2				
526.89(19)	10.9(10)	527.0	9.6				
563.47(23)	18.2(71)						
607.42(13)	19.5(16)						
707.10(8)	28.9(23)						
815.52(20)	24.1(20)	815.3	9.6				
845.82(7)	55.6(43)	845.7	82.8			845.8	63
879.49(5)	184(14)	880.2				880.4	

Table B.5: List of γ-ray transitions in ^{199m}Po and their intensities in this work and the previous studies [Jon71, Kor76, Sto85].

This work		[Sto85]		[Kor76]		[Jon71]	
E_γ [keV]	I_γ	E_γ [keV]	I_γ	E_γ [keV]	I_γ		
^{199m}Po							
145.74(2)	9.9(5)	145.6	19.4			145.8	16.3
227.91(15)	1.2(1)			229.1	10.2		
239.12(7)	2.1(1)	239.3	7.5				
351.65(10)	1.6(1)						
361.88(1)	24.5(13)	361.9	36.6	361.6	47	361.6	27
383.50(3)	12.4(6)						
394.13(2)	14.7(8)	394.2					
499.47(2)	21.7(11)	499.7	21.9	499.8	42.3		
601.32(4)	7.4(4)	601.2	10.9				
616.90(4)	7.7(4)	616.4	1.3				
675, 73(7)	11.7(6)						
717.94(8)	4.4(2)	717.8	6.1				
824.56(17)	2.8(2)	825.2	3.6				
845.69(5)	11.3(6)	845.7	19.8			845.8	35
1001.74(1)	100	1001.7	100	1002.0	100	1002.0	100
1034.00(1)	102.7(53)	1033.8	83	1034.4	100	1034.0	117
1077.86(26)	3.2(2)						
1147.33(16)	3.5(2)						
1197.19(13)	2.7(2)	1197.5	4.2				
1248.43(7)	7.8(4)	1248.4	8.7				
1263.64(25)	2.6(2)	1262.8	3.2				
1321.00(8)	9.8(5)	1320.1	10.0				
1396.22(11)	7.0(4)	1395.9	7.3				
1523.66(12)	6.8(4)	1523.6	6.8				
1621.9(4)	2.3(1)						
1647.38(33)	1.4(1)						
1663.57(9)	6.6(3)	1663.4	7.5				
1683.47(15)	4.4(2)	1683.2	6.3				
1707.19(16)	7.8(4)	1706.2	6.5				
1735.3(4)	3.4(2)						
1822.07(21)	5.3(3)	1822.1	4.0				
1857.19(19)	0.8(1)						
1948.53(15)	1.8(1)	1949.4	3.3				
2037.6(5)	2.4(1)	2036.7	1.7				
2133.92(21)	3.9(2)	2133.1	3.4				
2322.42(34)	1.6(1)						
2376.01(55)	2.1(1)						

Table B.6: Identification of possible cross-over transitions or of summing effects in the detector by summing γ-ray energies.

E_γ [keV]	Sum	Known coincidence
^{199g}Po		
452.69	206.83+245.88	√
526.89	245.88+278.76	
707.10	313.07+393.95	
879.49	313.07+563.47	
^{199m}Po		
1147.33	145.75+1001.74	
1197.19	351.65+845.69	
1263.64	227.91+1034	
1396.22	145.75+1248.43	
	361.88+1034	√
	394.13+1001.74	√
1523.66	675.73+845.69	
1647.38	383.5+1264.64	
	499.47+1147.33	
1707.19	675.73+1034	
1822.07	499.47+1321	
	675.73+1147.33	
1857.19	824.56+1034	
1948.53	239.12+1707.19	
2037.64	351.65+1683.47	
	717.94+1321	
	1001.74+1034	
2322.42	616.9+1707.19	
	675.73+1647.38	
	1001.74+1321	

Main bibliography

[And] A.N. Andreyev, M. Huyse, P. Van Duppen, S. Antalic, S. Saro, M. Venhart, S. Hofmann, D. Ackermann, F Heßberger, B. Kindler, B. Lommel, S. Heinz, K. Nishio, U. Köster, R. Page, S. Franchoo, S. Vermote, C. Wagemans, and M. Veselský. Identification and systematical studies of the electron-capture delayed fission (ECDF) in the lead region - Part I: ECDF of ^{178,180}Tl and ^{200,202}Fr isotopes. Proposal to the CERN INTC - accepted under experiment number IS466.

[And00] A.N. Andreyev, M. Huyse, P. Van Duppen, L. Weissman, D. Ackermann, J. Gerl, F.P. Heßberger, S. Hofmann, A. Kleinböl, G Münzenberger, S¿ Reshitko, C. Schlegel, H. Schaffner, P. Cagarda, M. Matos, S. Saro, A. Keenan, C. Moore, C.D. O'Leary, R.D. Page, M. Taylor, H. Kettunen, M. Leino, A. Lavrentiev, R. Wyss, and K.H. Heyde. A triplet of differently shaped spin-zero states in the atomic nucleus ^{186}Pb. *Nature*, 405 (2000) 430–433.

[And06] A.N. Andreyev, S. Antalic, D. Ackermann, S. Franchoo, F.P. Heßberger, S. Hofmann, M. Huyse, I. Kojouharov, B. Kindler, P. Kuusiniemi, S.R. Lesher, B. Lommel, R. Mann, G. Münzenberg, K. Nishio, R.D. Page, J.J. Ressler, B. Streicher, S. Saro, B. Sulignano, P. Van Duppen, D. Wiseman, and R. Wyss. α-decay of the new isotope ^{187}Po: probing prolate structures beyond the neutron mid-shell at $N = 104$. *Physical Review C*, 73 (2006) 044324.

[Ans86] M. Anselment, W. Faubel, A. Göring, S.and Hanser, G. Meisel, H. Rebel, and G. Schatz. Ithe odd-even staggering of the nuclear charge radii of Pb isotopes. *Nuclear Physics A*, 451 (1986) 471–480.

[Aud03] G. Audi, A.H. Wapstra, and C. Thibault. The AME2003 atomic mass evaluation. *Nuclear Physics A*, 729 (2003) 129–676.

[Avg06] M. Avgoulea, M. Mahgoub, J. Billowes, P. Campbell, A. Ezwam, D.H. Forest, M. Gardner, J. Huikari, A. Jokinen, A. Nieminen, G. Tungate, and J. Äystö. Laser spectroscopy of stable Os isotopes. *Hyperfine Interactions*, 171 (2006) 217–223.

[Basa] B. Bastin, Janssens R.V.F., M. Carpenter, F. Kondev, B. Laurent, J. Cederkäl, P. Delahaye, A. Dorsival, L.M. Fraile, J. Van de Walle, D. Voulot, F. Wenander, E. Clément, K. Hadynska, J. Iwanicki, P.J. Napiorkowsko, J. Srebrny, K. Wrzosek, M. Zielinska, A.N. Andreyev, N. Bree, T.E. Cocolios, J. Diriken, M. Huyse, O. Ivanov, N. Patronis, P. Van Duppen, L. Achouri, F. Delaunay, M. Marquès, N.A. Orr, T. Behrens, V. Bildstein, T. Fästermann, R. Gernhäuser, Th. Kröll, R. Krücken, P. Mahgoub, M. Maierbeck, K. Wimmer, T. Davinson, P. Woods, P.T. Greenlees, P. Jones, R. Julin, S. Juutinen, P. Peura, P. Rahkila, P.A. Butler, T. Grahn, R.-D. Hersberg, D.T. Joss, R.D. Page, E.S. Paul, J. Pakarinen, A. Petts, M. Scheck, I. Stefanescu, D.G. Jenkins, and A. Robinson. Shape coexistence measurements in even-even neutron-deficient polonium isotopes by Coulomb excitation using REX-ISOLDE and the Ge MINIBALL array. Proposal to the CERN INTC - accepted under experiment number IS479.

[Basb] B. Bastin, Janssens R.V.F., M. Carpenter, F. Kondev, B. Laurent, J. Cederkäl, P. Delahaye, A. Dorsival, L.M. Fraile, J. Van de Walle, D. Voulot, F. Wenander, E. Clément, K. Hadynska, J. Iwanicki, P.J. Napiorkowsko, J. Srebrny, K. Wrzosek, M. Zielinska, A.N. Andreyev, N. Bree, T.E. Cocolios, J. Diriken, M. Huyse, O. Ivanov, N. Patronis, P. Van Duppen, L. Achouri, F. Delaunay, M. Marquès, N.A. Orr, T. Behrens, V. Bildstein, T. Fästermann, R. Gernhäuser, Th. Kröll, R. Krücken, P. Mahgoub, M. Maierbeck, K. Wimmer, T. Davinson, P. Woods, P.T. Greenlees, P. Jones, R. Julin, S. Juutinen, P. Peura, P. Rahkila, P.A. Butler, T. Grahn, R.-D. Hersberg, D.T. Joss, R.D. Page, E.S. Paul, J. Pakarinen, A. Petts, M. Scheck, I. Stefanescu, D.G. Jenkins, and A. Robinson. Thallium isobaric contaminants of neutron-deficient polonium beams from UCx-RILIS units at ISOLDE. Status report to the CERN INTC - related to the proposal for experiment IS479.

[Bas07] B. Bastin, S. Grévy, D. Sohler, O. Sorlin, Zs. Dombràdi, N.L. Achouri, J.C. Angélique, F. Azaiez, D. Baiborodin, R. Borcea, C. Bourgeois, A. Buta, A. Bürger, R. Chapman, J.C. Dalouzy, Z. Dlouhy, A. Drouard, Z. Elekes, S. Franchoo, S. Iacob, B. Laurent, M. Lazar, X. Liang, B. Liénard, J. Mrazek, L. Naplas, F. Negoita, N.A. Orr, Y. Penionzhkevich, Zs. Podolyàk, F. Pougheon, P. Roussel-Chomaz, M.G. Saint-Laurent, M. Stanoiu, I. Stefan, F. Nowacki, and A. Poves. Collapse of the $N = 28$ shell closure in ^{42}Si. *Physical Review Letters*, 99 (2007) 022503.

[Bas09] B. Bastin. private communication, 2009.

[Ben06] M. Bender, G.F. Bertsch, and P.-H. Heenen. Global study of quadrupole correlation effects. *Physical Review C*, 73 (2006) 034322.

[Ber97] P. Van den Bergh, S. Franchoo, J. Gentens, M. Huyse, Yu.A. Kudryavtsev, A. Piechaczek, R. Raabe, I. Reusen, P. Van Duppen, L. Vermeeren, and A. Wohr. The SPIG, improvement of the efficiency and beam qutwoality of an ion-guide based on-line isotope separator. *Nuclear Instruments and Methods in Nuclear Physics Research B*, 126 (1997) 194–197.

[Ber03] U.C. Bergmann, G. Auböck, R. Catherall, J. Cederkäll, C.Aa. Diget, L.M. Fraile, S. Franchoo, H. Fynbo, H. Gausemel, U. Georg, T. Giles, H. Jeppesen, O.C. Jonsson, U. Köster, J. Lettry, T. Nilsson, K. Peräjärvi, H. Ravn, K. Riisager, L. Weissman, J. Äystö, and ISOLDE Collaboration. Production yields of noble-gas isotopes from ISOLDE UC_x/graphite targets. *Nuclear Instruments and Methods in Nuclear Physics Research B*, 204 (2003) 220–224.

[Bij95] N. Bijnens, P. Decrock, S. Franchoo, M. Gaelens, M. Huyse, H.-Y. Hwang, I. Reusen, J. Szerypo, J. von Schwarzenberg, J. Wauters, J.G. Correia, A. Jokinen, and P. Van Duppen. Intruder states and the onset of deformation in the neutron-deficient even-even polonium isotopes. *Physical Review Letters*, 75 (1995) 4571–4574.

[Bla03] K. Blaum, C. Geppert, H.-J. Kluge, M. Mukherjee, S. Schwarz, and K. Wendt. A novel scheme for a highly selective laser ion source. *Nuclear Instruments and Methods in Nuclear Physics Research B*, 204 (2003) 331–335.

[Boh50] A. Bohr and V.W. Weisskopf. The influence of nuclear structure on the hyperfine structure of heavy elements. *Physical Review*, 77 (1950) 94–98.

[Bou07a] E. Bouquerel. private communication, 2007.

[Bou07b] E. Bouquerel, R. Catherall, M. Eller, J. Lettry, S. Marzari, and T. Stora. Purification of Zn radioactive ion beam by alkali suppression in a quartz line target prototype. *European Physical Journal - Special Topics*, 150 (2007) 277–280.

[Bre08] N. Bree, I. Stefanescu, P.A. Butler, J. Cederkäll, J. Davinson, P. Delahaye, J. Eberth, D. Fedorov, V.N. Fedosseev, L.M. Fraile, S. Franchoo, G. Georgiev, K. Gladnishki, M. Huyse, O. Ivanov, J. Jolie, U. Köster, Th. Kröll, R. Krücken, B.A. Marsh, O. Nidermaier, P. Reiter, H. Scheit, D. Schwalm, T. Sieber, J. Van de Walle, P. Van Duppen, N. Warr, D. Weisshaar, F. Wenander, and S. Zemlyanoy. Coulomb excitation of $^{68}_{28}Ni_{40}$ at "safe" energies. *Physical Review C*, 78 (2008) 047301.

[Buc83] B. Buck and S.M. Perez. New look at magnetic moments and beta decays of mirror nuclei. *Physical Review Letters*, 50 (1983) 1975–1978.

[Büt84] S. Büttgenbach. Magnetic hyperfine anomalies. *Hyperfine Interactions*, 20 (1984) 1–64.

[Cam95] P. Campbell, J. Billowes, J.A. Behr, G. Gwinner, S.D. Sprouse, and F. Xu. Isotope shifts of the neutron-deficient bismuth isotopes: charge radii systematics across the $Z = 82$ shell closure. *Physics Letters B*, 346 (1995) 21–26.

[Cas00] R.F. Casten. *Nuclear structure from a simple perspective.* Orford University Press, Oxford, UK, 2000.

[cer] http://www.cern.ch/. Multimedia section.

[Cha66] G.W. Charles. Spectra of ^{208}Po and the hyperfine structure of ^{209}Po. *Journal of the Optical Society of America*, 56 (1966) 1292–1297.

[Coc09] T.E. Cocolios, A.N. Andreyev, B. Bastin, N. Bree, J. Büscher, J. Elseviers, J. Gentens, M. Huyse, Yu. Kudryavtsev, D. Pauwels, T. Sonoda, P. Van den Bergh, and P. Van Duppen. Magnetic dipole moment of ^{57,59}Cu measured by in-gas-cell laser spectroscopy. *Physical Review Letters*, 103 (2009) 102501.

[crc] http://www.cyc.ucl.ac.be/.

[Dav06] D.A. Davies, D.J. Morrissey, G. Bollen, P.A. Lofy, S. Schwarz, and J. Ottarson. A laser ablation ion source for gas cell studies. *Nuclear Instruments and Methods in Nuclear Physics Research A*, 569 (2006) 883–889.

[De 04] H. De Witte, A.N. Andreyev, I.N. Borzov, E. Curier, J. Cederkäll, A. De Smet, S. Eeckhaudt, D.V. Fedorov, V.N. Fedosseev, S. Franchoo, M. Górska, H. Grawe, G. Huber, M. Huyse, Z. Janas, U. Köster, W. Kurcewicz, J. Kurpeta, A. Plochocki, K. Van de Vel, P. Van Duppen, and L. Weissman. First observation of the β decay of neutron-rich ^{218}Bi by the pulsed-release technique and resonant laser ionization. *Physical Review C*, 69 (2004) 044305.

[De 07] H. De Witte, A.N. Andreyev, N. Barré, M. Bender, T.E. Cocolios, S. Dean, D. Fedorov, V.N. Fedoseyev, L.M. Fraile, S. Franchoo, V. Hellemans, P.H. Heenen, K. Heyde, G. Huber, M. Huyse, H. Jeppessen, U. Köster, P. Kunz, S.R. Lesher, B.A. Marsh, I. Mukha, B. Roussière, J. Sauvage, M. Seliverstov, I. Stefanescu, E. Tengborn, K. Van de Vel, J. Van de Walle, P. Van Duppen, and Yu. Volkov. Nuclear charge radii of neutron deficient lead isotopes beyond N=104 mid-shell investigated by in-source laser spectroscopy. *Physical Review Letters*, 98 (2007) 112502.

[Dea04a] S. Dean. *The beta-decay of neutron-deficient rhodium and ruthenium isotopes.* Katholieke Universiteit Leuven, 2004.

[Dea04b] S. Dean, M. Górska, F. Aksouh, H. de Witte, M. Facina, M. Huyse, O. Ivanov, K. Krouglov, Yu. Kudryavtsev, I. Mukha, D. Dmirnov, J.-C.

Thomas, K. Van de Vel, J. Van de Walle, P. Van Duppen, and J. Van Roosbroeck. The beta decay of neutron-deficient rhodium and ruthenium isotopes. *European Physical Journal A*, 21 (2004) 243–255.

[Den92] P. Dendooven. *Reflektieasymmetrie in het actinidegebied: α-vervalstudies met behulp van de ionengeleidertechniek*. Katholieke Universiteit Leuven, 1992.

[Dex10] W. Dexters. In-source laser spectroscopy of neutron-rich polonium isotopes ^{211,216,218}po at ISOLDE. Master's thesis, Katholieke Universiteit Leuven, 2010.

[Din87] U. Dinger, J. Eberz, G. Huber, R. Menges, S. Schröder, R. Kirchner, O. Klepper, T. Kühl, D. Marx, and G.D. Sprouse. Inuclearmoments and change in the charge radii of neutron deficient lead isotopes. *Zeitschrift für Physik A*, 328 (1987) 253–254.

[Dug03] T. Duguet, M. Bender, P. Bonche, and P.-H. Heenen. Shape coexistence in ^{186}Pb: beyond-mean-field description by configuration mixing of symmetry restored wave functions. *Physics Letters B*, 559 (2003) 201–206.

[Dut91] S.B. Dutta, R. Kirchner, O. Klepper, T.U. Kühl, D. Marx, G.D. Sprouse, R. Menges, U. Dinger, G. Huber, and S. Schröder. Measurement of the isotop shift and hyperfine splitting of ^{190,191,193,197}Pb isotopes by collinear laser spectroscopy. *Zeitschrift für Physik A*, 341 (1991) 39–45.

[DW04] H. De Witte. *Probing the nuclear structure along the $Z = 82$ closed shall: decay- and laser spectroscopic studies of exotic Pb, Bi and Po nuclei*. Katholieke Universiteit Leuven, 2004.

[Ell73] C. Ellegaard, P.D. Barnes, R. Eisenstein, E. Romberg, T.S. Bhatia, and T.R. Canada. Inelastic scattering of deuterons, protons and tritons on ^{210}Po. *Nuclear Physics A*, 206 (1973) 83–96.

[Els09] J. Elseviers. Electron-capture-delayed fission of ^{180}Tl. Master's thesis, Katholieke Universiteit Leuven, 2009.

[eur] http://www.eurisol.org/.

[Fac04a] M. Facina. *A gas catcher for nthe selective production of radioactive beams through laser ionzation*. Katholieke Universiteit Leuven, 2004.

[Fac04b] M. Facina, B. Bruyneel, S. Dean, J. Gentens, M. Huyse, Yu. Kudryavtsev, P. Van den Bergh, and P. Van Duppen. A gas cell for thermalizing, storing and transporting radioactive ions and atoms. Part II: on-line studies with a laser ion source. *Nuclear Instruments and Methods in Nuclear Physics Research B*, 226 (2004) 401–418.

[Fla09] K.T. Flanagan, P. Vingerhoets, M. Avgoulea, J. Billowes, M.L. Bissell, K. Blaum, B. Cheal, M. De Rydt, V.N. Fedosseev, D.H. Forest, Ch. Geppert, J. Krämer, A. Krieger, U. Köster, M. Kowalska, K.L. Kratz, E. Mané, B.A. Marsh, T. Materna, L. Mathieu, P.L. Molkanov, R. Neugart, G. Neyens, W. Nörterhäuser, J. Rikovska Stone, M.D. Seliverstov, O. Serot, M. Schug, M.A. Sjoedin, N.J. Stone, H.H. Stroke, G. Tungate, D.T. Yordanov, and Yu.M. Volkov. Nuclear spins and magnetic moments of ^{71,73,75}Cu: inversion of $\pi p_{3/2}$ and $f_{5/2}$ levels in ^{75}cu. *Physical Review Letters*, 103 (2009) 142501.

[For01] O. Forstner, H. Herndl, H. Oberhummer, H. Schatz, and B.A. Brown. Thermonuclear reaction rate of ^{56}Ni$(p,\gamma)^{57}$Cu and ^{57}Cu$(p,\gamma)^{58}$Zn. *Physical Review C*, 64 (2001) 045801.

[Fra98] S. Franchoo, M. Huyse, K. Krugov, Yu. Kudryavtsev, W.F. Mueller, R. Raabe, R. Reusen, P. Van Duppen, J. Van Roosbroack, L. Vermeeren, A. Wöhr, K.-L. Kratz, B. Pfeiffer, and W.B. Walters. Beta decay of $^{68-74}$Ni and level- structure of neutron-rich Cu isotopes. *Physical Review Letters*, 81 (1998) 3100–3103.

[Fra99] S. Franchoo. *Evolution of nuclear structure towards ^{78}Ni investigated by the β decay of laser-ionized $^{68-74}$Ni.* Katholieke Universiteit Leuven, 1999.

[Fra01] S. Franchoo, M. Huyse, K. Kruglov, Yu. Kudryavtsev, W.F. Mueller, R. Raabe, I. Reusen, P. Van Duppen, J. Van Roosbroeck, L. Vermeeren, A. Wöhr, H. Grawe, K.-L. Kratz, B. Pfeiffer, and B. Walters. Monopole migration in ^{69,71,73}Cu observed from beta decay of laser-ionized ^{6874}Ni. *Physical Review C*, 64 (2001) 054308.

[fri] http://www.frib.msu.edu/.

[Fri01] S. Fritzsche. RATIP - a toolbox for studying the properties of open-shell atoms and ions. *Journal of Electron Spectroscopy and Related Phenomena*, 114-116 (2001) 1155–1164.

[Fri02] S. Frizsche. Large-scale accurate structure calculations for open-shell atoms and ions. *Physica Scripta*, T100 (2002) 37–46.

[Fri05] G. Fricke and K. Heilig. *Nuclear charge radii.* Springer, Berlin, Germany, 2005.

[Gad03] A. Gade, D. Bazin, C.M. Campbell, J.A. Church, D.C. Dinca, J. Enders, T. Glasmacher, Z. Hu, K.W. Kemper, W.F. Mueller, H. Olliver, B.C. Perry, L.A. Riley, B.T. Roeder, B.M. Sherrill, and J.R. Terry. Detailed experimental study on intermadiate-energy coulomb excitation of ^{46}Ar. *Physical Review C*, 68 (2003) 014302.

[Gau09] L. Gaudefroy, J.M. Daugas, M. Hass, S. Grévy, Ch. Stodel, J.C. Thomas, L. Perrot, M. Girod, B. Rossé, J.C. Angélique, D.L. Balabanski, E. Fiori, G. Force, F. amd Georgiev, D. Kameda, V. Kumar, R.L. Lozeva, I. Matea, V. Méot, P. Morel, B.S. Nara Singh, F. Nowacki, and G. Simpson. Shell erosion and shape coexistence in $^{43}_{16}S_{27}$. *Physical Review Letters*, 102 (2009) 092501.

[Gil66] V. Gillet, A.M. Green, and A. Sanderson. Particle-hole excitations in ^{208}pb. *Nuclear Physics*, 88 (1966) 321–343.

[GM50] M. Goeppert Mayer. Nuclear configurations in the spin-orbit coupling model. I. Empirical evidence. *Physical Review*, 78 (1950) 16–21.

[Gol04] V.V. Golovko, I. Kraev, T. Phalet, N. Severijns, B. Delauré, M. Beck, V. Kozlov, A. Lindroth, S. Versyck, D. Zákoucký, D. Vénos, D. Srnka, M. Honusek, P. Herzog, C. Tramm, U Köster, and I.S. Towner. Nuclear magnetic moment of ^{59}Cu with on-line β-NMR on oriented nuclei. *Physical Review C*, 70 (2004) 014312.

[Gra08] T. Grahn, A. Dewald, O. Möller, R. Julin, C.W. Beausang, S. Christen, I.G. Darby, S. Eeckhaudt, P.T. Greenelees, A. Görgen, K. Helriutta, J. Jolie, P. Jones, S. Juutinen, H. Kettunen, T. Kröll, R. Krücken, Y. Le Coz, M. Leino, A.-P. Leppänen, P. Maierbeck, D.A. Meyer, B. Melon, P. Nieminen, M. Nyman, R.D. Page, J. Pakarinen, P. Petkov, P. Rahkila, B. Saha, M. Sanzelius, J. Sarén, C. Scholey, J. Uusitalo, M. Bender, and P.-H. Heenen. Lifetimes of intruder states in ^{186}Pb, ^{188}Pb and ^{194}Po. *Nuclear Physics A*, 801 (2008) 83–100.

[Hab] D. Habs, O. Kester, F. Ames, Th. Sieber, H. Bongers, S. Emhofer, M. Loewe, P. Reiter, R. Lutter, P. Thirolf, M. Groß, D. Schwalm, R. von Hahn, H. Scheit, O. Niedermaier, F. Wenander, T. Nilsson, U. Bergmann, J. Cederkäll, B. Wolf, S. Franchoo, K. Reisinger, J. Eberth, D. Weißhaar, N. Warr, J. Julie, P. Van Duppen, M. Huyse, T. Davinson, P. Butler, T. Faestermann, and R. Krücken. Coulomb excitation of neutron-rich $A \sim 140$ nuclei. Proposal to the CERN INTC - accepted under experiment number IS411.

[Hag06] U. Hager, T. Eronen, J. Hakala, A. Jokinen, V.S. Kolhinen, S. Kopecky, I. Moore, A. Nieminen, M. Oinonen, S. Rinta-Antila, J. Szerypo, and J. Äystö. First precision mass measurements of refractory fission fragments. *Physical Review Letters*, 96 (2006) 042504.

[Hag07] U. Hager, V.-V. Elomaa, T. Eronen, J. Hakala, A. Jokinen, A. Kankainen, S. Rahaman, S. Rinta-Antila, A. Saastamoinen, T. Sonoda, and J. Äystö. Precision mass measurements of neutron-rich Tc, Ru, Rh, and Pd isotopes. *Physical Review C*, 75 (2007) 064302.

[Hel96] K. Helariutta, T. Enqvist, P. Jones, R. Julin, S. Juutinen, P. Jämsen, H. Kankaanpää, P. Kuusiniemi, M. Leino, M. Muikku, M. Piiparinen, A. Savelius, W.H. Trzaska, S. Törmänen, J. Uusitalo, R.G. Allatt, P.A. Butler, P.T. Greenlees, and R.D. Page. First observation of excited states in ^{192}Po. *Physical Review C*, 54 (1996) R2799–R2801.

[Hey90] K.L.G. Heyde. *The nuclear shell model*. Springer-Verlag, New York, NY, 1990.

[Hon04] M. Honma, T. Otsuka, B.A. Brown, and T. Mizusaki. New effective interaction for pf-shell nuclei and its implication for the stability of the $N = Z = 28$ closed core. *Physical Review C*, 69 (2004) 034335.

[Hul61] R.J. Hull and H.H. Stroke. Nuclear moments and isotope shifts of Tl^{199},Tl^{200},Tl^{201},Tl^{202}, and Tl^{204} - isotope shifts in odd-odd nuclei. *Physical Review*, 122 (1961) 1574–1575.

[iso] http://isolde.web.cern.ch/isolde/.

[iup] http://www.iupac.org/web/nt/2009-07-21_naming_element_112.

[Iva07] O. Ivanov. *Decay of ^{66}Fe studied with a new beta-gamma detection setup at LISOL*. Katholieke Universiteit Leuven, 2007.

[Jon71] B. Jonson, M. Alpsten, Å. Appelqvist, and G. Astner. Properties of neutron-deficient odd-masspolonium isotopes. *Nuclear Physics A*, 174 (1971) 225–250.

[Jul01] R. Julin, K. Helariutta, and M. Muikku. Intruder states in very neutron-deficient Hg, Pb and Po nuclei. *Journal of Physics G*, 27 (2001) R109–R139.

[Kan05] A. Kankainen, G.K. Vorobjev, S.A. Eliseev, W. Huang, J. Huikari, A. Jokinen, A. Nieminen, Yu.N. Novikov, H. Penttila, A.V. Popov, S. Rinta-Antila, H. Schatz, D.M. Seliverstov, Yu.P. Suslov, and J. Äystö. Isomers of astrophysical interest in neutron-deficient nuclei at masses $A = 81, 85, 86$. *European Physical Journal A*, 25 (2005) 355–363.

[Kar07] P. Karvonen, T. Sonoda, I.D. Moore, J. Billowes, A. Jokinen, T. Kessler, H. Penttilä, A. Popov, B. Tordoff, and J. Äystö. List developments at igisol. *European Physical Journal - Special Topics*, 150 (2007) 283–284.

[Kes08] T. Kessler. *Development and application of laser technologies at radioactive ion beam facilities*. University of Jyväskylä, 2008.

[Kin84] W.H. King. *Isotope shift in atomic spectra*. Plenum Press, New York, NY, 1984.

[Klu03] H.-J. Kluge and W. Nörterhäuser. Lasers for nuclear physics. *Spectrochimica Acta B*, 58 (2003) 1031–1045.

[Kor76] A. Korman, D. Chlebowska, T. Kempisty, and S. Chojnacki. Excited states in ^{199}Bi,^{201}Bi, ^{203}Bi isotopes. *Acta Physica Polonica B*, 7 (1976) 141–157.

[Kös02] U. Köster. Resonance ionization laser ion sources. *Nuclear Physics A*, 701 (2002) 441c–451c.

[Kös07] U. Köster, P. Carbonez, A. Dorsival, J. Dvorak, R. Eichler, S. Fernandes, H. Frånberg, J. Neuhausen, A. Novackova, R. Wilfinger, and A. Yakushev. (Im-)possible ISOL beams. *European Physical Journal - Special Topics*, 150 (2007) 285–291.

[Kow91] D. Kowalewska, K. Bekk, S. Göring, A. Hanser, W. Kälber, G. Meisel, and H. Rebel. Isotope shifts and hyperfine structure in polonium isotopes by atomic-beam laser spectroscopy. *Physical Review A*, 44 (1991) R1142–R1445.

[Kra88] K.S. Krane. *Introductory nuclear physics*. Wiley, New York, NY, 1988.

[Kud96] Yu. Kudryavtsev, J. Andrzejewski, N. Bijnens, S. Franchoo, J. Gentens, M. Huyse, A. Piechaczek, J. Szerypo, I. Reusen, P. Van Duppen, P. Van Den Bergh, L. Vermeeren, J. Wauters, and J. Wöhr. Beams of short lived nuclei produced by selective laser ionization in a gas cell. *Nuclear Instruments and Methods in Nuclear Physics Research B*, 114 (1996) 350–365.

[Kud01] Yu. Kudryavtsev, B. Bruyneel, J. Gentens, M. Huyse, P. Van den Bergh, P. Van Duppen, and L. Vermeeren. A gas cell for thermalizing, storing and transporting radioactive ions and atoms. Part I: off-line studies with a laser ion source. *Nuclear Instruments and Methods in Nuclear Physics Research B*, 179 (2001) 412–435.

[Kud03] Yu. Kudryavtsev, M. Facina, M. Huyse, J. Gentens, P. Van den Bergh, and P. Van Duppen. Beams of isotopes produced at LISOL by laser ionization after thermalization of energetic ions in a gas cell. *Nuclear Instruments and Methods in Nuclear Physics Research B*, 204 (2003) 336–342.

[Kug92] E. Kugler, D. Fiander, B. Johnson, H. Haas, A. Przewloka, H.L. Ravn, Simon D.J., and K. Zimmer. The new CERN-ISOLDE on-line mass-separator facility at the PS-Booster. *Nuclear Instruments and Methods in Nuclear Physics Research B*, 70 (1992) 41–49.

[Le 93] F. Le Blanc et al. J. Kern, editor, *Proceedings of the 8th international symposium on capture gamma-ray spectroscopy and related topics*, page 1001, World Scientific, Singapore, 1993.

[Le 99] F. Le Blanc, D. Lunney, J. Obert, J. Oms, J.C. Puteaux, B. Roussière, J. Sauvage, S. Zemlyanoi, J. Pinard, L. Cabaret, H.T. Duong, G. Huber, M. Krieg, V. Sebastian, J.E. Crawford, J.K.P Lee, M. Girod, S. Péru, J. Genevey, and J. Lettry. Large odd-even radius staggering in the very light platinum isotopes fromlaser spectroscopy. *Physical Review C*, 60 (1999) 054310.

[Let97] J. Lettry, R. Catherall, P. Drumm, P. Van Duppen, A.H.M. Evensen, G.J. Focker, A. Jokine, O.C. Jonsson, E. Kugler, H. Ravn, and ISOLDE collaboration. Pulse shape of the ISOLDE radioactive ion beams. *Nuclear Instruments and Methods in Nuclear Physics Research B*, 126 (1997) 130–134.

[Lis03] A.F. Lisetskiy, N. Pietralla, M. Honma, A. Schmidt, I. Schneider, A. Gade, P. von Brentano, T. Otsuka, T. Mizusaki, and B.A. Brown. Experimental evidence for ^{56}Ni-core breaking form the low-spin structure of the $N = Z$ nucleus $^{58}_{29}\mathrm{Cu}_{29}$. *Physical Review C*, 68 (2003) 034316.

[Luk06] S. Lukić, F. Gevaert, A. Kelić, M.V. Ricciardi, K.-H. Schmidt, and O. Yordanov. Systematic comparison of ISOLDE-SC yields with calculated in-target production rates. *Nuclear Instruments and Methods in Nuclear Physics Research A*, 565 (2006) 784–800.

[Luk07] S. Lukić. private communication, 2007.

[Lut78] O. Lutz, H. Oehler, and P. Kroneck. ^{63}Cu and ^{65}Cu Fourier transform nuclear magnetic resonance studies. *Zeitschrift für Physik A*, 288 (1978) 17–21.

[Mai60] M. Maiman. Stimulated optical radiation in ruby masers. *Nature*, 187 (1960) 493–494.

[Man09a] E. Mané, J. Billowes, K. Blaum, P. Campbell, B. Cheal, P. Delahaye, K.T. Flanagan, D.H. Forest, H. Franberg, C. Geppert, T. Giles, A. Jokinen, M. Kowalska, R. Neugart, G. Neyens, W. Nörterhäuser, I. Podadera, G. Tungate, P. Vingerghoets, and D.T. Yordanov. An ion cooler-buncher for high-sensitivity collinear laser spectroscopy at ISOLDE. *European Physical Journal A*, 2009DOI: 10.1140/epja/i2009–10828–0.

[Man09b] E. Mané Jr. *High resolution laser spectroscopy of radioactive isotopes using a rfq cooler-buncher at CERN-ISOLDE*. University of Manchester, 2009.

[Men69] Di Mendeleev. Sootnoshenie svoistv s atomnym vesoom elementov. *Zhurnal Ruskogo Khimicheskogo Obshchestva*, 1869.

[Min06] K. Minamisono, P.F. Mantica, T.J. Mertzimekis, A.D. Davies, M. Hass, J. Pereira, J.S. Pinter, W.F. Rogers, J.B. Stoker, B.E. Tomlin, and R.R.

Weerasiri. Nuclear magnetic moment of the ^{57}Cu ground state. *Physical Review Letters*, 96 (2006) 102501.

[Mis93] V.I. Mishin, V.N. Fedoseyev, H.-J. Kluge, V.S. Letokhov, H.L. Ravn, F. Scheerer, Y. Shirakabe, S. Sundell, and O. Tengblad. Chemically selective laser ion-source for the CERN-ISOLDE on-line mass separator facility. *Nuclear Instruments and Methods in Nuclear Physics Research B*, 73 (1993) 550–560.

[Möl95] P. Möller, J.R. Nix, W.D. Myers, and W.J. Switecki. Nuclear ground-state masses and deformations. *Atomic Data and Nuclear Data Tables*, 59 (1995) 185–381.

[Moo05] I.D. Moore, A. Nieminen, J. Billowes, Ch. Geppert, A. Jokinen, T. Kessler, B.A. Marsh, H. Penttilä, S. RInta-Antilla, B. Tordoff, K.D.A. Wendt, and J. Äystö. Development of a laser ion source at igisol. *Journal of Physics G*, 31 (2005) S1499–S1502.

[Mye69] W.D. Myers and W.J. Swiatecki. Average nuclear properties. *Annals of Physics*, 55 (1969) 395–505.

[Mye74] W.D. Myers and W.J. Swiatecki. The nuclear droplet model for arbitrary shapes. *Annals of Physics*, 84 (1974) 186–210.

[Mye83] W.D. Myers and K.-H. Schmidt. An update on droplet-model charge distributions. *Nuclear Physics A*, 410 (1983) 61–73.

[Nav00] P. Navrátil, J.P. Vary, and B.R. Barrett. Properties of ^{12}C in the *ab initio* nuclear shell model. *Physical Review Letters*, 84 (2000) 5728–5731.

[Ney03] G. Neyens. Nuclear magnetic and quadrupole moments for nuclear structure research on exotic nuclei. *Reports on Progress in Physics*, 66 (2003) 633–689.

[nnd] http://www.nndc.bnl.gov/.

[Nör06] W. Nörterhäuser and P. Campbell. LaSpec at FAIR's low energy beamline: a new perspective for laser spectroscopy of radioactive nuclei. *Hyperfine Interactions*, 171 (2006) 149–156.

[Ott76] E.W. Otten. Topics in atomic hyperfine structure and isotope shift. *Hyperfine Interactions*, 2 (1976) 127–149.

[Oza00] A. Ozawa, T. Kobayashi, T. Suzuki, K. Yoshida, and I. Tanihata. New magic number,$N = 16$, near the neutron drip line. *Physical Review Letters*, 84 (2000) 5493–5495.

[Par96] F.A. Parpia, C. Froese Fischer, and I.P. Grant. GRASP92: a package for large-scale relativistic atomic structure calculations. *Computer Physics Communications*, 94 (1996) 249–271.

[Pau24] W. Pauli. Zur Frage der theoretischen Deutung der Satelliten einiger Spektrallinien und ihrer Beeindflussung durch magnetische Felder. *Die Naturwissenschaften*, 12 (1924) 741–743.

[Pau08a] D. Pauwels, O. Ivanov, N. Bree, J. Büscher, T.E. Cocolios, J. Gentens, M. Huyse, A. Korgul, Yu. Kudryavtsev, R. Raabe, M. Sawicka, I. Stefanescu, J. Van de Walle, P. Van den Bergh, P. Van Duppen, and W.B. Walters. Shape isomerism at $N = 40$: Discovery of a proton intruder state in ^{67}Co. *Physical Review C*, 78 (2008) 041307R.

[Pau08b] D. Pauwels, O. Ivanov, J. Büscher, T.E. Cocolios, J. Gentens, M. Huyse, A. Korgul, Yu. Kudryavtsev, R. Raabe, M. Sawicka, I. Stefanescu, J. Van de Walle, P. Van den Bergh, and P. Van Duppen. Decay correlations in the seconds range with laser-ionized, mass-separated beams. *Nuclear Instruments and Methods in Nuclear Physics Research B*, 266 (2008) 4600–4605.

[Pau09] D. Pauwels. *Nuclear structure around $Z = 28$ and $N = 40$ investigated by the beta decay of Fe, Co and Ni isotopes.* Katholieke Universiteit Leuven, 2009.

[Per06] O. Perru, O. Sorlin, S. Franchoo, F. Azaiez, E. Bouchez, C. Bourgeois, A. Chatillon, J.M. Daugas, Z. Dlouhy, Zs. Dombrádi, C. Donzaud, L. Gauderoy, H. Grawe, S. Grévy, D. Guillemaud-Mueller, F. Hammache, F. Ibrahim, Y. Le Coz, S.M. Lukyanov, I. Matea, J. Mrazek, F. Nowacki, Yu.-E. Penionzhkevich, F. de Oliveira Santos, F. Pougheon, M.G. Saint-Laurent, G. Sletten, M. Stanoiu, C. Stodel, Ch. Thiesen, and D. Verney. Enhnaced core polarization in ^{70}Ni and ^{74}Zn. *Physical Review Letters*, 96 (2006) 232501.

[Pie02] S.C. Pieper, K. Varga, and R.B. Wiringa. Quantum Monte Carlo calculations of $A = 9, 10$ nuclei. *Physical Review C*, 66 (2002) 044310.

[Ram01] S. Raman, C.W. Nestor Jr., and P. Tikkanen. Transition probability from the ground state to the first-excited 2^+ state of even-even nuclides. *Atomic Data and Nuclear Data Tables*, 78 (2001) 1–128.

[Rin80] P. Ring and P. Schuck. *The nuclear many-body problem.* Springer-Verlag, New York, NY, 1980.

[s3] http://pro.ganil-spiral2.eu/spiral2/instrumentation/s3/.

[Sán06] R. Sánchez, W. Nörtershäuser, G. Ewald, D. Albers, J. Behr, P. Bricault, B.A. Bushaw, A. Dax, J. Dilling, M. Dombsky, G.W.F. Drake, S. Götte, R. Kirchner, H.-J. Kluge, Th. Kühl, J. Lassen, C.D.P. Levy, M.R. Pearson, E.J. Prime, V. Ryjkov, A. Wojtaszek, Z.-C. Yan, and C. Zimmermann. Nuclear charge radii of ^{9,11}Li: the influence of halo neutrons. *Physical Review Letters*, 96 (2006) 033002.

[Sch66] F.P. Schäfer, W. Schmidt, and J. Volze. Organic dye solution laser. *Applied Physics Letters*, 9 (1966) 306–309.

[Sel69] E.C. Seltzer. K X-ray isotope shifts. *Physical Review*, 188 (1969) 1916–1919.

[Sel09] M.D. Seliverstov, A.N. Andreyev, N. Barré, A.E. Barzakh, S. Dean, H. De Witte, D.V. Fedorov, V.N. Fedosseyev, L.M. Fraile, S. Franchoo, J. Genevey, G. Huber, M. Huyse, U. Köster, P. Kunz, S.R. Lesher, B.A. Marsh, I. Mukha, B. Roussière, J. Sauvage, I. Stefanescu, K. Van de Vel, P. Van Duppen, and Yu.M. Volkov. Charge radii and magnetic moments of odd-A $^{183-189}$Pb isotopes. *European Physical Journal A*, 41 (2009) 315–321.

[Sem96] D.R. Semon, M.C. Allen, H. Dejbakhsh, C.A. Gagliardi, S.E. Hale, J. Jiang, L. Trache, R.E. Tribble, S.J. Yennello, H.M. Xu, and X.G. Zhou. l-forbidden Gammow-Teller β decay pf ^{57}Cu. *Physical Review C*, 53 (1996) 96–105.

[Sim] http://simion.com/.

[Son09] T. Sonoda, M. Wada, A. Takamine, K. Okada, P. Schury, A. Yoshida, T . Kubo, Y. Matsuo, T. Furukawa, T. Wakui, T. Shinozuka, H. Iimura, Y. Yamazaki, I. Katayama, S. Ohtani, H. Wollnik, H.A. Schüßler, Yu. Kudryavtsev, P. Van Duppen, and M. Huyse. Restoration of RI-beams froma projectile fragment separator by laser ionization gas catcher -PALIS-. *AIP Conference Proceedings*, 1104 (2009) 132–137.

[Sor02] O. Sorlin, S. Lennhardt, C. Donzaud, J. Duprat, F. Azaiez, F. Nowacki, H. Grawe, Zs. Dombrádi, F. Amorini, A. Astier, D. Baiborodin, M. Belleguic, C. Borcea, C. Bourgeois, D.M. Cullen, Z. Dlouhy, E. Dragulescu, M. Górska, S. Grévy, D. Guillemaud-Mueller, G. Hagemann, B. Herskind, J. Kiener, R. Lemmon, M. Lewitowicz, S.M. Lukyanov, P. Mayet, F. de Oliveira Santos, D. Pantalica, Yu.-E. Penionzhkevich, F. Pougheon, A. Poves, N. Redon, M.G. Saint-Laurent, J.A. Scarpaci, G. Sletten, M. Stanoiu, O. Tarasov, and Ch. Theisen. $^{68}_{28}$Ni$_{40}$: magicity versus superfluidity. *Physical Review Letters*, 88 (2002) 092501.

[Sor08] O. Sorlin and M.-G. Porquet. Nuclear magic numbers: new features far from stability. *Progress in Particle and Nuclear Physics*, 61 (2008) 602–673.

[Ste07] I. Stefanescu, G. Georgiev, F. Ames, J. Äystö, D.L. Balabanski, G. Bollen, P.A. Butler, J. Cederkäll, N. Champault, T. Davinson, A. De Maesschalck, P. Delahaye, J. Eberth, D. Fedorov, V.N. Fedosseev, L.M. Fraile, S. Franchoo, K. Gladnishki, D. Habs, K. Heyde, M. Huyse, O. Ivanov, J. Iwanicki, J. Jolie, B. Jonson, Th. Kröll, R. Krücken, O. Kester, U. Köster, A. Lagoyannis, L. Lilijeby, G. Lo Bianco, B.A. Marsh, O. Niedermaier, T. Nilsson, M. Oinonen, G. Pascovici, P. Reiter, A. Saltarelli, H. Scheit, D. Schwalm, T. Sieber, N. Smirnova, J. Van de Walle, P. Van Duppen, S. Zemlyanoi, N. Warr, D. Weisshaar, and F. Wenander. Coulomb excitation of ^{68,70}Cu: first use of postaccelerated isomeric beams. *Physical Review Letters*, 98 (2007) 122701.

[Sto85] R.E. Stone, C.R. Bingham, L.L. Riedinger, R.W. Lide, H.K. Carter, R.L. Mlekodaj, and E.H. Spejewski. Decay of mass-separated ^{199}Po^{m} and ^{199}Po^{g}. *Physical Review C*, 31 (1985) 582–592.

[Sto08a] N.J. Stone, U. Köster, J. Rokovska Stone, D.V. Fedorov, V.N. Fedoseyev, K.T. Flanagan, M. Hass, and M. Lakshmi. Magnetic dipole moment of ^{58}Cu and ^{59}Cu by in-source laser spectroscopy. *Physical Review C*, 77 (2008) 067302.

[Sto08b] N.J. Stone, K. Van Esbroeck, J. Rokovska Stone, M. Honma, T. Giles, M. Veskovic, G. White, A. Wöhr, V.I. Mishin, V.N. Fedoseyev, U. Köster, P.F. Mantica, and W.B. Walters. Nuclear dipole moment of ^{71}Cu from online β-NMR measurements. *Physical Review C*, 77 (2008) 014315.

[Sun92] S. Sundell and H. Ravn. Ion source with combined cathode and transfer line heating. *Nuclear Instruments and Methods in Nuclear Physics Research B*, 70 (1992) 160–164.

[sur] http://www.gsi.de/forschung/ap/projects/laser/survey.html.

[Tow87] I.S. Towner. Quenching of spin matrix elements in nuclei. *Physics Report*, 155 (1987) 263–377.

[Tri04] W. Trimble, G. Savard, B. Blank, J.A. Clark, F. Buchinger, T.E. Cocolios, J.E. Crawford, A. Frankel, J.P. Green, S. Gulick, J.K.P. Lee, A. Levand, M. Portillo, K.S. Sharma, J.C. Wang, B.J. Zabransky, and Z. Zhou. Development and first on-line tests of the RIA gas catcher prototype. *Nuclear Physics A*, 746 (2004) 415C–418C.

[Ulm86] G. Ulm, S.K. Bhattacherjee, P. Dabkiewicz, G. Huber, H.-J. Kluge, T. Kühl, H. Lochmann, E.-W. Otten, and K. Wendt. Isotope shift of ^{182}Hg and an update on nuclear moments and charge radii in the isotope range ^{181}Hg-^{206}Hg. *Zeitschrift für Physik A*, 325 (1986) 247–259.

[Van98] P. Van Duppen, A.N. Andreyev, J. Äystö, A.-H. Evensen, M. Huhta, M. Huyse, A. Jokinen, M. Karny, E. Kugler, J. Kurpeta, J. Lettry, A. Nieminen, A. Plochocki, M. Ramdhane, H.L. Ravn, K. Rykaczewski, J. Szerypo, G. Walter, A. Wöhr, and ISOLDE collaboration. A new pulsed release method for element selective production of neutron rich isotopes neat ^{208}Pb. *Nuclear Instruments and Methods in Nuclear Physics Research B*, 134 (1998) 267–270.

[Van04] J. Van Roosbroeck, C. Guénaut, G. Audi, K. Beck, D. andBlaum, G. Bollen, J. Cederkall, P. Delahaye, A. De Maesschalck, H. De Witte, D. Fedorov, V.N. Fedoseyev, S. Franchoo, H.O.U. Fynbo, M. Górska, F. Herfurth, K. Heyde, M. Huyse, A. Kellerbauer, H.-J. Kluge, U. Köster, K. Kruglov, D. Lunney, V.I. Mishin, W.F. Mueller, Sz. Nagy, S. Schwarz, L. Schweikhard, N.A. Smirnova, K. Van de Vel, P. Van Duppen, A. Van Dyck, W.B. Walters, L. Weissman, and C. Yazidjian. Unambiguous identification of three β-decaying isomers in ^{70}Cu. *Physical Review Letters*, 92 (2004) 112501.

[VD06] P. Van Duppen. Isotope separation on line and post acceleration. *Lecture Notes in Physics*, 700 (2006) 37–77.

[Vel03] K. Van de Vel, A.N. Andreyev, R.D. Page, H. Kettunen, P.T. Greenlees, P. Jones, R. Julin, S. Juutinen, H. Kankaanpää, A. Keenan, P. Kuusiniemi, M. Leino, M. Muikku, P. Nieminen, P. Rahkila, J. Uusitalo, K. Eskola, A. Hürstel, M. Huyse, Y. Le Coz, M.B. Smith, P. Van Duppen, and R. Wyss. In-beam γ-ray spectroscopy of ^{190}Po: first observation of a low-lying prolate band in Po isotopes. *European Physical Journal A*, 17 (2003) 167–171.

[Vin10] P. Vingerhoets. *Laser spectroscopy of the copper isotopes at COLLAPS*. Katholieke Universiteit Leuven, 2010.

[vW35] C.F. von Weizsäcker. Zur Theorie der Kernmassen. *Zeitschrift für Physik A*, 96 (1935) 431–458.

[Wad09] M. Wada, A. Takamine, K. Okada, T. Sonoda, P. Schury, Y. Yamazaki, Y. Kanai, T.M. Kojima, A. Yoshida, T. Kubo, H. Iimura, I. Katayama, S. Ohtani, H. Wollnik, and Schüßler. Precision hyperfine structure spectroscopy of be isotopes and SLOWRI prototype and prospects of SLOWRI at RIKEN. *AIP Conference Proceedings*, 1120 (2009) 109–113.

[Wau91] J. Wauters, P. Decrock, P. Dendooven, M. Huyse, P. Lievens, G. Reusen, and P. Van Duppen. The influence of recoil losses in subsequent α decay on the determination of α-branching ratios. *Nuclear Instruments and Methods in Nuclear Physics Research B*, 61 (1991) 178–182.

[Wau92] J. Wauters, P. Dendooven, M. Huyse, G. Reusen, and P. Van Duppen. α-decay propertiesof neutron-deficient polonium and radon nuclei. *Physical Review C*, 47 (1992) 1447–1454.

[Wau93] J. Wauters, P. Dendooven, M. Huyse, G. Reusen, P. Van Duppen, and P. Lievens. Alpha decay properties of neutron-deficient polonium and radon nuclei. *Physical Review C*, 47 (1993) 1447–1454.

[Wei02] L. Weissman, U. Köster, R. Catherall, S. Franchoo, U. Georg, O. Jonsson, V.N. Fedoseyev, V.I. Mishin, M.D. Seliverstov, J. Van Roosbroeck, S. Gheysen, M. Huyse, K. Kruglov, G. Neyens, and P. Van Duppen. Magnetic moments of ^{68}Cu^{g,m} and ^{70}Cu^{g,m_1,m_2} nuclei measured by in-source laser spectroscopy. *Physical Review C*, 65 (2002) 024315.

[Woo92] J.L. Wood, K.H. Heyde, W. Nazarewicz, M. Huyse, and P. Van Duppen. Coexistence in even-mass nuclei. *Physics Report*, 215 (1992) 101–201.

[Yuk35] Hi. Yukawa. On the interaction of elementary particles I. *Proceedings of the Physical and Mathematical Society of Japan*, 17 (1935) 48–57.

[Yur04] K.L. Yurkewicz, D. Bazin, B.A. Brown, C.M. Campbell, J.A. Church, D.C. Dinca, A. Gade, T. Glasmacher, M. Honma, T. Mizusaki, W.F. Mueller, H. Olliver, T. Otsuka, L.A. Riley, and J.R. Terry. Nuclear structure in the vicinity of $N = Z = 28$ ^{56}Ni. *Physical Review C*, 70 (2004) 054319.

Paper I bibliography

[1] G. Ulm, S.K. Bhattacherjee, P. Dabkiewicz, G. Huber, H.-J. Kluge, T. Kühl, H. Lochmann, E.-W. Otten, K. Wendt, S.A. Ahmad, W. Klempt, and R. Neugart. Isotope shift of ^{182}Hg and an update of nuclear moments and charge radii in the isotope range ^{181}Hg-^{206}Hg. *Zeitschrift für Physik A*, 325 (1986) 247–259.

[2] A.N. Andreyev, M. Huyse, P. Van Duppen, L. Weissman, D. Ackermann, J. Gerl, F.P. Heßberger, S. Hofmann, A. Kleinböl, G Münzenberger, S¿ Reshitko, C. Schlegel, H. Schaffner, P. Cagarda, M. Matos, S. Saro, A. Keenan, C. Moore, C.D. O'Leary, R.D. Page, M. Taylor, H. Kettunen, M. Leino, A. Lavrentiev, R. Wyss, and K. Heyde. A triplet of differently shaped spin-zero states in the atomic nucleus ^{186}Pb. *Nature*, 405 (2000) 430–433.

[3] A.N. Andreyev, M. Huyse, P. Van Duppen, J.F.C. Cocks, H. Helriutta, P. Kuusiniemi, M. Leino, W.H. Trzaska, K. Eskola, and R. Wyss. Hindered ($\Delta l = 0$) alpha decay and shape staggering in ^{191}Po. *Physical Review Letters*, 82 (1999) 1819–1822.

[4] H. De Witte, A.N. Andreyev, N. Barré, M. Bender, T.E. Cocolios, S. Dean, D. Fedorov, V.N. Fedoseyev, L.M. Fraile, S. Franchoo, V. Hellemans, P.H. Heenen, K. Heyde, G. Huber, M. Huyse, H. Jeppessen, U. Köster, P. Kunz, S.R. Lesher, B.A. Marsh, I. Mukha, B. Roussière, J. Sauvage, M. Seliverstov, I. Stefanescu, E. Tengborn, K. Van de Vel, J. Van de Walle, P. Van Duppen, and Yu. Volkov. Nuclear charge radii of neutron-deficient lead isotopes beyond $N = 104$ midshell investigated by in-source laser spectroscopy. *Physical Review Letters*, 98 (2007) 112502.

[5] E. Kugler, D. Fiander, B. Jonson, H. Haas, A. Przewloka, H.L. Ravn, D.J. Simon, and K. Zimmer. The new CERN-ISOLDE on-line mass-separator facility at the PS-Booster. *Nuclear Instruments and Methods in Nuclear Physics Research B*, 70 (1992) 41–49.

[6] U. Köster, V.N. Fedoseyev, A.N. Andreyev, U.C. Bergmann, R. Catherall, J. Cederkäll, M. Dietrich, H. De Witte, D.V. Fedorov, L. Fraile, S. Franchoo, H. Fynbo, U. Georg, T. Giles, M. Gorska, M. Hannawald, M. Huyse, A. Joinet, O.C. Jonsson, K.L. Kratz, K. Kruglov, Ch. Lau, J. Lettry, V.I. Mishin, M. Oinonen, K. Partes, K. Peräjärvi, B. Pfeiffer, H.L. Ravn, M.D. Seliverstov,

P. Thirolf, K. Van de Vel, P. Van Duppen, J. Van Roosbroeck, and L. Weissman. On-line yields obtained with the ISOLDE RILIS. *Nuclear Instruments and Methods in Nuclear Physics Research B*, 204 (2003) 347–352.

[7] V.N. Fedosseev, L.-E. Berg, N. Lebas, O.J. Launila, M. Lindroos, R. Losito, B.A. Marsh, F.K. Österdahl, T. Pauchard, G. Tranströmer, and J. Vannesjö. ISOLDE RILIS: new beams, new facilities. *Nuclear Instruments and Methods in Nuclear Physics Research B*, 266 (2008) 4378–4382. Proceedings to the EMIS 2007 conference.

[8] D. Kowalewska, K. Bekk, S. Göring, A. Hanser, W. Kälber, G. Meisel, and H. Rebel. Isotope shifts and hyperfine structure in polonium isotopes by atomic-beam laser spectroscopy. *Physical Review A*, 44 (1991) R1142–R1445.

[9] G.W. Charles. Spectra of ^{208}Po and the hyperfine structure of ^{209}Po. *Journal of the Optical Society of America*, 56 (1966) 1292–1297.

[10] E. Hagebø, P. Hoff, O.C. Jonsson, E. Kugler, J.P. Omtvedt, H.K. Ravn, and K. Steffensen. New production systems at ISOLDE. *Nuclear Instruments and Methods in Nuclear Physics Research B*, 70 (1992) 165–174.

[11] S. Sundell and H. Ravn. Ion source with combine cathode and transfer line heating. *Nuclear Instruments and Methods in Nuclear Physics Research B*, 70 (1992) 160–164.

[12] S. Lukić. private communication, 2007.

[13] S. Lukić, F. Gevaert, A. Kelić, M.V. Ricciardi, K.-H. Schmidt, and O. Yordanov. Systematic comparison of ISOLDE-SC yields with calculated in-target production rates. *Nuclear Instruments and Methods in Nuclear Physics Research A*, 565 (2006) 784–800.

[14] M. Eller, S. Miksch, J. Lettry, T. Stora, and R. Catherall. Calculation of production and decay of radioisotopes for future irradiation experiments and ion beam facilities. *European Physical Journal - Special Topic*, 150 (2007) 233–234. Proceedings to RNB7.

Paper II bibliography

[15] Yu. Kudryavtsev, J. Andrzejewski, N. Bijnens, S. Franchoo, J. Gentens, M. Huyse, A. Piechaczek, J. Szerypo, I. Reusen, P. Van Duppen, P. Van Den Bergh, L. Vermeeren, J. Wauters, and J. Wöhr. Beams of short lived nuclei produced by selective laser ionization in a gas cell. *Nuclear Instruments and Methods in Nuclear Physics Research B*, 114 (1996) 350–365.

[16] M. Huyse, M. Facina, Yu. Kudryavtsev, and P. Van Duppen. Intensity limitations of a gas cell for stopping, storing and guiding of radioactive ions. *Nuclear Instruments and Methods in Nuclear Physics Research B*, 187 (2002) 535–547.

[17] Yu. Kudryavtsev, M. Facina, M. Huyse, J. Gentens, P. Van den Bergh, and P. Van Duppen. Beams of isotopes produced at LISOL by laser ionization after thermalization of energetic ions in a gas cell. *Nuclear Instruments and Methods in Nuclear Physics Research B*, 204 (2003) 336–342.

[18] Yu. Kudryavtsev, B. Bruyneel, M. Huyse, J. Gentens, P. Van den Bergh, P. Van Duppen, and L. Vermeeren. A gas cell for thermalizing, storing and transporting radioactive ions and atoms. Part I: off-line studies with a laser ion source. *Nuclear Instruments and Methods in Nuclear Physics Research B*, 179 (2001) 412–435.

[19] S. Franchoo, M. Huyse, K. Kruglov, Yu. Kudryavtsev, W.F. Mueller, R. Raabe, I. Reusen, P. Van Duppen, J. Van Roosbroeck, L. Vermeeren, A. Wöhr, H. Grawe, K.-L. Kratz, B. Pfeiffer, and B. Walters. Monopole migration in ^{69,71,73}Cu observed from beta decay of laser-ionized $^{68-74}$Ni. *Physical Review C*, 64 (2001) 054308.

[20] I. Reusen, A.N. Andreyev, J. Andrzejewski, N. Bijnens, S. Franchoo, M. Huyse, Yu. Kudryavtsev, K. Kruglov, W.F. Mueller, A. Piechaczek, R. Raabe, K. Rykaczewski, J. Szerypo, P. Van Duppen, L. Vermeeren, J. Wauters, and A. Wöhr. Beta-decay study of ^{54,55}Ni produced by an element-selective laser ion source. *Physical Review C*, 59 (1999) 2416–2421.

[21] S. Dean, M. Gorska, F. Aksouh, H. de Witte, M. Facina, M. Huyse, O. Ivanov, K. Krouglov, Yu. Kudryavtsev, I. Mukha, D. Smirnov, J.-C. Thomas, K. Van de Vel, J. Van de Walle, P. Van Duppen, and J. Van Roosbroeck. The beta decay of

neutron-deficient rhodium and ruthenium isotopes. *European Physical Journal A*, 21 (2004) 243–255.

[22] M. Facina, B. Bruyneel, S. Dean, J. Gentens, M. Huyse, Yu. Kudryavtsev, P. Van den Bergh, and P. Van Duppen. A gas cell for thermalizing, storing and transporting radioactive ions and atoms. Part II: on-line studies with a laser ion source. *Nuclear Instruments and Methods in Nuclear Physics Research B*, 226 (2004) 401–418.

[23] A.C. Wahl. Nuclear-charge distribution and delayed-neutron yields for thermal-neutron-induced fission of ^{235}U, ^{233}U, and ^{239}Pu and for spontaneous fission of ^{252}Cf. *Atomic Data and Nuclear Data Tables*, 39 (1988) 1–156.

[24] J.F. Ziegler and J.P. Biersack. http://www.srim.org.

[25] P. Van Den Bergh, S. Franchoo, J. Gentens, M. Huyse, Yu. Kudryavtsev, A. Piechaczek, R. Raabe, I. Reusen, P. Van Duppen, L. Vermeeren, and A. Wöhr. The SPIG, improvement of the efficiency and beam quality of an ion-guide based on-line isotope separator. *Nuclear Instruments and Methods in Nuclear Physics Research B*, 126 (1997) 194–197.

[26] G. Lhersonneau, J.C. Wang, S. Hankonen, P. Dendooven, P. Jones, R. Julin, and J. Äystö. Decays of ^{110}Rh and ^{112}Rh to the near neutron midshell isotopes ^{110}Pd and ^{112}Pd. *Physical Review C*, 60 (1999) 014315.

[27] L. Weissman, N.V.S.V. Prasad, B. Bruyneel, M. Huyse, K. Kruglov, Yu. Kudryavtsev, W.F. Mueller, P. Van Duppen, and J. Van Roosbroeck. Short-lived fission products as a diagnostics tool for studying atom and ion behavior in a gas-based laser ion source. *Nuclear Instruments and Methods in Nuclear Physics Research A*, 483 (2002) 593–602.

[28] Y. Wang, P. Dendooven, J. Huikari, A. Jokinen, V.S. Kolhinen, G. Lhersonneau, A. Nieminen, S. Nummela, H. Penttilä, K. Peräjävi, S. Rinat-Antila, J. Szerypo, J.C. Wang, and Äystö. Beta decay of neutron-rich ^{116}Rh and the low-lying level structure of even-even ^{116}Pd. *Physical Review C*, 63 (2001) 024309.

[29] J. Äystö, C.N. Davids, J. Hattula, J. Honkanen, K. Honkanen, P. Jauho, R. Julin, S. Juutinen, J. Kumpulainen, T. Lönnroth, A. Pakkanen, A. Passoja, H. Penttilä, P. Taskinen, E. Verho, A. Virtanen, and M. Yoshii. Levels in ^{110}Pd, ^{112}Pd, ^{114}Pd and ^{116}Pd from the beta decays of the on-line mass separated Rh isotopes. *Nuclear Physics A*, 480 (1988) 104.

[30] M. Petrick, W.R. Plaß, K.-H. Behr, K. Brünle, L. Caceres, J. Clark, Z. Di, S. Elisseev, M. Facina, A. Fettouhi, H. Geissel, W. Hüller, M. Huyse, C. Karagiannis, B. Kindler, R. Knöbel, Yu. Kudryavtsev, J. Kurcewicz, T. Levant, Yu.A. Litvinov, B. Lommel, M. Maierb, D.J. Morrissey, G. Münzenberg, M. Portillo, G. Savard, C. Scheidenberger, P. Van Duppen, H. Weick, M. Winkler, and

B. Zabransky. Online test of the FRS ion catcher at GSI. *Nuclear Instruments and Methods in Nuclear Physics Research B*, 266 (2008) 4493–4497. Proceedings to the EMIS 2007 conference.

[31] M. Facina, C. Bachelet, M. Block, G. Bollen, D. Davies, C.M. Folden III, C. Guenaut, J. Huikari, E. Kwan, D.J. Morrissey, G.K. Pang, A. Prinke, R. Ringle, J. Savory, P. Schury, S. Schwarz, C. Sumithrarachchi, and T. Sun. Charged particle transport and extraction studies in the NSCL gas cell for stopping radioactive fragments. *Nuclear Instruments and Methods in Nuclear Physics Research B*, 266 (2008) 4471–4474. Proceedings to the EMIS 2007 conference.

[32] M. Wada, Y. Ishida, T. Nakamura, Y. Yamazaki, T. Kambara, H. Ohyama, Y. Kanai, T.M. Kojima, Y. Nakai, N. Ohshima, A. Yoshida, T. Kubo, Y. Matsuo, Y. Fukuyama, K. Okada, T. Sonoda, S. Ohtani, K. Noda, H. Kawakami, and I. Katayama. Slow RI-beams from projectile fragment separators. *Nuclear Instruments and Methods in Nuclear Physics Research B*, 204 (2003) 570.

Paper III bibliography

[33] J. Ärje, J. Äystö, H. Hyvönen, P. Taskinen, V. Koponen, J. Honkanen, A. Hautojärvi, and K. Vierinen. Submillisecond on-line mass separation of nonvolatile radioactive elements: an application of charge exchange and thermalization processes of primary recoil ions in helium. *Physical Review Letters*, 54 (1984) 99–101.

[34] J. Äystö. Development and applications of the IGISOL technique. *Nuclear Physics A*, 693 (2001) 477–494.

[35] G. Savard, J. Clark, C. Boudreau, F. Buchinger, J.E. Crawford, H. Geissel, J.P. Greene, S. Gulick, A. Heinz, J.K.P. Lee, A. Levand, M. Maier, G. Münzenberg, C. Scheidenberger, D. Seweryniak, K.S. Sharma, G. Sprouse, J. Vaz, J.C. Wang, B.J. Zabransky, and Z. Zhou. Development and operation of gas catchers to thermalize fusion-evaporation and fragmentation products. *Nuclear Instruments and Methods in Nuclear Physics Research B*, 204 (2003) 582–586.

[36] M. Facina, C. Bachelet, M. Block, G. Bollen, D. Davies, C.M. Folden III, C. Guenaut, J. Huikari, E. Kwan, D.J. Morrissey, G.K. Pang, A. Prinke, R. Ringle, J. Savory, P. Schury, S. Schwarz, C. Sumithrarachchi, and T. Sun. Charged particle transport and extraction studies in the NSCL gas cell for stopping radioactive fragments. *Nuclear Instruments and Methods in Nuclear Physics Research B*, 266 (2008) 4471–4474.

[37] M. Petrick, W.R. Plaß, K.-H. Behr, A. Brünle, L. Caceres, J. Clark, Z. Di, S. Elisseev, M. Facina, A. Fettouhi, H. Geissel, W. Hüller, M. Huyse, C. Karagiannis, B. Kindler, R. Knöbelb, Yu. Kudryavtsev, J. Kurcewicz, T. Levant, Yu.A. Litvinov, B. Lommel, M. Maier, D.J. Morrissey, G. Münzenberg, M. Portillo, G. Savard, C. Scheidenberger, P. Van Duppen, H. Weick, W. Winkler, and B. Zabransky. Online test of the FRS ion catcher at GSI. *Nuclear Instruments and Methods in Nuclear Physics Research B*, 266 (2008) 4493–4497.

[38] M. Wada, Y. Ishida, T. Nakamura, Y. Yamazaki, T. Kambara, H. Ohyama, Y. Kanai, T.M. Kojima, Y. Nakai, N. Ohshima, A. Yoshida, T. Kubo, Y. Matsuo, Y. Fukuyama, K. Okada, T. Sonoda, S. Ohtani, K. Noda, H. Kawakami, and I. Katayama. Slow RI-beams from projectile fragment separators. *Nuclear Instruments and Methods in Nuclear Physics Research B*, 204 (2003) 570–581.

[39] J.B. Neumayr, L. Beck, D. Habs, S. Heinz, J. Szerypo, P.G. Thirolf, V. Varentsov, F. Voit, D. Ackermann, D. Beck, M. Block, Z. Di, S.A. Eliseev, H. Geissel, F. Herfurth, F.P. Heßberger, S. Hofmann, H.-J. Kluge, M. Mukherjee, G. Münzenberg, M. Petrick, W. Quint, S. Rahaman, C. Rauth, D. Rodríguez, C. Scheidenberger, G. Sikler, Z. Wang, C. Weber, W.R. Plaß, M. Breitenfeldt, A. Chaudhuri, G. Marx, L. Schweikhard, A.F. Dodonov, Y. Novikov, and M. Suhonen. The ion-catcher device for SHIPTRAP. *Nuclear Instruments and Methods in Nuclear Physics Research B*, 244 (2006) 489–500.

[40] M. Huyse, M. Facina, Yu. Kudryavtsev, and P. Van Duppen. Intensity limitations of a gas cell for stopping, storing and guiding of radioactive ions. *Nuclear Instruments and Methods in Nuclear Physics Research B*, 187 (2002) 535–547.

[41] A. Takamine, M. Wada, Y. Ishida, and T. Nakamura. Space-charge effects in the catcher gas cell of a RF ion guide. *Review of Scientific Instruments*, 76 (2005) 103503.

[42] I.D. Moore. New concepts for the ion guide technique. *Nuclear Instruments and Methods in Nuclear Physics Research B*, 266 (2008) 4434–4441.

[43] P. Van Duppen, P. Dendooven, M. Huyse, L. Vermeeren, Z.N. Qamhieh, R.E. Silverans, and E. Vandeweert. A laser ion source for on-line mass separation. *Hyperfine Interactions*, 74 (1992) 193.

[44] L. Vermeeren, N. Bijnens, M. Huyse, Yu. Kudryavtsev, P. Van Duppen, J. Wauters, Z.N. Qamhieh, P. Thoen, E. Vandeweert, and R.E. Silverans. An on-line laser ion source based on resonance photoionization in a gas cell. *Physical Review Letters*, 73 (1994) 1935–1938.

[45] Yu. Kudryavtsev, J. Andrzejewski, N. Bijnens, S. Franchoo, J. Gentens, M. Huyse, A. Piechaczek, J. Szerypo, I. Reusen, P. Van Duppen, P. Van Den Bergh, L. Vermeeren, J. Wauters, and J. Wöhr. Beams of short lived nuclei produced by selective laser ionization in a gas cell. *Nuclear Instruments and Methods in Nuclear Physics Research B*, 114 (1996) 350–365.

[46] T. Kessler, I.D. Moore, Yu. Kudryavtsev, K. Peräjärvi, A. Popov, P. Ronkanen, T. Sonoda, B. Tordoff, K.D.A. Wendt, and J. Äystö. Off-line studies of the laser ionization of yttrium at the IGISOL facility. *Nuclear Instruments and Methods in Nuclear Physics Research B*, 266 (2008) 681–700.

[47] I.D. Moore, T. Kessler, T. Sonoda, Yu. Kudryavtsev, K. Peräjärvi, A. Popov, K.D.A. Wendt, and J. Äystö. *Nuclear Instruments and Methods in Nuclear Physics Research B*, xxx (2009) xxxx. to be published.

[48] M. Sewtz, H. Backe, C.Z. Dong, A. Dretzke, K. Eberhardt, S. Fritzsche, C. Grüning, R.G. Haired, G. Kube, P. Kunz, J. Lassen, W. Lauth, G. Passler, P. Schwamb, P. Thörlec, and N. Trautmann. Resonance ionization spectroscopy of fermium ($Z = 100$. *Spectrochimica Acta B*, 58 (2003) 1077–1082.

[49] Yu. Kudryavtsev, M. Facina, M. Huyse, J. Gentens, P. Van den Bergh, and P. Van Duppen. Beams of isotopes produced at LISOL by laser ionization after thermalization of energetic ions in a gas cell. *Nuclear Instruments and Methods in Nuclear Physics Research B*, 204 (2003) 336–342.

[50] M. Facina, B. Bruyneel, S. Dean, J. Gentens, M. Huyse, Yu. Kudryavtsev, P. Van den Bergh, and P. Van Duppen. A gas cell for thermalizing, storing and transporting radioactive ions and atoms. Part II: on-line studies with a laser ion source. *Nuclear Instruments and Methods in Nuclear Physics Research B*, 226 (2004) 401–418.

[51] S. Franchoo, M. Huyse, K. Kruglov, Yu. Kudryavtsev, W.F. Mueller, R. Raabe, I. Reusen, P. Van Duppen, J. Van Roosbroeck, L. Vermeeren, A. Wöhr, H. Grawe, K.-L. Kratz, B. Pfeiffer, and B. Walters. Monopole migration in ^{69,71,73}Cu observed from beta decay of laser-ionized $^{68-74}$Ni. *Physical Review C*, 64 (2001) 054308.

[52] I.B. Smirnov. Modeling of ionization produced by fast charged particles in gases. *Nuclear Instruments and Methods in Nuclear Physics Research A*, 554 (2005) 474–493.

[53] R. Vennhof. Photon detection in a gas. *Nuclear Instruments and Methods in Nuclear Physics Research A*, 563 (2006) 291–298.

[54] J.C. Levin and G.B. Armen. Studies of fluorescence and Auger decay following inner-shell photoionization. *Radiation Physics and Chemistry*, 70 (2004) 105–121.

[55] T.A. Carlson and M.O. Krause. Atomic readjustment to vacancies in the K and L shells of argon. *Physical Review*, 137 (1965) A1655–1662.

[56] P. Van Den Bergh, S. Franchoo, J. Gentens, M. Huyse, Yu. Kudryavtsev, A. Piechaczek, R. Raabe, I. Reusen, P. Van Duppen, L. Vermeeren, and A. Wöhr. The SPIG, improvement of the efficiency and beam quality of an ion-guide based on-line isotope separator. *Nuclear Instruments and Methods in Nuclear Physics Research B*, 126 (1997) 194–197.

[57] Yu. Kudryavtsev, B. Bruyneel, M. Huyse, J. Gentens, P. Van den Bergh, P. Van Duppen, and L. Vermeeren. A gas cell for thermalizing, storing and transporting radioactive ions and atoms. Part I: off-line studies with a laser ion source. *Nuclear Instruments and Methods in Nuclear Physics Research B*, 179 (2001) 412–435.

[58] K. Blaum, C. Geppert, H.-J. Kluge, M. Mukherjee, S. Schwarz, and K. Wendt. A novel scheme for a highly selective laser ion source. *Nuclear Instruments and Methods in Nuclear Physics Research B*, 204 (2003) 331–335.

[59] T. Sonoda, T.E. Cocolios, J. Gentens, M. Huyse, O. Ivanov, Yu. Kudryavtsev, D. Pauwels, P. Van den Bergh, and P. Van Duppen. The Laser Ion Source Trap (LIST) coupled to a gas cell catcher. *Nuclear Instruments and Methods in Nuclear Physics Research B*, 267 (2009) 2918–2926.

[60] L. Weissman, J. Van Roosbroeck, K. Kruglov, A.N. Andreyev, B. Bruyneel, S. Franchoo, M. Huyse, Yu. Kudryavtsev, W.F. Mueller, R. Raabe, I. Reusen, P. Van Duppen, and L. Vermeeren. A detector setup to study the decay properties of exotic nuclei. *Nuclear Instruments and Methods in Nuclear Physics Research A*, 423 (1999) 328–336.

[61] http://www.cosmosfloworks.com.

[62] L. Weissman, N.V.S.V. Prasad, B. Bruyneel, M. Huyse, K. Kruglov, Yu. Kudryavtsev, W.F. Muller, P. Van Duppen, and J. Van Roosbroeck. Short-lived fission products as a diagnostics tool for studying atom and ion behavior in a gas-based laser ion source. *Nuclear Instruments and Methods in Nuclear Physics Research A*, 483 (2002) 593–602.

[63] U. Hager, V.-V. Elomaa, T. Eronen, J. Hakala, A. Jokinen, A. Kankainen, S. Rahaman, S. Rinta-Antila, A. Saastamoinen, T. Sonoda, and J. Äystö. Precision mass measurements of neutron-rich Tc, Ru, Rh, and Pd isotopes. *Physical Review C*, 75 (2007) 064302.

[64] M. Beck. WITCH internal report. Technical report, IKS, KULeuven, 2007.

Paper IV bibliography

[65] Yu. Kudryavtsev, J. Andrzejewski, N. Bijnens, S. Franchoo, J. Gentens, M. Huyse, A. Piechaczek, J. Szerypo, I. Reusen, P. Van Duppen, P. Van den Bergh, L. Vermeeren, J. Wauters, and A. Wöhr. Beams of shoft lived nuclei produced by selective laser ionization in a gas cell. *Nuclear Instruments and Methods in Nuclear Physics Research B*, 114 (1996) 350–365.

[66] P. Van Duppen. Laser ion sources for on-line isotope separators. *Nuclear Instruments and Methods in Nuclear Physics Research B*, 126 (1997) 66–72.

[67] Yu Kudryavtsev, B. Bruyneel, M. Huyse, J. Gentens, P. Van den Bergh, P. Van Duppen, and L. Vermeeren. A gas cell for thermalizing, storing and transporting radioactive ions and atoms. Part I: Off-line studies with a laser ion source. *Nuclear Instruments and Methods in Nuclear Physics Research B*, 179 (2001) 412–435.

[68] Yu Kudryavtsev, B. Bruyneel, S. Franchoo, M. Huyse, J. Gentens, K. Kruglov, W.F. Mueller, N.V.S.V. Prasad, R. Raabe, I. Reusen, P. Van den Bergh, P. Van Duppen, J. Van Roosbroeck, L. Vermeeren, and L. Weissman. The Leuven isotope separator on-line laser ion source. *Nuclear Physics A*, 701 (2002) 465–469.

[69] M. Huyse, M. Facina, Yu. Kudryavtsev, and P. Van Duppen. Intensity limitations of a gas cell for stopping, storing and guiding of radioactive ions. *Nuclear Instruments and Methods in Nuclear Physics Research B*, 187 (2002) 535–547.

[70] Yu. Kudryavtsev, M. Facina, M. Huyse, J. Gentens, P. Van den Bergh, and P. Van Duppen. Beams of isotopes produced at LISOL by laser ionization after thermalization of energetic ions in a gas cell. *Nuclear Instruments and Methods in Nuclear Physics Research B*, 204 (2004) 336–342.

[71] M. Facina, B. Bruyneel, S. Dean, J. Gentens, M. Huyse, Yu. Kudryavtsev, P. Van den Bergh, and P. Van Duppen. A gas cell for thermalizing, storing and transporting radioactive ions and atoms. Part II: On-line studies with a laser ion source. *Nuclear Instruments and Methods in Nuclear Physics Research B*, 226 (2004) 401–418.

[72] Yu. Kudryavtsev, T.E. Cocolios, J. Gentens, M. Huyse, O. Ivanov, D. Pauwels, T. Sonoda, P. Van den Bergh, and P. Van Duppen. Dual chamber laser ion source at lisol. *Nuclear Instruments and Methods in Nuclear Physics Research B*, 267 (2009) 2908-2917.

[73] K. Blaum, C. Geppert, H.-J. Kluge, M. Mukherjee, S. Schwarz, and K. Wendt. A novel scheme for a highly selective laser ion source. *Nuclear Instruments and Methods in Nuclear Physics Research B*, 204 (2003) 331–335.

[74] I.D. Moore, A. Nieminen, J. Billowes, . Campbell, Ch. Geppert, A. Jokinen, T. Kessler, B.M. Marsh, H. Penttila, S. Rinta-Antila, B. Tordoff, K. Wendt, and J. Äystö. Development of a laser ion source at IGISOL. *Journal of Physics G*, 31 (2005) s1499–s1502.

[75] P. Karvonen, T. Sonoda, I.D. Moore, J. Billowes, A. Jokinen, T. Kessler, H. Penttila, A. Popov, B. Tordoff, and J. Äystö. LIST developments at IGISOL. *European Physical Journal - Special Topic*, 150 (2007) 183–184.

[76] J. Äystö. Development and applications of the IGISOL technique. *Nuclear Physics A*, 693 (2001) 477–494.

[77] H.J. Xu, M. Wada, J. Tanaka, H. Kawakami, S. Ohtani, and I. Katayama. A new cooling and focusing device for ion guide. *Nuclear Instruments and Methods in Nuclear Physics Research A*, 333 (1993) 274–281.

[78] S. Fujitaka, H. Wada, M.and Wang, J. Tanaka, H. Kawakami, I. Katayama, K. Ogino, H. Katsuragawa, T. Nakamura, K. Okada, and S. Ohtani. Accumulation of ions from a recoil mass separator in a new type of linear ion trap. *Nuclear Instruments and Methods in Nuclear Physics Research B*, 126 (1997) 386–391.

[79] P. Van den Bergh, S. Franchoo, J. Gentens, M. Huyse, Yu. Kudryavtsev, A. Piechaczek, R. Raabe, I. Reusen, P. Van Duppen, L. Vermeeren, and A. Wöhr. The SPIG, improvement of the efficiency and beam quality of an ion-guide based on-line isotope separator. *Nuclear Instruments and Methods in Nuclear Physics Research B*, 126 (1997) 194–197.

[80] P. Karvonen, I.D. Moore, T. Sonoda, T. Kessler, H. Penttilä, K. Peräjärvi, Ronkanen P., and J. Äystö. A sextupole ion beam guide to improve the efficiency and beam quality at IGISOL. *Nuclear Instruments and Methods in Nuclear Physics Research B*, 266 (2008) 4794–4807.

[81] H. Backe, K. Eberhardt, R. Feldmann, M. Hies, H. Kunz, W. Lauth, R. Martin, H. Schope, P. Schwamb, M. Sewtz, P. Thorle, N. Trautmann, and S. Zauner. A compact apparatus for mass selective resonance ionization spectroscopy in a buffer gas cell. *Nuclear Instruments and Methods in Nuclear Physics Research B*, 126 (1997) 406–410.

[82] G. Yeandle, J. Billowes, P. Campbell, P. Dendooven, K. Peräjärvi, M.D. Seliverstov, and J. Tungate, G. andÄystö. Resonance ionization spectroscopy of radioisotopes at the IGISOL facility, JYFL. *Hyperfine Interaction*, 127 (2000) 91–94.

[83] http://physics.nist.gov/physrefdata/asd/index.html.

[84] J.J. Olivero and R.L. Longbothum. Empirical fits to the Voigt line width: a brief review. *Journal of Quantitative Spectroscopy and Radiative Transfer*, 17 (1977) 233–236.

[85] G.D. Alkhazov, A.E. Barzakh, V.P. Denisov, K.A. Mezilev, Yu.N. Novikov, V.N. Panteleyev, A.V. Popov, E.P. Sudentas, V.S. Letokhov, V.I. Mishin, V.N. Fedoseyev, S.V. Andreyev, D.S. Vedeneyev, and A.D. Zyuzikov. A new highly efficient method of atomic spectroscopy for nuclides far from stability. *Nuclear Instruments and Methods in Nuclear Physics Research B*, 69 (1992) 517–520.

[86] L. Weissman, U. Köster, R. Catherall, S. Franchoo, U. Georg, O. Jonsson, V.N. Fedoseyev, V.I. Mishin, M.D. Seliverstov, J. Van Roosbroeck, S. Gheysen, M. Huyse, K. Kruglov, G. Neyens, and P. Van Duppen. Magnetic moments of ^{68}Cu^{g,m} and ^{70}Cu^{g,m_1,m_2} nuclei measured by in-source laser spectroscopy. *Physical Review C*, 65 (2002) 024315.

[87] H. De Witte, A.N. Andreyev, N. Barré, M. Bender, T.E. Cocolios, S. Dean, D. Fedorov, V.N. Fedoseyev, L.M. Fraile, S. Franchoo, V. Hellemans, P.H. Heenen, K. Heyde, G. Huber, M. Huyse, H. Jeppessen, U. Köster, P. Kunz, S.R. Lesher, B.A. Marsh, I. Mukha, B. Roussière, J. Sauvage, M. Seliverstov, I. Stefanescu, E. Tengborn, K. Van de Vel, J. Van de Walle, P. Van Duppen, and Yu. Volkov. Nuclear charge radii of neutron deficient lead isotopes beyond N=104 mid-shell investigated by in-source laser spectroscopy. *Physical Review Letters*, 98 (2007) 112502.

[88] N.J. Stone, U. Köster, J. Rokovska Stone, D.V. Fedorov, V.N. Fedoseyev, K.T. Flanagan, M. Hass, and M. Lakshmi. Magnetic dipole moment of ^{5}8Cu and ^{5}9Cu by in-source laser spectroscopy. *Physical Review C*, 77 (2008) 067302.

[89] I.D. Moore, T. Kessler, J. Äystö, J. Billowes, P. Campbell, B. Cheal, B. Tordoff, M.L. Bissel, and G. Tungate. Resonance ionization spectroscopy of bismuth at the IGISOL facility. *Hyperfine Interaction*, 171 (2006) 135–141.

[90] B.A. Marsh. *In-Source Laser Resonance Ionization at ISOL Facilities*. PhD thesis, University of Manchester, 2007.

[91] T. Kessler. *Development and application of laser technologies at radioactive ion beam facilities*. PhD thesis, University of Jyväskylä, 2008.

Paper V bibliography

[92] M. Goeppert Mayer. Nuclear configurations in the spin-orbit coupling model. I. Empirical evidence. *Physical Review*, 78 (1950) 16–21.

[93] O. Sorlin and M.-G. Porquet. Nuclear magic numbers: new features far from stability. *Progress in Particle and Nuclear Physics*, 61 (2008) 602–673.

[94] B. Bastin, S. Grévy, D. Sohler, O. Sorlin, Zs. Dombrádi, N.L. Achouri, J.C. Angélique, F. Azaiez, D. Baiborodin, R. Borcea, C. Bourgeois, A. Buta, A. Bürger, R. Chapman, J.C. Dalouzy, Z. Dlouhy, A. Drouard, Z. Elekes, S. Franchoo, S. Iacob, B. Laurent, M. Lazar, X. Liang, E. Liénard, J. Mrazek, L. Nalpas, F. Negoita, N.A. Orr, Y. Panionzhkevich, Zs. Podolyák, F. Pougheon, P. Roussel-Chomaz, M.G. Saint-Laurent, M. Stanoiu, I. Stefan, F. Nowacki, and A. Poves. Collapse of the $N = 28$ shell closure in ^{42}Si. *Physical Review Letters*, 99 (2007) 022503.

[95] L. Gaudefroy et al. Shell erosion and shape coexistence in $^{43}_{16}S_{27}$. *Physical Review Letters*, 102 (2009) 092501.

[96] K.L. Yurkewicz, D. Bazin, B.A. Brown, C.M. Campbell, J.A. Church, D.C. Dinca, A. Gade, T. Glasmacher, M. Honma, T. Mizusaki, W.F. Mueller, H. Olliver, T. Otsuka, L.A. Riley, and J.R. Terry. Nuclear structure in the vicinity of $N = Z = 28$ ^{56}Ni. *Physical Review C*, 70 (2004) 054319.

[97] O. Perru, O. Sorlin, S. Franchoo, F. Azaiez, E. Bouchez, C. Bourgeois, A. Chatillon, J.M. Daugas, Z. Dlouhy, Zs. Dombrádi, C. Donzaud, L. Gaudefroy, H. Grawe, S. Grévy, F. Guillemaud-Mueller, D. ans Hammache, F. Ibrahim, Y. Le Coz, S.M. Lukyanov, I. Matea, J. Mrazek, F. Nowacki, Yu.-E. Penionzhkevich, F. de Olivera Santos, F. Pougheon, M.G. Saint-Laurent, G/ Sletten, M. Stanoiu, C. Stodel, Ch. Thiesen, and D. Verney. Enhanced core polarization in ^{70}Ni and ^{74}Zn. *Physical Review Letters*, 96 (2006) 232501.

[98] G. Audi, A.H. Wapstra, and C. Thibault. The AME2003 atomic mass evaluation. *Nuclear Physics A*, 729 (2003) 337–676.

[99] G. Kraus, P. Egelhof, C. Fischer, H. Geissel, A. Himmler, F. Nickel, G. Müzenberg, W. Schwab, A. Weiss, J. Friese, A. Gillitzer, H.J. Körner, M. Peter, W.F. Henning, J.P. Schiffer, J.V. Kratz, L. Chulkov, M. Golovkov,

A. Ogloblin, and B.A. Brown. Proton inelastic scattering on ^{56}Ni in inverse kinematics. *Physical Review Letters*, 73 (1994) 1773–1776.

[100] A.F. Lisetskiy, N. Pietralla, M. Honma, A. Schmidt, I. Schneider, A. Gade, P. von Bretano, T. Otsuka, T. Mizusaki, and B.A. Brown. Experimental evidence for ^{56}Ni-core breaking form the low-spin structure of the $N = Z$ nucleus $^{58}_{29}$Cu$_{29}$. *Physical Review C*, 68 (2003) 034316.

[101] M. Honma, T. Otsuka, B.A. Brown, and T. Mizusaki. New effective interaction for pf-shell nuclei and its implication for the stability of the $N = Z = 28$ closed core. *Physical Review C*, 69 (2004) 034335.

[102] J. Rikovska, T. Giles, N.J. Stone, K. van Esbroeck, G. White, A. Wöhr, M. Veskovic, I.S. Towner, P.F. Mantica, J.I. Prisciandaro, D.J. Morrissey, V.N. Fedoseyev, V.I. Mishin, U. Köster, and W.B. Walters. First on-line beta-NMR on oriented nuclei: magnetic dipole moments of the $(\nu p_{1/2})^{-1}$ $1/2^-$ ground state in ^{67}Ni and $(\pi p_{3/2})^{+1}$ $3/2^-$ ground state in ^{69}Cu. *Physical Review Letters*, 85 (2000) 1392–1395.

[103] L. Weissman, U. Köster, R. Catherall, S. Franchoo, U. Georg, O. Jonsson, V.N. Fedoseyev, V.I. Mishin, M.D. Seliverstov, J. Van Roosbroeck, S. Gheysen, M. Huyse, K. Kruglov, G. Neyens, and P. Van Duppen. Magnetic moments of ^{68}Cu^{g,m} and ^{70}Cu^{g,m_1,m_2} nuclei measured by in-source laser spectroscopy. *Physical Review C*, 65 (2002) 024315.

[104] V.V. Golovko, I. Kraev, T. Phalet, N. Severijns, B. Delauré, M. Beck, V. Kozlov, A. Lindroth, S. Versyck, D. Zákoucký, D. Vénos, D. Srnka, M. Honusek, P. Herzog, C. Tramm, U. Köster, and I.S. Towner. Nuclear magnetic moment of ^{59}Cu with on-line β-NMR on oriented nuclei. *Physical Review C*, 70 (2004) 014312.

[105] K. Minamisono, P.F. Mantica, T.J. Mertzimekis, A.D. Davies, M. Hass, J. Pereira, J.S. Pinter, W.F. Rogers, J.B. Stoker, B.E. Tomlin, and R.R. Weerasiri. Nuclear magnetic moment of the ^{57}Cu ground state. *Physical Review Letters*, 96 (2006) 102501.

[106] N.J. Stone, U. Köster, J. Rikovska Stone, D. Fedorov, V.N. Fedoseyev, K.T. Flanagan, M. Hass, and S. Lakshmi. Magnetic dipole moment of ^{5}8Cu and ^{5}9Cu by in-source laser spectroscopy. *Physical Review C*, 77 (2008) 067302.

[107] N.J. Stone, K. Van Esbroeck, J. Rikovska Stone, M. Honma, T. Giles, M. Veskovic, G. White, A. Wöhr, V.I. Mishin, V.N. Fedoseyev, U. Köster, P.F. Mantica, and W.B. Walters. Nuclear dipole moment of ^{71}Cu from online β-NMR measurements. *Physical Review C*, 77 (2008) 014315.

[108] D.R. Semon, M.C. Allen, H. Dejbakhsh, C.A. Gagliardi, S.E. Hale, J. Jiang, L. Trache, R.E. Tribble, S.J. Yennello, H.M. Xu, X.G. Zhou, and B.A. Brown.

l-forbidden Gammow-Teller β decay pf ^{57}Cu. *Physical Review C*, 53 (1996) 96–105.

[109] T. Sonoda, T.E. Cocolios, J. Gentens, M. Huyse, O. Ivanov, Yu. Kudryavtsev, D. Pauwels, P. Van den Bergh, and P. Van Duppen. The Laser Ion Source Trap (LIST) coupled to a gas cell catcher. *Nuclear Instruments and Methods B*, 267 (2009) 2918–2926.

[110] Yu. Kudryavtsev, T.E. Cocolios, J. Gentens, M. Huyse, O. Ivanov, D. Pauwels, T. Sonoda, P. Van den Bergh, and P. Van Duppen. Dual chamber laser ion source at LISOL. *Nuclear Instruments and Methods B*, 267 (2009) 2908–2917.

[111] Yu. Kudryavtsev, B. Bruyneel, J. Gentens, M. Huyse, P. Van den Bergh, P. Van Duppen, and L. Vermeeren. A gas cell for thermalizing, storing and transporting radioactive ions and atoms. Part I: off-line studies with a laser ion source. *Nuclear Instruments and Methods B*, 179 (2001) 412–435.

[112] D. Pauwels, O. Ivanov, J. Büscher, T.E. Cocolios, J. Gentens, M. Huyse, A. Korgul, Yu. Kudryavtsev, R. Raabe, M. Sawicka, I. Stefanescu, J. Van de Walle, P. Van den Bergh, and P. Van Duppen. Decay correlations in the seconds range with laser-ionized, mass-separated beams. *Nuclear Instruments and Methods B*, 266 (2008) 4600–4605.

[113] H. Figger, D. Schmitt, and S. Penselin. Direct measurement of the magnetic dipole moments of the nuclei Cu^{63}, Cu^{65} and Rb^{87} and determination of the chemical shift for some Cu- and Rb-compounds. *Coll. int. du CNRS*, 164 (1967) 355.

[114] O. Lutz, H. Oehler, and P. Kroneck. 63Cu and 65Cu Fourier transform nuclear magnetic resonance studies. *Zeitschrift für Physics A*, 288 (1978) 17–21.

[115] N.J. Stone. Table of nuclear magnetic dipole and electric quadrupole moments. *Atomic Data and Nuclear Data Tables*, 90 (2005) 75–176.

[116] I.S. Towner. Quenching of spin matrix elements in nuclei. *Physics Report*, 155 (1987) 263–377.

[117] T. Ohtsubo, D.J. Cho, Y. Yanagihashi, S. Ohya, and S. Muto. Measurement of the nuclear magnetic moments of 57ni and 59fe. *Physical Review C*, 54 (1996) 554–558.

[118] B. Buck, A.C. Merchant, and S.M. Perez. Magnetic moments of mirror nuclei. *Physical Review C*, 63 (2001) 037301.

[119] B. Buck and S.M. Perez. New look at magnetic moments and beta decays of mirror nuclei. *Physical Review Letters*, 50 (1983) 1975–1978.

[120] K. Blaum, C. Geppert, H.-J. Kluge, M. Mukherjee, S. Schwarz, and K. Wendt. A novel scheme for a highly selective laser ion source. *Nuclear Instruments and Methods B*, 204 (2003) 331–335.

Paper VI bibliography

[121] B. Bastin, S. Grévy, D. Sohler, O. Sorlin, Zs. Dombrádi, N.L. Achouri, J.C. Angélique, F. Azaiez, D. Baiborodin, R. Borcea, C. Bourgeois, A. Buta, A. Bürger, R. Chapman, J.C. Dalouzy, Z. Dlouhy, A. Drouard, Z. Elekes, S. Franchoo, S. Iacob, B. Laurent, M. Lazar, X. Liang, E. Liénard, J. Mrazek, L. Nalpas, F. Negoita, N.A. Orr, Y. Panionzhkevich, Zs. Podolyák, F. Pougheon, P. Roussel-Chomaz, M.G. Saint-Laurent, M. Stanoiu, I. Stefan, F. Nowacki, and A. Poves. Collapse of the $N = 28$ shell closure in ^{42}Si. *Physical Review Letters*, 99 (2007) 022503.

[122] L. Gaudefroy, J.M. Daugas, M. Hass, S. Grévy, Ch. Stodel, J.-C. Thomas, L. Perrot, M. Girod, B. Rossé, J.C. Angélique, D.L. Balabanski, E. Fiori, C. Force, G. Georgiev, D. Kameda, V. Kumar, R.L. Lozeva, I. Matea, V. Méot, P. Morel, B.S. Nara Singh, and G. Nowacki, F. ans Simpson. Shell erosion and shape coexistence in $^{43}_{16}S_{27}$. *Physical Review Letters*, 102 (2009) 092501.

[123] K.L. Yurkewicz, D. Bazin, B.A. Brown, C.M. Campbell, J.A. Church, D.C. Dinca, A. Gade, T. Glasmacher, M. Honma, T. Mizusaki, W.F. Mueller, H. Olliver, T. Otsuka, L.A. Riley, and J.R. Terry. Nuclear structure in the vicinity of $N = Z = 28$ ^{56}Ni. *Physical Review C*, 70 (2004) 054319.

[124] O. Perru, O. Sorlin, S. Franchoo, F. Azaiez, E. Bouchez, C. Bourgeois, A. Chatillon, J.M. Daugas, Z. Dlouhy, Zs. Dombrádi, C. Donzaud, L. Gaudefroy, H. Grawe, S. Grévy, F. Guillemaud-Mueller, D. ans Hammache, F. Ibrahim, Y. Le Coz, S.M. Lukyanov, I. Matea, J. Mrazek, F. Nowacki, Yu.-E. Penionzhkevich, F. de Olivera Santos, F. Pougheon, M.G. Saint-Laurent, G/ Sletten, M. Stanoiu, C. Stodel, Ch. Thiesen, and D. Verney. Enhanced core polarization in ^{70}Ni and ^{74}Zn. *Physical Review Letters*, 96 (2006) 232501.

[125] G. Audi, A.H. Wapstra, and C. Thibault. The AME2003 atomic mass evaluation. *Nuclear Physics A*, 729 (2003) 337–676.

[126] G. Kraus, P. Egelhof, C. Fischer, H. Geissel, A. Himmler, F. Nickel, G. Müzenberg, W. Schwab, A. Weiss, J. Friese, A. Gillitzer, H.J. Körner, M. Peter, W.F. Henning, J.P. Schiffer, J.V. Kratz, L. Chulkov, M. Golovkov, A. Ogloblin, and B.A. Brown. Proton inelastic scattering on ^{56}Ni in inverse kinematics. *Physical Review Letters*, 73 (1994) 1773–1776.

[127] A.F. Lisetskiy, N. Pietralla, M. Honma, A. Schmidt, I. Schneider, A. Gade, P. von Bretano, T. Otsuka, T. Mizusaki, and B.A. Brown. Experimental evidence for ^{56}Ni-core breaking form the low-spin structure of the $N = Z$ nucleus $^{58}_{29}\mathrm{Cu}_{29}$. *Physical Review C*, 68 (2003) 034316.

[128] M. Honma, T. Otsuka, B.A. Brown, and T. Mizusaki. New effective interaction for pf-shell nuclei and its implication for the stability of the $N = Z = 28$ closed core. *Physical Review C*, 69 (2004) 034335.

[129] J. Rikovska, T. Giles, N.J. Stone, K. van Esbroeck, G. White, A. Wöhr, M. Veskovic, I.S. Towner, P.F. Mantica, J.I. Prisciandaro, D.J. Morrissey, V.N. Fedoseyev, V.I. Mishin, U. Köster, and W.B. Walters. First on-line beta-NMR on oriented nuclei: magnetic dipole moments of the $(\nu p_{1/2})^{-1}$ $1/2^-$ ground state in ^{67}Ni and $(\pi p_{3/2})^{+1}$ $3/2^-$ ground state in ^{69}Cu. *Physical Review Letters*, 85 (2000) 1392–1395.

[130] L. Weissman, U. Köster, R. Catherall, S. Franchoo, U. Georg, O. Jonsson, V.N. Fedoseyev, V.I. Mishin, M.D. Seliverstov, J. Van Roosbroeck, S. Gheysen, M. Huyse, K. Kruglov, G. Neyens, and P. Van Duppen. Magnetic moments of $^{68}\mathrm{Cu}^{g,m}$ and $^{70}\mathrm{Cu}^{g,m_1,m_2}$ nuclei measured by in-source laser spectroscopy. *Physical Review C*, 65 (2002) 024315.

[131] V.V. Golovko, I. Kraev, T. Phalet, N. Severijns, B. Delauré, M. Beck, V. Kozlov, A. Lindroth, S. Versyck, D. Zákoucký, D. Vénos, D. Srnka, M. Honusek, P. Herzog, C. Tramm, U. Köster, and I.S. Towner. Nuclear magnetic moment of ^{59}Cu with on-line β-NMR on oriented nuclei. *Physical Review C*, 70 (2004) 014312.

[132] K. Minamisono, P.F. Mantica, T.J. Mertzimekis, A.D. Davies, M. Hass, J. Pereira, J.S. Pinter, W.F. Rogers, J.B. Stoker, B.E. Tomlin, and R.R. Weerasiri. Nuclear magnetic moment of the ^{57}Cu ground state. *Physical Review Letters*, 96 (2006) 102501.

[133] N.J. Stone, U. Köster, J. Rikovska Stone, D. Fedorov, V.N. Fedoseyev, K.T. Flanagan, M. Hass, and S. Lakshmi. Magnetic dipole moment of ^{5}8Cu and ^{5}9Cu by in-source laser spectroscopy. *Physical Review C*, 77 (2008) 067302.

[134] N.J. Stone, K. Van Esbroeck, J. Rikovska Stone, M. Honma, T. Giles, M. Veskovic, G. White, A. Wöhr, V.I. Mishin, V.N. Fedoseyev, U. Köster, P.F. Mantica, and W.B. Walters. Nuclear dipole moment of ^{71}Cu from online β-NMR measurements. *Physical Review C*, 77 (2008) 014315.

[135] T.E. Cocolios, A.N. Andreyev, B. Bastin, N. Bree, J. Büscher, J. Elseviers, J. Gentens, M. Huyse, Yu. Kudryavtsev, D. Pauwels, T. Sonoda, P. Van den Bergh, and P. Van Duppen. Magnetic dipole moment of ^{57,59}cu measured by in-gas-cell laser spectroscopy. *Physical Review Letters*, 103 (2009) 102501.

[136] K.T. Flanagan, P. Vingerhoets, M. Avgoulea, J. Billowes, M.L. Bissell, K. Blaum, B. Cheal, M. De Rydt, V.N. Fedosseev, D.H. Forest, Ch. Geppert, J. Krämer, A. Krieger, U. Köster, M. Kowalska, K.L. Kratz, E. Mané, B.A. Marsh, T. Materna, L. Mathieu, P.L. Molkanov, R. Neugart, G. Neyens, W. Nörterhäuser, J. Rikovska Stone, M.D. Seliverstov, O. Serot, M. Schug, M.A. Sjoedin, N.J. Stone, H.H. Stroke, G. Tungate, D.T. Yordanov, and Yu.M. Volkov. Nuclear spins and magnetic moments of ^{71,73,75}Cu: inversion of $\pi p_{3/2}$ and $f_{5/2}$ levels in ^{75}cu. *Physical Review Letters*, 103 (2009) 142501.

[137] S. Büttgenbach. Magnetic hyperfine anomalies. *Hyperfine Interactions*, 20 (1984) 1–64.

[138] K.T. Flanagan. IS439: Quantum state re-ordering in neutron-rich Cu isotopes. *ISOLDE Newsletter*, 200911.

[139] M.D. Seliverstov, A.E. Barzakh, I.Ya. Chubukov, D.V. Fedorov, V.N. Panteleev, and Yu.M. Volkov. Application of the laser ion source for isotope shift and hyperfine structure investigation. *Hyperfine Interactions*, 127 (2004) 425–430.

[140] J. Lettry, R. Catherall, P. Drumm, P. Van Duppen, A.H.M. Evensen, G.J. Focker, A. Jokinen, O.C. Jonsson, R. Kugler, and H. Ravn. Pusle shape of the ISOLDE radioactive ion beams. *Nuclear Instruments and Methods in Nuclear Physics Research B*, 126 (1997) 130–134.

[141] T. Sonoda, T.E. Cocolios, J. Gentens, M. Huyse, O. Ivanov, Yu. Kudryavtsev, D. Pauwels, P. Van den Bergh, and P. Van Duppen. The Laser Ion Source Trap (LIST) coupled to a gas cell catcher. *Nuclear Instruments and Methods in Nuclear Physics Research B*, 267 (2009) 2918–2926.

[142] Yu. Kudryavtsev, T.E. Cocolios, J. Gentens, M. Huyse, O. Ivanov, D. Pauwels, T. Sonoda, P. Van den Bergh, and P. Van Duppen. Dual chamber laser ion source at LISOL. *Nuclear Instruments and Methods in Nuclear Physics Research B*, 267 (2009) 2908–2917.

[143] Yu. Kudryavtsev, B. Bruyneel, J. Gentens, M. Huyse, P. Van den Bergh, P. Van Duppen, and L. Vermeeren. A gas cell for thermalizing, storing and transporting radioactive ions and atoms. Part I: off-line studies with a laser ion source. *Nuclear Instruments and Methods in Nuclear Physics Research B*, 179 (2001) 412–435.

[144] D. Pauwels, O. Ivanov, J. Büscher, T.E. Cocolios, J. Gentens, M. Huyse, A. Korgul, Yu. Kudryavtsev, R. Raabe, M. Sawicka, I. Stefanescu, J. Van de Walle, P. Van den Bergh, and P. Van Duppen. Decay correlations in the seconds range with laser-ionized, mass-separated beams. *Nuclear Instruments and Methods in Nuclear Physics Research B*, 266 (2008) 4600–4605.

[145] Yu. Kudryavtsev, J. Andrzejewski, B. Bijnens, S. Franchoo, J. Gentens, M. Huyse, A. Piechaczek, J. Szerypo, I. Reusen, P. Van den Bergh, P. Van Duppen, L. Vermeeren, J. Wauters, and A. Wöhr. Beams of short-lived nuclei produced by selective laser ionization in a gas cell. *Nuclear Instruments and Methods in Nuclear Physics Research B*, 114 (1996) 350–365.

[146] S. Gheysen, G. Neyens, and J. Odeurs. Calculated hyperfine spectra for in-source laser spectroscopy and deduced magnetic moments and isomer shifts of ^{68}Cu and ^{70}Cu isomeric states. *Physical Review C*, 69 (2004) 064310.

[147] H. Figger, D. Schmitt, and S. Penselin. Direct measurement of the magnetic dipole moments of the nuclei Cu^{63}, Cu^{65} and Rb^{87} and determination of the chemical shift for some Cu- and Rb-compounds. *Coll. int. du CNRS*, 164 (1967) 355.

[148] O. Lutz, H. Oehler, and P. Kroneck. 63Cu and 65Cu Fourier transform nuclear magnetic resonance studies. *Zeitschrift für Physik A*, 288 (1978) 17–21.

[149] N.J. Stone. Table of nuclear magnetic dipole and electric quadrupole moments. *Atomic Data and Nuclear Data Tables*, 90 (2005) 75–176.

[150] P.R. Locher. Ratio of the magnetic dipole moments of ^{63}Cu and ^{65}Cu and the hyperfine-structure anomalies $^{63}\Delta^{65}$. *Physical Review B*, 10 (1974) 801–804.

[151] D.R. Semon, M.C. Allen, H. Dejbakhsh, C.A. Gagliardi, S.E. Hale, J. Jiang, L. Trache, R.E. Tribble, S.J. Yennello, H.M. Xu, X.G. Zhou, and B.A. Brown. l-forbidden Gammow-Teller β decay pf ^{57}Cu. *Physical Review C*, 53 (1996) 96–105.

[152] T. Ohtsubo, D.J. Cho, Y. Yanagihashi, S. Ohya, and S. Muto. Measurement of the nuclear magnetic moments of ^{57}Ni and ^{59}Fe. *Physical Review C*, 54 (1996) 554–558.

[153] P.C. Zalm, J.F.A. van Hienen, and P.W.M. Glaudemans. Simple relations for nuclear moments. *Zeitschrift für Physik A*, 287 (1978) 255–263.

[154] G. Hermann, G. Lasnitschka, C. Schwabe, and D. Spengler. Hyperfine structures ans isotopic shifts of the Cu D_1 and D_2 lines measured by high-resolution laser fluorescence spectroscopy with a collimated atomic beam. *Spectrochimica Acta*, 48B (1993) 1259–1264.

[155] W.H. King. *Isotope shift in atomic spectra.* Plenum Press, New York, NY, 1984.

[156] K. Blaum, C. Geppert, H.-J. Kluge, M. Mukherjee, S. Schwarz, and K. Wendt. A novel scheme for a highly selective laser ion source. *Nuclear Instruments and Methods in Nuclear Physics Research B*, 204 (2003) 331–335.

[157] V.P. Denisov. On high-efficient Doppler-free atomic spectroscopy of unstable nuclides. *Nuclear Instruments and Methods in Nuclear Physics Research A*, 345 (1994) 99–101.

Paper VII bibliography

[158] W. Pauli. Zur Frage der theoretischen Deutung der Satelliten einiger Spektrallinien und ihrer Beeindflussung durch magnetische Felder. *Die Naturwissenschaften*, 12 (1924) 741–743.

[159] J. Wauters, N. Bijnens, P. Dendoover, M. Huyse, H.Y. Hwang, G. Reusen, J. von Schwarzenberg, P. Van Duppen, R. Kirchner, and E. Roeckl. Fine struture in the alpha decay of even-even nuclei as an experimental proof for the stability of the $Z = 82$ magic shell at the very neutron-deficient side. *Physical Review Letters*, 72 (1994) 1329–1332.

[160] J.L. Wood, K.H. Heyde, W. Nazarewicz, M. Huyse, and P. Van Duppen. Coexistence in even-mass nuclei. *Physics Report*, 215 (1992) 101–201.

[161] R. Julin, K. Helariutta, and M. Muikku. Intruder states in very neutron-deficient Hg, Pb and Po nuclei. *Journal of Physics G*, 27 (2001) R109–R139.

[162] A.N. Andreyev, M. Huyse, P. Van Duppen, L. Weissman, D. Ackermann, J. Gerl, F.P. Heßberger, S. Hofmann, A. Kleinböl, G Münzenberger, S¿ Reshitko, C. Schlegel, H. Schaffner, P. Cagarda, M. Matos, S. Saro, A. Keenan, C. Moore, C.D. O'Leary, R.D. Page, M. Taylor, H. Kettunen, M. Leino, A. Lavrentiev, R. Wyss, and K.H. Heyde. A triplet of differently shaped spin-zero states in the atomic nucleus ^{186}Pb. *Nature*, 405 (2000) 430–433.

[163] T. Grahn, A. Dewald, O. Möller, R. Julin, C.W. Beausang, S. Christen, I.G. Darby, S. Eeckhaudt, P.T. Greenelees, A. Görgen, K. Helriutta, J. Jolie, P. Jones, S. Juutinen, H. Kettunen, T. Kröll, R. Krücken, Y. Le Coz, M. Leino, A.-P. Leppänen, P. Maierbeck, D.A. Meyer, B. Melon, P. Nieminen, M. Nyman, R.D. Page, J. Pakarinen, P. Petkov, P. Rahkila, B. Saha, M. Sanzelius, J. Sarén, C. Scholey, and J. Uusitalo. Collectivity and configuration mixing in ^{186,188}Pb and ^{194}Po. *Nuclear Physics A*, 801 (2006) 83–100.

[164] H. De Witte, A.N. Andreyev, N. Barré, M. Bender, T.E. Cocolios, S. Dean, D. Fedorov, V.N. Fedoseyev, L.M. Fraile, S. Franchoo, V. Hellemans, P.H. Heenen, K. Heyde, G. Huber, M. Huyse, H. Jeppessen, U. Köster, P. Kunz, S.R. Lesher, B.A. Marsh, I. Mukha, B. Roussière, J. Sauvage, M. Seliverstov, I. Stefanescu, E. Tengborn, K. Van de Vel, J. Van de Walle, P. Van Duppen,

and Yu. Volkov. Nuclear charge radii of neutron deficient lead isotopes beyond N=104 mid-shell investigated by in-source laser spectroscopy. *Physical Review Letters*, 98 (2007) 112502.

[165] T. Grahn, A. Dewald, O. Möller, R. Julin, C.W. Beausang, S. Christen, I.G. Darby, S. Eeckhaudt, P.T. Greenelees, A. Görgen, K. Helriutta, J. Jolie, P. Jones, S. Juutinen, H. Kettunen, T. Kröll, R. Krücken, Y. Le Coz, M. Leino, A.-P. Leppänen, P. Maierbeck, D.A. Meyer, B. Melon, P. Nieminen, M. Nyman, R.D. Page, J. Pakarinen, P. Petkov, P. Rahkila, B. Saha, M. Sanzelius, J. Sarén, C. Scholey, J. Uusitalo, M. Bender, and P.-H. Heenen. Lifetimes of intruder states in ^{186}Pb, ^{188}Pb and ^{194}Po. *Nuclear Physics A*, 801 (2008) 83–100.

[166] K. Helariutta, T. Enqvist, P. Jones, R. Julin, S. Juutinen, P. Jämsen, H. Kankaanpää, P. Kuusiniemi, M. Leino, M. Muikku, M. Piiparinen, A. Savelius, W.H. Trzaska, S. Törmänen, J. Uusitalo, R.G. Allatt, P.A. Butler, P.T. Greenlees, and R.D. Page. First observation of excited states in ^{192}Po. *Physical Review C*, 54 (1996) R2799–R2801.

[167] K. Van de Vel, A.N. Andreyev, R.D. Page, H. Kettunen, P.T. Greenlees, P. Jones, R. Julin, S. Juutinen, H. Kankaanpää, A. Keenan, P. Kuusiniemi, M. Leino, M. Muikku, P. Nieminen, P. Rahkila, J. Uusitalo, K. Eskola, A. Hürstel, M. Huyse, Y. Le Coz, M.B. Smith, P. Van Duppen, and R. Wyss. In-beam γ-ray spectroscopy of ^{190}Po: first observation of a low-lying prolate band in Po isotopes. *European Physical Journal A*, 17 (2003) 167–171.

[168] A.N. Andreyev, S. Antalic, D. Ackermann, S. Franchoo, F.P. Heßberger, S. Hofmann, M. Huyse, I. Kojouharov, B. Kindler, P. Kuusiniemi, S.R. Lesher, B. Lommel, R. Mann, G. Münzenberg, K. Nishio, R.D. Page, J.J. Ressler, B. Streicher, S. Saro, B. Sulignano, P. Van Duppen, D. Wiseman, and R. Wyss. α-decay of the new isotope ^{187}Po: probing prolate structures beyond the neutron mid-shell at $N = 104$. *Physical Review C*, 73 (2006) 044324.

[169] G.W. Charles. Spectra of ^{208}Po and the hyperfine structure of ^{209}Po. *Journal of the Optical Society of America*, 56 (1966) 1292–1297.

[170] D. Kowalewska, K. Bekk, S. Göring, A. Hanser, W. Kälber, G. Meisel, and H. Rebel. Isotope shifts and hyperfine structure in polonium isotopes by atomic-beam laser spectroscopy. *Physical Review A*, 44 (1991) R1142–R1445.

[171] W.D. Myers and K.-H. Schmidt. An update on droplet-model charge distributions. *Nuclear Physics A*, 410 (1983) 61–73.

[172] T.E. Cocolios, B.A. Marsh, V.N. Fedosseev, S. Franchoo, G. Huber, M. Huyse, A.M. Ionan, K. Johnston, U. Köster, Yu. Kudryavtsev, M.D. Seliverstov, E. Noah, T. Stora, and P. Van Duppen. Resonant laser ionization of polonium at RILIS-ISOLDE for the study of ground- en isomer-state properties.

Nuclear Instruments and Methods in Nuclear Physics Research B, 266 (2008) 4403–4406.

[173] S. Fritzsche. Large-scale accurate structure calculations for open-shell atoms and ions. *Physica Scripta*, T100 (2002) 37–46.

[174] F.A. Parpia, C. Froese Fischer, and I.P. Grant. GRASP92: a package for large-scale relativistic atomic structure calculations. *Computer Physics Communications*, 94 (1996) 249–271.

[175] S. Fritzsche. RATIP - a toolbox for studying the properties of open-shell atoms and ions. *Journal of Electron Spectroscopy and Related Phenomena*, 114-116 (2001) 1155–1164.

[176] T.E. Cocolios, A.N. Andreyev, S. Antalic, B. Bastin, A. Barzakh, J. Büscher, I.G. Darby, W. Dexters, S. Fedorov, V.N. Fedosseyev, K.T. Flanagan, S. Franchoo, G. Huber, M. Huyse, U. Keupers, M. Köster, Yu. Kudryavtsev, E. Mané, B.M. Marsh, P. Molkanov, R.D. Page, M.D. Seliverstov, M.A. Sjoedin, I. Stefan, J. Van de Walle, P. Van Duppen, M. Venhart, and S. Zemlyanoy. Intruder configurations and single particle levels in ^{191}pb. *Physical Review C*, page in preparation.

[177] M.D. Seliverstov, A.N. Andreyev, N. Barré, A.E. Barzakh, S. Dean, H. De Witte, D.V. Fedorov, V.N. Fedosseyev, L.M. Fraile, S. Franchoo, J. Genevey, G. Huber, M. Huyse, U. Köster, P. Kunz, S.R. Lesher, B.A. Marsh, I. Mukha, B. Roussière, J. Sauvage, I. Stefanescu, K. Van de Vel, P. Van Duppen, and Yu.M. Volkov. Charge radii and magnetic moments of odd-A $^{183-189}$Pb isotopes. *European Physical Journal A*, 41 (2009) 315–321.

[178] W.H. King. *Isotope shift in atomic spectra.* Plenum Press, New York, NY, 1984.

[179] E.C. Seltzer. K X-ray isotope shifts. *Physical Review*, 188 (1969) 1916–1919.

[180] P. Möller, J.R. Nix, W.D. Myers, and W.J. Switecki. Nuclear ground-state masses and deformations. *Atomic Data and Nuclear Data Tables*, 59 (1995) 185–381.

[181] M. Bender, G.F. Bertsch, and P.-H. Heenen. Global study of quadrupole correlation effects. *Physical Review C*, 73 (2006) 034322.

[182] P. Van Duppen and M. Huyse. Shape coexistence around the $Z = 82$ closed shell probed by α-decay. *Hyperfine Interactions*, 129 (2000) 149–161.

[183] K. Van de Vel. *Shape coexistence in neutron-deficient polonium and lead nuclei.* PhD thesis, Katholieke Universiteit Leuven, 2003.

[184] M. Anselments, W. Faubel, S. Göring, A. Hanser, G. Meisel, H. Rebel, and G. Schatz. The odd-even staggering of the nuclear charge radii of Pb isotopes. *Nuclear Physics A*, 451 (1986) 471–780.

[185] M.R. Pearson, P. Campbell, K. Leerungnavarat, J. Billowes, I.S. Grant, M. Keim, J. Kilgallon, I.D. Moore, R. Neugart, M. Neuroth, and S. Wilbert. Nuclear moments and charge radii of bismuth isotopes. *Journal of Physics G*, 26 (2000) 1829–1848.

[186] M.M. Sharma, G.A. Lalazissis, and P. Ring. Anomaly in the charge radii of pb isotopes. *Physics Letters B*, 317 (1993) 9–13.

Paper VIII bibliography

[187] K. Heyde, P. Van Isacker, M. Waroquier, J.L. Wood, and R.A. Meyer. Coexistence in odd-mass nuclei. *Physics Report*, 102 (1983) 291–393.

[188] J.L. Wood, K.H. Heyde, W. Nazarewicz, M. Huyse, and P. Van Duppen. Coexistence in even-mass nuclei. *Physics Report*, 215 (1992) 101–201.

[189] A.M. Oros, K.H. Heyde, C. De Coster, B. Decroix, R. Wyss, B.R. Barrette, and P. Navratil. Shape coexistence in the light Po isotopes. *Nuclear Physics A*, 645 (1999) 107–142.

[190] A.N. Andreyev, M. Huyse, P. Van Duppen, L. Weissman, D. Ackermann, J. Gerl, F.P. Heßberger, S. Hofmann, A. Kleinböl, G Münzenberg, S¿ Reshitko, C. Schlegel, H. Schaffner, P. Cagarda, M. Matos, S. Saro, A. Keenan, C. Moore, C.D. O'Leary, R.D. Page, M. Taylor, H. Kettunen, M. Leino, A. Lavrentiev, R. Wyss, and K.H. Heyde. A triplet of differently shaped spin-zero states in the atomic nucleus ^{186}Pb. *Nature*, 405 (2000) 430–433.

[191] P. Van Duppen and M. Huyse. Shape coexistence around the $Z = 82$ closed shell probed by α-decay. *Hyperfine Interactions*, 129 (2000) 149–161.

[192] R. Julin, K. Helariutta, and M. Muikku. Intruder states in very neutron-deficient Hg, Pb and Po nuclei. *Journal of Physics G*, 27 (2001) R109–R139.

[193] K. Van de Vel, A.N. Andreyev, M. Huyse, P. Van Duppen, J.F.C. Cocks, O. Dorvaux, P.T. Greenlees, K. Helariutta, P. Jones, R. Julin, S. Juutinen, H. Kettunen, P. Kuusiniemi, M. Leino, M. Muikku, P. Nieminen, K. Eskola, and R. Wyss. Identification of low-lying proton-based intruder states in $^{189-193}$Pb. *Physical Review C*, 65 (2002) 064301.

[194] A.N. Andreyev, M. Huyse, K. Van de Vel, P. Van Duppen, O. Dorvaux, P. Greenlees, K. Helariutta, P. Jones, R. Julin, S. Juutinen, H. Kettunen, P. Kuusiniemi, M. Leino, M. Muikku, P. Nieminen, P. Rahkila, J. Uusitalo, R. Wyss, K. Hauschild, and Y. Le Coz. In-beam α-decay spectroscopy of ^{191}Po and evidence for triple shape coexistence at low energy in the daughter nucleus ^{187}Pb. *Physical Review C*, 66 (2002) 014313.

[195] M. Bender, T. Cornelius, G.A. Lalazissis, J.A. Maruhn, W. Nazarewicz, and Reinhard P.-G. The $Z = 82$ shell closire in neutron-deficient Pb isotopes. *European Physical Journal A*, 14 (2002) 23–28.

[196] T. Niksić, D. Vretenar, P. Ring, and G.A. Lalazissis. Shape coexistence in the relativistic Hartree-Bogoliubov approach. *Physical Review C*, 65 (2002) 054320.

[197] K. Van de Vel, A.N. Andreyev, R.D. Page, H. Kettunen, P.T. Greenlees, P. Jones, R. Julin, S. Juutinen, H. Kankaanpää, A. Keenan, P. Kuusiniemi, M. Leino, M. Muikku, P. Nieminen, P. Rahkila, J. Uusitalo, K. Eskola, A. Hürstel, M. Huyse, Y. Le Coz, M.B. Smith, P. Van Duppen, and R. Wyss. Fine structure in the α decay of ^{188,192}Po. *Physical Review C*, 68 (2003) 054311.

[198] N. Smirnova, P.-H. Heenen, and G. Neyens. Self-consistent approach to deformation of intruder states in neutron-deficient Pb and Po. *Physics Letters B*, 569 (2003) 151–158.

[199] A. Frank, P. Van Isacker, and C.E. Vargas. Evolving shape coexistence in the lead isotopes: the geometry of configuration mixing in nuclei. *Physical Review C*, 69 (2004) 034323.

[200] V. Hellemans, S. De Bardemacker, and K.H. Heyde. Configuration mixing in the neutron-deficient $^{186-196}$Pb isotopes. *Physical Review C*, 77 (2008) 064324.

[201] T. Grahn, A. Dewald, O. Möller, R. Julin, C.W. Beausang, S. Christen, I.G. Darby, S. Eeckhaudt, P.T. Greenlees, A. Görgen, K. Helriutta, J. Jolie, P. Jones, S. Juutinen, H. Kettunen, T. Kröll, R. Krücken, Y. Le Coz, M. Leino, A.-P. Leppänen, P. Maierbeck, D.A. Meyer, B. Melon, P. Nieminen, M. Nyman, R.D. Page, J. Pakarinen, P. Petkov, P. Rahkila, B. Saha, M. Sanzelius, J. Sarén, C. Scholey, J. Uusitalo, M. Bender, and P.-H. Heenen. Lifetimes of intruder states in ^{186}Pb, ^{188}Pb and ^{194}Po. *Nuclear Physics A*, 801 (2008) 83–100.

[202] P. Van Duppen, E. Coenen, K. Deneffe, Huyse M., K. Heyde, and P. Van Isacker. Observation of low-lying $J^\pi = 0^+$ states in the single-closed-shell nuclei $^{192-198}$Pb. *Physical Review Letters*, 52 (1984) 1974–1977.

[203] E. Coenen, K. Deneffe, M. Huyse, P. Van Duppen, and J.L. Wood. α decay of neutron-deficient odd Bi nuclei: shell-model intruder states in Tl and Bi isotopes. *Physical Review Letters*, 54 (1985) 1783–1786.

[204] P. Van Duppen, E. Coenen, K. Deneffe, and M. Huyse. β^+/electron-capture decay of ^{192,194,196,198,200}bi: experimental evidence for low lying 0^+ states. *Physical Review C*, 35 (1987) 1861–1877.

[205] J.C. Griffin, R.A. Braga, R.W. Fink, J.L. Wood, H.K. Carter, R.L. Mlekodaj, C.R. Bingham, E. Coenen, M. Huyse, and P. Van Duppen. Decay of mass-separated 3.0 min ^{195g}Bi to levels in ^{195}Pb and shape coexistence in the neutron-deficient odd-mass Pb isotopes. *Nuclear Physics A*, 530 (1991) 401–419.

[206] J. Vanhorenbeeck, P. Del Marmol, E. Coenen, M. Huyse, P. Van Duppen, and J. Wauters. Highly converted transitions in ^{197}Pb: evidence for shape coexistence. *Nuclear Physics A*, 531 (1991) 63–76.

[207] K.H. Hicks, T.E. Ward, J. Wiggins, C.A. Fields, and F.W.N. de Boer. Decays of ^{194,195,196}Pb. *Physical Review C*, 25 (1982) 2710–2721.

[208] T.E. Cocolios, B.A. Marsh, V.N. Fedosseev, S. Franchoo, G. Huber, M. Huyse, A.M. Ionan, K. Johnston, U. Köster, Yu. Kudryavtsev, M.D. Seliverstov, E. Noah, T. Stora, and P. Van Duppen. Resonant laser ionization of polonium at RILIS-ISOLDE for the study of ground- en isomer-state properties. *Nuclear Instruments and Methods in Nuclear Physics Research B*, 266 (2008) 4403–4406.

[209] J.F. Ziegler. SRIM-2003. *Nuclear Instruments and Methods in Nuclear Physics Research B*, 219-220 (2004) 1027–1036.

[210] J. Van Roosbroeck, C. Guénaut, G. Audi, D. Beck, K. Blaum, G. Bollen, J. Cederkall, P. Delahaye, A. De Maesschalck, H. De Witte, D. Fedorov, V.N. Fedoseyev, S. Franchoo, H.O.U. Fynbo, M. Górska, F. Herfurth, K.H. Heyde, M. Huyse, A. Kellerbauer, H.-J. Kluge, U. Köster, K. Kruglov, D. Lunney, V.I. Mishin, W.F. Mueller, Sz. Nagy, S. Schwarz, L. Schweikhard, N.A. Smirnova, K. Van de Vel, P. Van Duppen, A. Van Dyck, W.B. Walters, L. Weissman, and C. Yazudjian. Unambiguous identification of three β-decaying isomers in ^{70}Cu. *Physical Review Letters*, 92 (2004) 112501.

[211] I. Stefanescu, G. Georgiev, F. Ames, J. Äystö, D.L. Balabanski, G. Bollen, P.A. Butler, J. Cederkäll, N. Champault, T. Davinson, A. De Maesschalck, P. Delahaye, J. Eberth, D. Fedorov, V.N. Fedosseev, L.M. Fraile, S. Franchoo, K. Gladnishki, D. Habs, K. Heyde, M. Huyse, O. Ivanov, J. Iwanicki, J. Jolie, B. Jonson, Th. Kröll, R. Krücken, O. Kester, U. Köster, A. Lagoyannis, L. Lilijeby, G. Lo Bianco, B.A. Marsh, O. Niedermaier, T. Nilsson, M. Oinonen, G. Pascovici, P. Reiter, A. Saltarelli, H. Scheit, D. Schwalm, T. Sieber, N. Smirnova, J. Van de Walle, P. Van Duppen, S. Zemlyanoi, N. Warr, D. Weisshaar, and F. Wenander. Coulomb excitation of ^{68,70}Cu: first use of postaccelerated isomeric beams. *Physical Review Letters*, 98 (2007) 122701.

[212] J. Wauters, P. Dendoovern, M. Huyse, G. Reusen, P. Van Duppen, and P. Lievens. Alpha decay properties of neutron-deficient polonium and radon nuclei. *Physical Review C*, 47 (1993) 1447–1454.

[213] S.B. Dutta, R. Kirchner, O. Klepper, T.U. Kühl, D. Marx, G.D. Sprouse, R. Menges, U. Dinger, G. Huber, and S. Schröder. Measurement of the isotope shift and hyperfine splitting of ^{190,191,193,197}Pb isotopes by collinear laser spectroscopy. *Zeitschrift für Physik A*, 341 (1991) 39–45.

[214] J. Wauters, P. Decrock, P. Dendooven, M. Huyse, P. Lievens, G. Reusen, and P. Van Duppen. The influence of recoil losses in subsequent α decay on the determination of α-branching ratios. *Nuclear Instruments and Methods in Nuclear Physics Research B*, 61 (1991) 178–182.

[215] P. Hornshøj, B. Jonson, H.L. Ravn, L. Westgaard, and O.B. Nielsen. Widths for s- and d-wave α-decay of neutron-deficient isotopes with $Z \leq 82$. *Nuclear Physics A*, 230 (1974) 365–379.

[216] J.O. Rasmussen. Alpha-decay barrier penetrabilities with an exponential nuclear potential: even-even nuclei. *Physical Review*, 113 (1959) 1593,1598.

[217] J. Wauters, P. Dendooven, P. Decrock, M. Huyse, R. Kirchner, O. Klepper, G. Reusen, E. Roeckl, and P. Van Duppen. The alpha-branching ratios of the ^{188,190,192}Pb isotopes. *Zeitschrift für Physik A*, 342 (1992) 277–282.

[218] J. Bonn, G. Huber, H.-J. Kluge, U. Köpf, L. Kugler, and E.-W. Otten. ptical pumping of neutron deficient ^{187}Hg. *Nuclear Physics A*, 230 (1974) 365–379.